Three-dimensional magnetohydrodynamic phenomena in circular pipe flow

Zur Erlangung des akademischen Grades eines
DOKTORS DER INGENIEURWISSENSCHAFTEN (Dr.-Ing.)

von der KIT-Faktultät für Maschinenbau des
Karlsruher Instituts für Technologie (KIT)
angenommene

DISSERTATION

von

M. Sc. Viktor Klüber

Tag der mündlichen Prüfung	06.02.2023
Hauptreferent	apl. Prof. Dr.-Ing. Leo Bühler
Korreferent	Prof. Dr.-Ing. Robert Stieglitz

Three-dimensional magnetohydrodynamic phenomena in circular pipe flow

Abstract

A numerical code for the simulation of liquid metal magnetohydrodynamic (MHD) flow in breeding blankets of future fusion reactors has been extended to address complex MHD phenomena in geometries with curved walls such as circular pipes. In these MHD flows, induced electric currents interact with the magnetic field that confines the fusion plasma leading to strong Lorentz forces, substantial fluid redistribution, and high-pressure losses. Applying either a skew-corrected Green-Gauss or Least-Squares formulation to compute the electric potential gradients shows that the higher accuracy of these discretization schemes is mandatory for the solution of the poorly conditioned equations when solving the Poisson equation for the electric potential and when determining electric current density. The detailed verification of different discretization schemes carried out on structured and unstructured computational grids demonstrates the challenge to adequately resolve non-rectilinear geometries, where a major issue is the fine resolution of extremely thin and curved MHD boundary layers without excessively increasing the number of grid points in the fluid core. The new robust schemes lead to a significant improvement in accuracy of results and code performance and allow for the first time the usage of unstructured grids, even when the magnetic field is very strong.

The improved code is applied to three-dimensional simulations of liquid metal pipe flow in a nonuniform magnetic field and for MHD flows entering or leaving insulating flow channel inserts that are foreseen in applications as means of pressure drop reduction. These examples have been selected since experimental results for pressure and surface electric potential are both available for validation. The simulations provide detailed insight into physical phenomena and expose pressure loads on flow channel inserts, which are difficult to gain from experimental techniques. In both investigated cases, axial potential gradients drive additional large-scale 3D current loops with consequences on pressure distribution and flow patterns. A comparison of experimental and numerical surface data proves very good agreement. Simulations show that the major balance of forces occurs between Lorentz force and pressure force, and only a small residual fraction, introduced as magnetodynamic force, is available for acceleration and deceleration of the fluid to balance inertia and viscous effects. The simulations reveal further that regions of significant deformation in velocity profiles, as well as regions of highest braking Lorentz force, may occur at different axial positions so that the entire problem can be solved only using a reliable 3D numerical predictive tool on well-resolved computational grids. Achieved findings of the present work contribute to foreseeable demands of fusion engineering and research and thus will extend the code's field of application to more complex geometries and entire blanket modules.

Dreidimensionale magnetohydrodynamische Phänomene in Kreisrohrströmungen

Kurzfassung

Ein numerischer Rechencode für die Simulation magnetohydrodynamischer (MHD) Flüssigmetallströmungen in Blankets zukünftiger Fusionsreaktoren wurde erweitert, um komplexe MHD-Phänomene in Geometrien mit gekrümmten Wänden wie z.B. kreisförmigen Rohren zu untersuchen. In diesen MHD-Strömungen wechselwirken induzierte elektrische Ströme mit dem Magnetfeld, welches das Fusionsplasma einschließt, was letztendlich zu starken Lorentz-Kräften, erheblicher Fluidumverteilung und hohen Druckverlusten in der Flüssigmetallströmung führt. Die Anwendung eines schiefheitskorrigierten Green-Gauss- oder eines Least-Squares-Verfahrens zur Berechnung des elektrischen Potentialgradienten zeigt, dass die höhere Genauigkeit dieser Diskretisierungsmethoden für die Lösung der schlecht konditionierten Gleichungen für das elektrische Potential und die elektrische Stromdichte zwingend erforderlich ist. Die detaillierten Untersuchungen auf strukturierten und unstrukturierten Rechengittern spiegeln die große Herausforderung wider, nicht-geradlinige Geometrien adäquat aufzulösen, wobei ein Hauptproblem die Diskretisierung extrem dünner und gekrümmter MHD-Grenzschichten darstellt, ohne dabei die Anzahl der Gitterpunkte im Strömungskern übermäßig zu erhöhen. Die neuen robusteren Methoden führen so zu einer erheblichen Verbesserung der Genauigkeit der Ergebnisse und damit der Leistungsfähigkeit des Codes. Sie ermöglichen zum ersten Mal die Verwendung unstrukturierter Rechengitter, selbst wenn das Magnetfeld sehr stark ist.

Der weiterentwickelte Code wird für dreidimensionale Simulationen von Flüssigmetall-rohrströmungen in einem inhomogenen Magnetfeld sowie von ein- und austretenden MHD-Strömungen in Strömungskanaleinsätze, die der Druckverlustreduzierung dienen, angewandt. Diese Beispiele wurden ausgewählt, da experimentelle Ergebnisse sowohl für den Druck als auch für das elektrische Oberflächenpotential als Validierungsdaten zur Verfügung stehen. Die Simulationen bieten detailreiche Einblicke in physikalische Phänomene und zeigen Druckbelastungen in Strömungskanaleinsätzen, die mit experimentellen Methoden schwer zugänglich sind. In beiden untersuchten Fällen führen axiale Potentialgradienten zu großräumigen dreidimensionalen Rezirkulationsschleifen elektrischer Ströme, die sich auf Druckverteilung und Geschwindigkeitsprofil auswirken. Ein Vergleich von experimentellen und numerischen Ergebnissen entlang der Rohroberfläche zeigt eine gute Übereinstimmung. Die Simulationen offenbaren zudem, dass ein Kräfteausgleich hauptsächlich zwischen der Lorentzkraft und der Druckkraft besteht. Nur ein kleiner Restanteil der elektromagnetischen Kraft, der als magnetodynamische Kraft eingeführt wird, gleicht sich über Trägheits- und Reibungskräfte aus. Die in der vorliegenden Arbeit gewonnenen Erkenntnisse tragen zur Verbesserung des verwendeten numerischen Codes bei und erweitern seine Anwendbarkeit für zukünftige Anforderungen der Blanketentwicklung und Fusionsforschung. Dies betrifft insbesondere Anwendungen des Codes für komplexere Geometrien und ganze Blanket-Module.

Acknowledgments

I have written the work at hand during my activities as a research associate at the Institute of Thermal Energy Technologies and Safety (ITES) of the Karlsruhe Institute of Technology (KIT). I am most grateful to the many people in my environment that have guided my development.

My particular gratitude is due to my mentor apl. Prof. Dr.-Ing. Leo Bühler for his outstanding supervision of my thesis. I am thankful for his guidance and willingness in giving well-thought advice on practical and technical issues consistently throughout my work.

I thank Prof. Dr.-Ing. Robert Stieglitz for taking the role as Korreferent and for providing his critical remarks on the manuscript.

Moreover, my thanks go to my colleagues for making my stay at ITES a great experience that allowed me to grow professionally and personally. I thank Dr.-Ing. Chiara Mistrangelo, Christina Köhly, Hans-Jörg Brinkmann, Hans-Joachim Wiemer, Dr.-Ing. Stephan Gabriel, and Frank Kretzschmar as well as my peers Dr.-Ing. Thomas Arlt, Dr.-Ing. Martin Raquet, Dr.-Ing. Hiroshi Madokoro, and Richard Henning.

My special thanks go to my family and friends for their support and encouragement, in particular to my wife María José Rosas Oliveros.

Contents

1 Introduction

Magnetohydrodynamics (MHD) describes the motion of electrically conductive fluids in magnetic fields, combining fluid mechanics and electrodynamics to predict their mutual interaction. On the one hand, a magnetic field induces electric fields and currents inside a moving conductor, which exerts a Lorentz force on the object. On the other hand, electric currents generate or modify magnetic fields. Such mutual interaction leads to complex coupling phenomena that are difficult to understand at first sight and therefore require elaborate investigative tools, as demonstrated throughout this work.

MHD is used in natural science to describe cosmic phenomena in astrophysics, such as the emergence of plasma eruptions in the Sun's chromosphere or the geodynamo effect, which explains the relation of the Earth's moving liquid iron core and its self-induced magnetic field. Moreover, MHD gives rise to research in engineering science resulting in applications for technical devices or industrial fabrication processes. For example, the latter corresponds to controlling liquid metal motion in the casting industry, where the proper knowledge about MHD phenomena enables the design of induction furnaces using transient magnetic fields that stir and heat the melt simultaneously. Knowing the interaction between moving electrically conducting liquids and imposed magnetic fields is furthermore exploited in energy conversion processes either in form of pumps or generators. An imposed voltage and magnetic field on a liquid metal duct may drive the fluid. If, instead, motion is imposed on liquid metal under a magnetic field, a voltage can be tapped from electrodes on the channel walls.

This work investigates liquid metal MHD phenomena occurring in a fusion reactor, such as shown by the sketch in figure 1.1. A complex arrangement of magnet coils, highlighted blue, confines a hot plasma in the toroidal plasma chamber using strong magnetic fields. The plasma is composed of the hydrogen isotopes deuterium and tritium, and it releases energy due to nuclear reactions while forming helium and fast neutrons. The promising idea of this concept is to extract the heat generated in the fusion plasma and provide continuous electricity. Therefore, so-called breeding blankets highlighted red cover the chamber's inner surface. As they directly face the fusion plasma, their major tasks are to

- breed the rare hydrogen isotope tritium required as fuel for the fusion reaction,
- shield the reactor environment from the strong neutron irradiation, and
- remove heat from the reactor's first wall and from the blanket volume to generate

electricity.

Attractive concepts to meet those requirements are liquid metal blankets, in which eutectic lead-lithium flows through a network of channels behind the plasma-facing wall. Due to its lithium content, this alloy serves as liquid breeder material from which, by nuclear reaction with neutrons emitted by the fusion plasma, the fuel component tritium is generated. Moreover, the breeder material constitutes an effective heat carrier and neutron multiplier. However, its high electric conductivity leads to dominant MHD phenomena upon moving under the reactor's strong magnetic plasma confinement. Induced currents inside the breeder interact with the magnetic field and generate Lorentz forces opposing the liquid metal flow and thus produce high MHD pressure drops.

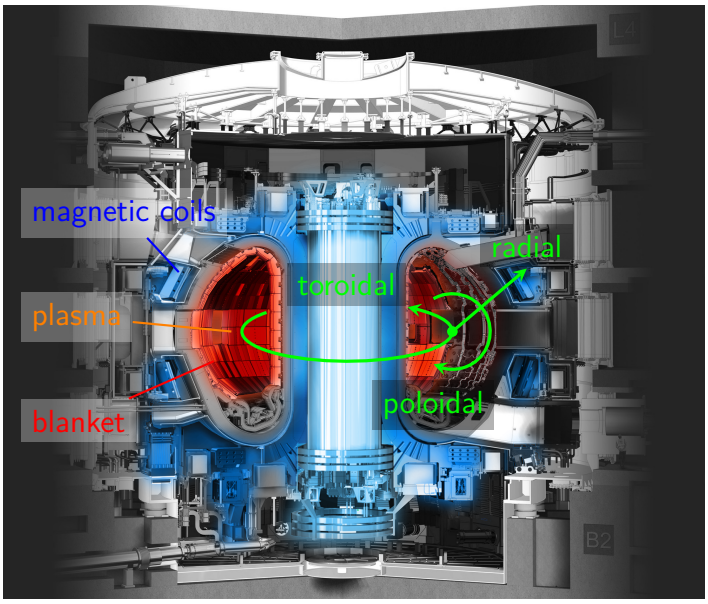

Figure 1.1: Sectional view of the ITER fusion reactor including toroidal coordinate directions in green. Blue highlighted elements generate magnetic fields to initiate, shape, confine, and control the fusion plasma. Fusion blankets, shown red, cover the inner wall of the toroidal plasma chamber and thus directly face the hot fusion plasma. (source: adopted from https://www.iter.org)

In order to assess the impact of MHD effects on flows of breeder material, fusion engineering depends on profound knowledge and capable predictive tools. However, the application of analytical solutions is restricted only to a number of basic geometrical problems under ideal conditions, such as so-called 2D MHD phenomena, where the flow is fully developed in straight channels and electric currents close in cross-sectional planes. Yet imposed variations by the fusion reactor environment in the form of nonuniform magnetic fields, changing wall thickness, dimensions, orientation, or electrical conductivity of pipes lead to additional axial current flow that may propagate over large distances through fluid and solid domains. Axial currents generate transversal Lorentz forces that highly disturb the flow of the liquid breeder at large scales, resulting in strong three-dimensional (3D) MHD phenomena. On the other hand, employing experimental investigations to study

more realistic problems of developing blanket flow quickly becomes expensive, which limits practical methods for investigations to specific problems. Moreover, since liquid metals are opaque and highly reactive in most cases, fluid-internal properties are difficult to explore. For that reason, experimental data often refers only to the outer surface of investigated test sections.

Along with the advancement of numerical methods and high-performance computers (HPC), numerical codes have entered and nowadays dominate the field of fusion MHD research (Smolentsev, 2021, pp. 28-30). Computational MHD codes, like the one used in the present work (Mistrangelo & Bühler, 2011), discretize, linearize, and numerically solve the governing equations on computational grids that decompose the flow geometry of the problems under investigation by means of finite volumes. In this manner, numerical approaches provide valuable, theoretical insights into elaborate problems of fusion-relevant MHD phenomena at affordable costs. Hence, where experiments become too expensive or lack insight, and analytical methods fail due to the problem's complexity, computational MHD codes constitute a promising tool of investigation. However, while complex rectilinear flow geometries are already well replicated by numerical approaches, basic curved geometries, such as flow in circular pipes, still pose major difficulties to the numerical procedure (Vantieghem, 2011, pp.89-96) (Mistrangelo & Bühler, 2011). The reason for such insufficiency, on the one hand, is the great challenge of spatially resolving relevant details of the varying electric current flow within extremely thin and curved boundary layers. On the other hand, associated discontinuities in the computational mesh structure lead to initially minor numerical errors that are magnified up to a significant extent by discretizing and solving the MHD equation for strong magnetic fields. Therefore, applying the code to circular pipe flow requires a more robust numerical approach in the form of a consistent discretization scheme involving a well-suited computational grid.

Early works considered complex 3D developing flows in breeding blanket geometries, where conditions vary in the axial direction along circular pipes, e.g., in Picologlou et al. (1986) and Barleon et al. (1989). In order to serve as an extension to those prior works and to complement the validation base for numerical approaches, a broad experimental campaign had been conducted at the MEKKA laboratory (**M**agnetohydrodynamic **E**xperiments in Na**K** **Ka**rlsruhe) at KIT. In those experiments, liquid metal enters the magnetic field of the laboratory magnet (Bühler et al., 2020b) or traverses sections that involve wall discontinuities occurring in the vicinity of so-called flow channel inserts (FCI), which are devices designed for MHD pressure drop reduction in liquid metal blankets (Bühler et al., 2019, 2020a). Experimental measurements of electric potential and pressure from the outer wall surface of the test sections suggest the occurrence of strong, fluid-internal 3D MHD phenomena that lead to additional pressure drops.

Since the MEKKA experimental campaign has been conducted in circular pipes, the obtained results constitute an outstanding benchmark opportunity that addresses the needs of fusion MHD research in two major challenging fields. Those are the improvement of powerful and reliable MHD codes towards fusion realistic applications and a deep numerical analysis of complex 3D MHD phenomena occurring in the liquid breeder. The underlying ideas of the

work at hand are

- extend the applicability of the computational code used at KIT for MHD flows in circular geometries and very strong magnetic fields
- verify the robustness of the numerical approach by means of known analytical solutions and validate results for more complex 3D MHD phenomena with the MEKKA experimental data
- analyze liquid metal flow in blanket subsystems such as nonuniform magnetic fields and in FCIs to predict and optimize the performance of flows of breeder material at reactor relevant conditions
- reveal fluid-internal details of 3D MHD phenomena occurring in the breeder material, which are experimentally inaccessible

The motivation is to conduct a deep analysis of numerical results to be obtained in order to verify introduced discretization schemes, supplement experimental findings, gain knowledge about relevant 3D MHD phenomena, support blanket development, expose critical loads, and validate the computational approach with experimental measurements.

To reach those goals, chapter 2 first introduces governing equations, knowledge from literature about fully developed MHD pipe flow and corresponding asymptotic models, developing MHD flow, as well as the implementation of MHD equations into the used computational code. The first part of this work then investigates in chapter 3 the code's capability to consider fully developed MHD pipe flow, where, for the first time, the code's convergence and robustness are examined on unstructured computational meshes. Knowledge about the code's ability to address curved geometries on unstructured grids is furthermore crucial to foreseeable demands in fusion engineering as blanket geometries become increasingly complex and may therefore not necessarily be discretized by rectilinear structured grids. The chapter ends by providing recommendations for the choice of spatial discretization and numerical schemes to appropriately resolve MHD flow in circular pipes. Based on those findings, the MEKKA experiments are replicated by detailed numerical simulations, as presented and discussed in terms of MHD flow in a nonuniform magnetic field and in close vicinity to flow channel inserts (FCI) in chapters 4 and 5, respectively. Chapter 6 concludes with a summary and presents major findings of this work as well as possible outlooks.

2 Fundamentals of magnetohydrodynamic pipe flow

First investigations on liquid metal flow in magnetic fields date back to Julius Hartmann, who studied the behavior of mercury flow in rectangular and circular pipes (Hartmann, 1937). His analytical approach describes a one-dimensional, fully developed flow between two infinite plates, where pressure losses become larger with increasing transverse magnetic field strength. He further observed that the core velocity flattens along magnetic field lines, and viscous effects are confined to very thin boundary layers. The analytical work of Shercliff (1953) demonstrates the great benefit of treating the core flow as inviscid and separate from the viscous boundary domain, resulting in an asymptotic approach that is valid for strong magnetic fields. This yields a simple solution for circular pipes, in the case of dominant magnetic field strengths for electrically insulating pipe walls (Shercliff, 1956). The work of Chang & Lundgren (1961) extends this approach to thin walls of arbitrary conductivity, providing a more general formulation, which shows that pressure losses strongly depend on wall conductance in addition. When walls are better conducting than the viscous layers, Miyazaki et al. (1983) introduce a convenient solution that is valid for arbitrary wall thicknesses. Where the evaluation of exact solutions, as, e.g., introduced by Uflyand (1961), becomes difficult for strong fusion-relevant magnetic fields, asymptotic approaches, like Chang and Lundgren's, serve today as effective evaluation tools for fully developed flow in straight pipes. However, their applicability remains limited to rather specific problems, such as MHD pipe flow or flow in rectangular ducts.

With the advancement of computational devices, numerical approaches have been introduced to solve MHD problems (Kit et al., 1970). While those methods initially referred to fully developed stationary flows in simple geometries and weak magnetic fields, computational codes have become more efficient and robust along with the progress of high-performance computers and numerical methods. Meanwhile, numerical approaches constitute the major tool of investigation in fusion MHD research as they are capable of addressing most complex problems of fusion-relevant MHD phenomena (Smolentsev et al., 2015). As demonstrated within the present work, the application of a numerical approach significantly extends the investigative possibilities for complex MHD problems and thus essentially contributes to ongoing fusion MHD research.

2.1 Magnetohydrodynamic equations

An electrically conducting liquid moves through a strong externally applied magnetic field. The velocity vector field $\mathbf{v}(\mathbf{x},t) = (v_x, v_y, v_z)$ describes the movement of fluid elements in spatial coordinates $\mathbf{x} = (x, y, z)$ and time t, while the magnetic field $\mathbf{B}(\mathbf{x})$ is assumed stationary. Moving under a magnetic field, the liquid conductor experiences a flow-induced electric field $\mathbf{v} \times \mathbf{B}$, orthogonal on both vectors, velocity $\mathbf{v}$ and magnetic field $\mathbf{B}$. This drives electric currents inside the conducting liquid and imposes an electrostatic field in the form of the electric potential gradient $\nabla\phi(\mathbf{x},t)$.

The relation of electric current density $\mathbf{j}(\mathbf{x},t)$, electric potential gradient, and induced electric field satisfy, in dimensionless formulation, Ohm's law (Müller & Bühler, 2001, equation 2.26)

$$\mathbf{j} = -\nabla\phi + \mathbf{v} \times \mathbf{B} \ , \tag{2.1}$$

and charge conservation (Müller & Bühler, 2001, equation 2.13)

$$\nabla \cdot \mathbf{j} = 0 \ . \tag{2.2}$$

Throughout this work, variables $\mathbf{B}$, $\mathbf{v}$, $\mathbf{j}$, and ϕ are scaled by characteristic values for the magnetic field strength B_0, velocity v_0, $j_0 = \sigma\, v_0\, B_0$, and $\phi_0 = v_0\, B_0\, L$, respectively. Here L stands for a typical length scale in the problem, v_0 is the average velocity in a cross section, and σ denotes the specific electric conductivity of the fluid. Equations 2.2 and 2.1 combined result in the Poisson equation for the electric potential

$$\Delta\phi = \nabla \cdot (\mathbf{v} \times \mathbf{B}) \ . \tag{2.3}$$

Equation 2.3 ensures charge conservation when currents are determined from Ohm's law.

The induced electric current interacts with the externally applied magnetic field, which generates a Lorentz force density in the fluid flow orthogonal on $\mathbf{j}$ and $\mathbf{B}$ (Müller & Bühler, 2001, p. 14), according to

$$\mathbf{f}_L = \mathbf{j} \times \mathbf{B} \ . \tag{2.4}$$

The electromagnetic force contributes to the momentum equation, which includes further relevant terms of fluid dynamics (Müller & Bühler, 2001, equation 6.1), according to

$$\underbrace{N^{-1}\left(\frac{\partial \mathbf{v}}{\partial t} + (\mathbf{v}\cdot\nabla)\,\mathbf{v}\right)}_{\text{intertia force}} = \underbrace{-\nabla p}_{\substack{\text{pressure}\\ \text{force}}} + \underbrace{Ha^{-2}\nabla^2\mathbf{v}}_{\text{viscous force}} + \underbrace{\mathbf{j}\times\mathbf{B}}_{\substack{\text{Lorentz}\\ \text{force}}} \ . \tag{2.5}$$

Equation 2.5 describes a balance of inertia force, pressure force, viscous force and electromagnetic Lorentz force. Since the fluid is assumed incompressible, it therefore satisfies mass

conservation (Müller & Bühler, 2001, equation 2.50), according to

$$\nabla \cdot \mathbf{v} = 0 \ . \tag{2.6}$$

The pressure $p\,(\mathbf{x}, t)$ is scaled by $p_0 = \sigma\, v_0\, B_0^2\, L$ and fluid properties such as the electric conductivity σ, density ρ and kinematic viscosity ν are assumed constant.

Two dimensionless groups in the momentum equation characterize such magnetohydrodynamic flow (Müller & Bühler, 2001, p. 23). On the one hand, there is the Stuart number, also known as the interaction parameter

$$N = \frac{\sigma L B_0^2}{\rho v_0} \cong \frac{\text{electromagnetic forces}}{\text{inertia forces}} \ , \tag{2.7}$$

describing the ratio of electromagnetic to inertia forces. The squared Hartmann number, on the other hand, indicates the ratio of electromagnetic to viscous forces

$$Ha = B_0 L \sqrt{\frac{\sigma}{\rho \nu}} \cong \sqrt{\frac{\text{electromagnetic forces}}{\text{viscous forces}}} \ . \tag{2.8}$$

The Hartmann number constitutes an indicator for MHD channel flow, since it may be interpreted as a nondimensional parameter that quantifies the intensity of the applied magnetic field. Both dimensionless groups define the Reynolds number according to $Re = Ha^2/N$. Their position in the momentum equation (equation 2.5) shows that with an increasing magnetic field B_0, the balance between electromagnetic force and pressure force dominates over viscous and inertia forces.

Equations 2.1, 2.3, 2.5, and 2.6 describe MHD flow in stationary applied strong magnetic fields, provided investigated length scales are sufficiently large and electromagnetic processes slow enough so that quantum mechanical effects and displacement currents are negligible. The fluid is seen as a continuum of uniformly distributed mass and charge density, whose state is described by laws of classical electromagnetism and fluid dynamics. Furthermore, investigated lengths and velocities are assumed sufficiently small on laboratory or engineering scales, which allows neglecting flow-induced magnetic fields in comparison to the externally applied one. The latter simplification applies for flows at small magnetic Reynolds numbers $R_m = \mu\, \sigma\, L\, v_0$, where μ denotes the magnetic permeability.

Figure 2.1 illustrates general spatial relations of vectors in the MHD equations, presented above. In the sketch on the left, velocity and magnetic field produce the induced electric field $\mathbf{v} \times \mathbf{B}$. This drives electric charge represented by electric current density $\mathbf{j}$ and generates the electric potential gradient $\nabla\phi$. The three vectors $\mathbf{v} \times \mathbf{B}$, $\nabla\phi$, and $\mathbf{j}$ form a closed triangle according to Ohm's law in equation 2.1. The sketch on the right shows how Lorentz forces establish orthogonally to electric current density $\mathbf{j}$ and magnetic field $\mathbf{B}$.

Figure 2.1 provides a general impression of how the orientation of the imposed magnetic field affects MHD phenomena. In contrast to hydrodynamic flow, the direction between

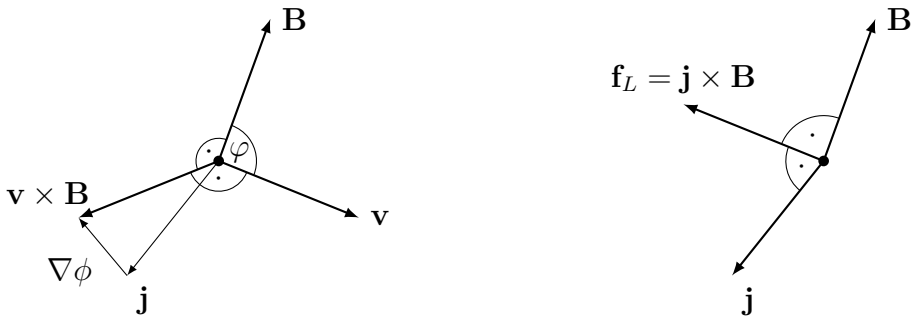

Figure 2.1: Vector representations illustrating magnetohydrodynamic relations for Ohm's law (left) and the Lorentz force (right). The symbol · in the angle bend marks perpendicular orientations of vectors.

the magnetic field and velocity imposes a preferential orientation leading to anisotropy of electrodynamics and fluid mechanics. This anisotropic behavior determined by the magnetic field orientation is one fundamental characteristic of MHD flow, which becomes apparent throughout the present work.

Concerning fusion applications, values of governing parameters in the momentum equation become very large, such as $N \sim \mathcal{O}(10^5)$ and $Ha \sim \mathcal{O}(10^4)$ (Smolentsev, 2021, table 1). Under such extreme conditions, inertia and viscous forces in equation 2.5 may be neglected, which is known as the magnetostatic approach. It was introduced originally by Kulikovskii (1968), and it nowadays serves as a useful approximation of MHD flow in some applications, see, e.g., (Bühler, 1995). The present work, on the other hand, considers the full set of equations 2.1, 2.3, 2.5, and 2.6 presented above and thus it is capable of describing also viscous and inertia effects. This is of particular importance when the transition of turbulent hydrodynamic flow towards a fully established MHD pipe flow is considered in chapter 4 or when jet-like flow patterns in MHD flows may become unstable (Arlt, 2018).

2.2 Stationary MHD flow

The movement of a conductive fluid inside a solid structure under a transverse magnetic field furthermore depends on the geometry and electric property of its containment. Simple cases of pressure-driven flow show that those parameters affect MHD phenomena significantly.

Fully developed flow between parallel plates

Hartmann (1937) investigated the flow between two plates under a transverse magnetic field, as shown in figure 2.2 where the plates have the nondimensional distance 2. Throughout the present work, the mean fluid velocity and magnetic field are generally oriented along x and y, respectively. The movement of conductive material in the magnetic field induces orthogonally directed electric currents perpendicular to both $v_0\mathbf{e}_x$ and $\mathbf{B}$, which in turn evoke axial Lorentz forces $\mathbf{j}\times\mathbf{B}$. They brake the core flow and drive the fluid in the boundary layers, as shown by red arrows. The fluid sticks to the wall, where the velocity becomes zero. With increasing magnetic field strength, i.e., growing Ha, the velocity profile transforms from the well-known hydrodynamic case of Poiseuille flow into a magnetohydrodynamicly dominated flow, often referred to as Hartmann-Poiseuille flow, shown by the blue dashed and solid line, respectively. Hartmann (1937) provides an exact solution for the underlying case of one-dimensional flow, where the axial velocity satisfies

$$v_x\left(y\right) \sim 1 - \frac{\cosh\left(Ha\, y\right)}{\cosh\left(Ha\right)} \ . \tag{2.9}$$

The flow separates into a core domain, where the velocity becomes uniform along magnetic field lines and thin viscous boundary layers, where the velocity sharply drops to zero. The latter are known as Hartmann layers, and their dimensionless thickness scales according to

$$\delta_{Ha} = \frac{1}{Ha} \ , \tag{2.10}$$

i.e., they become thinner with increasing magnetic field strength. Moreover, Hartmann layers provide a closure path for electric currents to guarantee charge conservation, as shown by green vector representations.

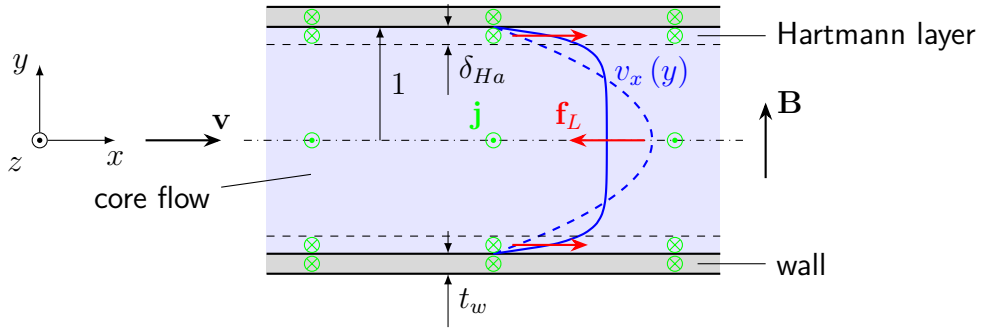

Figure 2.2: Sketch of Hartmann-Poiseuille flow. Velocity profiles v_x between two plates at $Ha = 0$ and $Ha = 9$, shown by the blue dashed and solid line, respectively. Orientation of electric currents and Lorentz force are depicted by green and red vector representations.

If the wall is electrically conducting, a fraction of electric current short-circuits over the solid domain as an additional closure path, depending on the wall's electric conductivity. Such relation of current flow through those regions is well illustrated by means of an

analogous electric circuit as shown in figure 2.3, describing the relation of current flow between the core, Hartmann layer, and wall domain.

The induced electric field inside the fluid poses an ideal voltage source with the dimensionless value $|\mathbf{v} \times \mathbf{B}| = 1$, where the fluid itself constitutes the internal resistance with the dimensionless value $R_i = 1$. In the case of an electrically insulating wall, the induced current in the core i_c may only return over the Hartmann layer, in order to guarantee charge conservation. Since Hartmann layers become thinner with increasing Ha (see equation 2.10), the layer becomes the bottleneck limiting the total current flow. Kirchhoff's circuit laws then yield

$$i_c = i_{Ha} = \frac{\delta_{Ha}}{1 + \delta_{Ha}} \ .$$

With increasing Hartmann number, the problem is dominated by the electric resistance of the Hartmann layer, which increases proportionally to Ha.

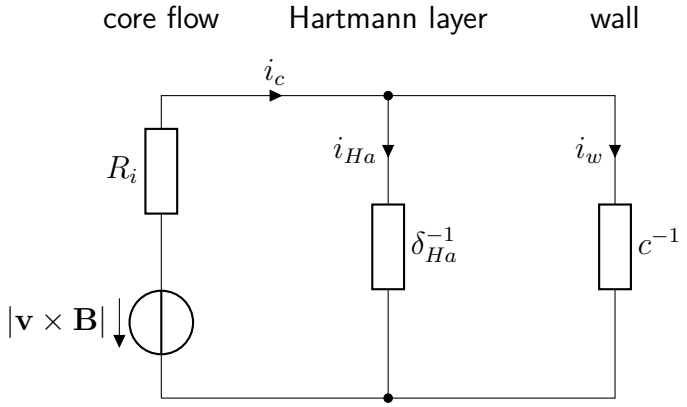

Figure 2.3: Analogous electric circuit of MHD flows describing the relation of electric currents trough the core flow domain, Hartmann layer, and wall.

In the case of electrically conducting walls, currents flow over the solid domain in addition, which increases the core currents according to

$$i_c = i_{Ha} + i_w = \frac{\delta_{Ha} + c}{\delta_{Ha} + c + 1} \ .$$

In this context, the wall conductance parameter

$$c = t_w \frac{\sigma_w}{\sigma} \tag{2.11}$$

describes the electric conductance of the wall compared to the electric conductance of the fluid region, where σ_w is the wall's specific electric conductivity and t_w its dimensionless thickness. For $c = 0$, the wall is a perfect insulator. The core flow becomes independent of Ha, when the wall is better conducting than the boundary layer, i.e., for $c \gg \delta_{Ha}$. The highest core currents are reached when walls are perfectly conducting, i.e., $c \to \infty$. Finally, it should be mentioned that a certain pressure gradient is required to balance the Lorentz

force, i.e., $\partial_x p = \mathbf{j}_c \times \mathbf{B}$. Therefore, the conductivities of walls and boundary layers, which determine core currents j_c, have an important influence on pressure drop, and the smallest values of the pressure gradient exhibit insulating walls.

Relations outlined above are fundamental characteristics of MHD channel flow, and they apply in an analogous way to flows with different types of cross-section such as circular pipes, as the following section reflects.

Fully developed circular pipe flow

Considering fully developed MHD flows in circular pipes, as shown in figure 2.4, leads to a more complex scenario. The blue highlighted flow domain may be split into different subdomains. The fluid sticks to the wall, where the velocity becomes zero. Hartmann layers evolve along top and bottom boundaries, where the magnetic field has a significant component normal to the wall. The varying thickness of viscous boundary layers along α is determined by the wall-normal component of $\mathbf{B}$ and evaluates according to (Shercliff, 1962) as

$$\delta_{Ha} = \frac{1}{\cos(\alpha)\, Ha} \,, \tag{2.12}$$

where, throughout this work, all length scales refer to the inner pipe radius, i.e., $R = L = 1$. At the side locations $\alpha \to \pm\pi/2$, where the wall-normal magnetic field components are small, and δ_{Ha} exhibits a singularity, so-called *Roberts* layers arise. Those boundary layers have been thoroughly investigated by Roberts (1967), who finds their geometric dimension scaling according to $Ha^{-\frac{1}{3}} \times Ha^{-\frac{2}{3}}$ in y and z-direction, respectively.

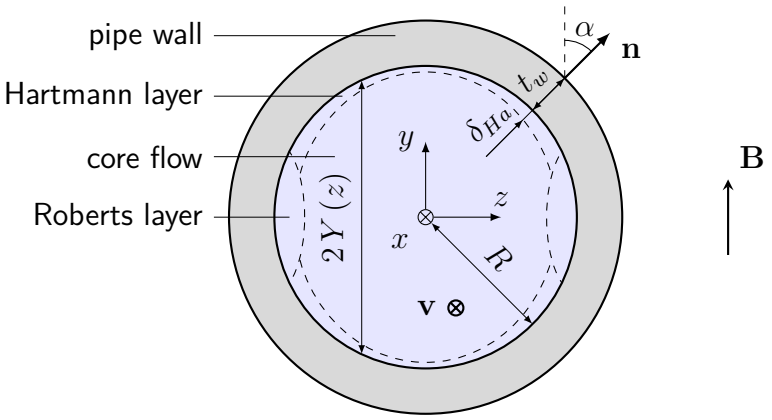

Figure 2.4: Geometric dimensions and flow regions of stationary fully developed MHD flow in a circular pipe at large Ha.

Figure 2.5 presents electric potential distributions, current streamlines, and velocity profiles for insulating, $c = 0$, and well-conducting pipe walls, $c = 1$. In both cases, the fluid-internal electric potential grows continuously along z according to the induced electric

field $\mathbf{v} \times \mathbf{B}$, and it remains constant along magnetic field lines in y-direction. The color scale is normalized by the maximum magnitude at both sides $\phi_{2D} = |\phi\,(y = 0, z = \pm 1)|$. Green lines represent current streamlines flowing in the core along the induced electric field in z-direction. In the case of insulating walls, currents can only close over the thin Hartmann layers, which therefore become the bottleneck of electric current flow. In terms of conducting walls $c > 0$, currents may short-circuit over the solid domain in addition, where they evoke a distribution of wall potential.

Velocity profiles displayed in the bottom row of figure 2.5 show for both cases of wall conductance parameter c a uniform core velocity v_c along magnetic field lines inside the core domain, which then sharply drops to zero in the form of thin viscous Hartmann layers. Along z, the core velocity shows an ellipsoidal profile for insulating and a uniform profile for well-conducting walls. The latter case shows the formation of small side jets, whose emergence has been investigated by Vantieghem et al. (2009).

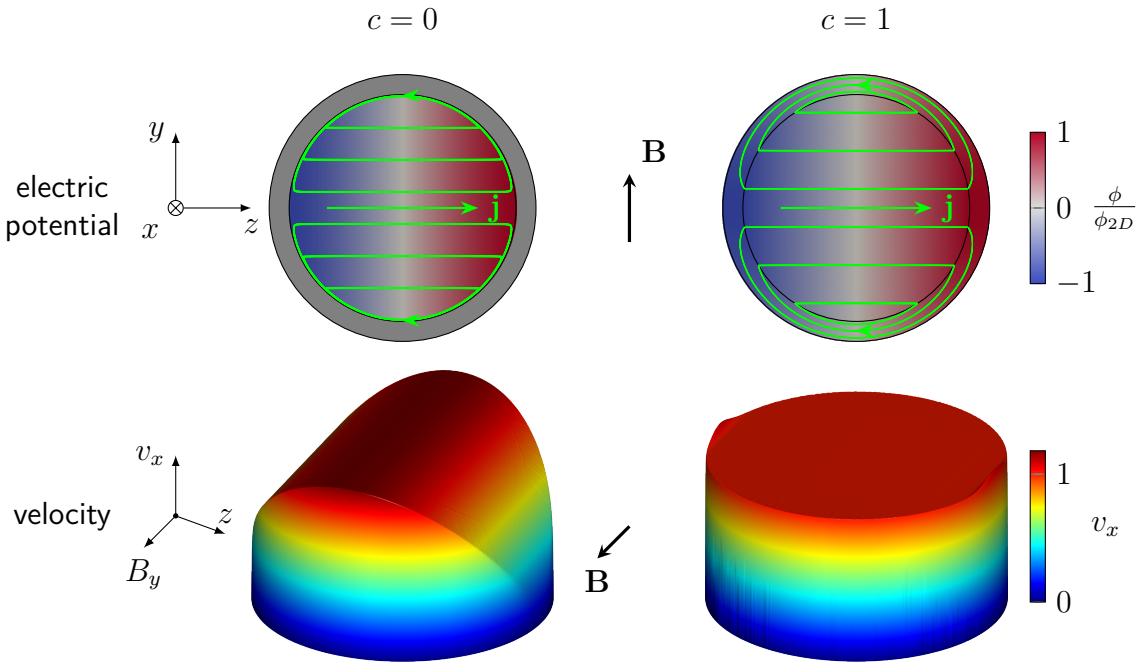

Figure 2.5: Stationary fully developed MHD flow at $Ha = 1000$ in a circular pipe. Illustrations show electric potential and velocity distributions in the case of an insulating (left, $c = 0$) and a well conducting (right, $c = 1$) pipe wall. Green streamlines indicate electric current flow.

Asymptotic theory provides a convenient solution to the core velocity as introduced by Chang & Lundgren (1961)

$$v_c\,(z) \sim (1 + c)\,\frac{Y}{1 + c\,Ha\,Y}\ , \tag{2.13}$$

where Y refers to the channel height in the magnetic field direction $Y\,(z) = \sqrt{1 - z^2}$,

which is shown in figure 2.4. The solution applies for strong magnetic fields $Ha \gg 1$, and it depends on the product $c\,Ha$ - the parameter that indicates where electric currents are more likely to close. The impact of this relation, which quantifies whether walls are better conducting than Hartmann layers, is shown in figure 2.6. Assuming perfectly insulating walls $c = 0$ yields an ellipsoidal profile, whereas v_c becomes uniform with an increasing value of $c\,Ha$. Blue and red lines refer to the cases for $c = 0$ and $c = 1$ in figure 2.5, respectively. Since the asymptotic solution in equation 2.13 constitutes an approximation of MHD flow, which neglects viscous effects in Roberts layers, it therefore misses the emergence of small jets in the case of $c\,Ha \gg 1$, which are exemplarily shown for $c = 1$ in figure 2.5 on the right.

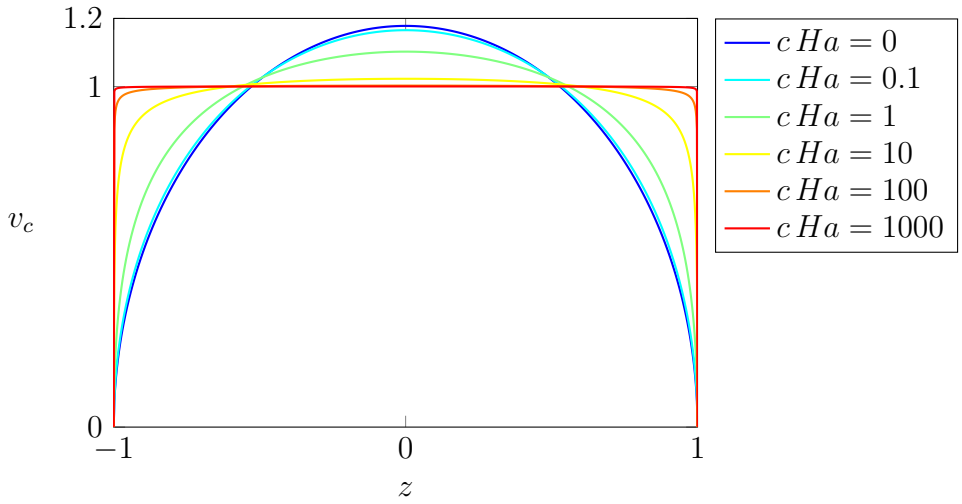

Figure 2.6: Velocity profiles in the plane $y = 0$ according to the asymptotic solution by Chang & Lundgren (1961) for $Ha \gg 1$. The core velocity becomes uniform when the wall is better conducting than the Hartmann layer, i.e., when $c\,Ha \gg 1$.

By means of the asymptotic solution, Chang & Lundgren (1961) determine the mass flow rate and the associated pressure gradient for different wall conductance parameters c as a function of the Hartmann number Ha. The obtained dimensionless gradient $K\,(c, Ha)$ is related to the dimensional one marked with * via the viscous pressure scaling $\rho\,\nu\,v_0/L^2$ as

$$K = \frac{L^2}{\rho \nu v_0} \frac{\partial p^*}{\partial x^*} \ . \tag{2.14}$$

The plots of the dimensionless pressure gradient K in figure 2.7 show that the MHD pressure gradient strongly depends on the wall conductance. While MHD pressure losses rise linearly to Ha for insulating walls according to the blue line, they start to rise quadratically as soon as walls become better conducting than the viscous layers, when $c\,Ha \gg 1$. The gray shaded area indicates that under fusion-relevant conditions, pressure losses due to MHD phenomena are in general enormous compared to hydrodynamic pipe flow when $Ha = 0$. However, they can be significantly reduced by lowering the wall conductance. This motivates the application of so-called insulating flow channel inserts (FCI), which interrupt the current

path and thus electrically decouple the fluid from the wall. Their impact on MHD flow is broadly discussed in chapter 5.

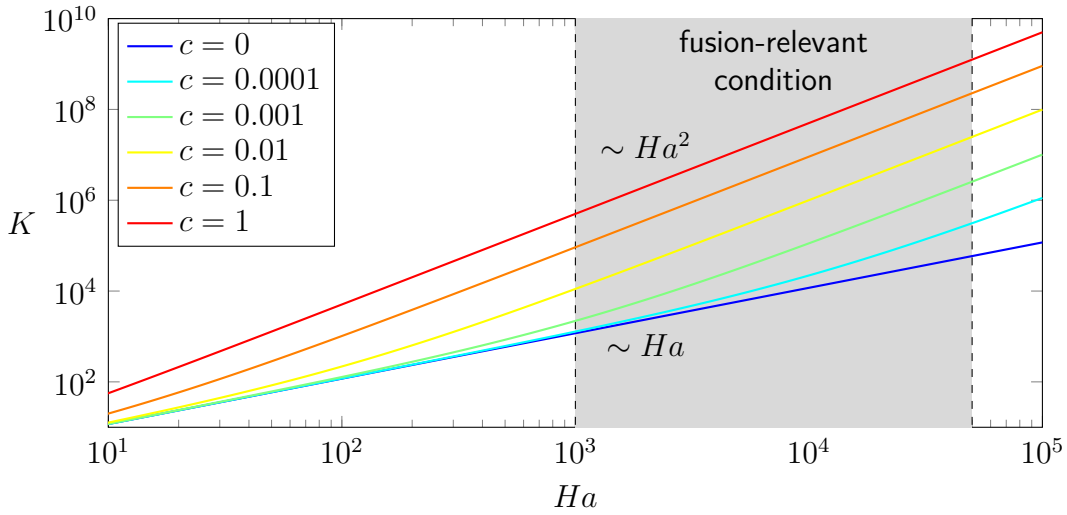

Figure 2.7: Dimensionless pressure gradient K in circular pipes as a function of the Hartmann number Ha for different wall conductance parameters c (Chang & Lundgren, 1961).

For the specific case $c\,Ha \gg 1$ the core velocity becomes uniform, and the approach by Miyazaki et al. (1983) provides a simplified solution of the underlying problem. The latter reference uses a more general definition of the wall conductance parameter for a circular pipe, which applies to walls of arbitrary thickness

$$c = \frac{\sigma_w}{\sigma} \frac{R_o^2 - R^2}{R_o^2 + R^2} \ , \tag{2.15}$$

where the outer wall radius satisfies $R_o = R + t_w$. The asymptotic solution of electric potential along both the inner and outer surface of the wall then becomes

$$\phi_{2D}\left(\alpha\right) = \frac{1}{1+c} \sin\left(\alpha\right) \ , \tag{2.16}$$

$$\phi_{w,2D}\left(\alpha\right) = \frac{2\,R\,R_o}{R^2 + R_o^2} \frac{1}{1+c} \sin\left(\alpha\right) \ . \tag{2.17}$$

These equations provide approximate values of the electric potential distribution along inner and outer wall surface as shown, e.g., in figure 2.5. This approach furthermore enables the determination of electric current density and axial pressure gradient, which for the underlying scaling become

$$j_{2D} = f_{L,2D} = -\partial_x p_{2D} = \frac{c}{1+c} \ . \tag{2.18}$$

The listed solutions of fully developed MHD flow in well-conducting pipes provide a valuable validation tool for numerical methods and they are used as a reference throughout this

work.

As such asymptotic considerations show, enormous MHD pressure loss is one of the main concerns about employing liquid metal flow in fusion reactor devices. In this context, Smolentsev (2021) provides comprehensive considerations and presents further ongoing research.

2.3 Developing MHD flow

In contrast to hydrodynamic flow, MHD flow under a strong magnetic field exhibits a predominant orientation of flow phenomena. As shown in figure 2.8 on the left, the direction of magnetic field and fluid flow defines electric current, Lorentz force, and the associated pressure drop. Pipe geometry, magnetic field strength, and electrical wall conductivity furthermore affect MHD phenomena via channel height $Y\,(z)$, Hartmann number Ha, and wall conductance parameter c. If those parameters do not change along the flow direction, stationary 2D MHD flow develops where electric potential differences and current flow occur exclusively within the pipe's cross-section. However, variations of one or multiple of those parameters in streamwise direction locally disturb the sensitive equilibrium, resulting in axial gradients of the electric potential $\partial_x \phi$. As shown in figure 2.8 (right), both induced electric field $\mathbf{v} \times \mathbf{B}$ and streamwise potential differences elongate current loops in axial direction according to Ohm's law in equation 2.1. Electric current flow and magnetic field then form transversal components of Lorentz forces that redistribute the fluid. This leads to so-called 3D MHD phenomena, which occur at large scales due to 3D current flow, and they may propagate over long distances through fluid and solid domains.

Early considerations on developing MHD phenomena focus on flows around obstacles, introduced by Ludford (1960). He describes internal shear layers, which detach from locations where magnetic field lines are tangent to the immersed body. Perturbations then propagate along magnetic field lines perpendicular to the flow direction. Those layers, referred to as Ludford layers, are governed depending on the relation of Hartmann and Stuart number by either a viscous-inertial, viscous-electromagnetic, or inertial-electromagnetic balance (Müller & Bühler, 2001, pp. 85-87). Hunt & Leibovich (1967) show that internal shear layers in duct flow generally originate from corners in the geometry or within rapidly varying cross-sections. Internal layers provide closure for extra current and therefore increase the total pressure drop. With growing magnetic field strength, Ludford layers become thinner, and their contribution to pressure drop reduces.

3D MHD phenomena in fusion blankets may furthermore arise close to bends and turns where the fluid is redirected. If the flow turns in the plane of the magnetic field, as in the case of a so-called backward elbow formed by rectangular ducts, Moon et al. (1991) describe the emergence of Ludford layers from sharp corners that traverse the fluid flow along the magnetic field lines. In the case when a rectangular bend turns the flow from a

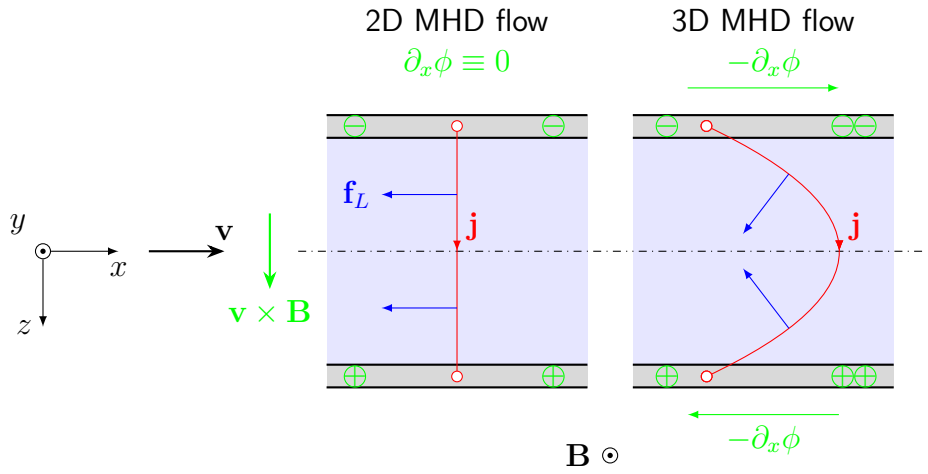

Figure 2.8: Principle sketch of MHD phenomena in fully developed 2D and developing 3D flow within the pipe symmetry plane $y = 0$. Green symbols indicate the transversal and axial difference of electric potential. Lorentz forces, shown blue, arise perpendicular to currents and magnetic field direction according to $\mathbf{f}_L = \mathbf{j} \times \mathbf{B}$.

perpendicular towards a tangential orientation with respect to magnetic field lines, boundary layers carry an essential fraction of flow rate, while the core flow mainly redistributes the fluid between boundary layers (Molokov & Bühler, 1994). Stieglitz et al. (1996) experimentally demonstrate the existence of Ludford layers, which detach from corners of the geometry and propagate along magnetic field lines. They furthermore derive a correlation for the associated pressure losses, demonstrating the electromagnetic-inertial and electromagnetic-viscous impact of Ludford layers on the pressure drop. Theoretical and experimental investigations show that redirecting the flow to magnetic field direction leads to more pronounced 3D phenomena and significantly complicates the problem of liquid breeder flow (Stieglitz & Molokov, 1997). Hence, various recent blanket design concepts try to avoid turning the flow in a direction parallel to the magnetic field. Instead, bends or U-turns may be oriented in planes perpendicular to magnetic field lines in order to minimize strong 3D MHD effects.

Varying the channel height Y in streamwise direction, as investigated by Hunt & Leibovich (1967), changes the mean velocity and thus the induced electric field $\mathbf{v} \times \mathbf{B}$ along fluid flow. The resulting streamwise potential difference drives axially elongated current loops, which are responsible for extra 3D pressure losses Δp_{3D} compared to fully developed flow (Mistrangelo, 2006, p. 51). Those effects have been observed in manifold devices, which in fusion blankets distribute the liquid metal to individual breeding units (Mistrangelo & Bühler, 2014).

Similar effects under fusion-relevant conditions arise when the magnetic field or wall conductance varies along the streamwise direction. The former case may be found at locations where the liquid breeder enters the plasma-confining magnetic field. Such a

problem has been addressed experimentally (Picologlou & Reed, 1989) and numerically (Kit et al., 1970). The latter case refers to a stream entering an insulating flow channel insert (FCI), a device developed for MHD pressure drop reduction in fusion applications, see, e.g., (Malang, 1987; Barleon et al., 1989; Koehly & Bühler, 2017). Both cases introduce streamwise potential differences driving current loops through the breeder material over large axial distances. They further interact with the magnetic field, evoking transversal Lorentz forces that manipulate the flow and produce additional 3D MHD pressure losses. To gain further insight into such complex problems, an extended experimental campaign conducted at KIT investigated developing MHD flow in a nonuniform magnetic field (Bühler et al., 2020b) as well as close to FCIs, at discontinuities of wall conductance (Bühler et al., 2019, 2020a). Obtained measurements of pressure and electric potential from the experiments indicate the occurrence of strong 3D MHD phenomena within the developing flow region.

The study at hand presents numerical simulations of 3D MHD phenomena in nonuniform magnetic fields and at discontinuities of wall conductance, as observed in the experimental campaign at KIT and likewise expected in fusion applications. While experiments detected 3D MHD phenomena from potential and pressure measurements on the outer wall of the test sections, the present computational results enable deep and comprehensive insights. An analysis of additional pressure losses and mechanical stress helps to assess the impact of 3D MHD phenomena on liquid breeder flow in fusion reactor devices. Moreover, the high spatial resolution of numerical results enables detailed evaluations of local momentum balances, such as inertia, pressure, viscous, and Lorentz forces. The complexity of 3D MHD flow investigated within the present work poses high demands on the numerical approach. Only powerful computational codes may satisfy the requirements imposed by the governing MHD equations for such complex geometries.

2.4 Numerical methodology

While analytical approaches are limited to basic MHD problems, e.g., fully developed straight pipe flow, numerical methods, on the other hand, are potentially capable of solving the full set of partial differential equations describing the coupling phenomena of fluid mechanics and electrodynamics in arbitrary complex geometries and for strong magnetic fields. First attempts having been introduced by (Kit et al., 1970) apply a numerical approach to calculate 2D liquid metal flow under a weak nonuniform magnetic field and thus demonstrate the applicability of numerical methods to complex MHD problems. Sterl (1990) extends the considerations and performs 3D numerical simulations for nonuniform magnetic fields up to moderate Hartmann numbers. If the magnetic field is particularly strong, magnetostatic theory permits to neglect inertia and viscous forces from the momentum equation resulting in $\mathbf{f}_L = \nabla p$ according to Kulikovskii (1968). For this specific case, Bühler (1995) derives a highly efficient numerical code, which works for arbitrary but high Hartmann numbers. Unfortunately, the latter approach applies only to flows in single ducts with thin walls, exposed to a transverse magnetic field. Flows in more complex geometries

and time-dependent flows, where inertia forces may become important, cannot be studied using this asymptotic technique.

For predictions of inertial MHD flows in very complex and electrically coupled geometries the finite volume method is the numerical technique preferred by various authors (Morley et al., 2008a; Smolentsev et al., 2020) as well as in the present work. For applications at fusion-relevant high Hartmann numbers, it turns out that a current-conservative formulation is required in order to keep numerical errors at an acceptable level, especially when unstructured grids are employed (Ni et al., 2007).

In the following, basic ideas of finite volume techniques and in particular details about the current-conservative formulation of governing equations used in the present work are outlined.

Finite volume method (FVM)

The idea behind a numerical approach is to linearize and to approximate a transport problem described by partial differential equations, e.g., for a physical quantity φ by a system of linear algebraic equations $\mathbf{A}[\varphi] = \mathbf{b}$ (Moukalled et al., 2016, equation 4.2). This system can be solved numerically by direct or iterative computational tools for the solution of linear algebraic problems. The composition of the coefficient matrix $\mathbf{A}$, discretized values of the physical quantity $[\varphi]$, and column vector $\mathbf{b}$ depend on the discretization procedures applied on both physical domain and physical phenomena (Moukalled et al., 2016, chapter 4). Among numerical approaches, the finite volume method (FVM) has evolved as a preferential approach in computational fluid dynamics due to its conservative nature. It considers the physical domain as being composed of a large number of small but finite volume elements. The partial differential equations governing the problem are satisfied integrally for each finite control volume by applying the divergence theorem and ensuring a balance of fluxes across the surface elements. This leads in general to a conservative formulation of the problem, but the accuracy depends on how the fluxes at surface positions are interpolated from data stored in the cell centers.

Figure 2.9 exemplarily shows a control volume as a single cell of such a computational grid in form of a two-dimensional illustration.

A typical transport problem for a variable φ is described for instance by (Moukalled et al., 2016, equation 5.1)

$$\underbrace{\frac{\partial(\rho\varphi)}{\partial t}}_{\substack{\text{transient}\\ \text{term}}} + \underbrace{\nabla\cdot(\rho\mathbf{v}\varphi)}_{\substack{\text{convective}\\ \text{term}}} = \underbrace{\nabla\cdot(\Gamma^{\varphi}\nabla\varphi)}_{\substack{\text{diffusion}\\ \text{term}}} + \underbrace{Q^{\varphi}}_{\substack{\text{source}\\ \text{term}}} \quad , \tag{2.19}$$

where Γ^{φ} is a diffusion coefficient. The MHD equations may be expressed accordingly by

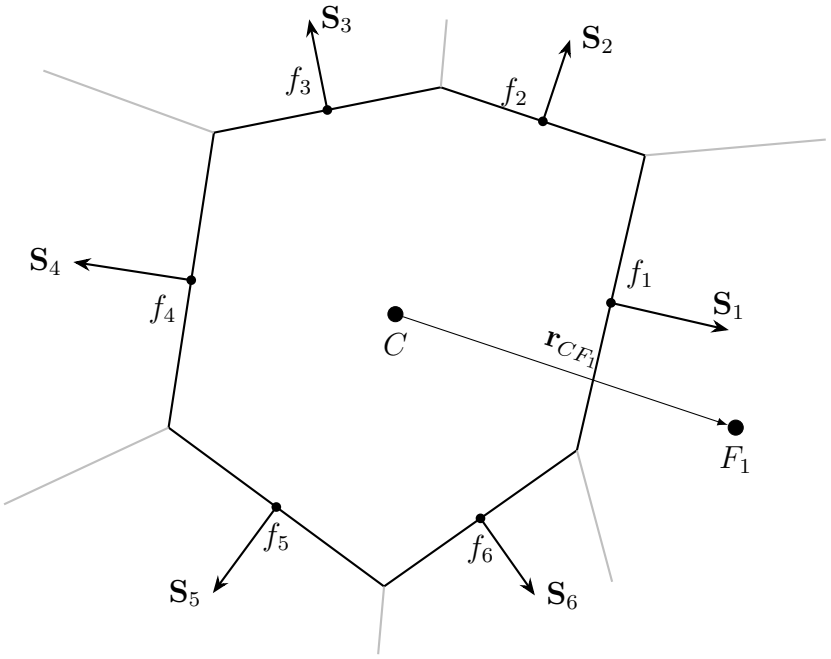

Figure 2.9: Topology of a computational cell and its direct neighbors in the grid. Symbols C,f, F indicate cell, face, and neighbor centroid and $\mathbf{S} = \mathbf{n}_f S$ is the face normal vector.

such generic expressions. Integrating this equation for a control volume results in terms of the depicted cell C in the following relation

$$\int_{V_C} \frac{\partial (\rho\varphi)}{\partial t} \mathrm{d}V + \int_{V_C} \nabla \cdot (\rho \mathbf{v} \varphi) \, \mathrm{d}V = \int_{V_C} \nabla \cdot (\Gamma^{\varphi} \nabla \varphi) \, \mathrm{d}V + \int_{V_C} Q^{\varphi} \mathrm{d}V \ . \tag{2.20}$$

Equation 2.20 satisfies equation 2.19 in an average sense for each considered finite control volume V_C. If the grid resolution is sufficiently high, variations of φ with respect to transient and source term are considered sufficiently uniform over a single cell (Moukalled et al., 2016, p. 108, p. 117), so that they can be taken out of the integral. Convective and diffusion terms, on the other hand, are treated by the divergence theorem, reducing the spatial derivative by one order transforming them into a flux equilibrium with adjacent cells across each corresponding cell surface

$$\frac{\partial (\rho\varphi)}{\partial t} V_C + \oint_{\partial V_C} (\rho \mathbf{v} \varphi) \, \mathrm{d}\mathbf{S} = \oint_{\partial V_C} (\Gamma^{\varphi} \nabla \varphi) \, \mathrm{d}\mathbf{S} + Q_C^{\varphi} V_C \ . \tag{2.21}$$

The resulting equation describes the balance between internal transient change, convective and diffusive fluxes over the entire cell boundary ∂V_C, where $\mathbf{S}$ is the face area vector, and Q_C^{φ} represents internal sources. Replacing fluxes by their average values across individual faces approximates the fluxes at the face centroids f, where $\mathbf{S}_f$ holds the face area. This leads to the definition of a semi-discretized equation according to Moukalled et al. (2016,

pp. 104-108)

$$\frac{\partial(\rho\varphi)}{\partial t}V_C + \sum_f^{n_f(C)} (\rho\mathbf{v}\varphi)_f \cdot \mathbf{S}_f = \sum_f^{n_f(C)} (\Gamma^\varphi \nabla\varphi)_f \cdot \mathbf{S}_f + Q_C^\varphi V_C \ . \tag{2.22}$$

While cell centroids hold all variables in a collocated arrangement, the coupling conditions to neighboring cells are defined on face centroids. Neighboring cell values are therefore required to interpolate the fluxes of φ to the face. However, as exemplarily shown by the connection vector $\mathbf{r}_{CF_1}$ between C and its neighbor cell F_1, skew or non-orthogonal faces may complicate the interpolation to the cell face. Therefore, the computational grid must provide a certain structure and regularity with only small variations of adjacent cells, such that values at the face centroid may be well interpolated. The further discretization and evaluation procedure of equation 2.22 to generate a linear system of equations requires a specific treatment of each term and has to be adjusted to the underlying transport problem with great care. There exist multiple discretization and correction procedures in order to reduce numerical errors to a minimum, as presented, e.g., in Moukalled et al. (2016, chapter 8-14).

Computational MHD code

The applied computational procedure, summarized as a flow chart in figure 2.10, iteratively solves the momentum equation and the Poisson equation for the electric potential at the next time step $t+\Delta t$, as originally implemented by Mistrangelo & Bühler (2011). The continuity and momentum equation simultaneously depend on both velocity $\mathbf{v}$ and pressure p. They are treated according to the PISO algorithm (Pressure-Implicit with Splitting of Operators), proposed by Issa (1986). This segregated procedure splits into a predictor and corrector step, which first solves the momentum equation without the pressure, so the divergence of the estimated velocity differs from zero. The next step of the PISO loop determines the pressure based on the predicted velocity and imposes mass conservation, which in turn results in solving a Poisson equation for the pressure. This yields both the adapted pressure and divergence-free velocity. The iterative process is repeated until either a residual condition or a maximum number of iterations are met. A detailed description of the PISO algorithm and its application can be found in literature, e.g., in Moukalled et al. (2016, section 15.7.3), Ferziger & Peric (2002, section 7.3.4), or Holzmann (2017, chapter 11).

Particular emphasis is required for the solution of the Poisson equation for the electric potential. The difficulty lies in solving the electric potential equation in a manner that guarantees charge conservation since even small numerical errors may be amplified during the iteration process for strong magnetic field strengths. Ni et al. (2007) propose a current density conservative scheme, which applies for strong magnetic fields. This so-called *Ni-algorithm* has been implemented in various MHD codes, and it is also used in the present

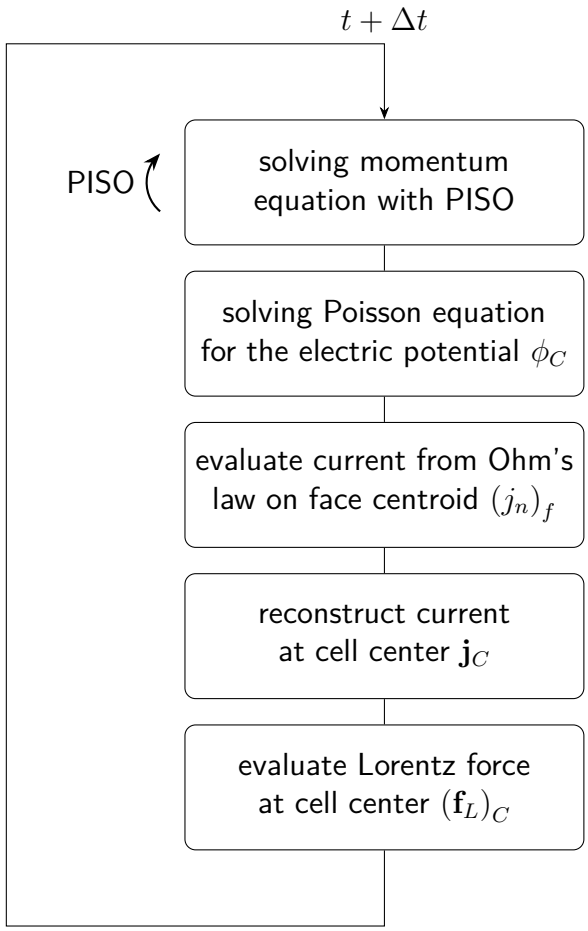

Figure 2.10: Summarizing flow chart of the computational approach.

work.

With the help of the divergence theorem, the Poisson equation for the electric potential may be written in a semi-discretized form on the face centroids f as

$$\sum_{f}^{n_f(C)} \left(\frac{\partial \phi}{\partial n}\right)_f S_f = \sum_{f}^{n_f(C)} (\mathbf{v} \times \mathbf{B})_f \cdot \mathbf{n}_f S_f \ , \tag{2.23}$$

where $\mathbf{n}_f$ and S_f are the normal and face area vector of the respective cell surface f, and $\frac{\partial}{\partial n}$ is the face-normal gradient. As proposed by Mistrangelo & Bühler (2011), the applied code uses a non-orthogonal correction scheme accounting for tilted faces during interpolation of the face-normal potential gradient at the cell surface. Further evaluation of Ohm's law on the face centroid using the electric potential gradient and induced electric field normal to the face results in the face-normal current density

$$(j_n)_f = -\left(\frac{\partial \phi_C}{\partial n}\right)_f + (\mathbf{v} \times \mathbf{B})_f \cdot \mathbf{n}_f \ . \tag{2.24}$$

Ni et al. (2007) stress that the discretization schemes of $\frac{\partial \phi}{\partial n}$ for the solution of equation 2.23 and the evaluation of equation 2.24 must be identical for a conservative current reconstruction on the cell center C. The latter reference further proposes to use the surface integral

$$\mathbf{j}_C = \frac{1}{V_C} \sum_f (j_n)_f \, \mathbf{r}_{Cf} S_f \tag{2.25}$$

for the evaluation of the electric current density at the cell centroid. The Lorentz force at the cell center then becomes

$$(\mathbf{f}_L)_C = \mathbf{j}_C \times \mathbf{B}_C \ . \tag{2.26}$$

With the evaluation of the Lorentz force at the cell center, the computational loop reiterates by initiating the next time step and updating $(\mathbf{f}_L)_C$ in the momentum equation. The loop proceeds until a converged state is achieved.

The applied computational code (Mistrangelo & Bühler, 2011) is implemented using the open-source software OpenFOAM (OpenFOAM-Foundation, 2021). The included library provides a comprehensive supply of FVM tools and functions required for general CFD (computational fluid dynamics) applications involving pre- and post-processing. Its Open source policy enables direct insight to the lowest level of the software architecture, which allows straightforward implementation of numerical operations and algorithms as well as arbitrary manipulation of customized approaches.

Furthermore, OpenFOAM is capable of executing large-scale problems on high-performance computing (HPC) devices. This approach decomposes massive computational grids into a specific number of subdomains that are processed in parallel on multiple processor cores, leading to a significant computational speed up (Keough, 2014). Computations performed for the present work have been conducted for grids with up to $2 \cdot 10^7$ cells using about 300 processor cores on different HPC clusters[1,2].

The computational code had been carefully validated and furthermore demonstrated its capability on a variety of problems in fusion research. To mention only a few particular applications, such as

- development of the code and validation up to $Ha = 10^4$
  (Mistrangelo & Bühler, 2011)

- magneto-convective flow in an entire breeder unit
  (Mistrangelo & Bühler, 2013)

- 3D MHD effects at discontinuous insulations
  (Mistrangelo & Bühler, 2015)

[1]I acknowledge the CINECA award under the ISCRA initiative, for the availability of high-performance computing resources and support.

[2]This work was performed on the supercomputer ForHLR funded by the Ministry of Science, Research and the Arts Baden-Württemberg and by the Federal Ministry of Education and Research.

- MHD coupled flow in manifold geometries
  (Bühler & Mistrangelo, 2016)

- stability analysis of transient Hunt-flow
  (Arlt & Bühler, 2019)

Moreover, the validity of the code has been demonstrated in a code-to-code comparison as part of an international benchmark activity (Smolentsev et al., 2020). Although those achievements confirm the applicability of the developed computational code to various MHD problems, conducted studies have been mainly restricted to rectilinear geometries so far.

There still exist significant difficulties in the application of MHD codes, even for fundamental problems which may pose critical challenges (Smolentsev et al., 2015). For instance, the computation of MHD flows in curved geometries, such as, e.g., circular pipe flow, may induce large numerical errors under strong magnetic fields as observed by Vantieghem (2011, pp. 89-96) or Mistrangelo & Bühler (2011). This constitutes a major issue that must be faced before MHD codes are applied to more complex realistic geometries in fusion blanket engineering. The study at hand therefore first addresses the code's robustness in chapter 3 by means of numerical simulations for circular pipe flow under fusion-relevant strong magnetic fields and provides recommendations for discretizing curved geometries. Subsequently, chapters 4 and 5 address 3D MHD problems in circular pipes for which experimental data is available (Bühler et al., 2019, 2020b,a).

3 Discretization schemes for MHD flows in circular pipes

For strong magnetic fields, i.e., for $Ha \gg 1$ and $N \gg 1$, MHD flows in ducts and pipes exhibit a nearly inertialess and inviscid core region that occupies almost the entire cross-section of the channels. The core velocity is constant along magnetic field lines, but it may vary in the transverse direction depending on duct geometry and wall conductivity. Viscous effects are confined to very thin boundary layers or internal layers, where velocity gradients are highest, and currents are large. Phenomena that vary on widely different length scales pose the highest demands on the involved discretization procedures. Moreover, the curved periphery of a circular pipe implicates a permanent reorientation of electric boundary currents, which significantly complicates achieving a consistent discretization in comparison to rectilinear geometries.

This chapter compares the results of MHD simulations of fully developed circular pipe flow in strong magnetic fields obtained by using different mesh topologies and discretization schemes. Especially for pipes with poor wall conductivity, perturbations caused by discretization errors may reach such magnitudes that the numerical solutions become useless. It will be shown that defects in the results have their origin in the discretization schemes of the electric potential equation. Therefore, the impact of more appropriate formulations of the potential gradient and the spatial resolution on numerical convergence and robustness are discussed, by verifying their performance with approximate analytical solutions and highly resolved numerical results. Eventually, those higher discretization schemes lead to substantial improvements concerning the capabilities of the code for applications with curved and complex geometries using for the first time unstructured grids.

3.1 Spatial Discretization

The topology of the computational mesh significantly determines numerical convergence and the quality of the results. In general, orthogonal non-skew cells constitute grids on which numerical simulations run with high efficiency. Structured, rectilinear grids typically consist of hexahedral elements and involve a systematic regularity across the entire domain, which benefits numerical stability and consistency.

A block-structured grid configuration, as shown in figure 3.1 on the left, is designed to resolve MHD flows in square ducts under a strong magnetic field. The underlying cell arrangement consists of separate blocks as indicated by red dashed lines and labeled by roman numerals. Each block contains grading, which is local grid refinement, along selected spatial orientations. Those attributes enable arbitrary densification or expansion of grid cells towards the rectilinear periphery in order to resolve the extremely thin MHD boundary layers, which require particularly high resolution in wall-normal direction. A block-structured grid thus enables the optimization of the mesh by relocating computational cells from the core to the boundaries, which generally reduces the number of cells and the associated computational effort. Moreover, the underlying orthogonal orientation of cell faces is beneficial for numerical consistency as it reflects the inherently mutually orthogonal nature of MHD phenomena between velocity, currents, and magnetic field lines. A block-structured grid is therefore well suited for simulation of MHD flow in rectilinear geometries for large Hartmann numbers (Mistrangelo & Bühler, 2011).

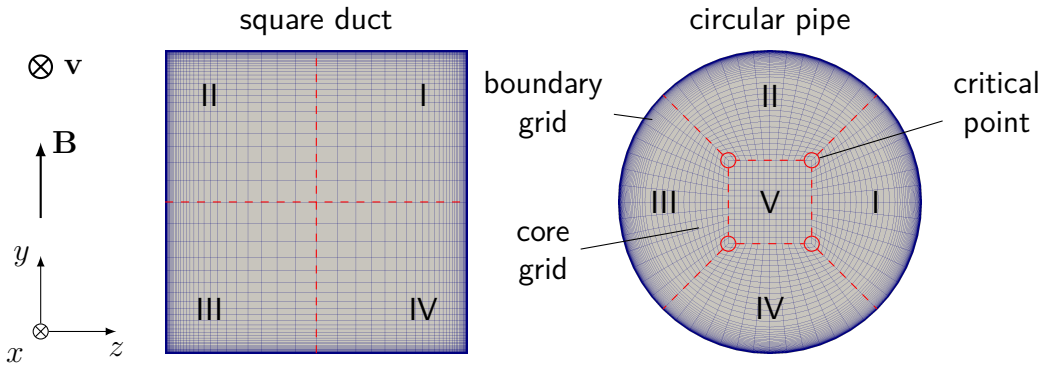

Figure 3.1: Block-structured discretization applied to rectangular (left) and circular (right) geometries. Red dashed lines separate block regions, labeled by roman numerals.

In the case of a circular pipe shown on the right, block-structured discretization leads to the O-grid type that is often used for resolving hydrodynamic flow problems. It consists of a center square block of uniform, structured topology. Four surrounding blocks adapt to the curved pipe periphery and provide adequate grading in wall-normal direction to resolve boundary layers. The corners of the inner block form critical points in the mesh structure, where block boundaries merge, as shown by red dashed lines, leading to so-called grid irregularities. Those are discontinuities in the mesh structure, which may inject zero-order errors during the discretization procedure that cannot be removed entirely by higher spatial resolutions (Moukalled et al., 2016, pp. 124-126).

While a structured grid is well suited to resolve the thin boundary layers with hexahedral prism layers, the core region may alternatively be resolved by other more general grid configurations. Such unstructured meshes will become mandatory for fusion MHD codes as future applications must address increasingly complex geometries, which may not be resolvable by structured grids. Knowledge about the algorithm's compatibility with unstructured and non-hexahedral-based grid types is therefore crucial to future fusion MHD research. Hence,

this chapter addresses the performance of discretization schemes on different grid types.

Core grid

In order to assess the impact of grid configuration on the computational outcome, the boundary layer has been resolved by a fine grid along the periphery with grading towards the wall, while different types of grids for the core region are investigated, as shown in the left column in figure 3.2. Simulations are conducted at a moderate magnetic field strength $Ha = 1000$. The core grid radius measures $R_{\text{core}} = 0.82$. Each mesh type is extruded by three layers in streamwise direction and 50 layers in radial direction involving a strong grading to resolve boundary layers. Applied boundary conditions are listed in table 3.1.

	inlet	outlet	wall interface
ϕ	cyclic	cyclic	$\partial_n \phi = 0$
p	cyclic	cyclic	$\partial_n p = 0$
$\mathbf{v}$	cyclic	cyclic	$\mathbf{v} = 0$

Table 3.1: Boundary conditions for simulations of fully developed MHD flows in pipes with electrically insulating walls.

Inlet and outlet are assumed as periodic for simulations of fully developed flow in long straight pipes. The electric potential gradient is zero along the wall interface, which prevents current leakage in order to model a perfectly insulating wall $c = 0$. The fluid sticks to the wall where velocity becomes zero $\mathbf{v} = 0$. Furthermore, an additional source term in the momentum equation adjusts the streamwise pressure gradient to satisfy $Re = 1000$.

Considering the block-structured O-grid configuration (BLOCK), singularities manifest in the form of high peaks in the numerical solution of the velocity distribution, as shown in the first row of figure 3.2. The result demonstrates the fatal impact of critical points and associated irregularities in the grid topology on the computational outcome. At a sufficient distance from critical points, the velocity v_x appears smooth. However, strong singularities emerge from locations of grid discontinuities, and perturbations propagate along magnetic field lines and block boundaries. The plot of velocity along the diagonal direction d, indicated by the red sample line, demonstrates this behavior by crossing two critical points. The black dashed line represents the asymptotic solution for the core velocity v_c by Chang & Lundgren (1961), extended by the viscous boundary layer correction proposed by Shercliff (1962)

$$v_x = v_c(z)\left(1 - e^{-\cos(\alpha) Ha\, n}\right) , \tag{3.1}$$

where α refers to the angular cylinder coordinate according to figure 2.4 and n to the distance from the wall. Vertical dashed lines indicate where core and boundary grids merge. The structured grid used in the boundary layer appears well suited for the numerical simulations. Independent of the type of core grid, the velocity distribution in the boundary layer is smooth and consistent with the theoretical prediction.

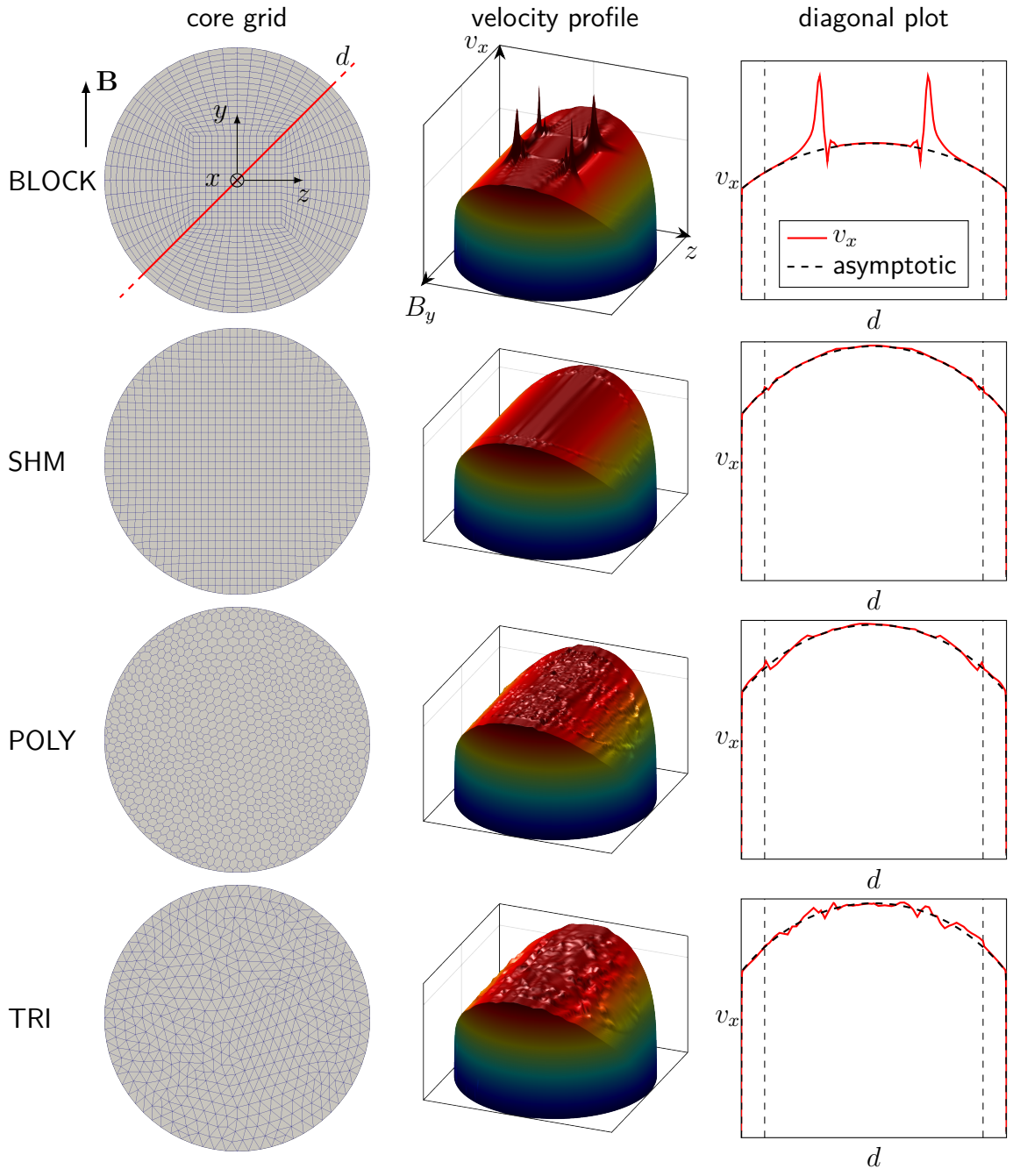

Figure 3.2: Qualitative relations between core grid structure and quality of numerical solutions for velocity. (left): topology of core grid, the boundary grid is not displayed; (middle): numerical solution for axial velocity; (right): velocity plot comparing numerical values of v_x (red solid line) to the asymptotic solution in equation 3.1 (black dashed line) along the diagonal direction d exemplarily shown as red sample line for the BLOCK core mesh. Vertical dashed lines indicate where the core grid merges with the graded grid in the boundary layer. Pipe flow with $c = 0$ and $Ha = 1000$.

The automatic mesh generation tool Snappy-Hex-Mesh (SHM), which is integrated into the OpenFOAM environment, crafts the SHM core grid as presented in the second row of figure 3.2. This approach crops the mesh out from a structured equally-spaced block and inserts unstructured elements to merge with the boundary layer grid. As a result, the grid mainly exhibits a uniform core structure, which benefits the computations. The results show a comparatively good agreement of v_x with the asymptotic solution. In contrast to the BLOCK configuration, the boundary and core grid of SHM form a sharp interface with a layer of highly unstructured elements, mainly triangular cells. However, these grid discontinuities generate only minor numerical errors in the form of a small circular silhouette on the velocity profile. Those perturbations further propagate along magnetic field lines and lead to slight wave-like ripple contours in the core along z.

The CFD software STAR-CCM+ has been applied to generate two fully unstructured core grids labeled POLY and TRI according to their basic element type, which is polygonal and triangular, respectively. In both cases, impacts of unstructured grids on simulations of MHD flow manifest in moderate ripples across the entire core.

In order to demonstrate how grid type and resolution affect the convergence of the solution, this study considers varying cross-section cell numbers N_c. In figure 3.3, the results are compared to simulations using an *optimized* mesh and discretization methods according to later findings in this chapter including a highly resolved cross-section at $(N_c)_{\mathrm{qe}} = 136048$. Referring the obtained numerical results to such a *quasi-exact* solution, as labeled by the subscript qe, allows to evaluate the numerical consistency of the computational approach in order to verify the underlying spatial resolution and numerical discretization schemes.

The top graph in figure 3.3 presents the difference between computed and *quasi-exact* reference velocity, i.e., v_x and $(v_x)_{\mathrm{qe}}$, being averaged across the pipe cross-sectional area $A_\varnothing$

$$\overline{(\Delta v)} = \frac{1}{A_\varnothing} \int_{A_\varnothing} \left| v_x - (v_x)_{\mathrm{qe}} \right| \mathrm{d}A \ . \tag{3.2}$$

This value indicates the mean error in comparison to the quasi-exact solution projected on the whole domain and thus provides a statement about the overall deviation. In this context, TRI and BLOCK type grids show poor performance as their mean error is hardly affected by grid refinement. While $\overline{(\Delta v)}$ for the TRI type seems not to converge at all with an increasing number of grid cells, it slowly starts descending for the BLOCK type only for higher resolutions $N_c > 10^4$. SHM and POLY grids, on the other hand, show a monotonous decline of the mean error along N_c.

The middle plot presents the maximum error of velocity deviations in the core flow domain, including the transition from core to boundary grid

$$(\Delta v_{\mathrm{core}})_{\max} = \max \left| v_x - (v_x)_{\mathrm{qe}} \right| \ . \tag{3.3}$$

This value indicates the highest occurring local deviation in the core region and thus enables

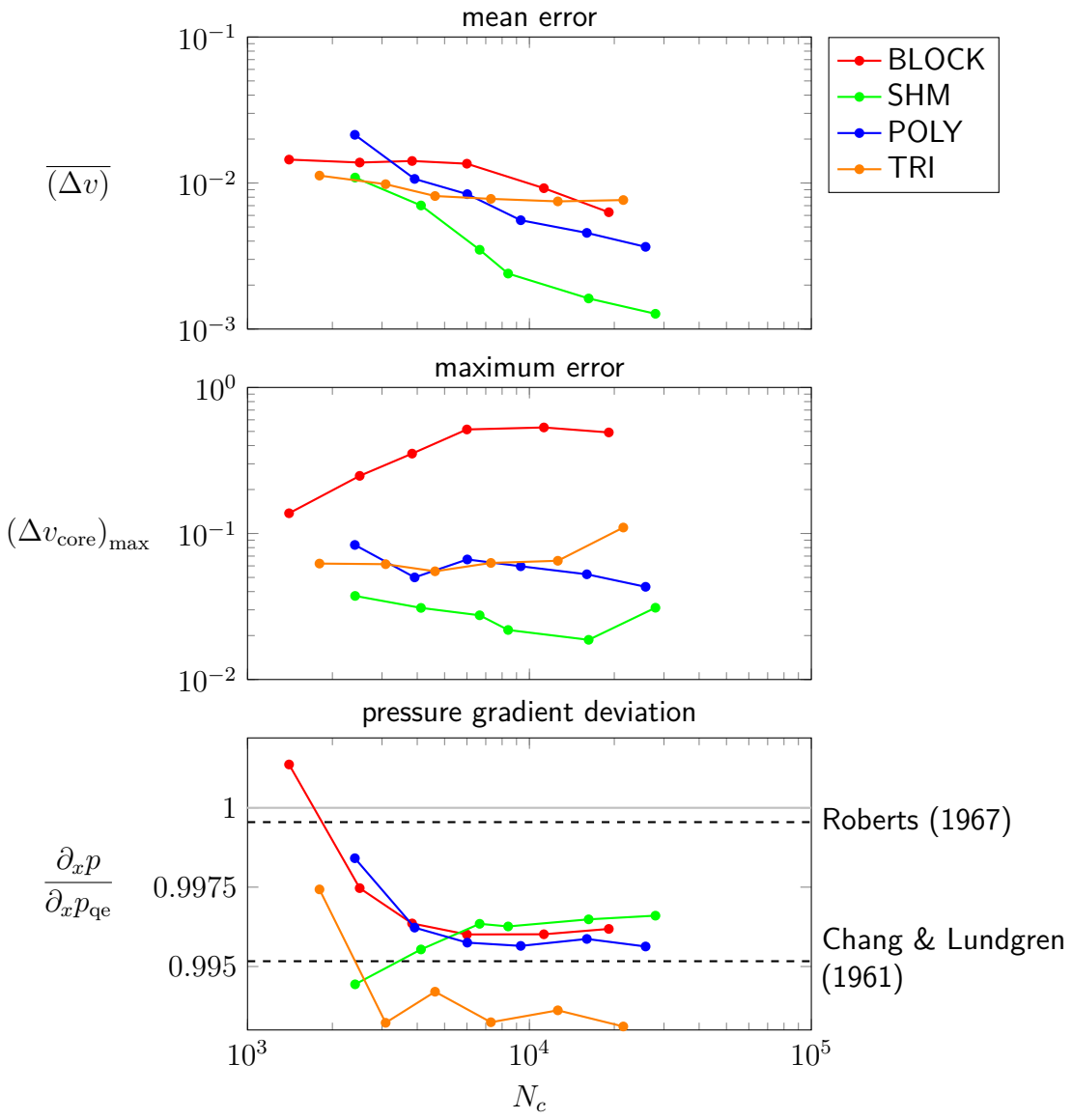

Figure 3.3: Error plots for circular MHD pipe flow showing convergence depending on grid-type and cross-section cell number. In the bottom plot showing pressure gradients, the horizontal gray line indicates the quasi-exact computed solution $\partial_x p_{\mathrm{qe}}$ and black dashed lines represent asymptotic solutions. Pipe flow with $c = 0$ and $Ha = 1000$.

the assessment of the most pronounced perturbations. As expected from figure 3.2, critical points of BLOCK type grids involve by far the highest errors of up to $(\Delta v_{\mathrm{core}})_{\mathrm{max}} \approx 0.6$, shown by the red line in the center plot of figure 3.3. Furthermore, average and maximum errors of the BLOCK type, presented red, show a correlating pattern where the former remains constant and descends for $N_c > 10^4$ while the latter rises and then remains constant for $N_c > 10^4$. This indicates that the velocity perturbations at the critical points approach the highest values when the flow region is well resolved. From there on highest perturbation

magnitudes remain constant (no convergence), while the average error starts to decrease. This furthermore demonstrates the impact near critical points inducing zero-order errors, which become independent from mesh refinement, as stated by Moukalled et al. (2016, pp. 124-126). The maximum error of unstructured grid types, POLY and TRI, are moderate and refer to the constant core ripple shown in figure 3.2. The SHM grid provides the lowest perturbations, which originate from the unstructured transitions between the core and boundary grid.

The bottom plot shows that the calculated streamwise pressure gradients $\partial_x p$ agree well with the quasi-exact reference $\partial_x p_{\mathrm{qe}}$, with deviations below $5‰$, except for the TRI grid type where differences are slightly higher. The asymptotic solutions, shown by the horizontal dashed lines, suggest that pressure gradient deviations occur within an acceptable range already at moderate grid size. While the more general approach by Chang & Lundgren (1961) considers only the core flow, the asymptotic solution by Roberts (1967), in addition, accounts for Hartmann and Roberts layers and thus agrees much better with the quasi-exact numerical solution, shown as a horizontal gray line. Since both asymptotic references are not exact solutions, some deviation towards $\partial_x p_{\mathrm{qe}}$ is expected.

Boundary grid

When the wall conductance is low, the majority of electric current closes over the thin Hartmann layer. Therefore, a proper resolution of the viscous layers is essential for good results since current paths along the boundary layers influence core solutions and affect the total pressure drop. A principle sketch of a boundary layer grid along a curved periphery is shown in figure 3.4. For curved boundaries, the layer thickness δ_{Ha} depends on the wall-normal strength of the magnetic field, and it reduces to a minimum at locations where the wall-normal vector and magnetic field align. This position on the periphery is labeled as Hartmann point and shown as a red dot in the figure. Here the boundary layer poses a bottleneck for the closure path of the electric current, and prism layers of the boundary grid, shaded in light blue, must accurately resolve such domains.

The sketch demonstrates the general insufficiency of any polyhedral cell-type to accurately resolve curved boundaries. Flat cell faces approximate the circular pipe as a polygon leaving empty spaces that are not captured by the spatial resolution, shown as white areas between flow domain periphery and computational mesh. Moreover, the representation of wall contour is not smooth and exhibits a large number of corners. The permanent reorientation of boundary currents and the inability of rectilinear prism layers to resolve curved boundaries, therefore, requires a particularly high resolution in both radial and tangential direction. Otherwise, empty spaces between prism layers and flow domain periphery might significantly impede the current reconstruction. In addition, each corner that is created between adjacent boundary faces constitutes a discontinuity in the curved pipe geometry, to which MHD flows are particularly sensitive, as shown and discussed in an upcoming chapter for annular cross-sections in figure 5.19. Those geometric discontinuities in the computational boundary

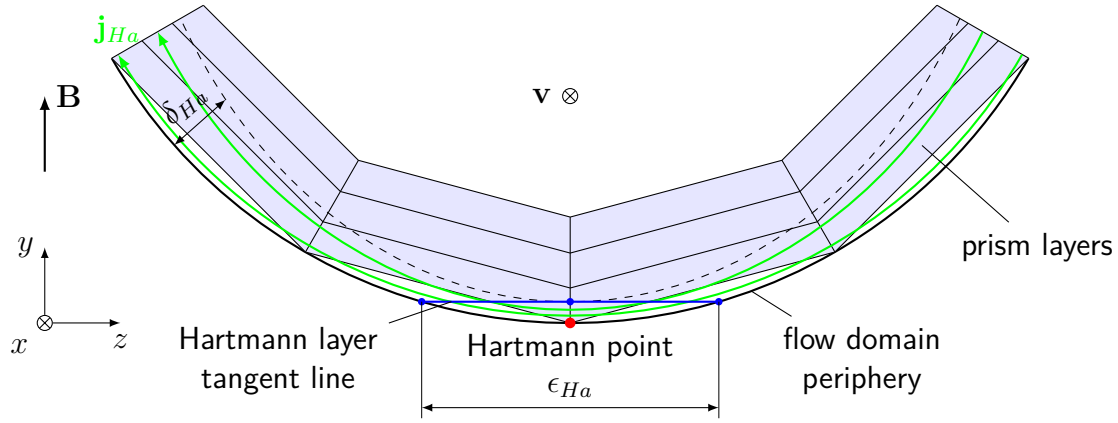

Figure 3.4: Sketch of boundary grid resolving Hartmann layers along a curved wall. Aspect ratios are greatly downplayed for clarity. The red dot marks the Hartmann point, where the magnetic field and wall-normal vector align and where the Hartmann layer forms a bottleneck for electric current flow (green lines).

mesh can be the origin for perturbations that spread across the entire duct along magnetic field lines in the form of internal shear layers. A larger number of cells along the pipe circumference generally leads to a better alignment of boundary faces with the curved pipe periphery and helps to minimize these disturbances. In this context, the blue line in figure 3.4 illustrates the tangent line at the Hartmann boundary layer (dashed line), where the boundary layer becomes thinnest. Its intersection with the wall thus sets a critical restriction to the computational mesh. The tangent line ends at the periphery and has the length

$$\epsilon_{Ha} = 2\sqrt{1-(1-\delta_{Ha})^2}\ . \tag{3.4}$$

For strong magnetic fields, i.e. small Hartmann layer thickness $\delta_{Ha} \ll 1$, the length of the Hartmann layer tangent line scales according to

$$\epsilon_{Ha} \sim \sqrt{\delta_{Ha}}\ , \tag{3.5}$$

and boundary cells should be shorter than epsilon for a good peripheral resolution. This means that for curved boundaries, Hartmann layers require both radial and tangential refinement according to length scales of Ha^{-1} and $Ha^{-1/2}$, respectively. Provided that boundary grid points are uniformly distributed in the circumferential direction, assuming at least two boundary grid points per tangent length ϵ_{Ha} seems to be a reasonable first guess for a good mesh design. This assumption leads to a total number of circumferential boundary grid points

$$N_\circ \geq 2\frac{2\,\pi}{\epsilon_{Ha}} \tag{3.6}$$

that are necessary to sufficiently resolve the flow domain periphery.

The proposed tangential resolution of equation 3.6 required for curved boundaries, however, leads to a expensive computational refinement of the core grid when grid lines

have to be matched between the boundary and the core. An alternative approach, therefore, involves a local refinement, which inserts smaller cells close to boundaries in order to resolve the circumferential boundary grid in the tangential and radial direction, and which simultaneously maintains a comparatively coarser cost-effective core grid. Such SHM grid type, as shown by figure C.1 in the appendix, is capable of meeting those requirements at affordable costs. This approach maintains a coarse core grid while it splits the cells in direct boundary vicinity and thus enables a computationally efficient tangential and radial refinement.

Simulations of the core grid study shown in figure 3.3 have been repeated with such an enhanced refinement applied to the SHM grid type, which involves higher resolutions towards the boundary. However, for the investigated parameter of $c = 0$ and $Ha = 1000$, an outward-directed grading shows no relevant improvement. The reason is that this approach injects further grid irregularities in the form of sharp mesh transitions, to which the considered case of insulating pipe walls $c = 0$ is highly sensitive.

In summary, there exist strong dependencies of numerical errors on the type of grid, which in some cases even increase with the number of cells. Since a higher spatial resolution alone does not always lead to better results, more robust discretization schemes are required to improve the quality of simulations, especially for strong magnetic fields. In the upcoming section 3.2, it is shown that the quality of results depends essentially on the discretization scheme for the electric potential gradient, and a proper choice of scheme can lead to significant improvements.

3.2 Discretization schemes for the electric potential gradient

The determination of electric current density and electric potential gradient is particularly sensitive to grid topology when the wall conductance c is low. For this case, Vantieghem (2011, p. 54) denotes the calculation of electric current density as a *poorly conditioned* arithmetic operation since Ohm's law in equation 2.1 determines a comparatively low $\mathbf{j}$ as a difference between equally large terms in the form of the induced electric field $\mathbf{v} \times \mathbf{B}$ and electric potential gradient $\nabla\phi$. Continuity of currents is determined through a flux balance on the cell surfaces as implemented by equation 2.23. Mesh shortcomings like face skewness may therefore induce numerical errors that are magnified by the gradient discretization of the electric potential $\nabla\phi$ and thus transfer on the current density, Lorentz force, and eventually the momentum. This section presents two numerical schemes, which reduce the impact of mesh skewness on the gradient discretization of the electric potential. It is further shown how improved schemes may affect convergence.

Skew-corrected Green-Gauss gradient

The original MHD code determines the electric potential gradient by means of the Green-Gauss method combined with linear interpolation. If spatial discretization is high enough, gradients can be assumed uniform across each cell. Following the Green-Gauss method, the gradient at the cell center C then becomes (Moukalled et al., 2016, equation 8.75)

$$\nabla\phi_C = \frac{1}{V_C}\sum_{f}^{\mathrm{nb}(C)} \phi_f \mathbf{S}_f \ . \tag{3.7}$$

The gradient evaluation corresponds to a summation of electric potential flux across all cell surfaces $\mathrm{nb}\,(C)$ divided by the cell volume V_C. Figure 3.5 illustrates the gradient determination following Green-Gauss for a cell C and its direct face neighbor F adjacent to a critical point of the BLOCK-mesh type. This operation requires the evaluation of electric potential at the face centroid ϕ_f. The code's original approach applies a linear interpolation according to

$$\phi_{f'} = \mathrm{g}_C\phi_C + (1-\mathrm{g}_C)\,\phi_F \tag{3.8}$$

where the weight factor measures

$$\mathrm{g}_C = \frac{\mathbf{S}_f \cdot \mathbf{r}_{fF}}{\mathbf{S}_f \cdot \mathbf{r}_{Cf} + \mathbf{S}_f \cdot \mathbf{r}_{fF}} \tag{3.9}$$

with $\mathbf{S}_f$ as the respective face area Vector. In the case of orthogonal structured grids, the intersection f' and face centroid f coincide. Unstructured grids or grid irregularities, on the other hand, generally exhibit a deviation $\mathbf{r}_{f'f}$ of face centroids towards the linear connection of adjacent cells $\mathbf{r}_{CF}$, shown as a dashed line. This deviation is particularly high at critical points of the BLOCK mesh but also concerns unstructured cells of SHM as well as POLY and TRI grids, in general. Hence, the computation of the electric potential gradient leads to numerical errors, which, according to Vantieghem (2011), get amplified due to the ill-conditioned nature of Ohm's law in equation 2.1.

In the case of high face skewness, Ni et al. (2007) recommend an adaption of the face interpolation by $\mathbf{r}_{f'f}$. Since this vector is orthogonal to the face area vector $\mathbf{S}_f$, it can be determined according to

$$\mathbf{r}_{f'f} = \mathbf{r}_{Cf} - \frac{\mathbf{S}_f \cdot \mathbf{r}_{Cf}}{\mathbf{S}_f \cdot \mathbf{r}_{CF}}\mathbf{r}_{CF} \ . \tag{3.10}$$

This enables the adaption of interpolated face potential by means of an explicit correction scheme (Moukalled et al., 2016, equation 9.8)

$$\phi_f = \phi_{f'} + \underbrace{(\nabla\phi)_{f'} \cdot \mathbf{r}_{f'f}}_{\text{correction}} \ . \tag{3.11}$$

Such correction requires the interpolation of the gradient from the cell centroid $(\nabla\phi)_C$ to

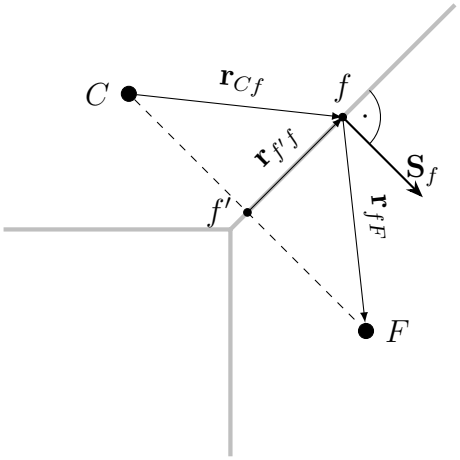

Figure 3.5: Grid topology between cell C and its direct face neighbor F at a critical point of the BLOCK mesh. The high face skewness leads to strong deviation between face intersection f' and face centroid f as represented by the skew-correction vector $\mathbf{r}_{f'f}$.

the intersection $(\nabla\phi)_{f'}$. Since the determination of both values depends on each other, this procedure is done iteratively by repeatedly adapting them in a loop. Moukalled et al. (2016, pp. 277-280) provide a detailed description of the implementation of face-skewness correction.

The grid study has been repeated with the presented skew-correction scheme exclusively applied to the electric potential gradient. Figure 3.6 shows the outcome where colored dashed lines indicate results from the original uncorrected approach from figure 3.3, and solid lines refer to the skew-corrected gradient scheme.

Skew-correction has a generally positive effect across all considered grid types and cell numbers, so it provides an overall improvement. In particular for larger grids $N_c > 10^4$, solid lines of the mean errors move closer together so that deviations towards the quasi-exact solution become increasingly independent from the grid type and ultimately depend only on the number of cells. This demonstrates that the originally observed perturbations are well treated by the underlying skew-correction scheme.

Skew-correction has an exceptionally high impact on the BLOCK grid type. As shown by red lines for the mean and maximum error of velocity, deviations decrease by around one order of magnitude. Maximum errors decrease to an acceptable range, and mean errors are lowest among the considered grid types. Since SHM is comparatively well structured and cells mostly align with the orientation of the magnetic field and current flow, it appears least affected by skew-correction. Only at the transition between core and boundary grid, where SHM grids contain skewed cells, the correction scheme leads to a minor reduction of numerical errors. Considering the mean error for POLY and TRI grid types, shown blue and orange, convergence rate differs significantly for small grid sizes $N_c < 10^4$. In contrast to

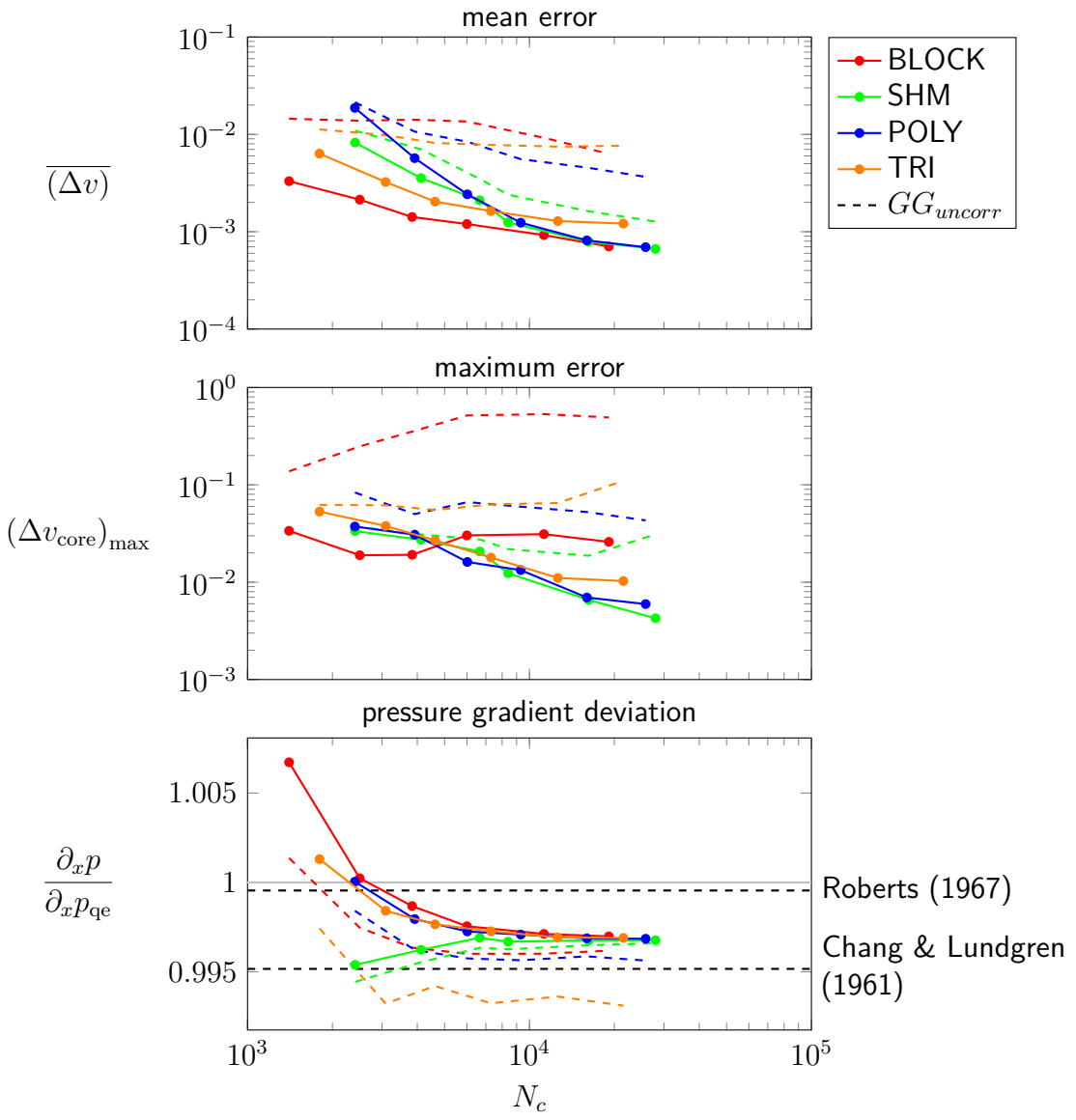

Figure 3.6: Error convergence for the skew-corrected Green-Gauss gradient scheme GG_{corr} (solid lines) depending on the grid type and cross-section cell number N_c. Colored dashed lines show the original uncorrected approach GG_{uncorr} from figure 3.3. In the bottom plot, showing the pressure gradient, the horizontal gray line indicates the quasi-exact computed solution and black dashed lines represent asymptotic solutions. Pipe flow with $c = 0$ and $Ha = 1000$.

the triangular grid type, polygonal cells offer more faces for correction, which leads to a higher convergence.

Although the pressure gradient is already well replicated by an uncorrected scheme, skew-correction further improves the outcome for all schemes but in particular for the TRI grid type. The comparatively poor convergence above $N_c > 10^4$ is due to the boundary resolution

layer in the tangential direction and associated relations discussed above in figure 3.4.

It has been noted that for higher numbers of grid cells $N_c > 10^4$, where the mean error and pressure gradient deviations increasingly become independent from the mesh topology, the investigated meshes also start to meet the proposed criteria of a sufficiently resolved pipe circumference according to equation 3.6. This convergent behavior would correspond to the assumption that MHD flow at a low wall conductance highly depends on the accurate replication of boundary currents. However, to which fraction the reconstruction of currents in either boundary layer or core domain affects the overall numerical accuracy is out of the scope of this grid study, but this should certainly be addressed in continuing works.

In summary, results demonstrate that for insulating walls, the determination of electric potential gradient by means of Green-Gauss considerably depends on the mesh topology and is highly vulnerable to grid irregularities (Moukalled et al., 2016, pp. 124-126). Applying the correction of face-skewness to the electric potential gradient results in a significant improvement where deviations occur within an acceptable tolerance. While the face-skewness correction for the determination of the potential gradient in the cell center $(\nabla\phi)_C$ is based on geometric arguments, it is possible to obtain also a good approximation in terms of a statistical approach. This is outlined in the next sub-section.

Least-Squares gradient

The Green-Gauss gradient presented above depends on mesh topology, i.e., face skewness has a great impact and must be corrected. The Least-Squares gradient, on the other hand, avoids this dependence by exclusively considering the spatial arrangement of adjacent cell centers, resulting in a statistical minimization problem.

Between cell C and all direct face neighbors F_k, where $k \in \mathrm{nb}(C)$, the electric potential gradient $(\nabla\phi)_C$ at each cell center should satisfy (Moukalled et al., 2016, equation 9.22)

$$\phi_{F_k} = \phi_C + (\nabla\phi)_C \cdot \mathbf{r}_{CF_k} \ . \tag{3.12}$$

However, there generally exist more face neighbors $k \in \mathrm{nb}(C)$ and thus more than three conditions have to be satisfied for the determination of three unknown components of the electric potential gradient $(\nabla\phi)_C = (\partial_x\phi, \partial_y\phi, \partial_z\phi)_C$, which prevents finding an exact solution. A Least-Squares approach using equation 3.12 then yields the optimization problem (Moukalled et al., 2016, equation 9.23)

$$\mathrm{G}_C = \sum_{k}^{\mathrm{nb}(C)} \left(w_k \left(\phi_{F_k} - (\phi_C + \nabla\phi_C \cdot \mathbf{r}_{CF_k}) \right)^2 \right) \ , \tag{3.13}$$

where w_k indicates an additional weighting factor

$$w_k = \frac{1}{|\mathbf{r}_{CF_k}|} \ . \tag{3.14}$$

The coefficients w_k account for highly stretched cells, like those in thin boundary layers, involving extreme aspect ratios. The three components of the potential gradient vector in the cell center C are determined such that the mean squared deviation G_C with all neighbors is minimized (Moukalled et al., 2016, equation 9.25). This requires

$$\frac{\partial \mathrm{G}_C}{\partial \left(\partial_x \phi\right)} = \frac{\partial \mathrm{G}_C}{\partial \left(\partial_y \phi\right)} = \frac{\partial \mathrm{G}_C}{\partial \left(\partial_z \phi\right)} = 0 \ . \tag{3.15}$$

Moukalled et al. (2016, pp. 285-288) furthermore provide a detailed description on solving the resulting linear system.

In contrast to the original Green-Gauss (GG) gradient scheme, the Least-Squares (LS) approach exclusively depends on geometric relations between adjacent cell centers independent of the arrangement of faces and face centroids. Syrakos et al. (2017) compare both schemes for hydrodynamic applications and find that LS outperforms GG on highly distorted grids where in special cases GG even may exhibit zero-order errors. The present study further compares the impact of both schemes on the electric potential gradient of MHD circular pipe flow involving different grid types.

The presented data in figure 3.7 shows results of the grid convergence study when the electric potential gradient is evaluated with the LS scheme. Dashed lines refer to the former skew-corrected Green-Gauss approach from figure 3.6, while solid lines correspond to the Least-Squares scheme.

Concerning the mean error $\overline{(\Delta v)}$, the Least-Squares scheme provides almost no further improvement towards GG_{corr} on POLY and SHM grid types, shown blue and green. Still, it shows minor improvements for TRI and BLOCK grids, which generally involve higher face skewness. Similar to the skew-corrected Green-Gauss gradient, simulations with high cell numbers, i.e., $N_c > 10^4$, converge independently from the grid type. This suggests that LS likewise resolves convergence differences of grid element types and, therefore the results only depend on the spatial resolution.

Maximum errors of Least-Squares gradient computations seem to have little impact on POLY, SHM and TRI grid types. For the BLOCK type grid on the other hand, a significant reduction of the maximum error is observed compared to the former applied skew-corrected Green-Gauss gradient scheme. With Least-Squares approximated potential gradients, simulations on a BLOCK type mesh exhibit best results. This promotes the BLOCK grid type from initially the worst choice of grid configuration to one of the best if combined with the Least-Squares scheme for the electric potential gradient.

Considering the pressure gradient, impacts of LS are vanishingly small in comparison to the

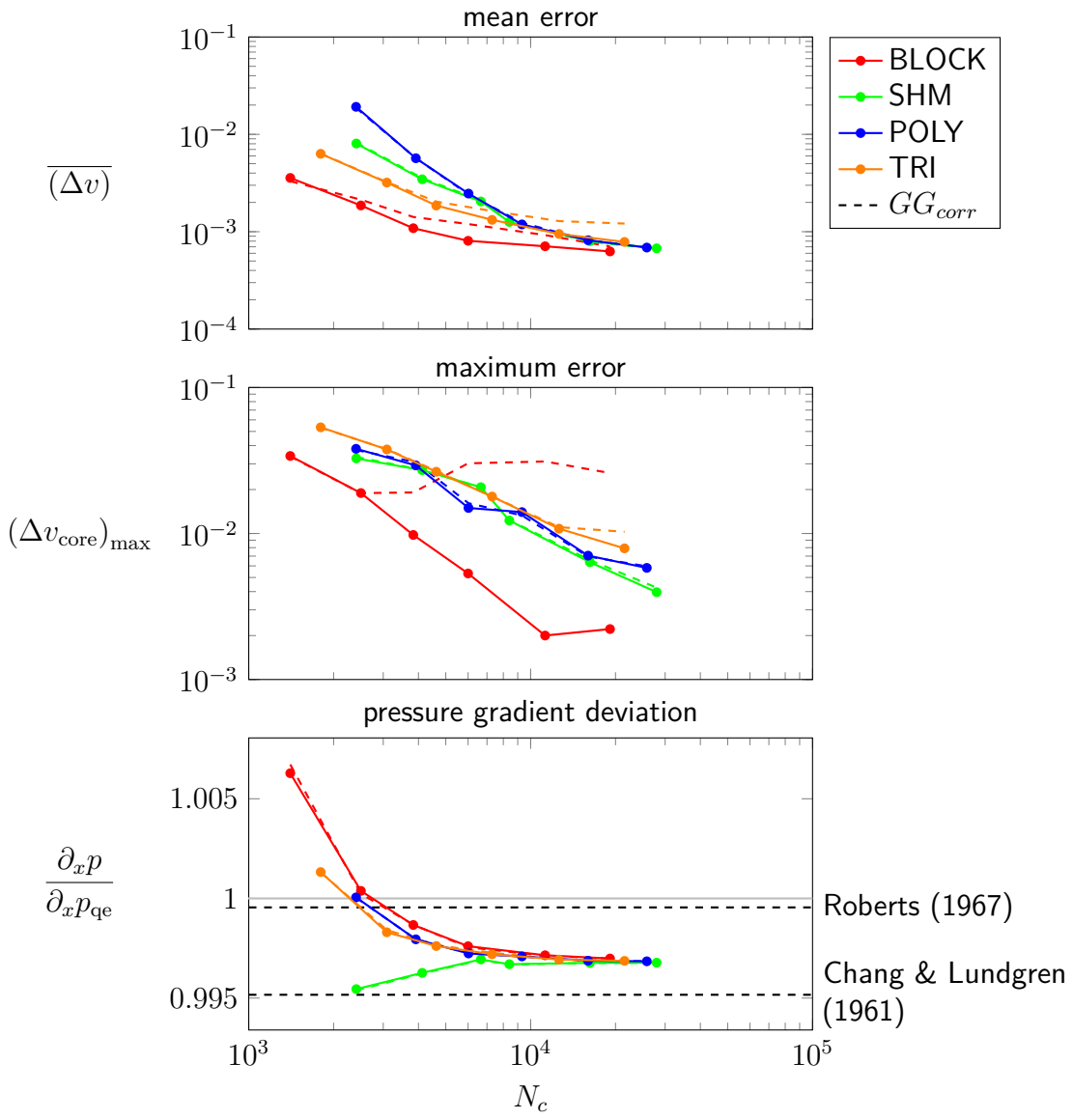

Figure 3.7: Error convergence for the Least Square gradient scheme LS (solid lines) depending on the grid type and cross-section cell number. Dashed lines refer to the skew-corrected Green-Gauss gradient scheme from figure 3.6. In the bottom plot, showing the pressure gradient, the horizontal gray line indicates the quasi-exact computed solution and black dashed lines represent asymptotic solutions. Pipe flow with $c = 0$ and $Ha = 1000$.

corrected Green-Gauss scheme since the latter one already provides very good results.

In order to illustrate the impact of the investigated gradient schemes for the electric potential on velocity profiles, figure 3.8 presents plots of axial velocity along the diagonal d, depending on the applied discretization schemes and grid type at specific cell numbers N_c. Vertical dashed lines indicate the border between core and boundary grid, and the black

dashed plot refers to the asymptotic solution according to equation 3.1.

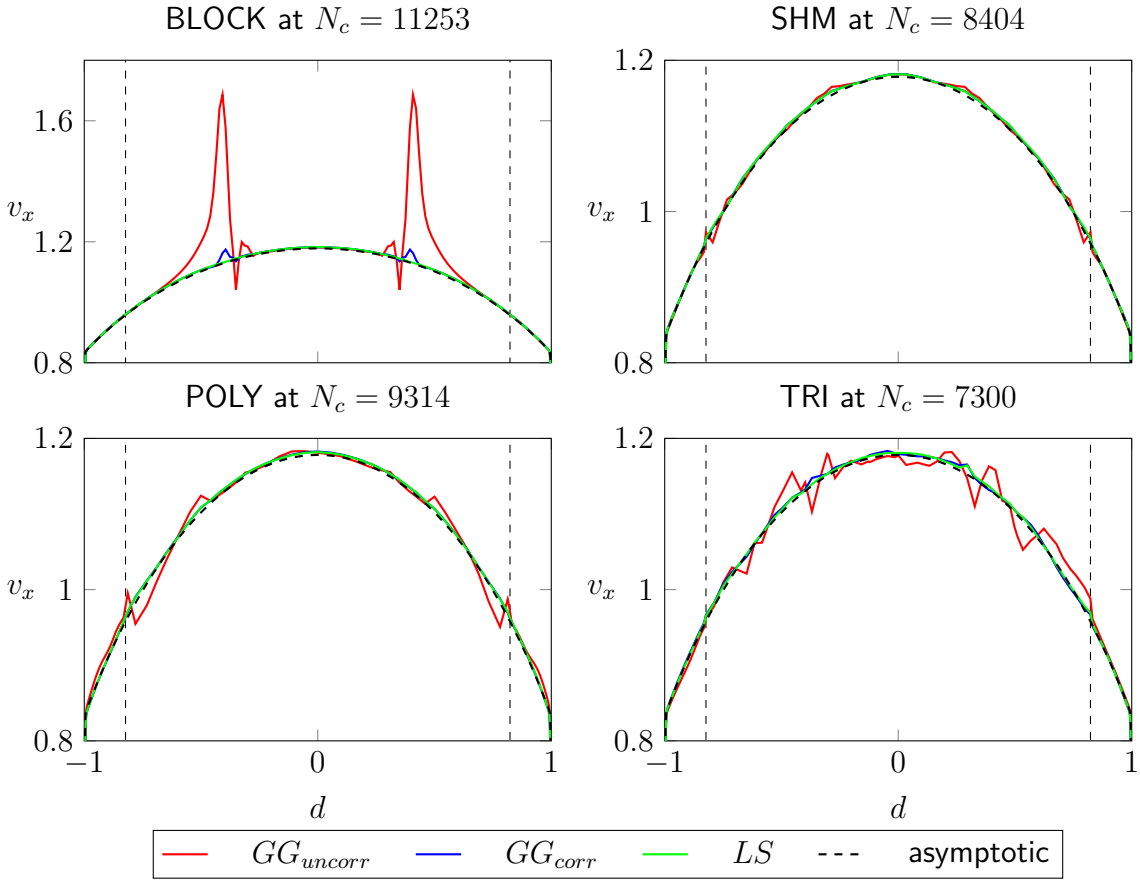

Figure 3.8: Diagonal plot of axial velocity v_x depending on grid structure and discretization of the electric potential gradient. Vertical dashed lines indicate where boundary and core grid merge. The black dashed curve shows the asymptotic solution according to equation 3.1. Pipe flow with $c = 0$ and $Ha = 1000$.

Considering the BLOCK grid type, strong perturbations occurring at critical points can effectively be removed by applying either a skew-correction or Least-Squares scheme, as presented in blue and green, respectively. While the former shows a remainder in the form of minor non-physical peaks, the latter entirely eradicates perturbations of mesh irregularities at critical positions.

The SHM grid type already shows the best convergence behavior for the originally uncorrected gradient scheme GG_{uncorr} since the core grid is for the most part well aligned with the orientation of magnetic field lines and current flow. Hence, only minor errors occur at the transition between core and boundary grid. Those errors are reduced to a minimum by using the skew-corrected Green-Gauss or Least-Squares gradient schemes, leading to reasonable results.

Both fully unstructured grid types, POLY and TRI, show a strong and persistent ripple

for the originally employed uncorrected Green-Gauss gradient scheme. Either a corrected Green-Gauss or a Least-Squares gradient scheme may significantly reduce such errors and lead to a comparatively smooth profile that agrees well with asymptotic theory.

In summary, treating mesh-skewness for the discretization of the electric potential gradient becomes indispensable for simulations of MHD flows in curved geometries, especially when unstructured or discontinuous computational grids are used. For low wall conductance, the evaluation of electric current may significantly amplify mesh-induced errors, which might become fatal to the computational outcome. The present study finds that applying either a corrected Green-Gauss or a Least-Squares scheme in order to determine the electric potential gradient minimizes skewness-related perturbations so that errors eventually decrease with an increasing number of computational cells for all types of meshes investigated in the present work. Results obtained so far address MHD flows in electrically insulating pipes. The next sections will extend the investigations to applications with conducting walls.

3.3 Perfectly conducting wall

The former section demonstrated the high vulnerability of the MHD code to mesh skewness in the case of an insulating pipe wall with associated low current density in the core. Electrically conducting walls, on the other hand, increase current flow and thus likewise reduce the strong imbalance in order of magnitudes between current density, electric potential gradient and induced electric field in Ohm's law. The highest differences compared to previous results are expected when walls are perfectly conducting, as investigated in the following.

If walls are perfectly conducting, potential gradients vanish along the wall, and the potential becomes uniform, i.e., $\phi = 0$ at the fluid-wall interface.

The grid study is repeated for the case of a perfectly conducting wall considering both a Least-Squares and an uncorrected Green-Gauss gradient scheme for the electric potential. Results are compared with an *quasi-exact* solution involving a highly resolved computational grid. Figure 3.9 presents the outcome where solid lines represent the application of Least-Squares and dashed lines the uncorrected Green-Gauss scheme.

For perfectly conducting walls, the associated higher current flow in the fluid leads to significantly less amplification of numerical errors since the current and induced electric field in Ohm's law have the same order of magnitude, and therefore they are better balanced. Imposed by the perfectly conducting condition of the wall, the potential gradient becomes vanishingly small. Since the influence of potential gradient remains marginal, it is already approximated good enough by the originally applied uncorrected Green-Gauss gradient scheme for all considered grid configurations.

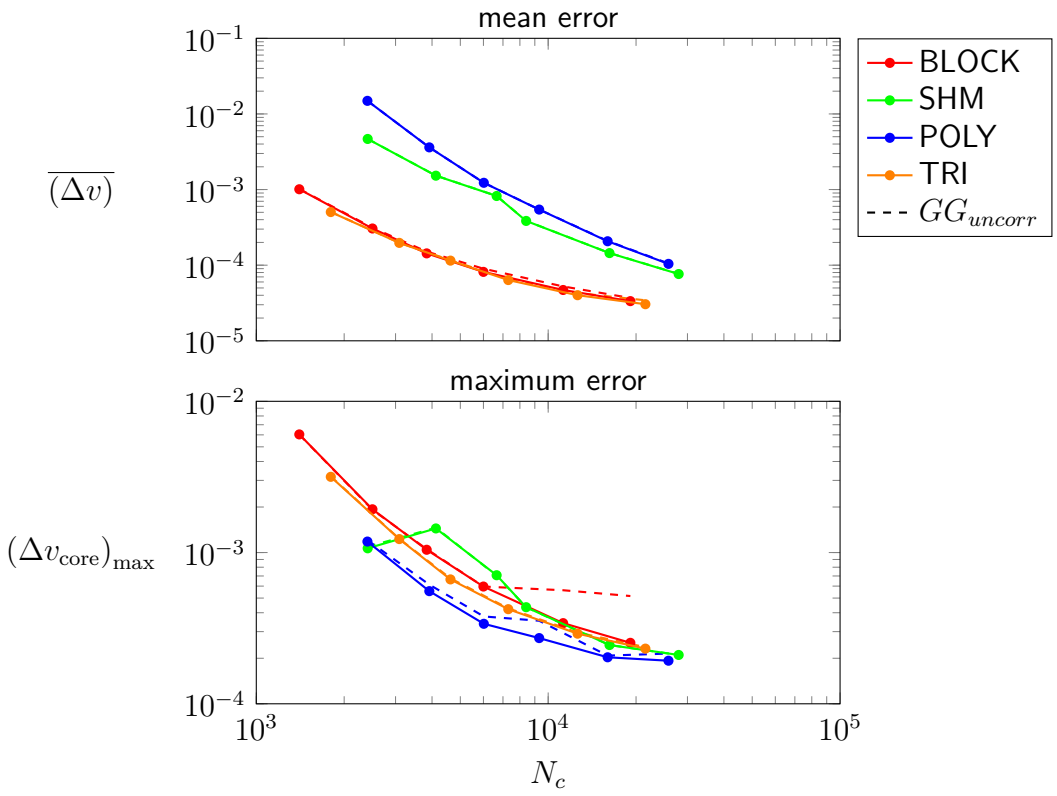

Figure 3.9: Error convergence for the Least-Square gradient scheme LS (solid lines) depending on the grid type and cell layer number. Dashed lines refer to the uncorrected Green-Gauss gradient scheme GG_{uncorr}. Pipe flow with $c \to \infty$ and $Ha = 1000$.

The improvement by using advanced gradient schemes such as Least-Squares LS does not lead to significantly better results. However, it is surprising that BLOCK and TRI grid types generally stand out against SHM and POLY configurations by showing lower deviations to the quasi-exact solution, already for a smaller number of cells. The maximum error $(\Delta v_{\text{core}})_{\text{max}}$, on the other hand, behaves similarly for different grid types and gradient schemes. Minor deviations of the uncorrected scheme for the BLOCK grid type, shown as red dashed line, suggest the emergence of small peaks from critical locations, which however appear in an acceptable range, i.e., $(\Delta v_{\text{core}})_{\text{max}} < 10^{-3}$ for $Nc > 10^4$. Deviations of the pressure gradient, which are not shown here, are negligibly small and correspond to OpenFOAM's precision of output decimals already at a moderate numbers of cells.

3.4 Finite wall conductance

So far, the conducted investigations addressed either fully insulating or perfectly conducting walls. In fusion-relevant problems, where walls have a finite thickness and

electric conductivity, wall currents must be taken into account as well. This requires solving the Poisson equation for the electric potential across fluid and solid domains, which both are resolved by the computational grid. Coupling between fluid and wall is achieved by assuming continuity of wall-normal current density and continuity of electric potential (no contact resistance). The outer surface of the wall is insulating, i.e., $\partial_n \phi_w = 0$. From a numerical point of view, the problem is analogous to the one of conjugate heat transfer, which is described by Magnusson (2010). A joint matrix for the solution of potential equations in the fluid and in the wall with implicit coupling conditions is formulated, and equations are solved collectively according to the approach by Jareteg (2013). The complete configuration of boundary conditions is listed in table 3.2.

	inlet	outlet	fluid-wall interface	outer wall surface
ϕ	cyclic	cyclic	$\phi = \phi_w$, $j_n = j_{n,w}$	$\partial_n \phi_w = 0$
p	cyclic	cyclic	$\partial_n p = 0$	
$\mathbf{v}$	cyclic	cyclic	$\lvert\mathbf{v}\rvert = 0$	

Table 3.2: Boundary conditions for simulation of fully developed MHD flows in pipes with finite electrically conducting walls.

In order to demonstrate the code's capability to predict MHD flows for fusion-relevant conditions, particularly high values of Hartmann numbers are chosen according to table 3.3. Furthermore, a low wall conductance c is set in a manner so that $c\,Ha = 10$ involving a non-dimensional wall thickness of $t_w = 0.1$. This poses an additional challenge to the numerical approach since current flow closing over wall and Hartmann layers have similar orders of magnitude, and therefore both must be computed accurately. The strong magnetic fields and associated thin Hartmann layers require a highly refined boundary grid in radial and tangential direction, which is best met by an SHM based grid, as shown by figure C.1 in the appendix. The underlying grid for curved geometries might magnify numerical errors upon computation of the electric potential gradients. Hence, the Least-Squares scheme is applied as proposed above to suppress the amplification of numerical errors during the solution of the potential equation on unstructured grids. Moreover, an additional skew-correction is applied to interpolation schemes. The requirement of a high tangential boundary resolution results in a rather large number of cells as indicated by the number of cross-sectional grid points N_c. For fully developed flow, the grid is extruded by three layers of cells in the axial direction with imposed cyclic conditions (see in table 3.2). This results in a high computational effort where the largest number of cells requires 192 processor cores and an operating time of several days for the computations to fully converge.

According to table 3.3, the calculated pressure gradient $\partial_x p$ is compared to the asymptotic solution $\partial_x p_{2D}$ by Chang & Lundgren (1961). Since the asymptotic model is not exact, it neglects viscous boundary layers and applies only to thin walls. A deviation of about 5% in each case seems plausible.

As demonstrated for $Ha = 5000$ by the top plot in figure 3.10, the velocity remains constant along y. Still, v_x shows a significant curvature orthogonal to magnetic field lines

Ha	c	N_c	$\frac{\partial_x p}{\partial_x p_{2D}}$
5000	$2 \cdot 10^{-3}$	441 196	0.96
10000	$1 \cdot 10^{-3}$	569 436	0.95
50000	$2 \cdot 10^{-4}$	1 193 196	0.96

Table 3.3: Case specifications for high Hartmann numbers where $c\,Ha = 10$. N_c refers to the cell number within one cross-sectional layer. The pressure gradient is compared to the asymptotic solution $\partial_x p_{2D}$ according to Chang & Lundgren (1961).

along the z-axis, captured by red and blue sample lines. This indicates an essential impact of boundary layer currents due to the relatively low wall conductance $c\,Ha = 10$.

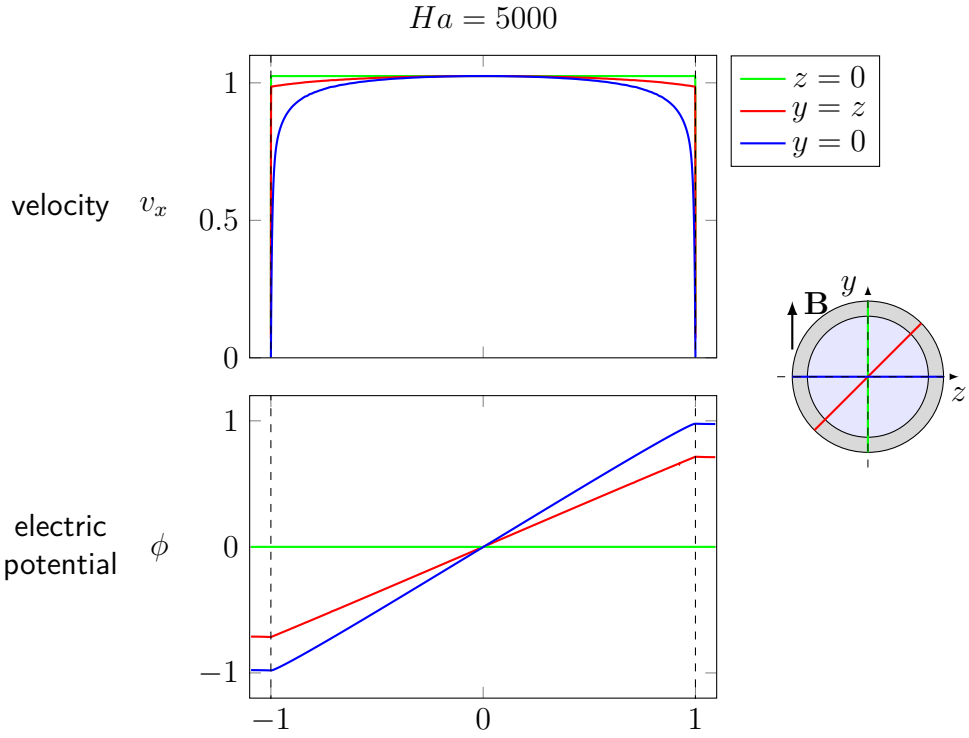

Figure 3.10: Velocity profiles (top) and electric potential distribution (bottom) at specific pipe axes according to the sketch. Vertical dashed lines indicate the fluid-wall interface. $Ha = 5000$, $c\,Ha = 10$.

The bottom plot shows the electric potential distribution along the same sample lines, as illustrated by color. The electric potential difference is highest between the sides of the pipe across the horizontal line, shown in blue. It is lower for the pipe's diagonal and eventually becomes zero across its vertical line, shown red and green, respectively. Moreover, the wall potential $\phi\,(r > 1)$ approximately persists in the radial direction across the solid domain since the wall is relatively thin. Currents induced in the core close their paths either over the Hartmann layer or the solid domain driven by the varying wall potential. Due to the

imposed condition $c = 10\,\delta_{Ha}$, current densities in the boundary layer and wall are both important.

Figure 3.11 presents values of computed axial velocity over the wall distance n at different angles α. The logarithmic scaling of the abscissa enables a closer examination of the extremely thin boundary layers, where the velocity rises from zero at the fluid-wall interface $n = 0$ to approach the core velocity v_c.

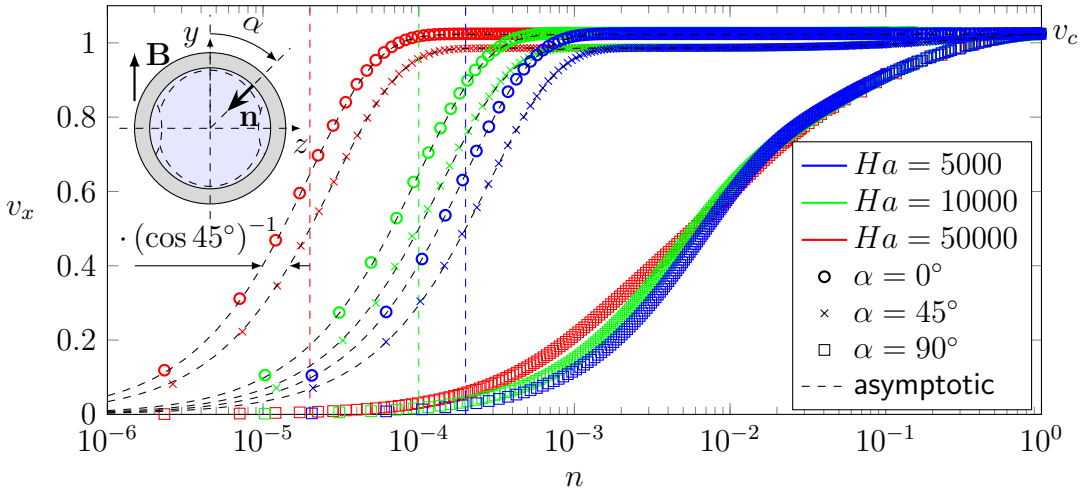

Figure 3.11: Values of axial velocity v_x as a function of wall distance n displayed in logarithmic scale and for specific angular cylinder coordinates α. Black dashed lines indicate the asymptotic solutions by Chang & Lundgren (1961) extended by the viscous boundary layer correction of equation 3.1 by Shercliff (1962). Vertical colored lines show the theoretical Hartmann layer thickness $\delta_{Ha} = Ha^{-1}$. Pipe flow with $c\,Ha = 10$.

As introduced with formula 2.12 the thickness of the Hartmann layer scales according to $\delta_{Ha} \sim 1/(Ha\cos\alpha)$ and the velocity in the viscous shear layer is well described by Shercliff (1962) in equation 3.1.The layer becomes thinner with increasing Ha, shown by color. The thickness of the Hartmann layer increases with increasing α as $\delta_{Ha} \sim 1/(Ha\cos\alpha)$, presented in figure 3.11. Vertical dashed lines indicate the Hartmann layer thickness at $\alpha = 0$, where the viscous boundary layer thickness reaches a minimum. For the case of $Ha = 50000$ and an assumed pipe radius of $5\,\mathrm{cm}$ the associated Hartmann layer thickness (red dashed line) at vertical positions $\alpha = 0$ corresponds to a value smaller than one micron. The graph thus reflects the great challenge of calculating MHD flows at large Ha, where multiple grid points are required to resolve variations of velocity and currents across the extremely thin shear layer, while variations inside the core flow domain occur at much larger length scales. Roberts layers, as shown by square symbols for $\alpha = 90°$, are thicker than Hartmann layers, and scale along n with $\delta_{Ro} \sim Ha^{-2/3}$ (Roberts, 1967). Outside the boundary layers, v_x rapidly approaches the core velocity $v_c\,(z)$, shown above in figure 3.10.

Black dashed lines represent the solutions of axial velocity according to the asymptotic theory by Chang & Lundgren (1961) in combination with the viscous boundary layer correction proposed by Shercliff (1962). They perfectly agree with numerical results across both Hartmann layer and core region, as shown by circle and cross symbols. Unfortunately, theoretical values of velocities in Roberts' layers for $\alpha = 90^\circ$ are not available for validation in a simple form comparable with equation 3.1.

In summary, computations demonstrate that the applied discretization schemes lead to an outstanding agreement with asymptotic theory in the core as well as across boundary layers. Under extraordinarily challenging high magnetic field strengths and a demandingly low wall conductance, the numerical approach demonstrates a robust outcome for MHD flow in circular pipes.

3.5 Divergence-based Lorentz force discretization

The code proposed in Mistrangelo & Bühler (2011) reconstructs the Lorentz force on the cell center in form of a conservative interpolation, as shown in equations 2.25 and 2.26. For possible further improvement, Ni et al. (2007) introduce a reconstruction method based on a divergence formulation of the Lorentz force

$$\mathbf{j} \times \mathbf{B} = -\nabla \cdot (\mathbf{j} (\mathbf{B} \times \mathbf{r})) + \nabla \cdot (\mathbf{j}\mathbf{B}) \times \mathbf{r} \ . \tag{3.16}$$

Both terms on the right-hand side (RHS) are preceded by the divergence operator. During the FVM discretization procedure, they are transformed into a flux balance at the cell surfaces according to the divergence theorem (Ni et al., 2007, equation 35)

$$(\mathbf{j} \times \mathbf{B})_C = -\frac{1}{V_C} \sum_f (j_n)_f (\mathbf{B}_f \times \mathbf{r}_f) S_f - \mathbf{r}_C \times \frac{1}{V_C} \sum_f (j_n)_f \mathbf{B}_f S_f \ . \tag{3.17}$$

The discretized expression requires the face-normal component of current density evaluated at the cell surface centroid $(j_n)_f$. This avoids the explicit reconstruction of current density at the cell center in equation 2.25 for the evaluation of the Lorentz force and could improve numerical consistency.

Equation 3.17 has been implemented in the computational MHD code. Throughout this entire work, however, no significant impact has been noted between the new divergence-based formulation of the Lorentz force and the originally implemented conservative current interpolation scheme according to equations 2.25 and 2.26.

The conclusion can be drawn that under the investigated cases, major errors arise from the discretization of the electric potential gradient upon solving the Poisson equation and reconstructing the face normal current density in equations 2.23 and 2.24, respectively. Numerical errors caused by skew cell faces upon the discretization of the electric potential

gradient are therefore identified as the primary source of possible shortcomings in comparison to the ones caused by the interpolation of electric current density.

3.6 Conclusions and recommendations

Comparing numerical results with either asymptotic or quasi-exact numerical solutions enables the verification of different mesh topologies and gradient discretization schemes. According to the obtained results, following measures apply to the discretization of more arbitrary geometries.

Arbitrary geometries are best resolved by grid configurations, which fundamentally reflect the essence of MHD flow, namely that quantities such as magnetic field, velocity, and current density often have mutually orthogonal orientation. The SHM approach, which results in a cross-sectional grid, as shown in figure C.1 in the appendix, proves to be well suited for simulations of MHD flow in strong magnetic fields. Its uniformly distributed hexahedral cells within the center domain are capable of resolving the core flow by aligning them with the orientation of MHD phenomena, i.e., the imposed magnetic field, electric currents, and mean velocity. Simulations tolerate much higher axial length scales of computational cells than in transverse direction, which enables high cell aspect ratios in comparison to grids designed for hydrodynamic computations.

MHD boundary layers are best resolved by prism layers. Considering strong magnetic fields, i.e., $Ha > 1000$, an additional high tangential refinement of curved boundary layers becomes indispensable in order to resolve the current density that may vary along Hartmann layers. A local tangential and radial refinement is particularly crucial where magnetic field lines and wall normal vector align, and the Hartmann layer is thinnest. Typical signs of poorly resolved MHD boundary layers at curved geometries are artificial shear layers that detach from virtual corners at the wall and propagate along magnetic field lines or the formation of high axial velocity jets inside the boundary layers.

For numerical prediction of fully developed MHD flow in pipes with low wall conductance, the type of grid used in simulations as well as the discretization scheme for electric potential gradient have a significant impact on convergence and quality of the numerical results. The reason is that the current density in the core j_c is limited by the conductivity of the wall and viscous layers, i.e., $j_c \sim (c + \delta_{Ha})$. Since the (small) core currents result from a balance of two order-one quantities, namely the electric potential gradient and the induced electric field, it is important that both latter quantities are determined with high precision because even small numerical errors in these quantities become relevant when compared to the magnitude of current density. Relative errors in j_c are therefore larger by a factor of $(c + \delta_{Ha})^{-1}$ compared with relative errors for the potential and induced electric field. For $c \ll 1$ and $\delta_{Ha} \ll 1$, an amplification of these errors in iterative loops may yield non-physical results or divergence of the numerical procedure. Hence, if walls are poorly conducting, computation

of the electric potential gradient requires appropriate and highly accurate schemes, such as Least-Squares or skew-corrected Green-Gauss. Under those adaptations, unstructured grids lead to reasonable results for strong magnetic fields. In this context, Oxtoby et al. (2019) propose an adapted gradient scheme that determines cell-face values based on a truncated Taylor series yielding *favorable* results on perpetuated grids, which might be relevant to future works.

In summary, this chapter presents essential aspects of the discretization procedure for simulations of fully developed MHD flow in circular pipes. The investigated schemes demonstrate their capability at arbitrary wall conductance and fusion-relevant magnetic fields. As a result, the numerical approach is verified and thus regarded as capable to address 3D effects in developing MHD flows. As presented in the following two chapters, the Green-Gauss approach is selected to yield gradients, and interpolation schemes are skew-corrected on a generally refined SHM grid type according to figure C.1 in the appendix, if not stated otherwise.

4 MHD flows in a nonuniform magnetic field

The numerical code described above has been applied to simulate 3D MHD flows entering a strong magnetic field. Liquid metal flow under a streamwise varying magnetic field poses a fundamental problem in fusion engineering and magnetohydrodynamics. Depending on the location in the fusion reactor environment, the liquid breeder may encounter spatially varying fields foreseen for the magnetic plasma confinement, which cause complex 3D MHD phenomena. In contrast to two-dimensional fully developed flow, streamwise electric currents arise, leading to spanwise directed Lorentz forces and additional pressure drops. First studies to cover such MHD flow in nonuniform magnetic fields refer to a numerical analysis by Kit et al. (1970), and an experimental series run at the ALEX facility at Argonne National Laboratory by Picologlou et al. (1986). The latter addresses a straight pipe flow entering or leaving a strong magnetic field. Findings based on the experimental data guide numerical approaches as in Hua & Walker (1989) or Reed et al. (1987) and promote further works such as Barleon et al. (1991) or turbulence damping in nonuniform magnetic fields according to Albets-Chico et al. (2013) or Mao et al. (2019). Eventually, results of the ALEX experiments have been proposed as relevant benchmark data to validate computational MHD codes for fusion applications, as summarized by Smolentsev et al. (2015). In this context, Gajbhiye et al. (2018) point out that validation requires additional data, including a more detailed description of the nonuniform magnetic field.

Motivated by Gajbhiye et al. (2018), and furthermore to supplement validation data, Bühler et al. (2020b) present experimental results obtained using the MEKKA facility at KIT. In the latter reference, the liquid metal flow enters the strong magnetic field of the laboratory magnet, as shown schematically in figure 4.1.

One experimental configuration in the magnet involves a fusion-relevant magnetic field strength at $Ha = 2000$ and comparatively high velocity with $Re = 20000$, i.e., the incoming flow from outside the magnet, where $\mathbf{B} = 0$, is turbulent. The wall is relatively thick, $t_w = R_o - R = 0.177$ with a wall conductance parameter $c = 0.0718$. Geometric parameters R_o and $R = 1$ are dimensionless.

The flow inside the magnet becomes laminar and is well described by the asymptotic theory presented in Miyazaki et al. (1983). Within the nonuniform region, measurements of pressure and electric wall potential indicate impacts of strong 3D MHD phenomena, which are the subject of the numerical analysis presented in the following subsections. The present

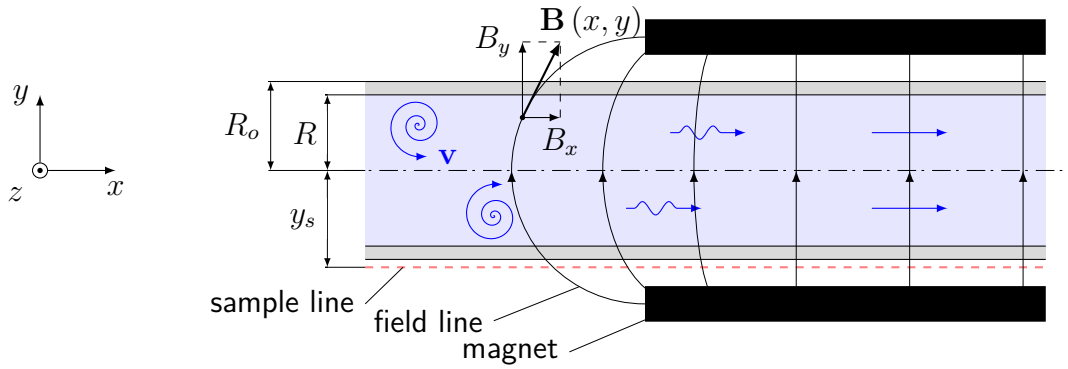

Figure 4.1: Geometry and coordinates of the MEKKA experiment. The incoming stream transforms from turbulent hydrodynamic to laminar MHD flow while entering the strong transverse magnetic field, as indicated by the blue arrow shapes.

numerical study, on the one hand, complements by complete 3D data in the fluid region the experimental observations, where pressure and potential have been obtained only on the external surface of the pipe. On the other hand, available experimental results can be compared to numerical simulations and serve as a validation database for the applied numerical code.

4.1 Consistent distribution of the magnetic field

While for the numerical simulations, the distribution of the magnetic field must be known at any point in the flow domain, measurements of $\mathbf{B}$ are available only along the pipe axis and along a second line that is shifted out of the symmetry plane by a distance y_s. As figure 4.1 illustrates, the magnetic field traversing the test section is basically a two-dimensional vector field described by

$$\mathbf{B}\,(x,y) = (B_x\,(x,y)\,, B_y\,(x,y)\,, 0) \ , \tag{4.1}$$

being constant along z, involving B_y as the major component, and $B_z = 0$. In order to implement an accurate magnetic field representation into the numerical model, one requires an analytical description, which satisfies the properties of a conservative field. For this purpose, the conditions for a solenoidal and irrotational vector field

$$\nabla \cdot \mathbf{B} = 0 \ , \tag{4.2}$$

$$\nabla \times \mathbf{B} = 0 \ , \tag{4.3}$$

enable a spatially consistent reconstruction of the magnetic field by means of a one-dimensional analytical formulation of $B_y\,(x,0)$ on the centerline. In other words, the underlying approach consistently reconstructs the magnetic field from a single functional

fit $B_{y,f}(x,0)$ of its measured major component along the magnet's centerline, see, e.g., Albets-Chico et al. (2011).

The black cross symbols in figure 4.2 indicate measurements (subscript m) of B_y along the magnet's centerline, where the coordinate $x = 0$ refers to the position where the magnetic field reaches half of its maximum value, $B_y = 0.5$. As an outstanding specialty of the MEKKA magnet and in contrast to other experiments, e.g., the well-known ALEX experiment (Picologlou et al., 1986), a large section between x_1 and x_2 shows linear growth of the magnetic field. This is why a pure $\tanh$-based fit, shown by the orange dashed line, yields only a poor approximation of magnetic field in MEKKA experiments, although such a type of fit was good enough to describe the field in the ALEX experiment (Albets-Chico et al., 2011). A better approximation is achieved by the piecewise-defined fitting function (subscript f) in equation 4.4, which defines the flux density on three sections along the central axis

$$B_{y,f}(x) = \begin{cases} b_1\left(\tanh\left(a_1\left(x - x_1\right)\right) + 1\right) & \text{if } x < x_1 \\ mx + 0.5 & \text{if } x_1 \leq x \leq x_2 \\ (1 - b_2)\tanh\left(a_2\left(x - x_2\right)\right) + b_2 & \text{if } x > x_2 \end{cases} . \tag{4.4}$$

The coefficients a_i, b_i for $i \in \{1, 2\}$, and m define growth, function values at x_i, and slope of the linear section, respectively. The coefficients a_i, b_i, m as well as positions x_i are determined from a Least-Squares fitting with the experimental data under the constraints that axial derivatives of $B_{y,f}$ are continuous up to the second order. The latter point is important for a consistent reconstruction of the field. As demonstrated by the blue curve in figure 4.2, the fit results in excellent agreement with the measured field $B_{y,m}$. Values of parameters a_i, b_i, x_i, and m are shown in table C.1 in the appendix.

Equations 4.5 and 4.6 then reconstruct the magnetic field $\mathbf{B}$ in the entire computational domain by means of the fit from the magnet's centerline $B_{y,f}$

$$B_x(x,y) = \frac{\partial B_{y,f}}{\partial x} y \tag{4.5}$$

$$B_y(x,y) = B_{y,f} - \frac{\partial^2 B_{y,f}}{\partial x^2}\frac{y^2}{2}. \tag{4.6}$$

Equations 4.5 and 4.6 are the first three terms in an infinitely long Taylor series that would satisfy the conditions of equations 4.2 and 4.3 exactly. According to Albets-Chico et al. (2011), truncating derivatives higher than the second order from the series is sufficient for an adequately consistent reconstruction, where higher orders would result only in marginal improvement. From $\partial_x B_{y,f}$, portrayed red in figure 4.2, and equation 4.5, we conclude that the axial component of the magnetic flux density B_x exists in the range of $-5 < x < 5$, it is constant for $x_1 < x < x_2$, and it is proportional to the distance y from the centerline. According to equation 4.6, the major component B_y, however, is supposed to remain constant along y within the region of linear growth, where $\partial_x^2 B_{y,f} = 0$. In order to verify the magnetic field reconstruction in the next paragraph, results are compared with measurements

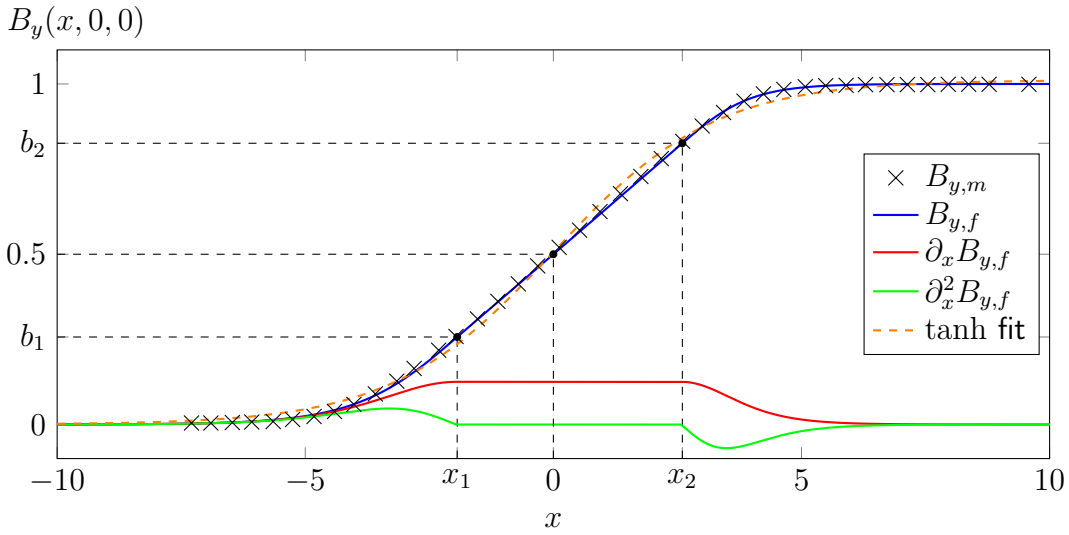

Figure 4.2: Piecewise fitting function $B_{y,f}$ (blue) at the pipe's centerline compared to the measured major magnetic field component $B_{y,m}$ (symbols), where x_1 and x_2 limit the section of linear variation. The functional fit's derivatives are continuous up to their second order. The pure $\tanh$ based fit yields only a poor approximation. Adopted from Klüber et al. (2020b).

along a line at the distance $y_s = 1.255$ from the pipe axis.

Data in figure 4.3 confirms the agreement between the analytical representation and measurement of both magnetic field components B_x and B_y at the constant distance $y_s = 1.255$ from the centerline.

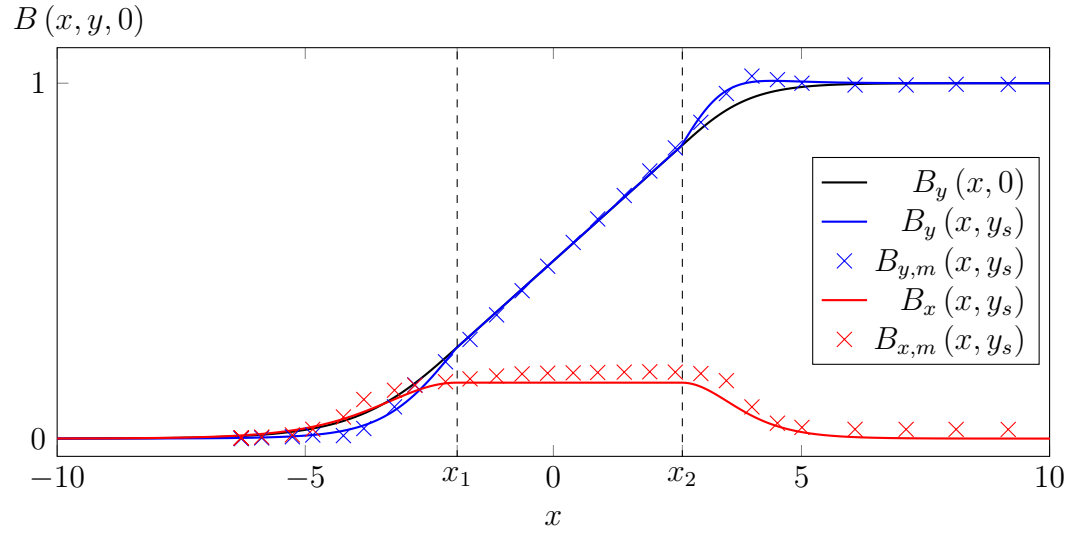

Figure 4.3: Comparison of measured (cross symbols) and reconstructed (solid lines) magnetic field components at the vertical distance $y_s = 1.255$.

As equations 4.5 and 4.6 suggest, and measurements confirm, B_x appears proportional to

the gradient of $B_{y,f}$, whereas B_y results from the superposition of $B_{y,f}$ with its second order derivative. Variations of B_y along y occur only where $B_y\,(x,0)$ along the axis has sufficient curvature. The analytical representation of $B_y\,(x,y_s)$ agrees well with measured data. A comparison of calculated and measured axial field component $B_x\,(x,y_s)$ is also good, but measured values are systematically slightly higher, which has its origin in a non-perfect alignment of the sensor used in the experiment (for perfect alignment of the sensor, B_x would vanish in the uniform magnetic field).

It can be concluded that the consistent analytical representation of the magnetic field agrees well with measured data. The obtained expressions have been therefore implemented in the computational model for 3D simulations of MHD pipe flow entering the MEKKA magnet.

4.2 Pipe geometry and boundary conditions

The magnetic field profile in figure 4.2 shows that it evolves approximately within $-5 < x < 5$. In order to avoid any interference between the entrance and exit conditions and 3D MHD phenomena, the computational domain extends along the axial range within $-15 < x < 15$. Due to the relatively thick pipe walls $t_w = 0.177$, the thin-wall approximation as a model to emulate electric fluid-wall interaction, as, e.g., applied in Albets-Chico et al. (2013), is rather inappropriate. Instead, the computational mesh used in the present simulations includes the wall geometry as well. In this manner, the MHD solver directly determines the electric wall currents via the solution of the potential equation in both fluid and wall domain. In summary, table 4.1 contains the essential mesh parameters.

cell number		prism layers	
fluid	$4.6 \cdot 10^6$	streamwise	175
solid	$1.9 \cdot 10^6$	boundary grid	30
total	$6.5 \cdot 10^6$	wall	20

Table 4.1: Mesh details of the pipe model.

The cross-sectional grid resolution is of SHM type, as shown in figure C.1 in the appendix, which extrudes in the form of prism layers downstream as well as into the wall domain. Higher resolutions are used streamwise within the region of interest $-5 < x < 5$ and towards the fluid-wall interface, where at least four grid-points resolve the extremely thin Hartmann layer. Since the physical conditions of incoming hydrodynamic turbulence and fully developed MHD flow at the exit differ fundamentally, the implementation of streamwise periodic conditions is unfeasible. Instead, boundary conditions are defined as summarized in table 4.2.

The electric potential ϕ constitutes the only variable to be calculated within both the liquid

	inlet	outlet	fluid-wall int.	outer wall surface
ϕ	$\partial_n \phi = 0$	$\partial_n \phi = 0$	$\phi = \phi_w$, $j_n = j_{n,w}$	$\partial_n \phi = 0$
p	$\partial_n p = 0$	$p = 0$	$\partial_n p = 0$	-
$\mathbf{v}$	turbulent	$\partial_n \mathbf{v} = 0$	$\mathbf{v} = 0$	-

Table 4.2: Boundary conditions of the pipe model.

and solid domain. Details about the coupling between fluid and wall have been described above in section 3.4. Along the remaining boundaries, including the outer wall surface, the electric potential gradient is zero, which means current may not escape across the outer pipe surface.

The fluid velocity at the wall satisfies the no-slip condition, and the reference pressure of the fully developed flow at the exit is set to zero. Ferziger & Peric (2002, sections 7.6 and 8.10.5) remark that the problem of pressure-velocity coupling imposes further numerical restriction on the remaining boundaries. Accordingly, if velocity is prescribed along boundaries, the numerically imposed pressure gradient must be zero $\partial_n p = 0$ (inlet and fluid-wall interface). On the other hand, if the pressure gradient differs from zero, values for velocity cannot be prescribed. Similar thoughts on this exclusively numerically imposed restriction on boundary conditions can be found in Mück (1998, section 3.3).

The determination of the turbulent hydrodynamic entrance flow and its integration into the inlet boundary is more complex, so it is described separately in the next section.

4.3 Turbulent entrance flow

Although it is known that turbulence is rapidly damped in strong magnetic fields when $Re/Ha < 250$ or entirely suppressed for $Re/Ha < 140$ (Albets-Chico et al., 2013; Mao et al., 2019), an appropriate simulation of the present flow at $Re = 20000$ requires an adequate description of hydrodynamic turbulence before the fluid enters the magnetic field. While some references suggest internal back mapping for implicitly generating turbulent entrance conditions (see, e.g., Mao et al. (2019)), the present work applies a segregated procedure. Prior to the simulations of flow entering a magnetic field, hydrodynamic simulations are performed on a sufficiently long ($8\,R$) section of the pipe to which cyclic conditions in axial direction are applied.

The approach described in Komen et al. (2014) is strictly followed to conduct a quasi-direct numerical simulation (DNS). Further computational details are listed in table C.2 in the appendix. The resulting turbulent velocity field at the pipe's middle cross-sectional plane is then stored at selected discrete time steps. This sequence of velocity data is then transferred for MHD simulations to the pipe inlet. The special inlet condition

timeVaryingMappedFixedValue, provided by the OpenFOAM library, enables transient smooth interpolation of the stored data.

Due to the finite resolution of the computational mesh, a quasi-DNS considers only a specific range of the turbulence spectrum, as, e.g., outlined in Tennekes & Lumley (1972, pp. 262-267). This restriction may significantly impair the quality of results. It is, therefore, common practice to assess such impact by comparison of numerical velocity data with the well-understood law of the wall, which describes wall-bounded shear flow (Tennekes & Lumley, 1972, pp. 156-160). A dimensionless representation, marked by the superscript $+$, enables the definition of the streamwise velocity u^+ depending exclusively on the wall-normal coordinate y^+. Accordingly, the dimensioned quantities (denoted by *) of time-averaged streamwise velocity $\bar{u^*}$ and wall distance y_w^* define

$$u^+ = \frac{1}{u_\tau} \cdot \bar{u^*} \tag{4.7}$$

$$y^+ = \frac{u_\tau}{\nu} \cdot y_w^* \ , \tag{4.8}$$

where the shear velocity

$$u_\tau = \sqrt{\frac{\tau_w}{\rho}} = \sqrt{\nu \left(\frac{\partial \bar{u^*}}{\partial y_w^*} \right)_{y_w^*=0}} \ , \tag{4.9}$$

is determined through the wall shear stress τ_w. Eventually, the law of the wall then describes the near-wall velocity, which depends exclusively on the wall coordinate (Spurk & Aksel, 1989, pp. 235-237)

$$u^+ \left(y^+ \right) = \begin{cases} y^+ & \text{if } y^+ < 5 \\ 2.5 \ln \left(y^+ \right) + 5 & \text{if } y^+ > 30 \end{cases} \ . \tag{4.10}$$

The description addresses two specific sublayers, represented by the black curves in figure 4.4. Close to the wall, for $y^+ < 5$ a thin viscous sublayer exists, where the velocity rises as the wall coordinate $u^+ = y^+$. A buffer layer smoothly matches the viscous sublayer with the inertial layer, where for $y^+ > 30$, the velocity profile exhibits a characteristic logarithmic growth.

Time-averaged results for velocity distribution as a function of the wall distance are displayed in a dimensionless form in figure 4.4. A study involving a highly refined core grid with a total number of $6 \cdot 10^6$ cells (red line) shows quite good agreement between numerical simulations and the law of the wall in both the viscous and the inertial sub-layer. This demonstrates that the code is capable of predicting turbulent pipe flow accurately. Results shown in blue are obtained using a grid that also has a good resolution along and normal to the wall but a coarser SHM grid in the fluid core. This grid has been designed to resolve the thin Hartmann and Roberts layers in MHD simulations while the core, where the MHD flow is smooth, is represented by larger cells in order to keep the total amount of grid points for developing MHD flow at a reasonable number. Simulations using the coarser grid are still able to capture general features of turbulent flow, although some deviations from

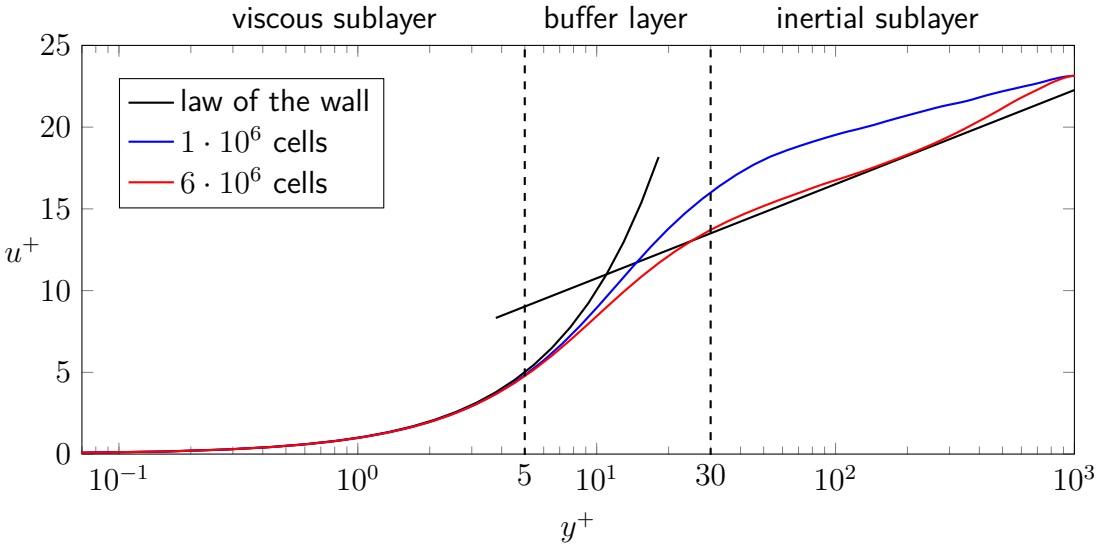

Figure 4.4: Comparison of computed boundary velocity profiles with the law of the wall. Results shown in red and blue are obtained by a highly resolved simulation with $6 \cdot 10^6$ cells and one with a relatively coarse grid with $1 \cdot 10^6$ in the core, respectively.

the logarithmic velocity profile occur in the inertial layer. Since detailed studies of turbulent flows are out of the scope of the present work, the coarser core grid seems good enough to be used for generating hydrodynamic turbulent entrance conditions for subsequent MHD simulations, where turbulence is going to be rapidly suppressed when the flow enters the magnetic field.

4.4 3D MHD phenomena in a nonuniform magnetic field

This section presents the results of numerical simulations for MHD pipe flow in nonuniform magnetic fields. Observed complex physical phenomena are analyzed and discussed. As outlined above, the magnetic field transverse to the pipe varies along the axis with a relatively long section of almost linear growth. Here the induced electric field leads to a constant streamwise electric potential gradient, additional axial currents, and transverse electromagnetic forces. The closure of these 3D current loops in the region where the magnetic field approaches its final high value affects velocity and pressure distributions via the Lorentz force. While for strong magnetic fields, pressure and Lorentz forces form a dominant balance, their difference eventually accelerates or brakes the flow in regions of strong 3D effects. As an indicator for the strength of the magnetohydrodynamic momentum transfer, the so-called magnetodynamic force is introduced. The latter constitutes a useful quantity for the explanation of major observations, and it could be deployed for future

investigations of more general 3D MHD applications.

Velocity

In order to give a first impression about flow entering a strong magnetic field, figure 4.5 illustrates distributions of velocity and electric current streamlines. The profile at $x = -12$ demonstrates that for zero magnetic field strength, the incoming velocity varies randomly within the cross-section exhibiting hydrodynamic turbulent behavior.

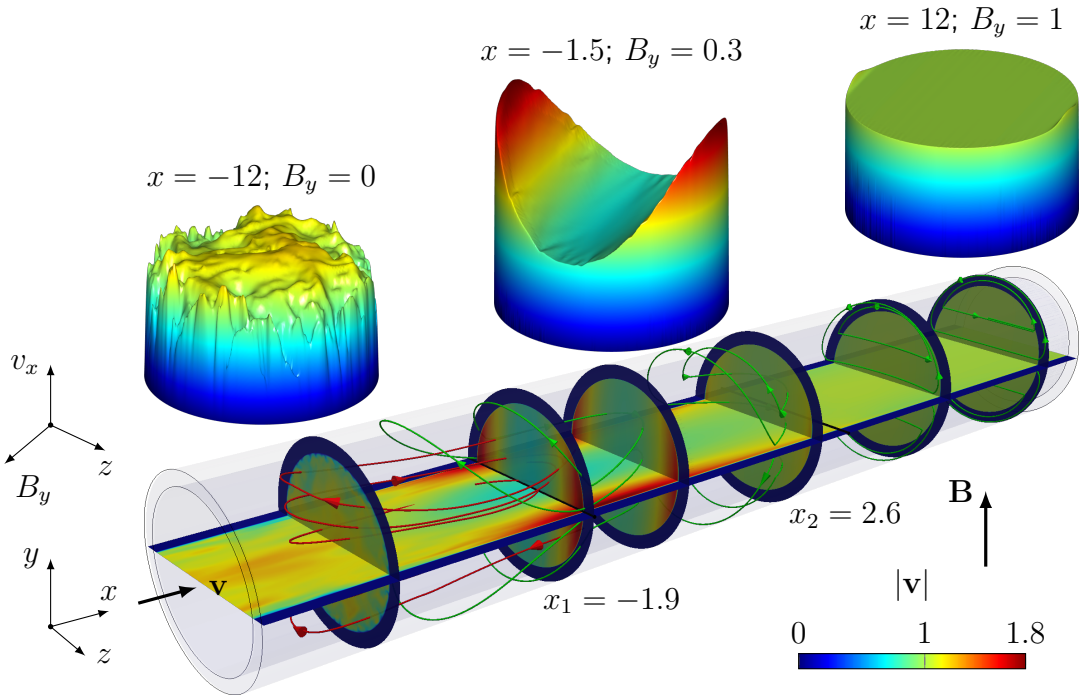

Figure 4.5: Visualization of instantaneous velocity and currents upon entering the magnetic field. Currents fully circulating within the fluid and currents partly closing over the wall domain are shown in red and green, respectively. Transverse black straight lines outline the region of linear magnetic field growth between x_1 and x_2. Velocity distribution adopted from Klüber et al. (2020b).

At an early stage of the magnetic field development close to x_1, turbulence vanishes rapidly, and the core velocity becomes uniform along magnetic field lines and drops to zero in thin viscous boundary layers along the fluid-wall interface. The fluid rapidly evades to the sides resulting in a concave or M-shaped velocity profile as exemplarily shown for $x = -1.5$. At this position, turbulence is already strongly damped, but some weak residual turbulence can still be observed. This behavior is characteristic for 3D MHD phenomena known from observations of MHD flow under discontinuous wall conductance or in expansions, e.g., in chapter 5 or Müller & Bühler (2001, pp. 93-96). Along the evolving magnetic field $x > x_1$, this behavior slowly fades, and core velocity converges towards 2D developed flow in the

form of a uniform profile involving small overspeeds at the sides.

Green streamlines indicate electric currents partly closing over the wall domain. Far downstream currents close exclusively within the pipe's cross-section, as expected for fully developed 2D MHD flow. In the upstream direction, however, increasingly 3D current flow occurs involving axial components. Concerning $x < x_1$, red streamlines furthermore show currents that exclusively close inside the fluid in the form of horizontal recirculation loops. Those are a consequence of the developing magnetic field and associated axial differences of the electric potential.

Electric potential and currents

Figure 4.6 presents the electric potential distribution across fluid and wall domain in the lower half of the pipe according to the color scale. Close to the inlet, both magnetic field and electric potential are zero. With the downstream developing magnetic field, an internal potential gradient arises induced by fluid motion according to $\mathbf{v} \times \mathbf{B}$, which orients along z and reaches the highest magnitudes at the side positions $z = \pm 1$. When entering the region of the uniform magnetic field for $x > 5$, the electric potential converges towards the theoretical maximum for laminar MHD pipe flow in a constant uniform magnetic field (Miyazaki et al., 1983)

$$\phi_{2D} = \frac{1}{1+c} = 0.93 \; . \tag{4.11}$$

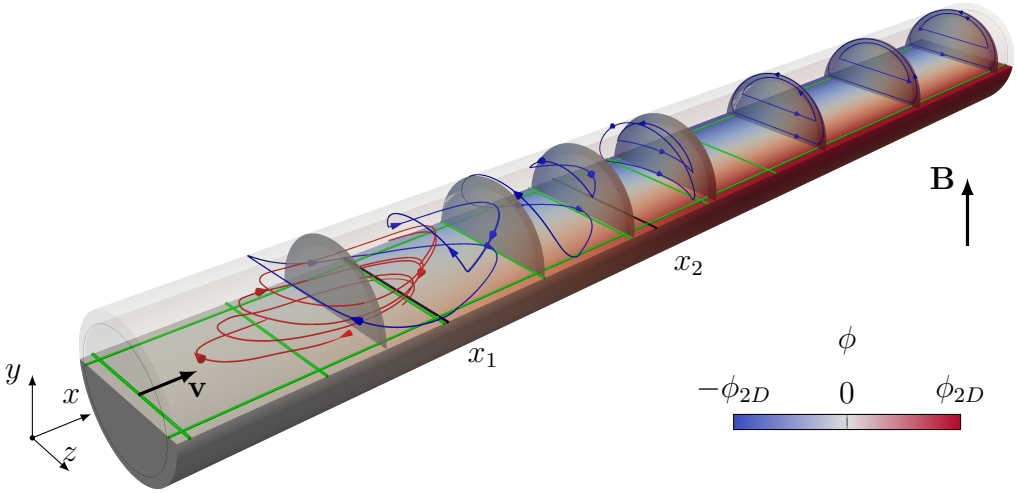

Figure 4.6: Electric potential distribution in the lower half of the pipe - electric current streamlines (blue and red arrow-headed lines) in the upper half. Straight green lines indicate sample paths referring to results displayed in figure 4.7. Black lines at x_1 and x_2 enclose the section of linear magnetic field growth.

Within the nonuniform magnetic field region, the downstream growing transversal po-

tential gradient $\partial_z \phi$ automatically entails an additional axial component $\partial_x \phi \neq 0$. The superimposition of both is the cause of 3D MHD phenomena. This becomes particularly evident in regards of the local electric current streamlines, shown in the upper half of the pipe. Downstream within the fully developed region, electric currents exclusively circulate spanwise. They flow across the fluid domain from one pipe side to the other and then close over the well-conducting wall domain showing the behavior of fully developed MHD flow as predicted by Miyazaki et al. (1983). Across the nonuniform region, however, the axial potential gradient increasingly stretches those currents upstream towards the inlet, where $\phi = 0$. This occurs up to the point close to x_1, where not all electric currents close over the well-conducting wall. Instead, currents form internal concentric swirls, highlighted by red streamlines and known from literature in Müller & Bühler (2001, pp. 93-94) and Moreau (1990, pp. 158-160). Moreover, the electric potential appears comparatively constant across the wall, which suggests a negligible voltage drop across the solid region due to the high wall conductance.

The green lines in figure 4.6 within the plane $y = 0$ indicate sample paths, which correspond to plots in figure 4.7 showing axial and transversal potential distributions. In the graph on the left, side potentials develop proportionally to the magnetic field profile with opposite signs, evoking spanwise and streamwise potential gradients. This implies multi-directional current flow as long the magnetic field varies. The potentials along the sides converge towards the theoretical value ϕ_{2D} as soon as the magnetic field becomes uniform. The graph on the right shows the transversal potential distribution along z. It rises linearly when the flow is fully developed for $x > 5$, as represented by the solid red line but otherwise exhibits a slight curvature with comparatively higher side layer gradients. This suggests higher axial velocity close to the sides that induce locally stronger electric fields $\mathbf{v} \times \mathbf{B}$. In the wall for $|z| > 1$, currents flow preferentially in the tangential direction so that the potential difference across the wall remains small.

Furthermore, figure 4.6 suggests that the electric potential in y-direction remains constant, which would exclude vertical current flow. In fact, this property only applies to fully developed MHD flow in y-symmetric cross-sections under a uniform magnetic field (Müller & Bühler, 2001, p. 70), which in the underlying case merely corresponds to $x > 5$. Within the nonuniform field region, however, electric currents may vary along y as well. This results from the fact that a balance of currents in planes perpendicular to field lines results in field-tangential components when the magnetic field is nonuniform (Müller & Bühler, 2001, pp. 68-69). In addition, other effects like the curvature of magnetic field lines and residual turbulence further affect the orientation of current flow within the nonuniform region. As a consequence for the nonuniform field region, we may identify components of potential gradients in every direction, leading to complex three-dimensional electric current paths.

In order to assess the relation between electric potential profile and electric currents, figure 4.8 shows by color representative current densities component-wise along the axial direction at the pipe center as well as close to the Hartmann layer $(x, 0.8, 0)$ and close to the Roberts layer $(x, 0, -0.8)$, as indicated by respective line-styles. Results are normalized

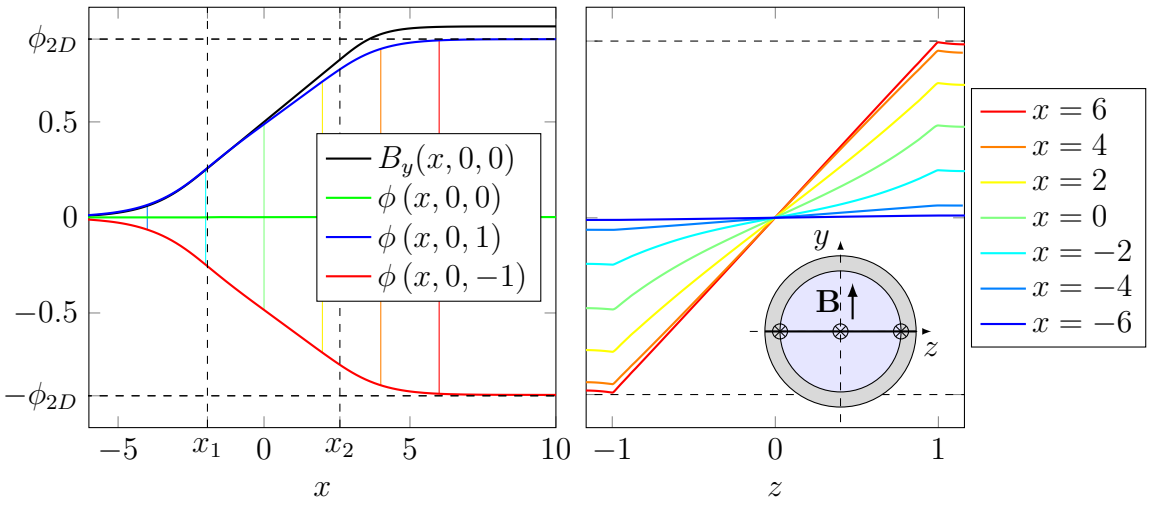

Figure 4.7: Electric potential ϕ in axial and transversal direction along the green sample lines in figure 4.6. Colored vertical lines in the left graph indicate respective projections from plots on the left. Axial distribution of electric potential adopted from Klüber et al. (2020b).

by the theoretical current density for fully developed MHD flow (Miyazaki et al., 1983)

$$j_{2D} = \frac{c}{1+c} = 0.067\ . \tag{4.12}$$

The most noticeable feature within the nonuniform magnetic field region $-5 < x < 5$ is the broad rise and fall of the axial current density along the sides, indicated by the red dash-dotted line. Within the section of linear magnetic field growth $x_1 < x < x_2$, it forms a plateau of the highest current densities. All transversal components j_z, on the other hand, grow monotonously with the linearly increasing magnetic field and the associated z-directed magnetic induction $\mathbf{v} \times \mathbf{B}$, as all blue colored lines indicate. This behavior agrees with the electric potential distribution in figure 4.7, where potential gradients in x- and z-direction occur highest along the sides and decrease towards the core. As anticipated from theory for the fully developed region $x > 5$, all blue colored lines show the convergence of j_z towards a uniform current distribution at j_{2D}. The reason for the one percent deviation to the asymptotic solution is that its underlying asymptotic theory neglects electric currents inside viscous boundary layers, which, however, the numerical solution takes into account. While within the section of linear magnetic field growth z-directed currents become larger towards the sides, this condition switches for $x > x_2$ showing a local maximum at $z = 0$ before converging to fully developed conditions. Such peak is not a consequence of a higher induction, but it results from strong axial currents in the nonuniform magnetic field section, which close in the last development stage by crossing the channel. In terms of the early development stage of the magnetic field $x < x_1$, the transversal currents j_z in the pipe center and top become zero before they start rising, as marked by the orange circle. This location corresponds to the center of the concentric internal current loops at $x_c \approx -2.7$, where the transversal potential gradient fully balances the induced electric field, and current

density vanishes according to $\partial_z \phi = v_x B_y$. Upstream from this position $x < x_c$, current flow is governed by the electric potential gradient and downstream, i.e., for $x > x_c$ by the induced electric field.

In contrast to x and z components of current density, vertical electric currents j_y, presented as green lines, are vanishingly small between $-5 < x < x_1$ and practically zero elsewhere, which indicates a negligible vertical current flow. Moreover, since "current components $\mathbf{j}_\perp$ perpendicular to the field do not vary along magnetic field lines" (Müller & Bühler, 2001, p. 68), j_z does not change along field lines. The slight difference of j_z along y therefore results from the fact that magnetic field lines are curved in the nonuniform region $x_1 < x < x_2$. When the magnetic field becomes uniform, values become uniform in y-direction. Accordingly, MHD effects become mostly independent from y and we may restrict the further description of the problem to the symmetry plane $y = 0$.

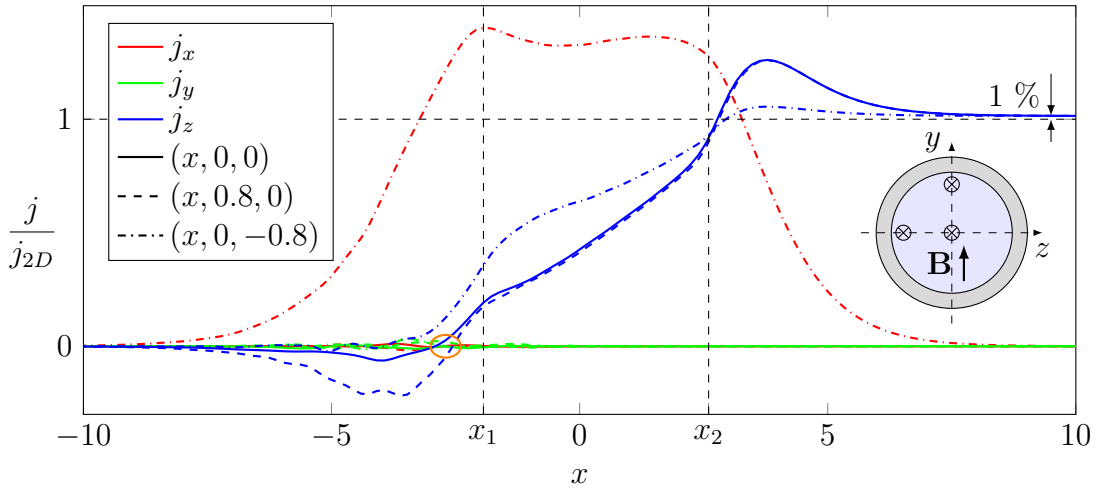

Figure 4.8: Current components scaled by j_{2D} and sampled in axial direction at the center as well as close to the top and side. The orange circle indicates the center of horizontal circulation loops.

Numerical results within the side regions of linear magnetic field growth show for $x_1 < x < x_2$ a constant axial potential gradient and a high axial current density, while $j_x\,(x, 0, 0)$ vanishes on the axis of the pipe due to symmetry. Those axially elongated current loops extend far beyond x_2. There, they lead to a maximum of transversal current density j_z by crossing the channel from one side to the other. The following section presents the impact of this current profile on the Lorentz force. Furthermore, the introduction of an auxiliary quantity, called the magnetodynamic force, effectively reveals the impact of 3D current loops on the inertial momentum balance.

Contour plots in figure 4.9 illustrate, from top to the bottom, electric current, Lorentz force, and velocity within the plane $y = 0$. Colorbars show the normalized magnitude, and illustrated arrow representations indicate orientation and relative intensity. As the yellow arrowed path in the upper contour plot highlights, the axial potential gradient leads between

x_1 and x_2 to the highest axial current densities along the sides (see also figure 4.8). Due to the special linear character of the imposed magnetic field, j_x along the sides remains comparatively constant along x. In the last development stage of magnetic field growth $x_2 < x < 5$, transversal electric currents cross the core region at high intensity to close current loops. In the case of rectangular channels, current loops may reach up to ten characteristic axial length units as outlined by Moreau (1990, p. 158), which has been observed in the underlying case as well.

Another striking characteristic of electric current distribution in the range of linear magnetic field growth is the persistent curvature of current streamlines, portrayed as solid green lines in figure 4.9. Up- and downstream, they transform rapidly into either internal swirls or fully developed spanwise loops, respectively. Current streamlines presented in Albets-Chico et al. (2013, figure 15) or Mao et al. (2019, figure 7) vaguely indicate that the current lines vary permanently downstream under purely $\tanh$-based magnetic field growth. Accordingly, a single side layer peak arises in the latter references instead of the constant plateau observed in the present case.

Magnetodynamic force

The Lorentz force $\mathbf{j} \times \mathbf{B}$ presented in figure 4.9 has been scaled by the maximum value expected for fully established flow according to the asymptotic analysis by Miyazaki et al. (1983)

$$f_{L,2D} = j_{2D} = \frac{c}{1+c} = 0.067 \ . \tag{4.13}$$

The profile of the Lorentz force magnitude in figure 4.9 shows similar characteristics as the current density multiplied with the local magnetic field strength $|\mathbf{B}|$. This results in V-shaped force contours within the region of linear magnetic field growth, where Lorentz forces point inward.

According to its definition in equation 2.4 the Lorentz force acts perpendicular to $\mathbf{j}$ and $\mathbf{B}$. Hence, within the section of linear magnetic field growth, the greatest Lorentz forces arise along the sides, pointing in an oblique manner upstream into the channel core. Considering such force distribution, it seems rather unexpected that the velocity profile, presented in the bottom contour plot, exhibits a low-velocity zone around x_1 at the channel center, where electromagnetic flow resistance is comparatively low. However, one explanation might be the aforementioned fluid internal current loops that cause an inward-directed Lorentz force along their circumference - first accelerating, then braking the fluid. Consequently, a local high-pressure region $p+$ arises in the core, as indicated by the orange ellipse. This occurs in the early development stage, where the induced electric field is still weak and electric currents mostly close along fluid-internal current loops. The flow, therefore, avoids the central high-pressure core region by evading to the sides and leaving a low-speed core region, while high-velocity jets arise along the sides.

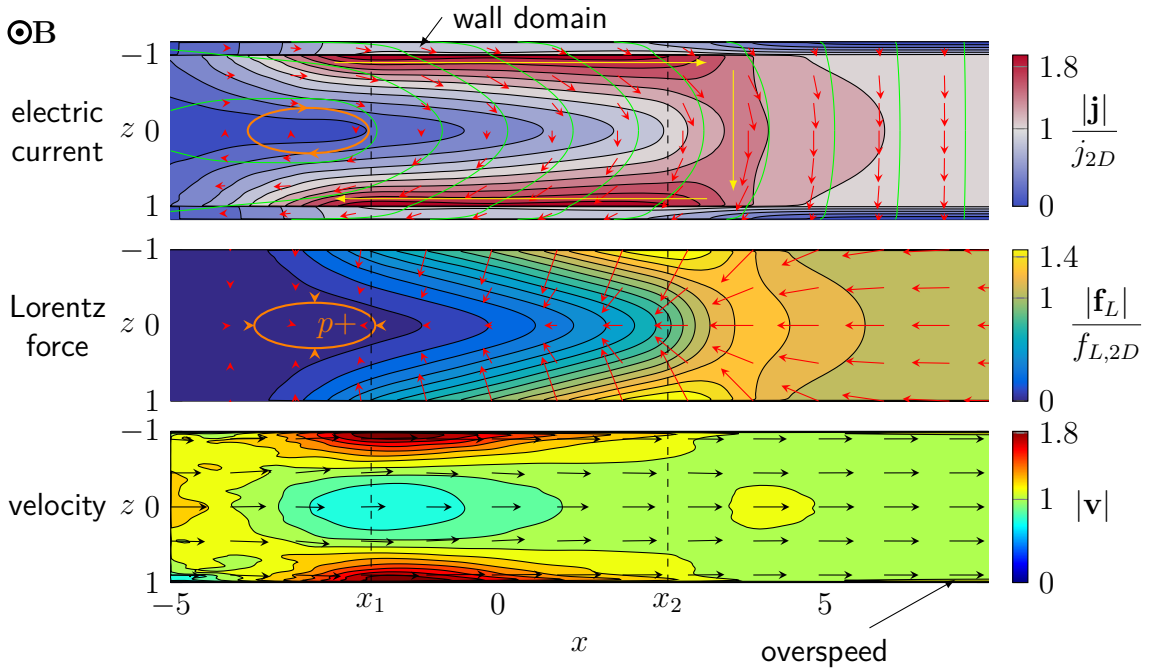

Figure 4.9: Magnitudes of electric current, Lorentz force, and velocity shown as contour plots at $y = 0$. Arrows show intensity and direction of the vector fields. Concerning the current density, green streamlines portray electric current pathways and yellow arrows have been added to indicate the 3D current loop. The orange ellipse visualizes the formation of a fluid-internal current loop resulting in a local high pressure region $p+$ in the core. Contours of Lorentz force adopted from Klüber et al. (2020b).

In terms of higher magnetic fields where induction governs the current flow when $x > x_c$, the Lorentz force profile and velocity distribution seem to disagree in general. This becomes particularly evident within the section of linear magnetic field growth. Along the sides, the strongest braking Lorentz forces develop, but also high-velocity side jets occur. The core flow region represents equally contradicting behavior by exhibiting a low velocity, although the braking Lorentz force is comparatively weak. The reason is a strongly disproportionate momentum balance inside the fluid (Albets-Chico et al., 2013). Due to the well-conducting wall and strong magnetic field, the balance between pressure gradient and Lorentz forces becomes overwhelming. In contrast, velocity-related contributions, such as inertia and viscous forces, remain comparatively weak. Since such a predominant fraction of the Lorentz force exclusively balances the pressure gradient independent from velocity, we further refer to it as *magnetostatic* force (subscript ms)

$$\mathbf{f}_{\mathrm{ms}} = \nabla p \ . \tag{4.14}$$

Exclusively a small remainder of $\mathbf{f}_L$ balances inertia and viscous forces, which therefore is denoted in the following as *magnetodynamic* force (subscript md). Accordingly the Lorentz

force may be split in two contribution $\mathbf{f}_{\mathrm{ms}}$ and $\mathbf{f}_{\mathrm{md}}$

$$\mathbf{f}_L = \mathbf{f}_{\mathrm{ms}} + \mathbf{f}_{\mathrm{md}} \ . \tag{4.15}$$

Magnetostatic theory, originally introduced by Kulikovskii (1968), neglects the second term, which reduces the momentum balance to equation 4.14. The present numerical approach, however, considers the full set of terms in the momentum equation. This allows determining the remaining magnetodynamic force, which balances inertia and viscous forces according to

$$\mathbf{f}_{\mathrm{md}} = \mathbf{f}_L - \nabla p = N^{-1}\left(\partial_t \mathbf{v} + \mathbf{v}\cdot\nabla\mathbf{v}\right) - Ha^{-2}\nabla^2\mathbf{v} \ . \tag{4.16}$$

Equation 4.16, therefore, constitutes a reasonable indicator to visualize magnetodynamic interaction and explain the relation between velocity and complex 3D MHD phenomena.

The plots in figure 4.10 present contours of the magnetodynamic force and velocity.

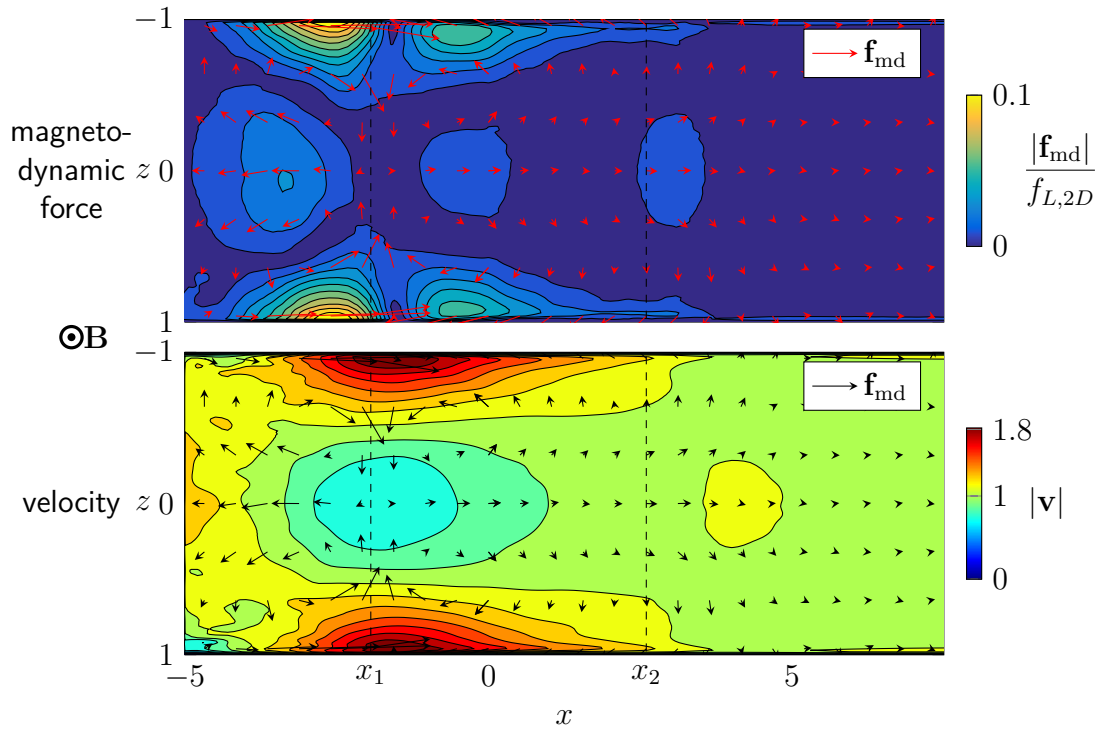

Figure 4.10: Contour plot showing the correlation of magnetodynamic force and velocity. Both plots contain $\mathbf{f}_{\mathrm{md}}$ as vector representations, in addition.

Both graphs include $\mathbf{f}_{\mathrm{md}}$ as a vector field, showing orientation and relative magnitude. In the first development stage of the magnetic field $x < x_1$, $\mathbf{f}_{\mathrm{md}}$ opposes the core flow, where internal current loops circulate and form a local high-pressure region. In addition, the highest force peaks accelerate the fluid along the sides, forming side jets. This constitutes the cause for an M-shape velocity profile, which typically occurs in the presence of strong 3D MHD effects.

The magnetodynamic behavior instantly reverses near $x = x_1$, where $\mathbf{f}_{\mathrm{md}}$ further on accelerates the core and brakes the side layers. Additionally, close to x_1, inward-directed components appear, which expand the side jet's width in the z-direction. This effect reverses gradually within the region of linear magnetic field growth, pushing the high-velocity stream against the sides, making it thinner again. For $x_1 < x < 0$ a moderate $\mathbf{f}_{\mathrm{md}}$ regime in the core accelerates, while side layer regimes oppose the fluid flow. This effect slowly fades up to the position x_2, where another small acceleration regime in the center leads further downstream to a small overspeed region in the core. When the magnetic field becomes uniform for $x > 5$, a fully developed MHD flow adjusts. Hence, the magnetodynamic force becomes zero in the entire core region and exclusively exists further on in the viscous boundary layer.

In summary, the magnetodynamic force and the velocity distribution draw a coherent picture that is capable of explaining their dynamic relations. It is remarkable that the highest magnetodynamic forces occur within the early development stage close to x_1, where $\mathbf{B}$ is rather weak and the highest difference of center and side current densities appear, as previously shown in figure 4.9. Those magnetodynamic peaks, however, correspond only to about 10% of fully developed flow $f_{L,2D}$, which confirms that the overwhelming part of the total Lorentz force $\mathbf{f}_L$ is in general magnetostatic and thus mainly balances the pressure force. This leads to the conclusion that the introduced magnetodynamic force is capable of revealing the impact of 3D MHD phenomena on velocity.

Figure 4.11 visualizes how the axial velocity component v_x varies along the centerline $(x, 0, 0)$ and close to the sides $(x, 0, 0.95)$.

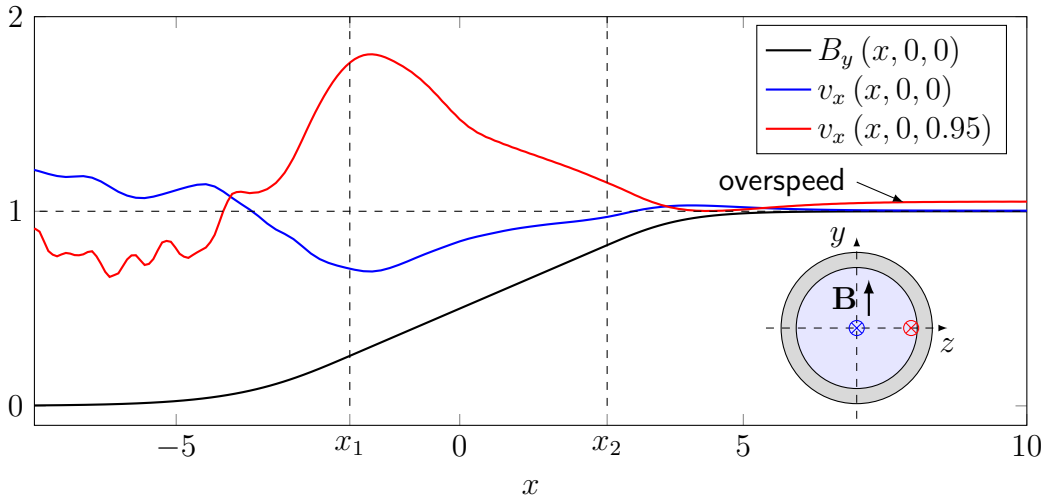

Figure 4.11: Velocity component v_x along the center and near the sides. Adopted from Klüber et al. (2020b).

The incoming turbulent flow has a bigger dispersion rate close to the sides, but its side velocity is in average lower than in the center. Turbulence vanishes rapidly when the magnetic field rises noticeably between $-4.5 < x < -3.8$, where local ratios of Reynolds

to Hartmann number drop below $\frac{Re}{Ha} \approx 250$, as discussed in Albets-Chico et al. (2013). As the magnetic field rises, the emerging magnetodynamic force blocks the center. The center velocity drops to a local minimum while side jets lead to a high velocity peak closely behind x_1, where $\mathbf{f}_{\mathrm{md}}$ mainly orients transversally according to figure 4.10. One may identify further impacts of moderate magnetodynamic force regimes at $x = 0$, where the center and side jet velocity exhibits kinks and bends, caused by forces accelerating the fluid in the center and braking it at the sides. When approaching the region of uniform magnetic field, core and side layer velocities level off with a small overshoot section of the center velocity between $x_2 < x < 5$, evoked by a moderate $\mathbf{f}_{\mathrm{md}}$ in the center. Downstream, the core velocity approaches uniformity of fully developed MHD flow, while the Roberts layers establish small overspeeds in accordance with Vantieghem et al. (2009).

In summary, the magnetodynamic force reveals the coupling phenomena between Lorentz force and velocity. This becomes particularly helpful when the magnetostatic momentum balance is overwhelming and thus dominates over inertia and viscous forces, i.e., for large Hartmann numbers and interaction parameters and for well conducting walls. In addition, contours of the magnetodynamic force could be employed to identify other dynamic effects effects, such as 3D MHD instabilities or internal shear layers. Those phenomena may occur at locations of discontinuous wall conductance, and are investigated by means of $\mathbf{f}_{\mathrm{md}}$ in chapter 5. The next section further presents the magnetostatic behavior under 3D MHD phenomena.

Pressure distribution

Figure 4.5 illustrates distributions of velocity, electric current streamlines, and pressure isosurfaces as a rendered view. As discussed above, the major force balance of fluid flow remains magnetostatic, where a large fraction of the Lorentz force balances the pressure force.

The figure presents the isobars, illustrated as gray contour surfaces, where some are presented cropped open to provide better insight. In a uniform magnetic field, they appear as cross-sectional planes and align perfectly with green portrayed electric current streamlines that close over the well-conducting pipe wall. As long the magnetic field is strong enough, this behavior also persists in the nonuniform region for $x > x_1$, where similar to electric current lines pressure isobars show V-shaped contours. In regions of smaller magnetic induction $x < x_1$, pressure contours arrange in the form of long bent tubes following the curved magnetic field lines and blocking the fluid in the center. It still appears as if currents, shown in red, flow tangentially to isobars, but since the magnetic field is weaker here, the alignment declines.

It is worth mentioning that structures of pressure, electric current loops, and the low-velocity region are non-concentric to each other. In this context, related works investigating pure $\tanh$-based magnetic field distributions find the highest velocity deformations at $x = 0$,

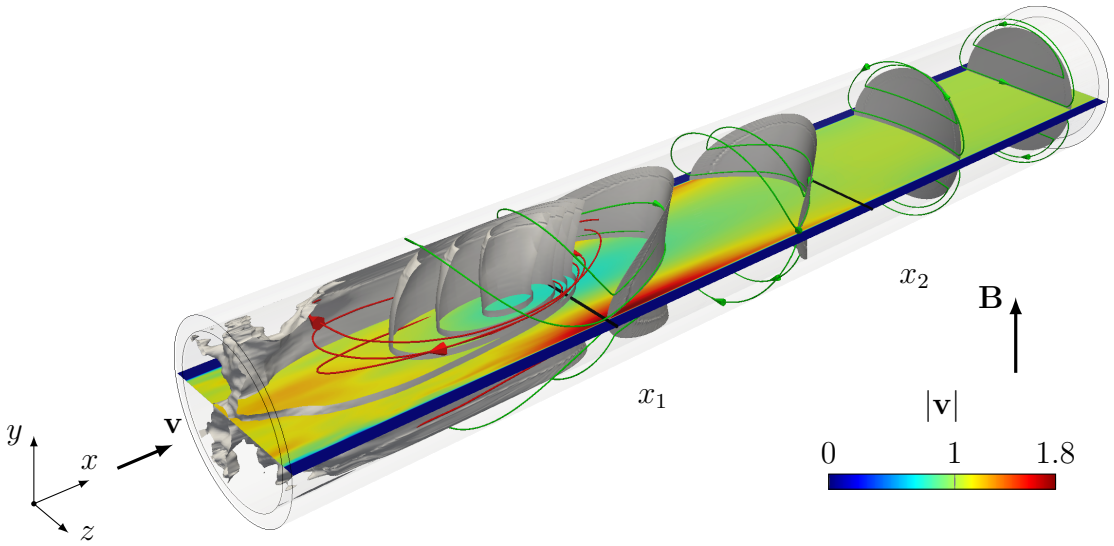

Figure 4.12: Visualization of velocity, currents, and pressure. Gray surfaces portray isobars, which are cropped open to reveal the central local maximum. Currents fully circulating in the fluid and currents partly closing over the wall domain are shown as red and green, respectively. Black straight lines indicate the cross-sections x_1 and x_2 (compare with figure 4.5).

where $B_y = 0.5$ and refer therefore to the magnetic field inflection point as the position for strongest 3D effects (Albets-Chico et al., 2013) or (Picologlou et al., 1986). Results at hand, however, indicate that fluid-internal current loops play a decisive role for the formation of a core velocity minimum. The smallest core velocities occur at an earlier development stage of the magnetic field where current loops close upstream in the fluid. Here, the electric potential gradient outweighs the induced electric field leading to a fluid-internal current reversal in the form of an internal loop and thus evokes the strongest flow opposing Lorentz forces. While strong currents, magnetostatic force contours, and pressure isosurfaces align well by forming V-shaped structures, characteristics of velocity clearly deviate from those attributes, which in literature is denoted as velocity decoupling Albets-Chico et al. (2013). However, the agreement of the center high-pressure tube and low velocity region show that when currents are comparatively weak, magnetodynamic force, pressure, and velocity may correlate very well.

Considering the pressure gradient provides further insights into developing 3D MHD effects. Axial pressure gradients in figure 4.13 illustrate their downstream distribution at different positions in the cross-section according to the color. Results are scaled with the obtained numerical result far downstream $x \gg 1$ where for a uniform magnetic field $\partial_x p$ likewise becomes uniform within the whole cross-section,

$$\partial_x p_{2D} = \partial_x p\,(x \gg 1) = -0.067\ . \tag{4.17}$$

The quantity $\partial_x p_{2D}$ deviates from the asymptotic solution (Miyazaki et al., 1983) by 2%,

as shown by the horizontal black dashed line in the figure. In general, pressure gradients in regions corresponding to zero magnetic field strength, i.e., $x < -5$, are negligibly small compared to the flow in the magnetic field. The side pressure gradient, portrayed red, falls monotonously along the region of the developing magnetic field and eventually converges as soon as the magnetic field becomes uniform. However, streamwise pressure gradients from both top and center positions, shown blue and green, collectively exhibit a slight positive peak upon passing the center high-pressure zone between $-5 < x < x_1$ and then descend along the section of linear magnetic field growth $x_1 < x < x_2$. Since "pressure does not vary along magnetic field lines" (Müller & Bühler, 2001, p. 68), small deviations between blue and green lines within the nonuniform magnetic field region reflect the curvature of field lines. The linear section of the magnetic field elongates axial current loops far downstream, as indicated in figure 4.9, where they eventually cross the pipe in the last development stage when $\mathbf{B}$ becomes large and uniform. There they lead to a strong recovery of streamwise pressure gradient at the center and top positions before the axial pressure gradient becomes uniform within the whole cross-section.

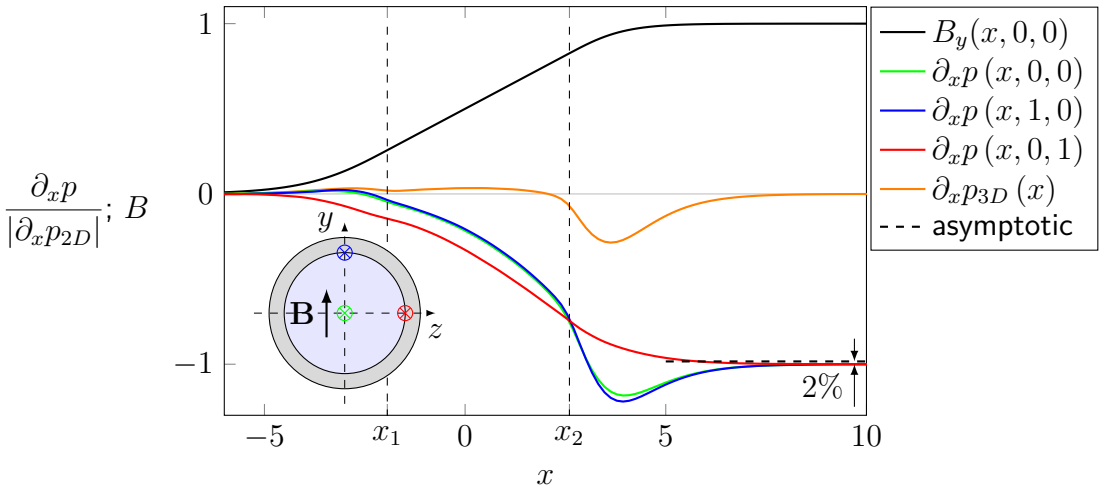

Figure 4.13: Axial pressure gradients along the center, top, and side. Results are scaled by the theoretical value of asymptotic pipe flow $\partial_x p_{2D}$. The orange line presents the local 3D pressure gradient $\partial_x p_{3D}$ due to 3D current flow. The horizontal black dashed line indicates the deviation towards the asymptotic solution according to Miyazaki et al. (1983). Pressure gradients adopted from Klüber et al. (2020b).

In order to quantify 3D effects on pressure drop, the underlying approach estimates the difference between the numerically obtained pressure gradient of the 3D flow on the axis $\partial_x p\,(x,0,0)$ and that of assumed locally fully established flow $\partial_x p_{fd}\,(x)$ as a reference. Since in the present scaling, pressure gradients scale proportionally to B^2, the reference becomes $\partial_x p_{fd}\,(x) = \partial_x p_{2D} \cdot B^2\,(x)$, which uses the numerically obtained solution representing the pressure gradient in fully developed pipe flow in a uniform magnetic field (Pulugundla et al.,

2015). The local fraction of pressure gradient caused by 3D effects then is

$$\partial_x p_{3D} = \partial_x p\,(x,0,0) - \partial_x p_{fd}\,(x) \ . \tag{4.18}$$

The orange line in figure 4.13 presents the local 3D pressure gradient $\partial_x p_{3D}$, which initially yields a positive balance between center pressure gradient and the one of assumed locally established flow along most of the range of nonuniform $\mathbf{B}$. This demonstrates the impact of axial potential gradient and associated current loops on magnetostatic momentum balance, where some fraction of circulating 3D current contributes to a reduction of the transverse currents, which in turn reduces the pressure drop in comparison to assumed fully developed conditions. Only in the last development stage of the magnetic field for $x > x_2$, $\partial_x p_{3D}$ exhibits a strongly pronounced negative peak before the magnetic field becomes uniform and the local 3D pressure gradient converges towards zero. Here, axially elongated current loops cross the channel in the same direction as currents in fully established flow, which leads to an increased pressure gradient and a negative balance of $\partial_x p_{3D}$.

The integration of the local 3D pressure gradient $\partial_x p_{3D}$ along the whole domain yields the additional pressure drop caused by the 3D effects in a spatially varying magnetic field

$$\Delta p_{3D} = \int_{-\infty}^{+\infty} \partial_x p_{3D} \mathrm{d}x = -0.0322 \ . \tag{4.19}$$

When Δp_{3D} is compared with the magnitude of pressure gradient of the fully established flow in the uniform magnetic field for $x \gg 1$, one can identify

$$l_{3D} = \frac{\Delta p_{3D}}{\partial_x p_{2D}} = 0.48 \tag{4.20}$$

as the length along which a fully established MHD flow would have to pass in order to create a comparable pressure drop. This means that the occurring additional 3D MHD losses are equivalent to an MHD pressure drop of fully developed flow over approximately half of a characteristic length unit. This is a relatively small value and should be acceptable in engineering applications.

4.5 Comparison with the MEKKA experiment

The numerical results presented in the preceding sections explain 3D MHD phenomena in nonuniform magnetic fields. In the present section, this knowledge is further used to support the interpretation of measurements performed in the MEKKA laboratory (Bühler et al., 2020b). Due to geometric constraints, it was not possible to perfectly align the pipe axis with the horizontal symmetry plane of the magnet. Since magnetic field lines in the nonuniform region are curved, the vertical displacement of the pipe axis by $y_d = 0.326$ disturbs the symmetry of the problem, which could have an impact on the outcome.

Numerical results presented below have been obtained by taking the pipe axis at the same y-position as in the experiment. However results suggest that the influence of non-symmetry on the results is negligible from an engineering point of view.

Pressure gradients

Ideally, one would like to compare numerical results for the pressure field, as show in figure 4.13, with experimental observation. Such direct comparison, however, is not possible since available experimental data for pressure gradient involves measurements of pressure differences between pressure taps that are axially spaced by a finite distance $d_p = 1.029$, as shown in figure 4.14a. Experimental results presented in the following show approximations for the axial pressure gradient in terms of pressure differences between taps located in two cross-sections, axially spaced by a finite distance d_p. Measurements have been performed at the surface of the Hartmann wall and presented as $\delta_x p_{Ha}(x) = (p_{Ha} - p_0)/d_p$, and the quantity $\delta_x p_s(x) = (p_s - p_0)/d_p$ describes transverse differences (Bühler et al., 2020b).

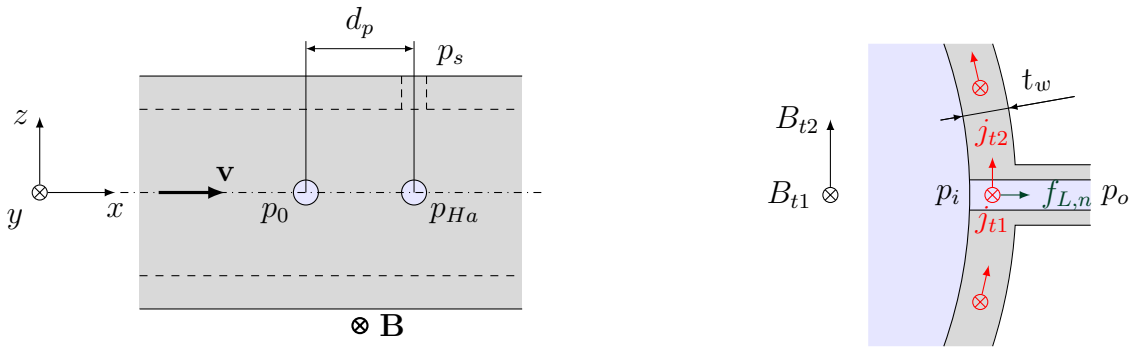

(a) (b)

Figure 4.14: Pressure taps in the MEKKA experiment.(a) Axial and transverse positions of pressure taps, (b) local currents and magnetic field resulting in Lorentz forces inside a pressure tap.

Another experimental drawback is the fact that the pressure-sensing lines are connected to the outer surface of the pipe at a distance t_w from the fluid-wall interface (figure 4.14b). Currents closing their paths along the wall penetrate the stagnant fluid in the tap and perturb the pressure reading p_o detected on the outer surface via related Lorentz forces. This problem has been identified by Hua et al. (1988) and by Stieglitz (1994, p. 40), where corrections for comparison with measurements at sidewalls of rectangular ducts have been proposed. In the present case that involves curved magnetic field lines having axial $\mathbf{B}$-components, such corrections should be considered for all pressure taps. One may estimate the difference between the pressure p_o recorded at the outer surface and the one

at the fluid-wall interface p_i from wall currents $\mathbf{j}_w$ as

$$p_o - p_i = \Delta_n p = \mathbf{n} \cdot (\mathbf{j}_w \times \mathbf{B})\, t_w \ , \tag{4.21}$$

assuming that tangential currents and components of $\mathbf{B}$ do not vary along the thickness of the wall. Since all quantities in equation 4.21 are known from the numerical simulations, it is possible to determine the pressure at the outer surface $p_o = p_i + \Delta_n p$ and compare those results with experimental observations.

The experimental data of $\delta_x p_{Ha}$ shown in figure 4.15 confirms results for $\partial_x p\,(x, 1, 0)$ displayed above in figure 4.13. However, due to the finite length d_p over which pressure gradients are measured, the results in figure 4.15 appear a bit *flattened* compared to the latter ones. Nevertheless, one may compare experimental values shown as symbols with numerical data that has been derived in the same way as the experiments have been performed, i.e., using a finite d_p and estimation of pressure data on the outer surface via equation 4.21. Both numerical and experimental results then show quite good agreement across the entire computational domain, as confirmed by the high values of the concordance correlation coefficient CCC (see appendix B). A similar agreement can be seen for numerical and experimental data of $\delta_x p_s$.

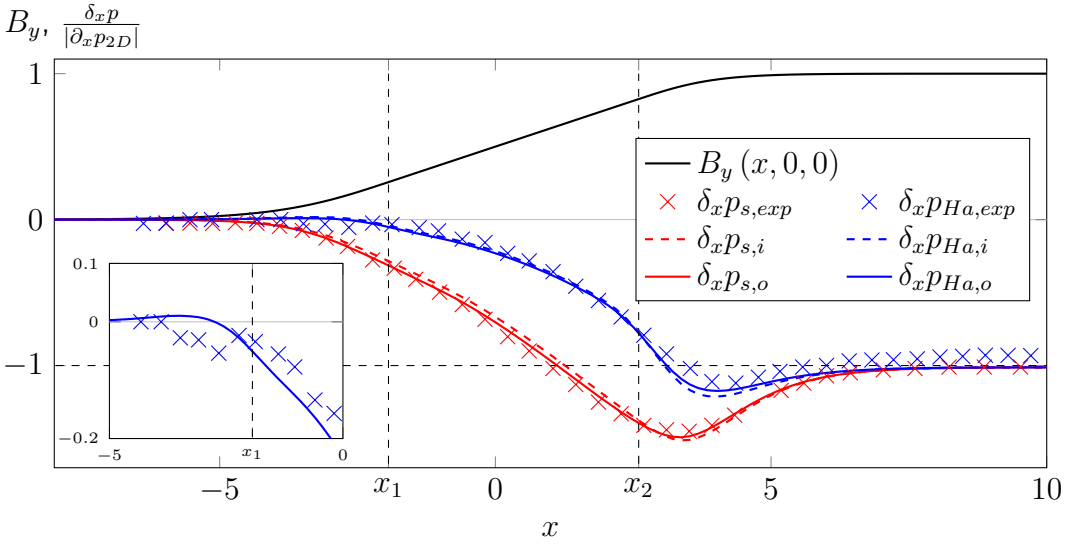

Figure 4.15: Comparison of $\delta_x p_{Ha}$ and $\delta_x p_s$ measured at the outer surface (symbols) with numerical predictions (solid lines). Within the section of the nonuniform magnetic field, Lorentz forces in pressure taps cause the difference between results on the outer surface (subscript o) and those calculated at the fluid-wall interface (subscript i). Correlation values between experimental measurements (symbols) and computational results (solid lines) are $CCC = 0.9992$ for $\delta_x p_s$ and $CCC = 0.9936$ for $\delta_x p_{Ha}$ (see appendix B).

While the experiment reveals data only on the external surface, the numerical results give further insight since flow properties in the pipe are known from the simulations. Results of

$\delta_x p$ at the fluid-wall interface are displayed in addition in 4.15. They show a similar trend as those on the surface, but they deviate from the latter ones by a small amount that is caused by electric currents crossing the pressure taps in the region where the magnetic field is nonuniform. Although differences between $\delta_x p$ on the outer surface and $\delta_x p$ at the fluid-wall interface remain small, one can observe that they play a role at the sides along the entire length where the magnetic field is nonuniform as expected by Hua et al. (1988) and Stieglitz (1994, p. 40). The present results, moreover, suggest that the largest $\Delta_n p$ occur at the Hartmann wall where in the past, those effects have not been considered. They reach their maximum when the magnetic field and currents become large, i.e., just before $\mathbf{B}$ approaches its highest values. When the magnetic field becomes uniform, $\Delta_n p$ disappears so that finally $p_i = p_o$.

Electric potential

The electric potential is an essential flow quantity that can be measured on the surface of the pipe with relatively simple techniques and high accuracy. For that reason, it is best suited for comparison with results from numerical simulations. In the experimental campaign, the electric potential has been recorded on the external surface of the pipe in a large number of cross sections. The experimental data has been published, e.g., in Bühler et al. (2020b), and made available for reproduction in figure 4.16 and for comparison with present numerical results. While numerical results in figure 4.7 have been shown in (x, y, z) coordinates, the experimental data has been collected at equidistant circumferential points and results are therefore presented in figure 4.16 in cylindrical $(x, r = R_o, \alpha)$ coordinates along the outer wall surface at radius R_o.

In a uniform magnetic field, the potentials on the inner and outer surface of the pipe are known to follow harmonic functions $\phi = \phi_{2D} \sin(\alpha)$ and $\phi_{w,2D} \sin(\alpha)$, with amplitudes

$$\phi_{2D} = \frac{1}{1+c} \text{ and } \phi_{w,2D} = \frac{2R_o R}{R_o^2 + R^2}\phi_{2D} \ , \tag{4.22}$$

respectively (Miyazaki et al., 1983). For the present geometry $\phi = \phi_{2D}$ and $\phi = \phi_{w,2D}$ differ only by about 1%. The behavior for fully developed flow is perfectly confirmed by the experimental and numerical data of wall potential for $x = 13$ with theoretical predictions of equation 4.22. Moreover, the agreement between computations and experimental results agree is excellent according to the values of the concordance correlation coefficients presented in appendix B. In regions where the magnetic field varies along x, the magnitude of potential shows a similar growth as the magnetic field (compare values for $\alpha = \pm\pi/2$ in figure 4.16 left) while the pure sinusoidal variation with α is lost (figure 4.16 right, e.g., at $x = -1.7$). From the comparison of simulations and experiments, it can be concluded that the numerical code is well suited for reliable predictions of electric potential on the surface of the duct. Since the latter one is an image of flow properties inside the fluid, one can expect that those values are accurately calculated as well.

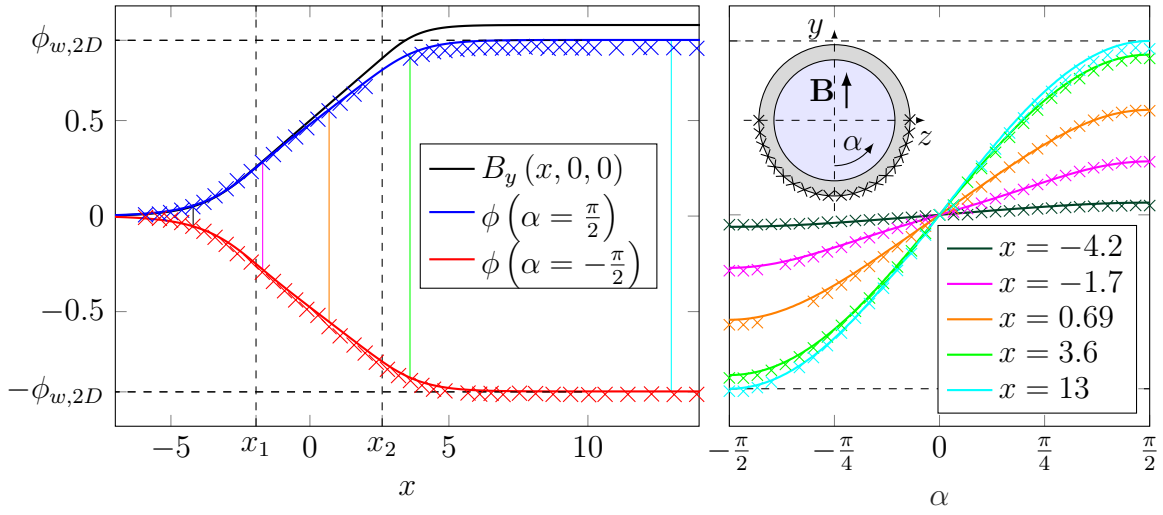

Figure 4.16: Electric potential on the outer surface of the pipe obtained from experiment (symbols (Bühler et al., 2020b)) and from numerical simulations (solid lines). Results for the sides at $\alpha = \pm\pi/2$ are shown along x (left) and for the half circumference of some cross-sections (right). Mean correlation values between experimental measurements and computational results are $\overline{CCC} = 0.9977$ for $\phi\left(\alpha = \pm\frac{\pi}{2}\right)$ (left) and $\overline{CCC} = 0.9946$ for $\phi\,(x)$ (right) (see appendix B).

Velocity

In a recent publication based on the same experimental potential data, an attempt is made to conclude from measured surface potential about internal flow properties such as velocity (Bühler et al., 2021). This is possible only under certain assumptions. Now, the present numerical simulations confirm the latter approach and quantify for the first time the uncertainty in those results.

According to Ohms law 2.1, velocity, currents, magnetic field and potential are related as

$$v_x = \underbrace{\frac{1}{B_y}\left(\frac{\partial\phi}{\partial z}\right)}_{(1)} + \underbrace{\frac{1}{B_y} j_z}_{(2)} + \underbrace{\frac{B_x}{B_y} v_y}_{(3)} \,. \tag{4.23}$$

Here, the axial component of velocity v_x is determined primarily by the transverse component of potential gradient (term (1) on RHS), while contributions from current density (term (2)) and from the axial component of the magnetic field (term (3)) are small in most applications. For that reason, and due to the fact that j_z and v_y are not accessible in experiments, the terms (2) and (3) have been neglected for evaluation of experimental data, as, e.g., by Reed et al. (1987) or Bühler et al. (2021).

In the following, results for axial velocity obtained from numerical simulations are

compared with term (1) of equation 4.23 $B_y^{-1}\partial_z\phi$ that has been used in various publications as an approximation to measure velocity. Figure 4.17 compares both quantities for two selected cross-sections, one at $x = 13$ (left) where the magnetic field is uniform and one at $x = -1.7$, in a region where the magnetic field varies along the axis (right).

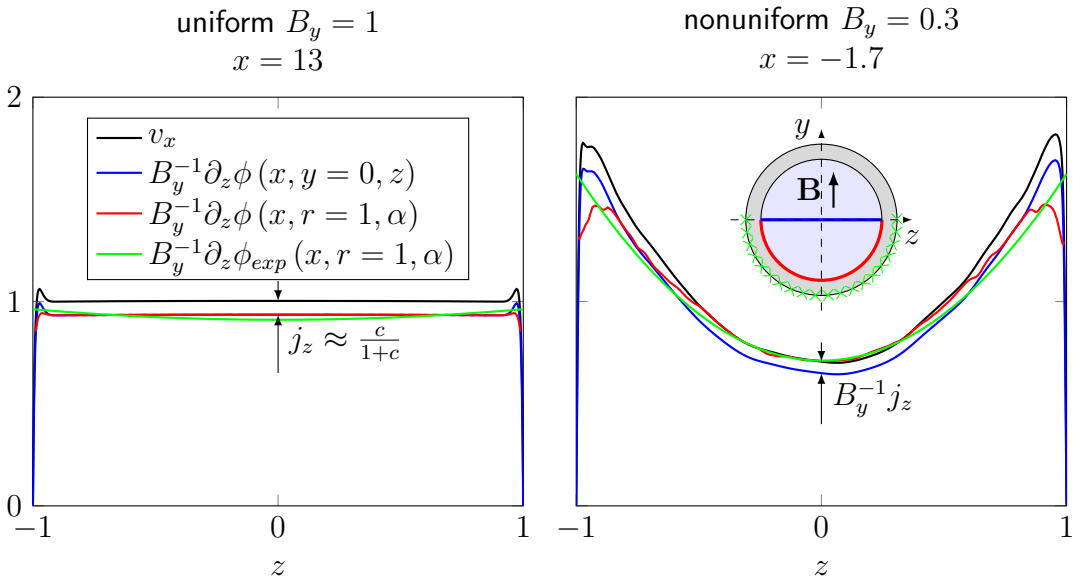

Figure 4.17: Numerically obtained transverse profiles of axial velocity in the region of uniform (left) and nonuniform (right) magnetic field. The velocity profiles are well approximated by transverse potential gradients as $B_y^{-1}\partial_z\phi$. A comparison of $B_y^{-1}\partial_z\phi\,(r = 1)$ with experimental data available at the fluid-wall interface (Bühler et al., 2021), in form of the green line, shows good agreement.

In the uniform field, the velocity $v_x\,(x = 13, y = 0, z)$ in the entire core along the blue line in the sketch is constant, with slightly higher values only in narrow layers near the sides. The quantity $B_y^{-1}\partial_z\phi\,(x = 13, y = 0, z)$ at identical locations exhibits a similar distribution so that it reasonably approximates the velocity. Both profiles differ by a small amount that is due to currents $B^{-1}j_z$, where the transversal currents are known from simulations or from theory, $j_z = c/\,(1 + c)$ (Miyazaki et al., 1983). The numerical simulations further confirm that the transversal potential gradient along the inner wall circumference at $r = 1$ portrayed red in the sketch leads practically to the same result as that in the horizontal symmetry plane $y = 0$. This justifies previous publications in which potential gradients on the walls have been interpreted as velocity signals by assuming that potential and velocity are uniform along magnetic field lines. A comparison with experimental data portrayed green confirms the transversal potential gradient at the wall, as predicted by the present simulations. Here it should be mentioned that the experimental data for potential at the fluid-wall interface has been obtained as a *projection* from measurements on the outer surface of the pipe by solving a Laplace equation for the wall (Bühler et al., 2021).

Figure 4.17 on the right presents for $x = -1.7$ a comparison of same flow quantities but in the nonuniform magnetic field. The black line reveals that the velocity $v_x\,(x = -1.7, y = 0, z)$

now shows strong deformations with reduced values in the center and increased velocity near the sides. These phenomena are well approximated by the transversal potential gradient as $B_y^{-1}\partial_z\phi\,(x=-1.7, y=0, z)$, where the difference between this quantity and velocity is again of the order of $B^{-1}j_z$. If an approximation for velocity derived from the transversal potential gradient at the wall is calculated as shown by the red line, one can observe apparent differences from results at $y=0$, portrayed by the blue line. Values in the center close to $z=0$ are a bit higher, and the curvature of the profile is slightly reduced. This results from the fact that the potential is no longer constant along the y-coordinate. This has two reasons, namely the curvature of field lines that are not perfectly aligned with y and the possibility that ϕ may vary along field lines in regions where the magnetic field is nonuniform and where a transversal pressure gradient is present (Kulikovskii, 1968). Therefore, potential gradients and velocity profiles consequently are not strictly uniform along the y-coordinate. A comparison of $B_y^{-1}\partial_z\phi\,(x=-1.7, r=1, z)$ obtained at the wall by numerical simulations (red line) and experiments (green line) shows quite good agreement in figure 4.17, confirming the accuracy of both the numerical simulations and the applied measuring technique. Since the potential varies marginally across Hartmann layers (Moreau, 1990, p. 129), this quantity may be considered as a reasonable approximation for the core velocity at the edge of the viscous layer.

4.6 Summary

The present numerical study on MHD pipe flow extends the findings of experiments performed in the MEKKA facility addressing 3D phenomena in a nonuniform magnetic field with a particularly long section of linear increase. The implementation of the numerical model accounts for a consistent reconstruction of the magnetic field from measurements and simulations of turbulent inlet conditions. Results are summarized in figure 4.18, which illustrates the main phenomena. The upper diagram shows the distribution of the imposed nonuniform magnetic field along the pipe axis. The lower plot sketches the pipe at $y=0$, highlighting the associated phenomena of physical quantities such as electric potential, currents, and velocity in green, red, and blue, respectively.

When the fluid moves into the magnetic field, growing transversal potential differences are induced as the magnetic field increases. Those are weak within the early development stage $x < x_1$, but they evoke large-scale current loops closing far upstream in the fluid. Lorentz forces created by these currents are directed towards $z=0$, creating a local pressure maximum. The high-pressure region blocks the core and forces the fluid to the sides, leading to a reduced core velocity near $z=0$ and high-velocity jets near the sides right behind x_1. Along the section of linear magnetic field growth, currents close their paths along the wall while current streamlines in the fluid are stretched in the downstream direction. This leads to an effective current path along axial, transverse (for $x > x_2$), and then again axial direction, as indicated by the red dashed arrows. At the position where the additional transverse currents cross the core, the highest currents and braking Lorentz forces create the

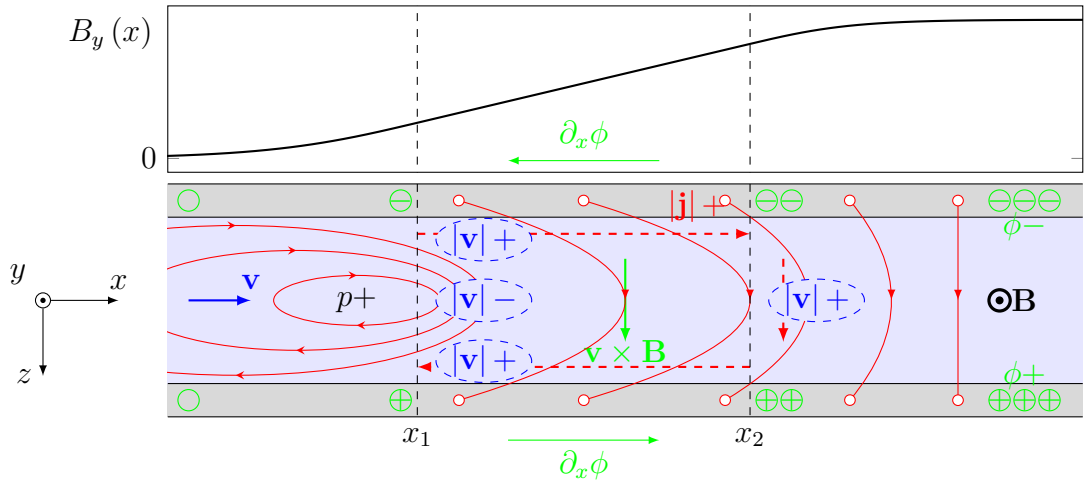

Figure 4.18: Major characteristics of 3D MHD phenomena in a spatially growing magnetic field. Currents, velocity and electric potential are marked in red, blue and green, respectively. The supplements $+$ and $-$ indicate local extrema, while the encircled signs along the wall domain show the axially varying electric potential.

steepest axial pressure gradient for $x > x_2$. Further downstream, the MHD flow becomes rapidly fully developed when $\mathbf{B}$ approaches a uniform condition.

The numerical solution of the problem provides deeper insight into the physical phenomena. While it can be confirmed that an overwhelming part of the Lorentz force opposes the pressure force in a sort of magnetostatic balance, the remaining residual fraction of the electromagnetic force has been identified as the one that balances inertia and viscous forces. The latter part of the force is therefore called the magnetodynamic force, and it poses a viable investigative tool for the analysis of complex 3D flows studied in chapter 5.

The Numerical models for entry flow and nonuniform magnetic field have been validated by the law of the wall and measured data, respectively. Simulation results have been further validated by comparison with experimental data for pressure and potential measured on the surface of the pipe. Moreover, the simulations support previous assumptions that transverse potential gradients may serve as suitable approximations for velocity even if they were recorded at the wall. It has been further shown that in a nonuniform magnetic field, electric potential and velocity are not necessarily constant along y. Such numerical investigations become indispensable for the evaluation of flow quantities that are not directly accessible by experimental techniques. As a result, the confident conclusion can be drawn that the applied code is qualified for numerical investigations of 3D MHD phenomena in fusion applications. This crucial statement on the solver's validity enables detailed numerical analyses of MHD flows in pipes with flow channel inserts that are devices designed for MHD pressure drop reduction in fusion blankets, as presented in the next chapter.

5 MHD flows in flow channel inserts (FCI)

The resistance to high pressures of breeding blankets requires thick structural walls, leading to a high electric wall conductance. As a consequence, those well conducting walls provide shortcuts over the solid domain, which in turn increases fluid-internal currents, Lorentz forces, and pressure drop. In order to mitigate such electromagnetic flow resistance occurring in fusion blankets, an early patent by Malang (1987) proposes electrically insulating flow channel inserts (FCI). They loosely fit inside the channels of blankets and manifolds, where they cover the walls and electrically decouple the fluid region from the well conducting structural material and thus reduce electric currents and associated MHD pressure drop.

Magnetohydrodynamic pressure drop reduction by means of insulating flow channel inserts constitutes a subject of ongoing research in fusion engineering, addressing this topic theoretically and experimentally, e.g., in Malang et al. (2011), Kim (2014), Norajitra et al. (2015), Rapisarda et al. (2017), Bühler et al. (2020a). One approach is to fabricate the FCI entirely from a ceramic material such as silicon carbide (Smolentsev et al., 2006). However, by testing a first prototype in liquid metal flow (Courtessole et al., 2016), Gonzalez et al. (2016) show that the highly conductive fluid may penetrate into the porous structure of the FCI and deteriorate its insulating property. This is why another FCI concept foresees thin steel sheets in the form of a sandwich-like structure that encloses and thus protects the ceramic insulator from fluid infiltration (Malang et al., 1988). However, enclosing the insulator with conductive material, in turn, enables electric currents to find shortcuts over those layers. If, therefore, the outer protective FCI layers are sufficiently thin in comparison to the bare pipe walls, this may both prevent fluid infiltration and enable an adequate MHD pressure drop reduction due to their high electrical resistivity. The present chapter presents investigations of MHD phenomena occurring in such sandwich-type FCIs and discusses the suitability of these devices for fusion applications.

5.1 Sandwich-type FCI in the MEKKA experiment

In the frame of the ongoing EUROfusion conceptual design phase for liquid metal blankets, a sandwich-type FCI for circular pipes has been developed and fabricated at KIT (Koehly & Bühler, 2017). Experiments at the MEKKA laboratory have been conducted,

where the FCI loosely fits into a thick-walled pipe, as shown in figure 5.1. Under fusion-relevant magnetic fields, measurements of pressure and electric potential detect the existence of strong 3D MHD phenomena occurring close to the FCI entry or across the conjunction between two consecutive FCIs, as presented in Bühler et al. (2019) and Bühler et al. (2020a). Complex 3D currents $\mathbf{j}_{3D}$ arise at such locations where the thin insulation layer, indicated by the orange lines, ends. The high thickness of the bare pipe wall $t_w = R_o - R_i$ offers a considerably higher conductance to electric currents than the extremely thin inner FCI layer with $t_{FCI} = R_{ins} - R_{FCI}$. The sudden jump of wall conductance leads to axial potential gradients within the transitional flow domain. Hence, electric currents align axially in order to bypass the insulation through the conductive ledge, where FCI protection layers are sealed, to eventually close over the well-conducting pipe wall. They evoke an additional MHD pressure drop and a complex flow manipulation at FCI entries or conjunctions at two consecutive FCIs, thus reducing the FCI's efficiency.

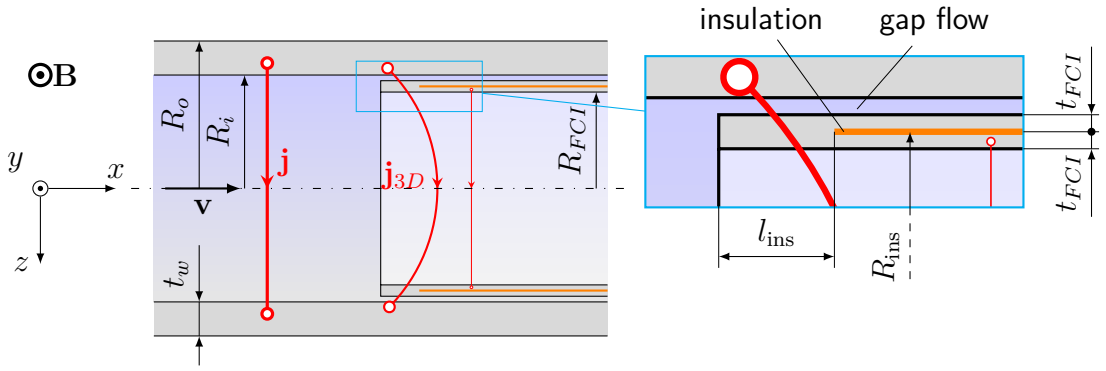

Figure 5.1: Sketch of the flow channel insert (FCI) tested for circular pipe flow in the MEKKA laboratory.

While the MEKKA experiments are constraint to measurements from the outer pipe surface, the computational analysis reveals the internal distribution of complex 3D MHD phenomena and associated pressure losses occurring close to conjunctions between FCIs and near entry regions. This makes numerical analyses mandatory in order to investigate relevant quantities, which experimental methods and analytical theory cannot provide. Hence, computationally obtained results help to assess 3D MHD phenomena occurring in FCIs and support the blanket design process.

The computational study at hand reveals the complex coupling phenomena of 3D MHD quantities and their impact on pressure losses occurring at FCI conjunctions and entries. Segregating magnetostatic and magnetodynamic momentum balances creates a direct link between the Lorentz force profile, streamline patterns, and the formation of internal shear layers. Moreover, the comparison of different FCI model approximations with increasing geometric complexity shows that already simple approaches robustly reflect the occurrence of 3D MHD phenomena and thus reduce computational effort. The most accurate FCI model is capable of resolving the flow in the thin gap between FCI and wall, as shown in the enlarged sub-view of figure 5.1. Contrary to original concerns that pressure differences between bulk

and gap flow might become critical (Malang, 1987), computations for a fusion-relevant parameter range show that the underlying FCI design withstands electromagnetic pressure imbalances without any countermeasures. However, a highly nonuniform flow distribution in the gap region seems important, for instance, concerning corrosion or tritium transport.

5.2 Implementation of FCI models

With increasing geometric details of a numerical model, expenses for development and simulation grow significantly. To keep costs reasonable and simultaneously gain physically consistent results, one major objective of this study is to reveal the impact of geometric model resolution on the numerical outcome. This work, therefore, approaches the implementation of FCI models by simplifying their geometries employing three different approximation levels, shown in figure 5.2.

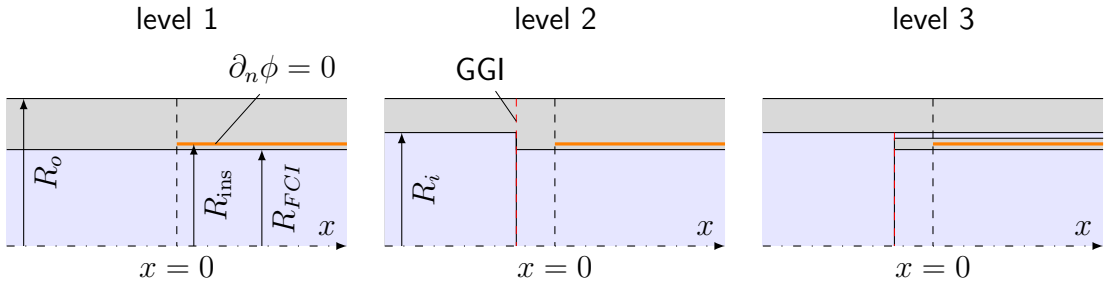

Figure 5.2: Cross-sectional view showing approximation levels of the FCI entry model. The orange line indicates the FCI's insulation layer.

The gray shaded areas, representing steel, are electrically conducting. Therefore computations generally take into account the propagation of the electric currents and potential in these areas, namely the thick pipe wall as well as in the thin FCI layers, by solving the Laplace equation $\Delta\phi = 0$ for the entire solid domain. The insulation layer of the investigated FCI measures in thickness only a few microns but constitutes a perfect insulator (Koehly & Bühler, 2017). Neglecting the thickness of the insulation, all numerical models assume the presence of an internal non-conducting layer, illustrated as an orange line. Along this cylindrical surface at radius R_{ins} for $x > 0$, all FCI models assume internal homogeneous Neumann conditions for the electric potential $\partial_n\phi = 0$. This prevents current flux from crossing the insulation layer and confines the flow-induced electric field to the fluid domain $r < R_{FCI}$ and thin inner conductive FCI layer $R_{FCI} < r < R_{\text{ins}}$. In this manner, the FCI models may be adjusted to the conductance of the FCI used in the MEKKA experiments, for which, according to Miyazaki et al. (1983), a wall conductance parameter may be defined for $x > 0$ as

$$c_{FCI} = \frac{\sigma_w}{\sigma} \frac{R_{\text{ins}}^2 - R_{FCI}^2}{R_{\text{ins}}^2 + R_{FCI}^2} = 0.00457 \ . \tag{5.1}$$

The implementation of the FCI in the global geometry has been accomplished via three levels of increasing complexity, as shown in figure 5.2. In approximation level 1, the fluid-wall and fluid-FCI interface have the same dimension R_{FCI}, assuming that small geometric effects on MHD phenomena are negligible in comparison to the impact of the FCI's electric insulation. The approach, therefore, fully merges pipe wall and FCI to a coherent solid domain involving a smooth fluid-wall interface. In this way, the model accounts for the FCI's insulation and conductance of the inner protection layer, which still allows for 3D leakage currents to close their paths along the thick conductive outer region. This keeps the inner radius constant at R_{FCI} and the wall conductance of the bare pipe upstream of the FCI, i.e., $x < 0$, becomes

$$c_1 = \frac{\sigma_w}{\sigma} \frac{R_o^2 - R_{FCI}^2}{R_o^2 + R_{FCI}^2} = 0.08616 \ . \tag{5.2}$$

The levels 2 and 3, on the other hand, consider in addition geometric constraints in the form of a sudden diameter contraction from radius R_i to R_{FCI} in front of the FCI at $x < -l_{\text{ins}}$, with l_{ins} representing the conductive ledge in figure 5.1, where the protective layers are welded together (Koehly & Bühler, 2017). This results in a slightly lower upstream wall conductance in comparison to c_1,

$$c_{2,3} = \frac{\sigma_w}{\sigma} \frac{R_o^2 - R_i^2}{R_o^2 + R_i^2} = 0.07178 \ . \tag{5.3}$$

While level 2 only models the sudden contraction at $x = -l_{\text{ins}}$, the most accurate level 3 also considers the fluid in the gap and the conductance of the outer sheet of the FCI. The geometry of level 3 is the most realistic model where the FCI concentrically "floats" inside the pipe fully enclosed by fluid. In this way, the most detailed level 3 also accounts for MHD phenomena occurring inside the annular gap between the wall and FCI.

Concerning the parameter range of investigated cases shown in table 5.1, the conductance of viscous Hartmann layers is $\delta_{Ha} = Ha^{-1} = 5 \cdot 10^{-4}$ and $\delta_{Ha} = 2 \cdot 10^{-4}$ for $Ha = 2000$ and $Ha = 5000$, respectively. The FCI conductance c_{FCI} is an order of magnitude larger than the conductance of the Hartmann layer and an order of magnitude smaller than the wall conductance of bare pipe flow $\delta_{Ha} \ll c_{FCI} \ll c_{1,2,3}$. This means that the FCI poses a substantial electric shortcut in comparison to the Hartmann layers. On the other hand, the large drop of wall conductance from the bare channel wall to the FCI reduces electric current flow significantly and this, independent from considered case or approximation level, leads to a large reduction of the pressure gradient.

	Ha	Re	N
case 1	2000	20000	200
case 2	5000	5000	5000
case 3	5000	10000	2500

Table 5.1: Three simulated cases of the parameter range of experiments conducted in MEKKA (Bühler et al., 2019, 2020a).

The length scales of pipe geometry and of MHD phenomena differ over several orders of magnitudes, and therefore their discretization requires a large number of grid points. An SHM grid type serves as base mesh in the cross-sectional plane from where the mesh is extruded in the streamwise direction by means of prism layers. Table 5.2 shows exemplarily for the level 3 approximation the number of applied cells and prism layers. Streamwise extruded prism layers concentrate towards $x = 0$, where the strongest 3D MHD phenomena are expected. Besides the large number of prism layers in boundaries and the FCI/wall gap, a particular fine grading is applied towards all fluid-solid interfaces. At least four grid points resolve the extremely thin Hartmann layers, which scale with $\delta_{Ha} \sim Ha^{-1}$ at vertical positions, where the magnetic field is orthogonal on fluid-solid interfaces.

numbers of cells		prism layers			
fluid	$10.7{\cdot}10^6$	streamwise	270	FCI/wall gap	35
solid	$4.9{\cdot}10^6$	boundary layers (pipe)	42	boundary layers (FCI)	30
total	$15.6{\cdot}10^6$	wall (solid)	40	FCI layer (solid)	5

Table 5.2: Mesh details exemplarily shown for the level 3 FCI approximation model.

As presented above, approximation levels 2 and 3 exhibit a sudden diameter contraction at the FCI's ledge position $x = -l_{\mathrm{ins}}$, as shown in figure 5.2. This complicates the local grid structure since resolving the boundaries at different diameters on a continuous streamwise grid increases the cell number and, thus, the computational effort considerably. For resolving this issue, OpenFOAM provides a general-grid-interface (*GGI*) that allows joining two computational grids with different spatial discretization. As indicated by the red dashed line shown in figure 5.2, this establishes a junction between grids of bare channel and FCI, where the interface of both domains may have a different cell structure. Further imposed conditions along boundaries and interfaces are listed in table 5.3.

	inlet	outlet	fluid-solid int.	insulation	wall surface	GGI
ϕ	$\partial_n\phi = 0$	$\partial_n\phi = 0$	$\phi = \phi_w$, $j_n = j_{n,w}$	$\partial_n\phi = 0$	$\partial_n\phi = 0$	cyclic
p	$\partial_n p = 0$	$p = 0$	$\partial_n p = 0$	-	-	cyclic
$\mathbf{v}$	$\mathbf{v}{=}v_{x,fd}\mathbf{e}_x$	$\partial_n\mathbf{v} = 0$	$\lvert\mathbf{v}\rvert = 0$	-	-	cyclic

Table 5.3: Boundary conditions of the numerical model.

The electric potential and currents are coupled along fluid-wall as well as fluid-FCI interfaces and determined collectively for all domains by a block-coupled matrix solver (Jareteg, 2013). Electric potential and wall-normal currents are continuous at the interface between the fluid and solid structures indicated by the subscript w, such as walls or FCIs. Pressure and velocity, on the other hand, exclusively exist within the fluid domain where at the outlet, the flow is assumed fully developed with a constant pressure reference $p = 0$. A separate simulation determines a fully developed velocity profile $v_{x,fd}$ of entering flow, which is then applied as a fixed inlet velocity. This allows limiting the flow domain upstream and downstream to ten times the radius of the FCI $-10 < x < 10$, whereby the FCI radius R_{FCI} serves as characteristic length throughout this entire study, i.e., the non-dimensional

FCI radius becomes

$$R_{FCI} = 1 \ . \tag{5.4}$$

Further relevant geometric dimensions are listed in table C.3 in the appendix. Moreover, the implementation of the FCI model at conjunctions involving a short gap in the insulation are presented in appendix A.

5.3 3D MHD phenomena at FCI entries

This section introduces 3D MHD phenomena occurring at FCI inlets, obtained by means of numerical simulations based on the approximation level 1 with plain inner pipe walls for $Re = 20000$ and $Ha = 2000$. The sharp drop of wall conductance upon FCI entry leads to axial potential gradients and current flow. This evokes strong 3D effects in close FCI entry vicinity, which redistribute the fluid flow and produce high-velocity jets near the sides. They may trigger localized instabilities in the Roberts regions right downstream behind the FCI entry. Eventually, by identifying additional 3D MHD pressure losses, computational results confirm the general applicability of the underlying FCI design.

Electric potential and currents

Figure 5.3 shows the electric potential distribution and current pathways occurring in the vicinity of an FCI entry. Sufficiently far upstream, the incoming flow is fully developed. There, the electric potential exclusively varies along z, reaching its maximal magnitude ϕ_{2D} near the sides in accordance with asymptotic theory (Miyazaki et al., 1983)

$$\phi_{2D} = \pm\frac{1}{1+c_1} \text{ and } \phi_{2D,FCI} = \pm\frac{1}{1+c_{FCI}} \ . \tag{5.5}$$

Electric currents circulate in cross-sectional planes, which is typical for fully developed flow. Blue lines show electric pathways that close over the well-conducting pipe wall. Downstream inside the FCI, red lines indicate induced currents that exclusively close over the inner conductive sheet of the FCI since the insulation prevents the penetration of current flux. In this way, the cylindrical insulator confines those currents, permitting induced electric fields only inside the FCI so that far downstream, the wall potential becomes zero.

The decay of wall potential downstream $x > 0$ leads to axial wall potential gradients. Wall currents, therefore, have x-directed components, and they preferably close over the low-potential domain in the form of large recirculation loops by wrapping around the insulation. This is shown by strongly bent blue lines near $x = 0$. Fluid currents, on the other hand,

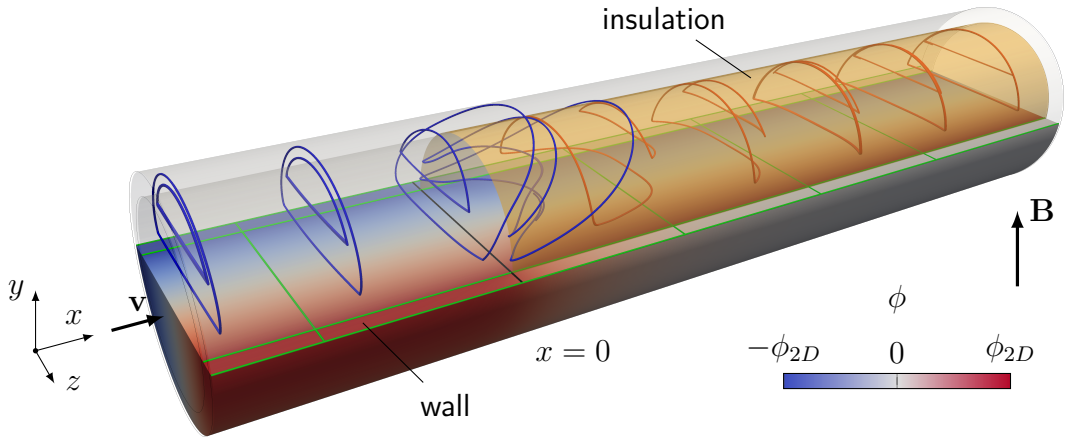

Figure 5.3: Electric potential distribution shown in the lower half and current paths in the upper half of the pipe. The insulation starts at $x = 0$, shown by the orange surface. Blue streamlines represent currents that close in the wall domain while red streamlines portray currents closing inside the inner conducting FCI sheet. The color scale is limited by $\pm\phi_{2D}$ according to Miyazaki et al. (1983) in equation 5.5. Green straight lines indicate sample paths referring to the plots in figure 5.4.

experience an increase of transverse potential difference upon FCI entry as the resistance of the surrounding conducting solid material increases. The resulting axial potential gradient causes fluid currents to bend in the axial direction. In contrast to bare channel flow for $x < 0$, where 3D effects occur only in the immediate vicinity of the entrance (blue lines), red lines show that 3D effects extend far downstream into the FCI over several characteristic lengths before a pure spanwise current profile of fully developed FCI flow evolves.

Figure 5.4 shows axial and transversal potential distributions in the horizontal symmetry plane $y = 0$. In the left plot, red and blue curves refer to outer wall potential and potential at the fluid-solid interface, respectively. The potential values have been taken along the green sample lines indicated in figure 5.3. The vertical lines in the left plot are projections representing the transversal potential distributions that are displayed in the graph on the right.

In the upstream region $x < 0$, fluid and wall potential differ slightly, in accordance with predictions by Miyazaki et al. (1983), by a marginal wall voltage, and both remain almost constant along x, shown by red and blue lines, respectively. Before entering the FCI, magnitudes of inner and outer wall potential decrease slightly until $x = 0$, where the insulation starts. For $x > 0$, radial current flow into the outer wall is interrupted. The outer wall potentials (red lines) monotonically decay to zero, while the potentials at the fluid-wall interface (blue lines) converge towards a higher magnitude. According to Ni et al. (2011), downstream development lengths of 3D Phenomena at FCI entries in rectangular ducts require up to approximately five characteristic lengths. The present simulations addressing

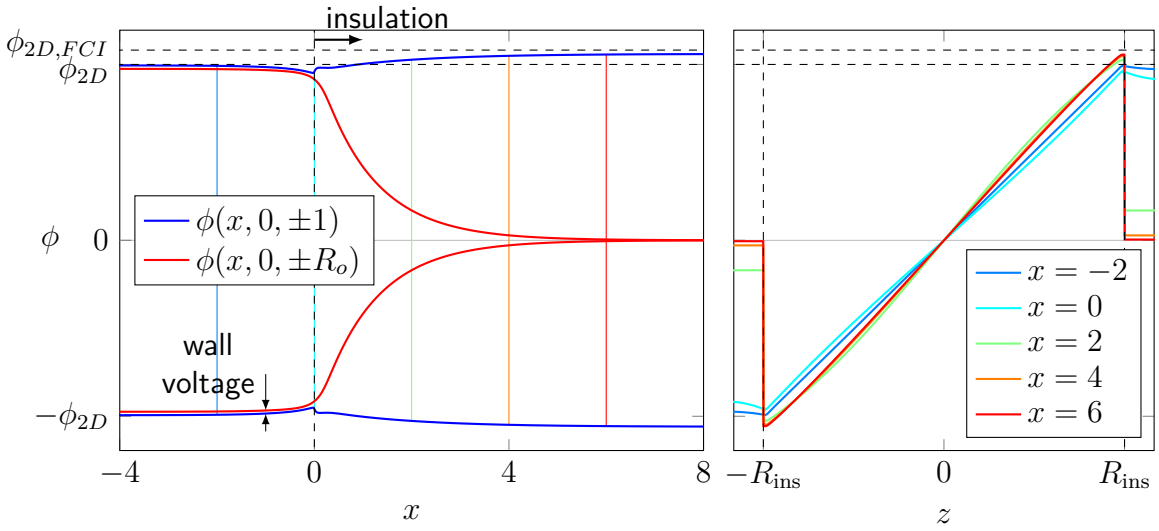

Figure 5.4: Axial (left) potential distribution sampled along the green lines in figure 5.3 for $y = 0$, and transversal (right) potential distributions for different axial positions.

a circular geometry find a similar trend. The associated gain of inner FCI potential may be explained by Ohm's law

$$j_z = -\partial_z \phi + v_x \ . \tag{5.6}$$

While the magnitude of the induced electric field, here represented in non-dimensional form by v_x, remains approximately the same along x, currents are reduced in the FCI due to the low conductance of the inner sheet. Smaller currents are compensated by higher potential gradients $-\partial_z \phi$, and when integrated along the transverse direction they result in a slightly higher transversal potential difference, as shown by blue lines upon FCI entry.

When approaching fully established conditions both upstream and downstream, the magnitudes of potential reach values as predicted for pipe flow by Miyazaki et al. (1983). A comparison of results with values obtained by the simple formulas 5.5 shows already a quite good agreement. However, their derivation (Miyazaki et al., 1983) neglects the electric conductance of the thin Hartmann layers compared to the conductance of the walls. Therefore, formulas 5.5 apply better for $x < 0$ where $\delta_{Ha} \ll c_1$.

Figure 5.4 (right) shows transversal potential profiles at several downstream positions. The electric field induced by the fluid motion becomes visible as a spanwise potential gradient with $\phi\,(z = 0) = 0$ due to symmetry. While in the upstream region $x < 0$, the flow-induced potential spreads continuously across the thick conducting wall, we observe downstream for $x > 0$ at $z = \pm R_{\text{ins}}$ a sudden jump since currents are interrupted at the insulation. With increasing distance from the entrance of the FCI, the potential of the outer wall decreases monotonically. In contrast, the potential of the inner conducting sheet slightly increases to meet values predicted by equation 5.5. A closer look to the potential distributions for $x \geq 0$ in the core region reveals some deviations from a linear behavior, which indicates that velocity profiles may exhibit transverse variations as well according to

equation 5.6.

Currents, Lorentz force, and velocity

For strong magnetic fields $Ha \gg 1$, values of flow properties such as pressure, potential, or core velocity remain constant along magnetic field lines. Therefore, contour plots in the plane $y = 0$, as shown in figure 5.5, provide already comprehensive insight in 3D MHD phenomena. Magnitudes of currents and Lorentz force density are normalized by the maximum values from the asymptotic solution of fully developed bare channel flow (Miyazaki et al., 1983) indicated by the subscript $2D$.

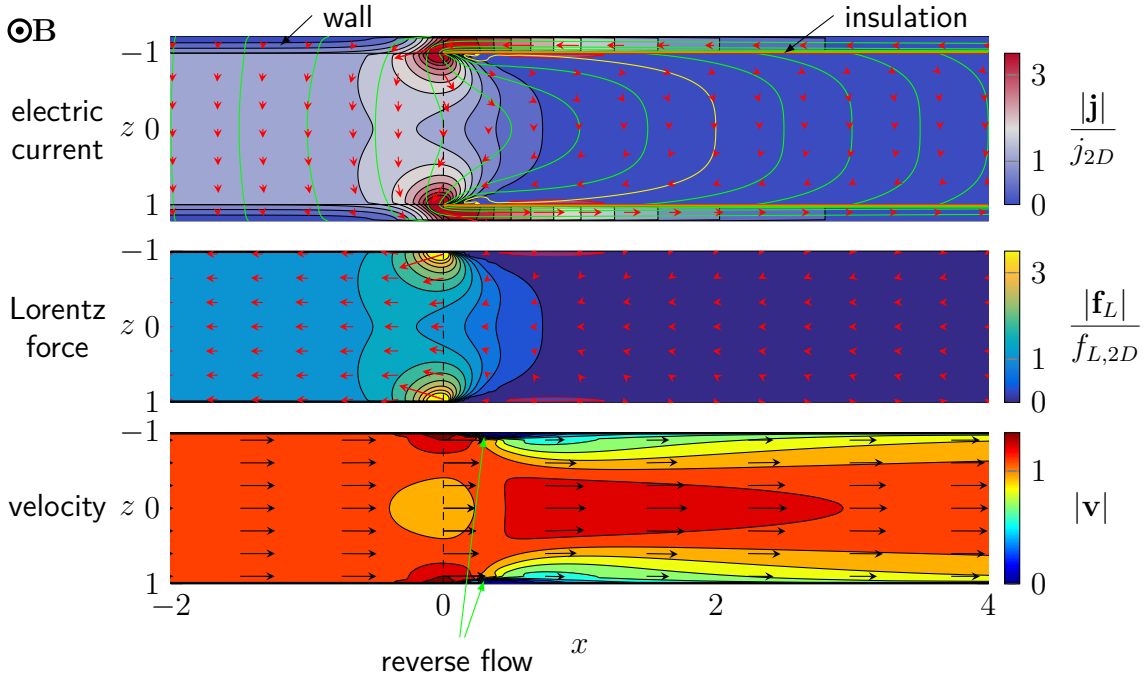

Figure 5.5: Contour plots presenting magnitudes of current density, Lorentz force and velocity at $y = 0$ combined with respective vector representations. Green streamlines mark electric current paths. The vertical black dashed line indicates the FCI entry $x = 0$.

The upper contour plot presents the magnitude of electric current density $\mathbf{j}$. As imposed by design, the electric conductance of the thin inner FCI layer for $x > 0$ is comparatively small in contrast to the thick wall of the pipe for $x < 0$, which significantly reduces the current density in the FCI. Current streamlines portrayed as green lines form long downstream directed recirculation loops upon FCI entry. Those axial distortions of currents in FCIs confirm the significant impact of 3D effects on the development length in pipes with low wall conductance, whereas the current distribution in bare channel flow is marginally affected. Behind the FCI entry $x > 0$, the yellow highlighted streamline exhibits swirls of electric

current flow in a small region close to the side. At the FCI entrance $x = 0$, electric currents bundle as they flow around the insulation in order to close over the well-conducting pipe wall, leading to high peaks of electric current density near the sides. While not visible in the figure with the used color scale, side regions evolve up to 20 times the current density as in fully developed bare pipe flow.

The Lorentz force density $\mathbf{f}_L = \mathbf{j} \times \mathbf{B}$, shown in the middle contour plot of figure 5.5, directly depends on the electric current density. Since the magnetic field $\mathbf{B} = \mathbf{e}_y$ is uniform, profiles of magnitudes of Lorentz force and electric current density coincide, and $\mathbf{f}_L$ stands orthogonal on $\mathbf{j}$ and $\mathbf{e}_y$, thus opposing the core flow in large parts of the fluid volume. The FCI reduces the electric current density and thus Lorentz forces significantly. At the FCI entry, strong transversal Lorentz force components occur, directed into the channel core region. Under particularly strong magnetic fields, a major momentum balance occurs between Lorentz force and pressure gradient, while velocity-related momentum, i.e., inertia and viscous forces, play a minor role. As shown in the bottom contour plot, this seems to decouple the velocity distribution from the Lorentz force where no apparent correlation exists between them.

Contours of velocity exhibit a uniform distribution in the bare channel upon approaching the FCI. In the vicinity of the inlet, the fluid evades to the side forming a concave velocity profile with high side jets and a low velocity in the center, as shown for $x = 0$. This effect reverses drastically downstream after the FCI entry $x > 0$, where the profile involves a center peak and low side velocity. As observed for electric potential and currents and in agreement with previous works (Mistrangelo & Bühler, 2015), the low wall conductance of the FCI results in a larger flow development length and less stable flow conditions in addition. Zones of locally reversed flow occur along the sides close to the FCI entry, where electric current exhibits a small swirl (yellow streamline). Observations show that for the underlying parameter range of $Ha = 2000$ and $Re = 20000$, side layers directly behind the FCI entry exhibit a small region of reversed flow with time-dependent perturbations.

Figure 5.6 illustrates the 3D developing MHD flow by presenting 3D profiles of v_x as well as the cross-sectional magnitude at characteristic axial positions.

The incoming pipe flow is fully developed and exhibits uniform velocity. 3D profiles displayed in figure 5.6 show characteristic stages of developing FCI flow. In general, core velocity remains constant along magnetic field lines and decays towards the fluid-wall boundary in the form of extremely thin viscous layers. Upon FCI entry at $x = 0$, fluid first moves to the sides, forming a concave curvature. This characteristic, however, instantly inverts shortly after by turning into a convex profile that involves a high center peak, as represented for the position $x = 1$. The high electric resistance of the inner FCI layer strongly restricts currents and Lorentz forces within the FCI, which results in a considerably longer development length. Accordingly, the profile flattens over several characteristic lengths, as shown, for example, at the position $x = 4$, until it establishes a profile of fully developed FCI flow.

Plots in figure 5.7 help to directly compare the stages of evolving FCI entry flow by

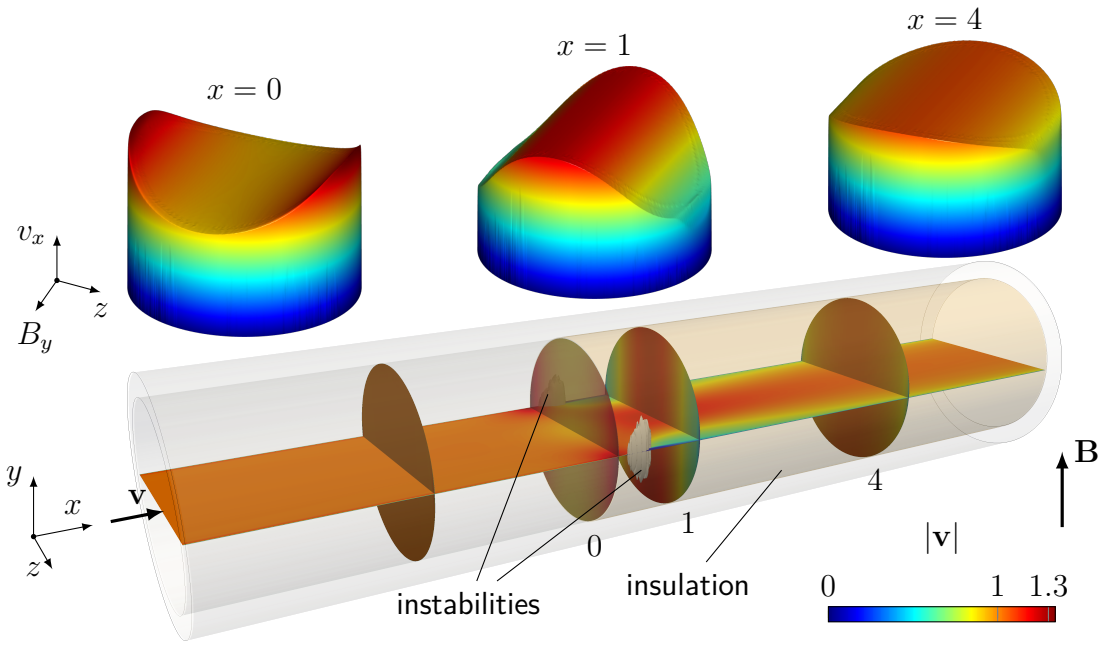

Figure 5.6: Profiles of axial velocity at $x = 0, 1, 4$ and colored contours on the plane $y = 0$ showing the distribution upon FCI entry. Local flow instabilities are marked as gray isosurfaces of turbulent kinetic energy $0.5\mathbf{v}'^2 = (\mathbf{v} - \bar{\mathbf{v}})^2$. They occur due to high velocity gradients in the side for $0 < x < 1$.

overlaying axial velocity profiles at $y = 0$ for several axial positions. For all profiles, one can observe thin viscous layers in close proximity to the sides at $z = \pm 1$. Starting in front of the FCI, the core velocity profile evolves from uniform (at $x = -1$) to a concave curvature at the FCI inlet $x = 0$ and then rapidly transforms downstream to a highly bent convex curvature. As mentioned above, the high resistance of the inner FCI sheet is the reason for the large downstream development length, respectively shown at positions $x = 1$, 4, and 10. In contrast to the high conductance ratio between wall and Hartmann layer of bare channel flow $c_1\, Ha \approx 170$, the ratio inside the FCI is rather low $c_{FCI}\, Ha \approx 9$. As a consequence, the fully developed velocity profile in the FCI, illustrated in red for $x = 10$, is not completely uniform but in perfect agreement with the asymptotic solution proposed by Chang & Lundgren (1961), as shown by the black dashed line.

The rapid flow transition from a concave to convex profile curvature occurring on a rather short distance between $0 < x < 1$, shown exemplarily in light-blue and green, involves steep velocity gradients downstream directly behind the FCI inlet near the sides. In combination with the low FCI wall conductance and associated drop of Lorentz forces, this destabilizes the flow in the sides. Transient perturbations arise, which are localized to a comparatively small domain, shown in figure 5.6 as gray isosurfaces illustrating velocity perturbations $|\mathbf{v}'| = |\mathbf{v} - \bar{\mathbf{v}}|$, i.e., deviations from time-averaged values $\bar{\mathbf{v}}$. Impacts propagate further downstream, e.g, in the form of kinks in the velocity profile at $x = 1$, represented green in

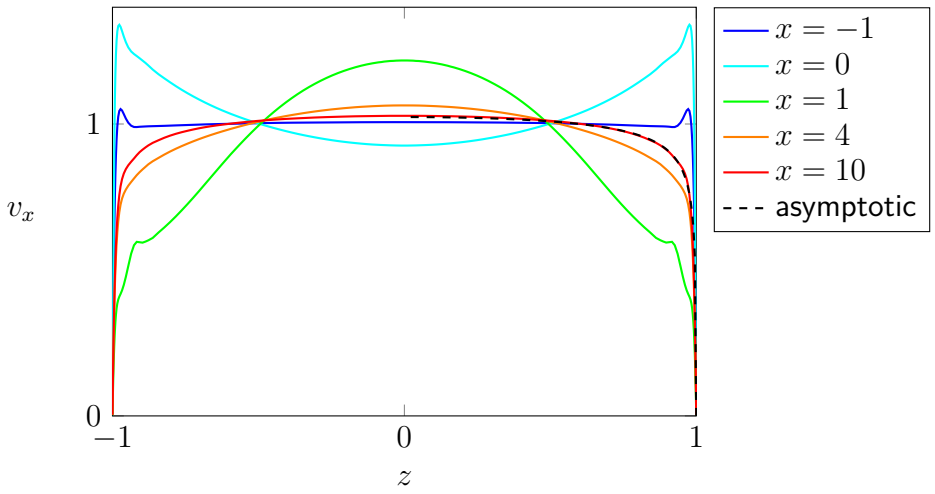

Figure 5.7: Velocity profiles in the symmetry plane $y = 0$ along z at specific streamwise locations. The black dashed line shows the asymptotic solution by Chang & Lundgren (1961) for fully developed pipe flow with FCI conductance.

figure 5.7. The following section presents the essence of those 3D MHD-induced instabilities in more detail.

Local flow instabilities

It is well known that MHD flows in electrically conducting rectangular ducts tend to become unstable. This occurs preferentially in so-called side layers along walls that are parallel to the magnetic field, where the fully developed regime involves jets with high velocities (Picologlou & Reed, 1989; Ting et al., 1991). In general, flows in circular pipes do not show increased velocities near the sides, and therefore such flows stay laminar up to high Reynolds numbers. While in rectangular ducts, 2D or quasi 2D (Q2D) turbulent patterns with low magnetic damping are possible (Sommeria & Moreau, 1982), such structures are excluded in pipes due to curvature of the wall. However, a few exceptions exist where also flows in circular pipes may develop some time-dependent structures. One example has been shown by Albets-Chico et al. (2013) for 3D pipe flow in a fringing magnetic field where localized jets near the sides may become unstable, and perturbations evolve through strong detaching Lorentz forces and locally reversed flow. Similar phenomena can be observed in the present model simulations when MHD pipe flow enters an FCI. Jets occur close to the sides with strong gradients for velocity and Lorentz force. As a result, the flow in a small vicinity near the sides becomes unstable directly behind the FCI entry $x = 0$. In contrast to hydrodynamic turbulence, the arising transient perturbations are highly correlated and aligned with the magnetic field.

In the present study, local instabilities exclusively appear with respect to the case 1 scenario

at the lowest investigated interaction parameter $N = 200$. Other cases such as $N = 2500$ and $N = 5000$ remain entirely stable due to stronger magnetic damping.

Figure 5.8 presents at one side of the FCI entry contours of the electric potential fluctuations $\phi' = \phi - \bar{\phi}$, i.e., deviations from time-averaged values $\bar{\phi}$.

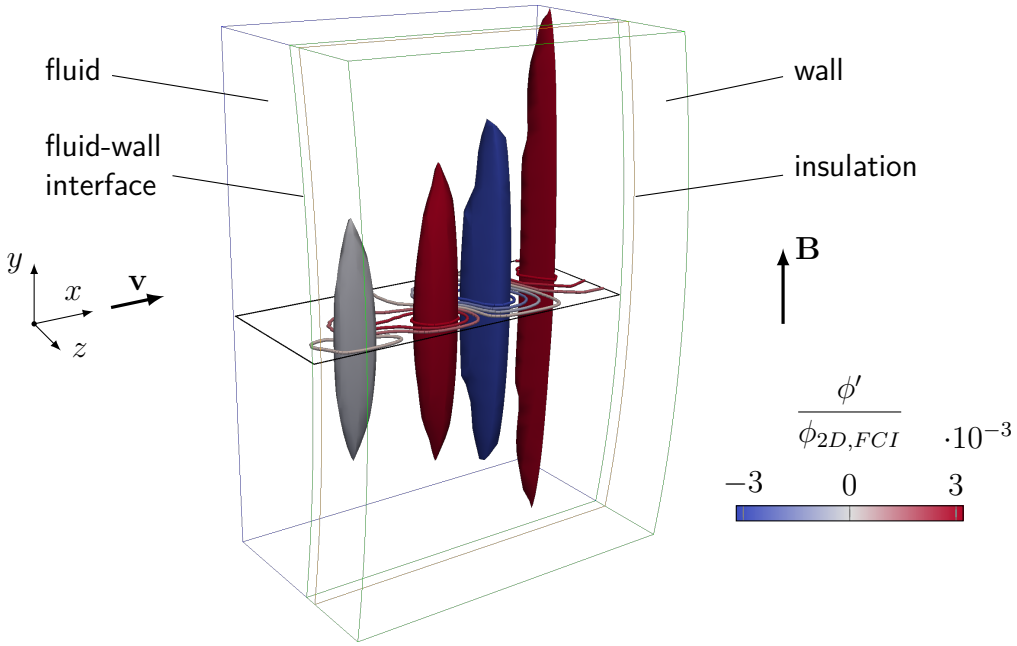

Figure 5.8: Contours and isosurfaces of ϕ' reveal alternating eddy structures. Intersections of fluid and wall domain as well as insulation are outlined by thin lines. Black lines indicate the cross-sectional plane $y = 0$.

Arising patterns show quasi-two-dimensional (Q2D) properties, where time-dependent structures are anisotropic and elongated along magnetic field lines up to pipe dimension (Smolentsev, 2021, pp. 14-16). In general, transient perturbations remain constant along magnetic field lines, thus connecting the top and bottom boundary layers in the form of elongated spinning columns, referred to as cigars (Mück et al., 2000) or barrels (Pothérat et al., 2000). In the present problem, patterns stretch along field lines, with growing distance from the sides due to the curvature of the pipe. Hence, perturbations dissolve rapidly due to ohmic and viscous losses, which preferentially occur where eddies merge with the Hartmann layers (Smolentsev, 2021, pp. 14-16).

Two probes at $(0.3, 0, \pm 0.9)$ monitor the time-dependent phenomena at opposite sides. Figure 5.9 presents the recorded transient fluctuation of the velocity component v_z' versus time and frequency for opposite side locations, which are separated from each other by the laminar core flow. The upper diagram shows a time history over three dimensionless time units.

The presented data samples of opposite probe locations, shown in figure 5.9 (upper diagram), are periodic for various time windows between $T = 3$ and $T = 120$. This consistent behavior

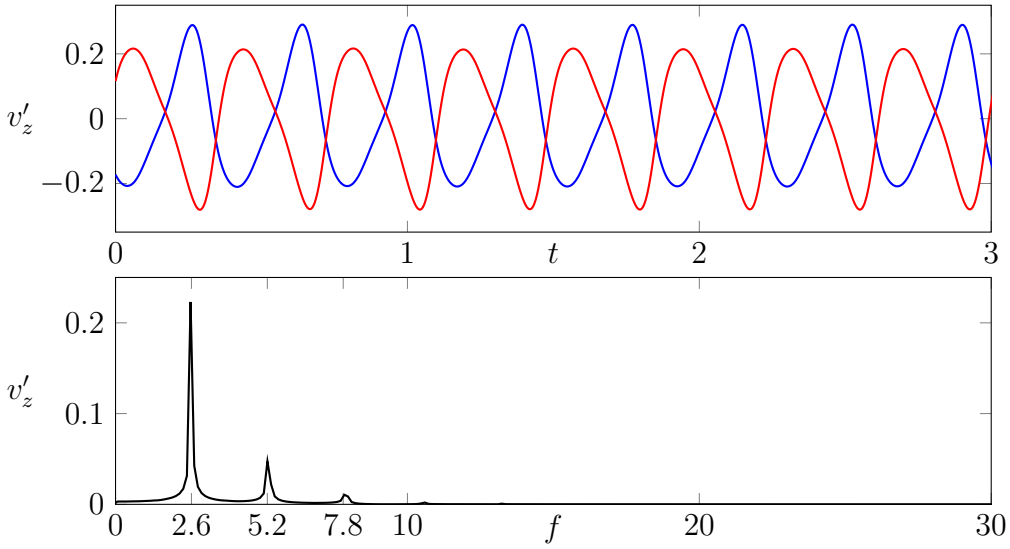

Figure 5.9: Simulated fluctuations of transversal velocity component v_z' at opposing sides $(0.3, 0, \pm 0.9)$ versus time and frequency. While both signals are phase shifted, their amplitudes are identical, as represented for both probes by the black line in the bottom graph. Time is scaled corresponding to its characteristic dimensional quantity L/u_0.

suggests that the unstable simulations are performed long enough to develop converged statistics. Accordingly, the Q2D columns show periodic velocity fluctuations. Observing amplitudes across frequency in the lower diagram reveals that those transverse fluctuations involve mainly one specific harmonic at a comparatively high amplitude of around 20 % compared to mean velocity as well as a few higher harmonics. Hence, the observed perturbations detach from the sides at a regular rate and migrate into the core flow on their downstream path. Moreover, unstable regimes at opposite sides seem to interact as their fluctuations exhibit similar inward and outward fluctuations at almost the same time. Thus, Q2D structures at opposing transverse positions have a different sense of rotation. Kinet (2009, pp. 123ff.) and Arlt (2018, pp. 76ff.) report similar behavior in their studies on unstable side layers in rectangular duct flows. They observe periodicity among detaching side layer instabilities and identify characteristic interaction modes between turbulent regimes of opposing side layers, separated by the laminar core. While time-dependent perturbations in rectangular channels persist or even grow downstream, the unstable patterns in the present problem exist only in a very narrow vicinity at the sides of the FCI entrance.

Figure 5.10 presents fluctuations of electric potential ϕ' and pressure p' within the symmetry plane $y = 0$. Unstable Q2D vortex structures detach shortly after the FCI entry. They grow in size for $x > 0$ and migrate towards the center before they dissolve. Perturbations of electric potential and pressure behave in a similar way. Moreover, fluctuating currents $\mathbf{j}'$, portrayed by black limiting streamlines in the symmetry plane $y = 0$, connect different vertical structures and show critical points such as sources and sinks.

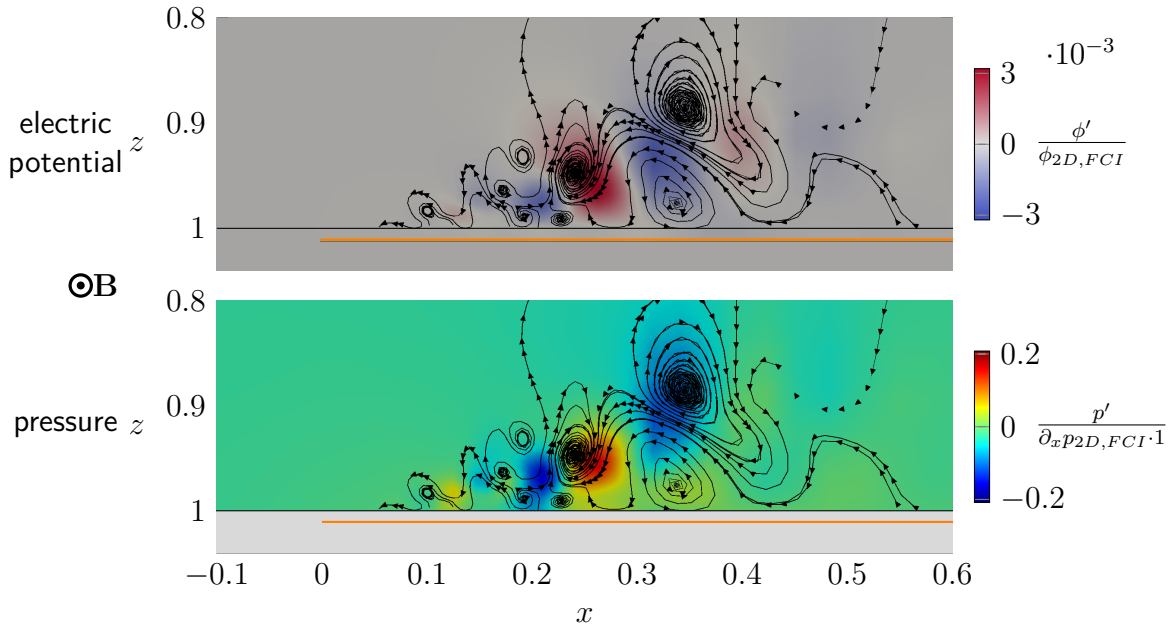

Figure 5.10: Distribution of fluctuating parts of electric potential ϕ' and pressure p' on the horizontal symmetry plane $y = 0$ and current $\mathbf{j}'$ shown as black streamlines. The orange straight lines mark the insulation layer. Variables are scaled with respective asymptotic solutions for developed FCI flow Miyazaki et al. (1983), indicated by the subscript $2D, FCI$.

In order to evaluate the significance of perturbations, their magnitude is compared with data from comparable fully developed flow according to the asymptotic solution by Miyazaki et al. (1983), indicated by the subscript $2D, FCI$. Hence, amplitudes of electric potential variations are three orders of magnitude smaller than the induced potential of fully developed flow. Pressure variations, on the other hand, account approximately for 20 % of the streamwise pressure drop of fully developed FCI flow along one characteristic unit length $\partial_x p_{2D,FCI} \cdot 1$. The pressure scale enables the estimation of local gradients. Local variations with magnitudes of approximately $\Delta p_{Q2D} \approx 0.4$ act on length scales of about $l_{Q2D} \approx 0.1$. The estimated local pressure gradient occurring between Q2D structures then becomes

$$\frac{\Delta p_{Q2D}}{\Delta l_{Q2D}} = 4 \ . \tag{5.7}$$

This means that local pressure gradients of Q2D regimes might reach up to four times the streamwise gradient of fully developed FCI flow and thus are significant. This simple estimation, however, accounts only within a close vicinity of the instability. Interesting, but out of scope of the present work, could be further analyses determining the turbulent Reynolds stresses or the determination of wall shear stress in order to assess in more detail turbulence production and vortex damping.

Pressure drop

For a large interaction parameter and Hartmann number $N, Ha \gg 1$, electric current density and pressure are linked via the leading order terms in the momentum equation $\nabla p \approx \mathbf{j} \times \mathbf{e}_y$. Under this assumption of a magnetostatic balance, transversal and axial currents determine the axial and transversal components of the pressure gradient

$$j_z = -\partial_x p \ , \tag{5.8}$$

$$j_x = \partial_z p \ . \tag{5.9}$$

As a result, the pressure becomes an approximate stream function for current density, i.e., currents flow preferentially on lines or surfaces of constant pressure. Figure 5.11 demonstrates this link between electric current streamlines and isosurfaces of pressure. Across the entire fluid domain, current paths stay on isosurfaces of the pressure. After leaving the fluid domain, currents either close inside the wall or the inner FCI layer, as marked by blue and red streamlines, respectively. The pressure is constant along magnetic field lines and varies only in xz-planes.

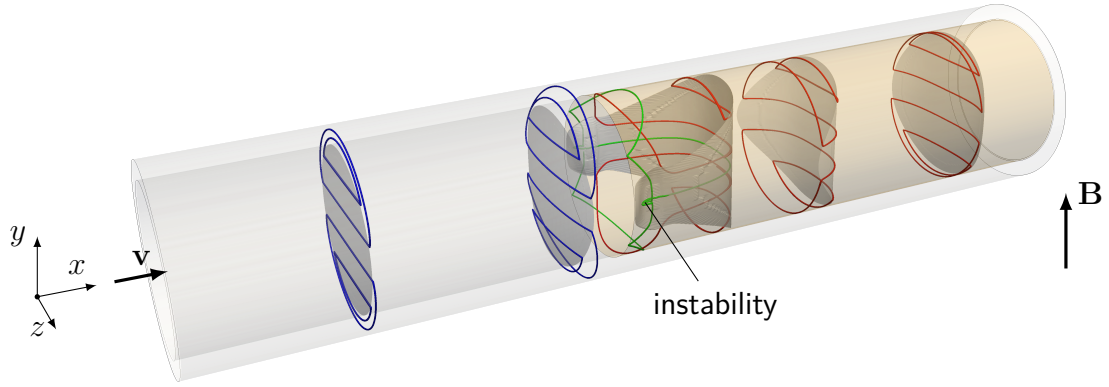

Figure 5.11: Isosurfaces of pressure (gray surfaces) and electric current streamlines. Blue lines close inside the pipe wall, and red lines over the inner FCI layer. The orange cylindrical surface represents the FCI's insulation.

In up- and downstream fully established flow, the pressure is constant in planes of cross-sections, and currents in the fluid have a pure transversal orientation. Close to the FCI entrance $x = 0$, however, currents start bending due to the axial potential gradient. The isosurfaces of pressure that coincide with current lines reflect this effect as they stretch far downstream. This indicates particularly high transversal pressure differences, which contribute to the strong fluid redistribution accompanied by the aforementioned rapid change of velocity profiles.

The green highlighted streamline represents an exceptional behavior of current flow as it connects both unstable domains, enters the inner FCI wall, flows around the insulation, and eventually closes over the upper and lower wall region. In this manner, the electric

current interacts with the unstable regimes as it first curls horizontally and then orients in the vertical direction in order to close over the solid domain. This behavior reaffirms the aforementioned magnetohydrodynamic coupling between left and right transient regimes across the laminar core flow.

The distribution of pressure and its gradients is shown in figure 5.12 on the left and right sub-plot, respectively. Since the absolute value of pressure is irrelevant for the physical behavior, the figure shows pressure differences with respect to a reference value in the center of the pipe at $x = 0$. This normalization has been chosen to simplify the comparison with experimental data of Bühler et al. (2020a) in section 5.6 where the same definition of a reference pressure is applied. In the FCI entry vicinity, center and side pressure differ, indicating a strong transversal pressure difference, as shown by blue and red lines, respectively. This behavior is expected from the curved and highly elongated isosurfaces of pressure at this location, as observed in figure 5.11. While the axial transition of the core pressure at $z = 0$, blue line, appears relatively smooth, the side pressure at $z = 1$, red line, experiences a rapid drop in front of the FCI entry. This effect becomes particularly evident by observing the pressure gradients in figure 5.12 (right). High current densities, preferably closing over the well-conducting wall in front of the FCI, result in large-scale current loops, leading along the side regions to high axial and transversal pressure gradient peaks, shown red. Of particular interest is the axial component of the pressure gradient along the side wall, since for hydrodynamic flow a change of sign of pressure gradient typically indicates a stagnation point (or separation line) and onset of flow separation. For further discussion on MHD flow separation see section 5.4.

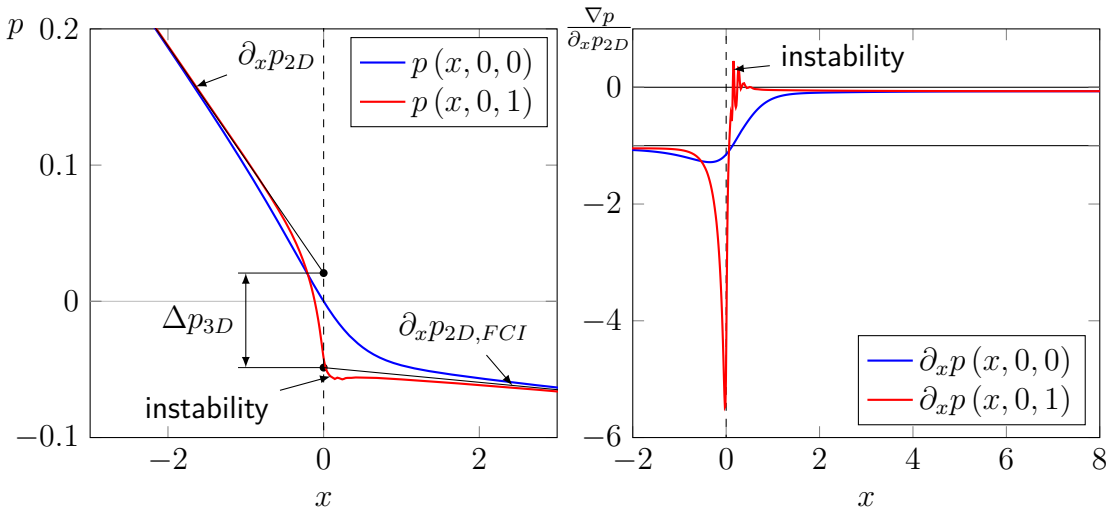

Figure 5.12: Axial distribution of pressure (left) and its gradients (right) along center and side wall. Thin black lines indicate asymptotic solutions of both bare pipe and FCI flow.

A closer look at axial pressure gradients in figure 5.12 (right) reveals localized spatial oscillations in the displayed results right behind $x = 0$ near the side. These oscillations have been discussed above with figure 5.10. They grow in size when moving with the flow before

they dissipate further downstream. The pressure distribution in the center remains laminar and stationary (blue line).

The distribution of pressure is shown on the left sub-plot along the center (blue) and along the side (red) . It can be observed that far upstream and downstream, the numerical simulations coincide with the theoretical predictions for fully developed flow in the pipe and in the FCI

$$-\partial_x p_{2D} = \frac{c_1}{1+c_1} \ , \tag{5.10}$$

$$-\partial_x p_{2D,FCI} = \frac{c_{FCI}}{1+c_{FCI}} \ , \tag{5.11}$$

as indicated by straight black lines. From the figure and from equations 5.10 and 5.11 one can see and quantify the benefit of FCIs by comparing both values

$$\frac{\partial_x p_{2D,FCI}}{\partial_x p_{2D}} = \frac{1}{16} \tag{5.12}$$

As a result, the fully developed pressure gradient in the FCI is by a so-called *pressure drop reduction factor* of 16 times smaller than it would be in the pipe without the FCI. However, 3D MHD phenomena occurring at the entrance and exit cause an additional pressure drop Δp_{3D}, which can be determined by extrapolating the fully developed solutions towards $x = 0$. This results in

$$\Delta p_{3D} = 0.07 \ . \tag{5.13}$$

Although such additional losses seem rather low in comparison to bare MHD channel flow, one must keep in mind that Δp_{3D} corresponds to a pressure drop in an FCI over more than 14 characteristic lengths

$$l_{3D} = \frac{\Delta p_{3D}}{\partial_x p_{2D,FCI}} = 14 \ . \tag{5.14}$$

In other words, an efficient design of the FCI should consider lengths much longer than l_{3D} in order to overcome its entrance-induced losses. Similar observations apply to FCI exits and conjunctions between FCIs. The latter is investigated in more detail in appendix A.

5.4 Magnetodynamic phenomena

Under 3D MHD developing flow, Lorentz force and velocity behave apparently decoupled from each other with respect to their dynamic relations, as shown throughout this study. Peaks in velocity occur at the sides although flow opposing Lorentz forces are highest and, likewise, low-velocity regions appear in the center where braking Lorentz forces are weakest. The reason is an overwhelming magnetostatic momentum balance between pressure gradient and Lorentz force. This leaves only a reduced momentum balance between inertia and viscous forces as well as a residual magnetodynamic force. The latter

becomes relevant in 3D MHD developing regions, where it redistributes the fluid flow. Accordingly, the magnetodynamic force introduced in equation 4.16 serves as an appropriate indicator to reveal the impacts of 3D MHD effects on the velocity distribution. Moreover, a deeper analysis of the magnetodynamic momentum profile reveals a good correlation with characteristic aspects of velocity in 3D MHD developing regions, such as local extrema and internal shear layers. Results shown within this section refer to an FCI approximation of level 1 at $Ha = 2000$ and $Re = 20000$.

Redistribution of the flow

Figure 5.13 presents contour plots of magnetodynamic force $\mathbf{f}_{\mathrm{md}}$ and velocity for FCI entry flow, including $\mathbf{f}_{\mathrm{md}}$ also as vector representation.

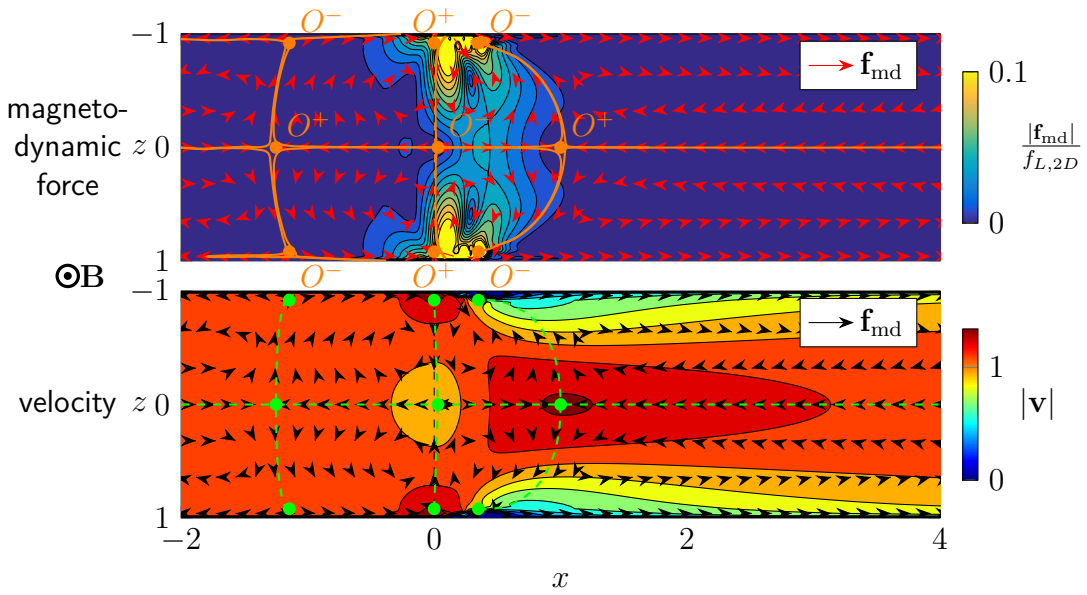

Figure 5.13: Contours of magnetodynamic force (top) and velocity (bottom) concerning FCI entry flow at $Ha = 2000$ and $Re = 20000$. $\mathbf{f}_{\mathrm{md}}$ is scaled by the Lorentz force $f_{L,2D}$ for fully developed pipe flow. While the color scale for $\mathbf{f}_{\mathrm{md}}/f_{L,2D}$ is limited to 0.1 for better visibility of structures in the core, highest magnitudes in vary narrrow regions may reach values up to 4. Orange solid lines and green dashed lines indicate so-called separation lines (Tobak & Peake, 1982), which enclose characteristic zones of $\mathbf{f}_{\mathrm{md}}$.

Relevant magnitudes of $\mathbf{f}_{\mathrm{md}}$ merely occur in regions of 3D MHD flow redistribution. While it remains across almost the entire domain below 10% of the Lorentz force $f_{L,2D}$ of fully developed pipe flow, across narrow, unstable side domains near the FCI entry it exceeds the displayed colorbar limit up to 4 times of $f_{L,2D}$. Especially close to the FCI entry $x = 0$, the orientation of the magnetodynamic force varies considerably, as shown by vector representations.

Orange lines in figure 5.13 (top) show so-called separation lines (Tobak & Peake, 1982) of the vector field $\mathbf{f}_{\mathrm{md}}$. They subdivide the magnetodynamic force distribution into eight cells (four for $z \lessgtr 0$, respectively), where each contains a rotational center of $\mathbf{f}_{\mathrm{md}}$. Adjacent cells exhibit an opposite sense of rotation. The vertices of those cells show nine locations, where lines of forces separate and $\mathbf{f}_{\mathrm{md}}$ becomes undetermined. Those are critical points of the magnetodynamic force distribution in the symmetry plane $y = 0$, labeled $O^{\pm}$. More precisely, they are saddle points involving either axially converging and transversally diverging behavior or vice versa. The former, marked by superscript $^{+}$, indicate axially converging acceleration force and therefore coincide with local velocity maxima, as shown by the velocity contour plot in figure 5.13 (bottom). The flow is first accelerated to the highest speed at O^{+} and retarded beyond that point. The other critical points, marked by the superscript $^{-}$, indicate axially diverging fluid acceleration and therefore reflect local velocity minima. Upstream located velocity extrema for $x < 0$ of bare pipe flow are comparatively small and are therefore not visible in the plot by the discrete velocity contour lines.

Far away from the FCI entry, $\mathbf{f}_{\mathrm{md}}$ is negligibly small. The developing FCI flow in the downstream direction $x > 1$ indicates that the evolving velocity distribution has not yet reached fully developed conditions within the axial region displayed in the figure. This agrees with former observations of development lengths in the FCI that extend over several characteristic lengths.

Internal shear layers

It is well known that for applications with very strong magnetic fields, internal layers may spread along magnetic field lines across the entire fluid domain. These layers typically emerge from singularities in wall properties such as sharp corners (Hunt & Leibovich, 1967), sudden change of wall conductance (Kolesnikov & Tsinober, 1972), or when the flow passes around obstacles (Ludford, 1960). The abrupt change in wall conductance when pipe flow enters an FCI constitutes such a case in which a so-called Ludford layer forms transverse to the main flow direction across the FCI entrance cross-section. The thickness of internal Ludford layers typically scales as

$$\delta_L \sim Ha^{-\frac{1}{2}} \quad \text{or} \quad \delta_L \sim N^{-\frac{1}{3}} \tag{5.15}$$

in the electromagnetic-viscous or electromagnetic-inertial regime, i.e., when $N \gg Ha^{3/2}$ or $N \ll Ha^{3/2}$, respectively. For the parameters used in the present study, $Ha = 2000$, $Re = 20000$, the latter definition applies.

Figure 5.14 shows contours of the transversal velocity component v_z for FCI entry flow.

Results are shown within a horizontal plane at $y = 0$ (top) and a vertical plane $z = -0.5$ (bottom), as indicated by the purple dashed lines in the sketch and plots. As highlighted by color for negative (blue) and positive (red) directed transverse flow, these regions

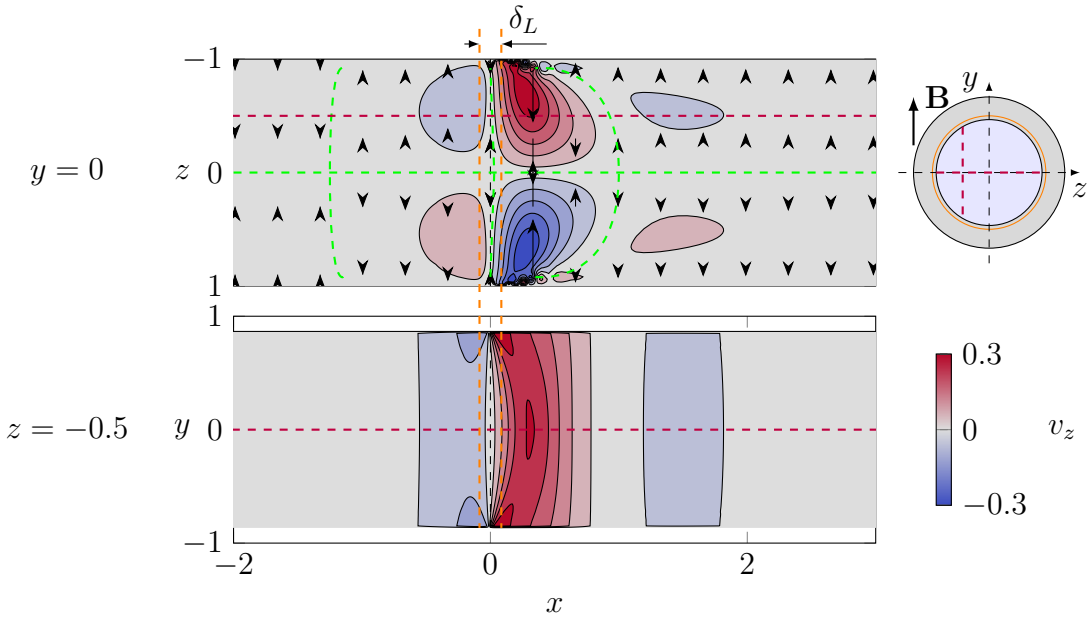

Figure 5.14: Contours and vector representations of the transverse velocity component v_z for FCI entry flow at $Ha = 2000$ and $Re = 20000$, displayed on the horizontal symmetry plane $y = 0$ (top) and on a vertical plane $z = -0.5$ (bottom) as shown by purple dashed lines. Orange dashed lines mark a Ludford layer of thickness δ_L. Green dashed lines illustrate the separation lines of $\mathbf{f}_{\mathrm{md}}$.

fundamentally comply with the characteristic cells defined by the separation lines of $\mathbf{f}_{\mathrm{md}}$, shown as green dashed lines. While far upstream and downstream, the transverse flow gradually evolves over relatively long distances, the figure reveals rapid changes within a narrow region near $x = 0$, indicating the presence of a transverse Ludford layer. For comparison, a layer of thickness $\delta_L = N^{-1/3}$ has been added to the figure shown by dashed orange lines. The latter quantity should be considered only as an order of magnitude estimate, and a comparison with present simulations shows that the real layer is a bit thicker. This observation is supported by analytical solutions for other types of Ludford layers where the transition across the layers may even take 4-5 times the value of δ_L (Hunt & Leibovich, 1967, figure 3).

The distribution of v_z in a plane $z = -0.5$ is shown in figure 5.14 (bottom). It can be seen that the velocity field is highly correlated along magnetic field lines, which is expected for a major balance between pressure force and Lorentz force. The curvature in the streamwise direction of some isolines shows deviations from the pure Q2D behavior, which are caused preferentially by inertia contributions near the FCI entrance. Similar deformations of *banana*-type patterns have been observed in unstable side layers of rectangular duct flow (Mück et al., 2000), and their origin is related to residual weak inertia effects (Pothérat et al., 2000). The fact that curvatures of isolines vanish with increasing interaction parameter, i.e., by increasing the Hartmann number for example to $Ha = 5000$ while keeping Re fixed (not shown here), is a clear indication that inertia effects become negligible for stronger

magnetic fields.

Further details on magnetodynamic phenomena at FCI conjuncations can be found in section appendix A.

Throughout this work, the magnetodynamic force has proven to be a reasonable indicator for the coupling between electromagnetic momentum and velocity. In particular, for 3D MHD flows, results show that critical points of $\mathbf{f}_{\mathrm{md}}$ coincide with local velocity extrema, and separation lines of $\mathbf{f}_{\mathrm{md}}$ and velocity almost coincide. This might be useful for future analyses of MHD flows in more complex blanket geometries.

5.5 Advanced FCI models

So far, results for FCI flow have been discussed exclusively assuming the level 1 approximation model with a constant inner radius. The present section shows results from the higher approximation levels 2 and 3 that consider geometric details of the FCI as introduced in figure 5.2 and discusses their impact on magnetohydrodynamic effects occurring at FCI entries. Level 3 is closest to the application and considers a fluid gap between pipe wall and FCI, which enables an elaborate analysis of flow in the gap and quantification of mechanical loads on the FCI.

Impact of FCI model approximations

In order to show the impact of FCI approximation levels on the MHD flow, figure 5.15 presents the axial velocity and pressure distributions along the duct center of FCI entry flow in the upper and lower plot, respectively, for the three approximation levels. Computations for all three levels show qualitatively comparable velocity v_x along the pipe axis with only slight differences inside the FCI $x > 0$. Strong 3D MHD effects first brake and then for $x > 0$ accelerate the core flow, followed by a slow convergence to the final fully developed state over several characteristic lengths. The data reflects the formerly observed rapid change in velocity profiles.

Concerning developed FCI flow far downstream $x \gg 0$, the level 1 model exhibits an increase of center velocity by 3%. This is due to the low FCI wall conductance, which increases the impact of boundary layer currents and results in a slight convex curvature of the velocity profile inside the FCI, as exemplarily shown for positions $x = 4$ and $x = 10$ in figures 5.6 and 5.7. For approximation level 2, the bare pipe has a larger inlet radius R_i. The latter is sharply reduced to the FCI radius R_{FCI} at $x = -0.1$, which affects the fluid flow in the form of a sudden contraction. As imposed by mass conservation, the mean FCI velocity

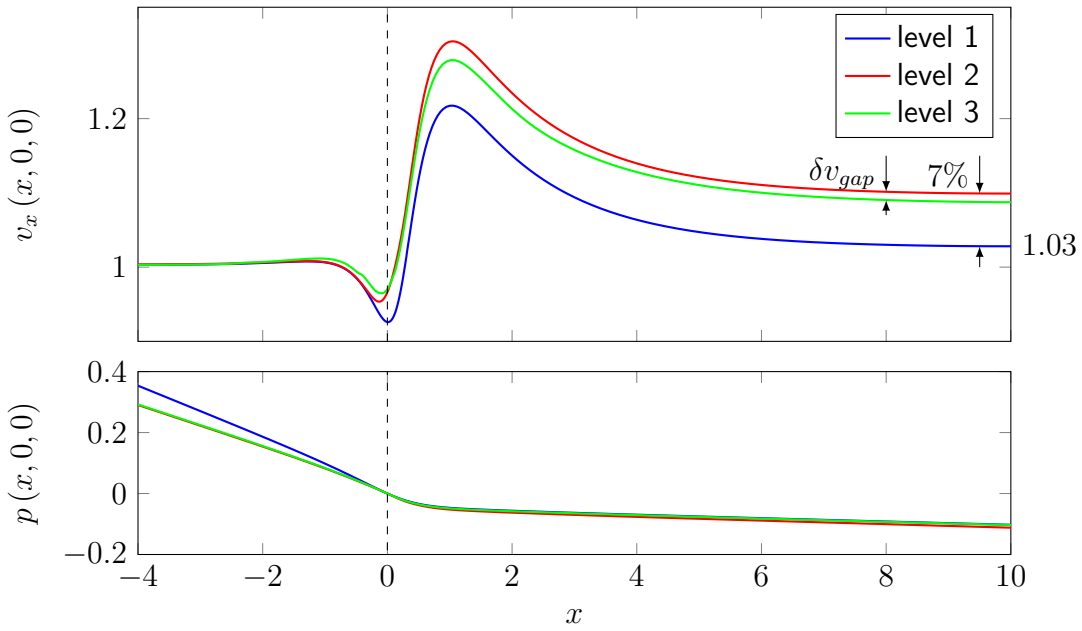

Figure 5.15: Nondimensional axial velocity and pressure for FCI entry flow at $Ha = 2000$ and $Re = 20000$, for different approximation levels. The pressure reference is set such that $p(x = 0) = 0$.

therefore rises according to the channel cross-section ratio

$$\frac{R_i^2}{R_{FCI}^2} = 1.07 \ , \tag{5.16}$$

which explains the 7% higher velocity of fully developed FCI flow compared with results from simplest level 1. The model of approximation level 3, in addition, considers the gap flow between FCI and duct wall. This enables a marginal portion of the fluid to bypass the FCI through the wall/FCI gap, which slightly reduces the mean velocity inside the FCI in comparison with level 2 by approximately

$$\delta v_{gap} \approx 1\% \ . \tag{5.17}$$

The pressure distribution appears rather unaffected by FCI approximation levels, as shown in the bottom plot, where the value of pressure reference has been chosen as $p(x = 0) = 0$. The pressure gradients inside the FCI for $x > 0$ show a good agreement for all considered approximation levels. Upstream, on the other hand, the thicker pipe wall of the level 1 poses a higher wall conductance, which leads to stronger currents and therefore to higher MHD pressure drops in agreement with asymptotic theory (Miyazaki et al., 1983).

Table 5.4 presents the 3D MHD pressure drop obtained by different FCI approximation levels for several simulated cases. Values of Δp_{3D} apparently increase with decreasing N, which suggests a slight impact of inertia on 3D MHD pressure loss. Since both N and Ha are large, inertia and viscous effects are of minor importance because the physics

is governed by a balance between pressure and electromagnetic forces so that Δp_{3D} is practically independent of N and Ha. In general, it would be possible to distinguish the viscous and inertial contribution of Δp_{3D}, as, e.g., described by Stieglitz et al. (1996) for the case of right-angle bends. However, it is out of the scope of the present work to determine these tiny fractions for the considered applications.

			FCI inlet			FCI conjunction	
	N	Ha	level 1	level 2	level 3	level 1	level 2
case 1	200	2000	0.0694	0.0742	0.0728	0.167	0.166
case 2	5000	5000	0.0676	0.0722	0.0694		
case 3	2500	5000	0.0682	0.0723	0.0698		

Table 5.4: 3D MHD pressure drop Δp_{3D} for Ha and N, as obtained by different approximation levels for flows entering an FCI and at the conjunction between two FCIs (see appendix A).

The most accurate model, level 3, foresees fluid flow and electric currents in the gap between FCI and pipe wall. Hence, only the level 3 model is capable of taking into account such effects, where complex 3D currents recover a part of the 3D MHD pressure drop by closing over the FCI/wall gap. However, it turns out that differences of Δp_{3D} among approximation models are fairly small, and thus the simplest level 1 approach is already able to determine pressure drop with sufficient accuracy. The model used in level 2 does not lead to a better description compared with level 1.

In summary, all approximation levels describe the overall flow and 3D MHD pressure drop with sufficient accuracy. Moreover, the geometric contraction considered by higher-order models has little impact on the formation of internal shear layers and spanwise velocity components. From an engineering point of view, it is therefore justified to omit the flow in the FCI/wall gap as well as the small pipe contraction upon FCI entry while focusing on MHD effects in the core flow in full blanket simulations as, e.g., in Klüber et al. (2019). On the other hand, when the interaction between the fluid in boundary layers, FCI, and wall domain, is of interest, significant localized discrepancies may arise depending on the FCI approximation level.

For different approximation levels, figure 5.16 presents the axial velocity component v_x within the plane $y = 0$ close to the side region near the FCI entry. Towards the core $z < 0.8$, all levels exhibit the same typical 3D MHD behavior, as shown by color distributions and black velocity streamlines. As described above, for all approximation levels, the velocity transforms from a uniform profile to a concave and then convex curvature involving a side maximum velocity close to $x = 0$ with a subsequent low-speed zone. However, the impact of the approximation level becomes apparent in direct boundary vicinity, where v_x varies most strongly among approximation levels. In this context, levels 1 and 2 differ marginally, as the latter shows slightly stronger side jets near $x = -0.1$ due to the fluid displacement at the sudden diameter contraction. Apart from that, both solutions show reversed boundary flow, highlighted in pink, upon FCI entry. Unstable Q2D patterns detach from the sides,

move towards the core, and disappear. In fact, the level 2 approximation, involving the sudden diameter contraction, provides no relevant impact on both core and boundary flow, in general, compared to results from level 1. This favors a more cost-effective level 1 model in place of a more elaborate level 2 approximation. The level 3 approach, on the other hand, exhibits neither transient effects nor backflow inside the FCI. Instead, a reversed flow in the gap between the pipe wall and FCI emerges from downstream (close to $x = 1.5$). This reversed flow leaves the gap in a jet-like manner and forms with the incoming flow a thin and stationary recirculation loop in front of the FCI. Inside the FCI, this jet orients downstream parallel to the wall, penetrates the low-velocity zone, and forms there a thin internal layer of high velocity.

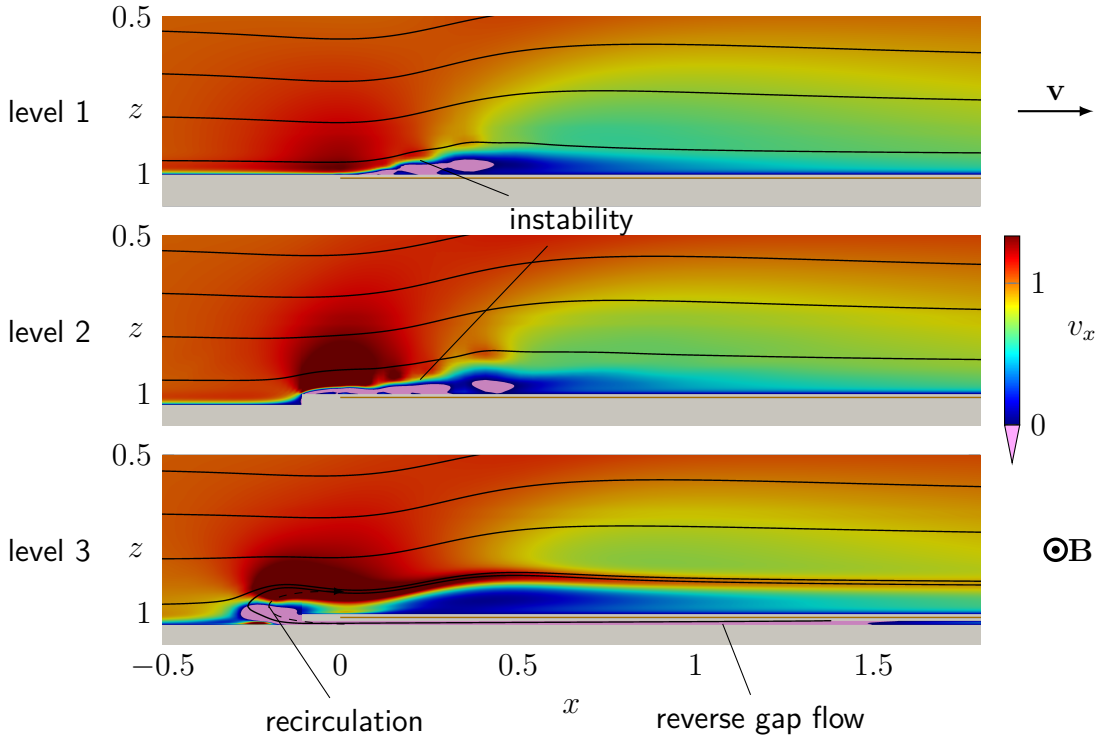

Figure 5.16: MHD flow near the entrance of an FCI for $Ha = 2000$ and $N = 200$. Distribution of axial velocity component v_x at $y = 0$ show the interaction between boundary fluid, FCI and pipe wall depending on the FCI approximation level. Pink illustrated areas highlight zones of reversed flow and light-gray ones the solid domain. The orange straight line indicates the insulation layer.

The fundamentally different boundary interaction of the level 3 model represents an exceptional case. First, the level 3 model shows no sign of transient behavior. The gap flow between FCI and the well-conducting pipe wall involves a jet of fluid upstream that prevents the core flow from detaching at the step in front of the FCI. Instead, the reversed flow emerging from the gap is redirected in front of the FCI entry region, which results in a stationary U-turn. Moreover, associated inertia pushes the redirected stream slightly towards the pipe center. Both other approximation levels show, in contrast, significantly higher near-wall velocity gradients, which promote instabilities when they detach from the

wall. The higher wall distance of the side jet in the level 3 approach, however, prevents such destabilizing boundary interaction. Instead of dissipating kinetic energy in side layer instabilities or dispersing into the core flow, the jet forms a high-velocity stream oriented parallel along the inner side of the FCI, reaching far downstream where it gradually dissipates.

Although the FCI approximation level has no essential impact on the overall flow, quite interesting phenomena may arise near boundaries that are revealed exclusively by simulations with the most detailed model in level 3. The correct description of flow in the gap between FCI and wall is required, such as gradients and distribution of velocity, for the prediction of transport of tritium or corrosion products and has to be known when designing FCIs. Further details of gap flow are discussed in the next section.

Annular flow in the FCI/wall gap

In order to visualize the redistribution of boundary fluid within the FCI entry region, velocity streamlines in figure 5.17 illustrate pathways of near-wall fluid elements. Depending on the initial location in the boundary layer, three different types of streamlines unfold as highlighted by color. The problem is symmetric in y and z, and it is therefore exemplarily shown for a quarter of the geometry, for $y, z > 0$. Fluid paths starting close to the side as those marked blue entangle in the static recirculation loop upon FCI entry and enter the FCI directly. Streamlines highlighted in green first enter the gap between FCI and pipe wall. Here, 3D electric current loops wrap around the FCI, as shown in figure 5.3, and Lorentz forces push the gap fluid towards the sides. Hence, the pressure in the side gap region rises to a value at which it deflects the fluid backward as a bundled stream. This stream then exits the gap and forms a stationary recirculation loop in the form of a U-turn before entering the FCI. Inside the FCI, green and blue streamlines come close to each other and constitute a downstream jet of high intensity (see also figure 5.16). Only a small fraction of incoming boundary flow, represented by red streamlines, enters the gap and passes downstream along the gap domain. The amount of gap flow that originates from top and bottom positions in the pipe eventually distributes around the insert to approach fully developed conditions far downstream. To the author's knowledge, the only existing reference describing similar behavior concerns a case involving rectangular duct flow, shown by Morley et al. (2008b, figure 4), but the underlying physics remains so far unaddressed.

As portrayed by streamline patterns, the flow separates between the green and red streamlines within the FCI/wall gap region. In this context, the study of characteristic velocity contours helps to gather further knowledge about flow topological features (Perry & Chong, 1987). Since the gap is extremely thin, radial velocity components v_r may be neglected. Consequently, the gap flow becomes two-dimensional involving velocity components only in the axial v_x and circumferential v_α direction. The purple line indicates the characteristic contour where the axial velocity component vanishes, $v_x = 0$. This line encloses the region of backflow. The most downstream position of reversed flow forms a saddle point close

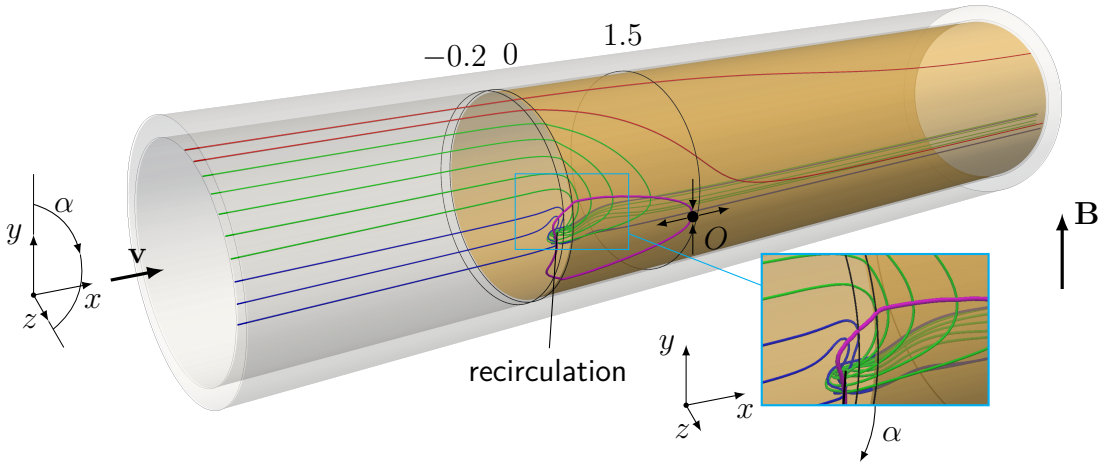

Figure 5.17: Redistribution of boundary fluid upon FCI entry depending on its initial upstream location as shown by different colors. Blue and green streamlines enter the FCI, while red ones pass through the annular gap. The purple line represents the contour $v_x = 0$, which encloses the region of back flow. Black circumferential lines at $x = -0.2,0,1.5$ mark axial locations for which velocity profiles are shown in figure 5.18. The transparent orange cylinder indicates the FCI insulation. $Ha = 2000$ and $N = 200$.

to $x = 1.5$ marked as O into which fluid converges from the line separating green and red streamlines. From the same point, fluid diverges upstream and downstream in the horizontal plane $y = 0$.

In order to illustrate the stages of evolving flow in the gap, figure 5.18 presents corresponding axial velocity profiles at several axial positions. The velocity profile of flow entering the FCI at $x = -0.2$ exhibits four positive jets, two at each side. They are separated from each other by the reverse stream exiting the gap, which forms the stationary U-turn. The inner FCI jets contain fluid from the upstream boundary, as portrayed by blue and green streamlines in figure 5.17. Further downstream, where the insulation starts at $x = 0$, the velocity in the gap is almost uniform and positive in regions where currents close, see figure 5.3, and thus evoke downstream directed Lorentz forces. Side gap regions, on the other hand, show an enormous reversed flow, which is present within the zone marked by the purple line in figure 5.17. The strong backward jet consists of the fluid collected from the green streamlines up to the downstream position of the saddle point close to $x = 1.5$. The remaining downstream motion originates from red streamlines and forms a quite uniform profile at a very low velocity near $x \gtrsim 1.5$. From there on, it takes a considerable distance for the gap flow to approach fully established conditions since the fluid redistributes slowly in the circumferential direction. The profile at position $x = 8$ demonstrates the fully developed gap flow, where major motion occurs in the form of high-velocity jets at the sides while the other fluid in the gap is almost stagnant.

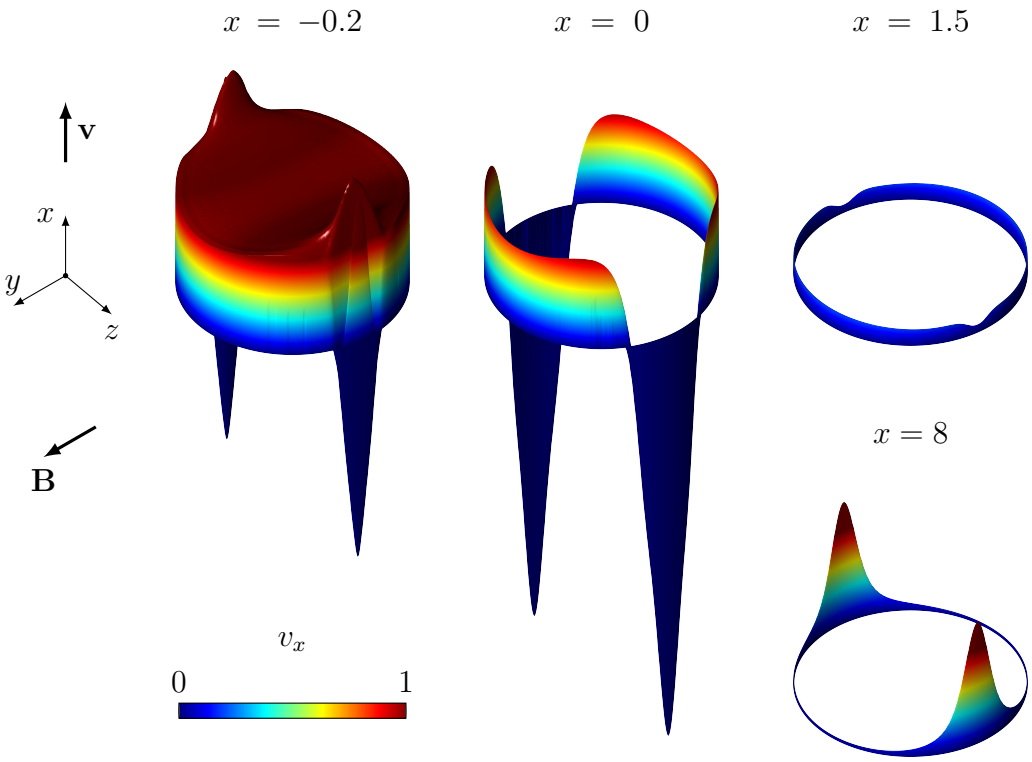

Figure 5.18: Development stages of velocity profiles in front of the FCI at $x = -0.2$ and in the annular gap at specific downstream locations $x = 0, 1.5, 8$, marked by black circles in figure 5.17. According to the color scale, dark blue or red marks velocities below 0 or above 1, respectively. $Ha = 2000$ and $N = 200$.

In order to explain the unusual velocity profiles observed in figure 5.18 for fully developed gap flow, it is useful to recall a simple asymptotic description of such flow in insulating channels of arbitrary geometry (Chang & Lundgren, 1961). Under these conditions, the core velocity is proportional to the local duct height measured in magnetic field direction

$$u_c \sim Y \ . \tag{5.18}$$

Similar behavior where the core velocity correlates with the duct shape becomes observable for more general cases as well, so that equation 5.18 may serve as a qualitative predictive tool for velocity profiles in general, (see, e.g., (Klüber et al., 2020a)). Figure 5.19 shows the definition of channel height in magnetic field direction 5.19a and its transversal distribution 5.19b for an annulus of gap thickness t_g. Channel height Y and consequently core velocity u_c are low starting from $z = 0$. They rise monotonically towards the sides. A discontinuity occurs at $z = \pm z_d$, where the channel height instantly doubles. It is close to this transverse position, where the highest velocities are observed in a tangent layer before dropping to zero near the sides. While the outlined explanation has been derived for insulating walls (Chang & Lundgren, 1961), similar phenomena can also be observed for channels with

electrically conducting walls. Thus simple geometric arguments support the explanation for the existence of observed side jets. An analytical and numerical analysis by Kumamaru (1984) confirms the existence of strongly pronounced velocity peaks in annular channel geometries.

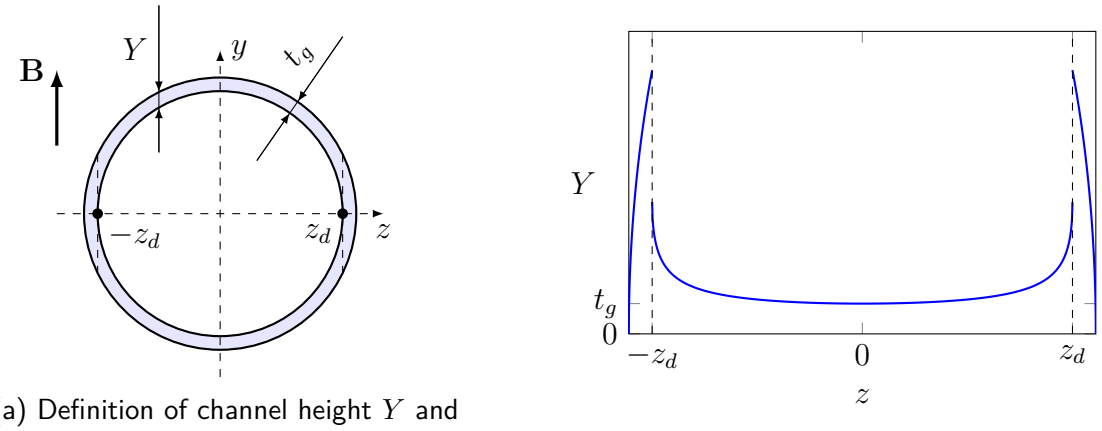

(a) Definition of channel height Y and wall discontinuities at $z = \pm z_d$.

(b) Distribution of channel height Y over z.

Figure 5.19: Qualitative description of channel height Y measured along $\mathbf{B}$. Concerning fully developed annular gap flow, the gap velocity directly correlates with Y.

The present work shows that while the annular gap makes up 2.5 % of the total cross-section, it carries only 1 % of the flow rate. Moreover, as shown in figure 5.18, practically all gap flow is carried by thin jets along the sides, whereas the fluid in the major part of the gap is nearly stagnant. Regions with strongly reduced flow in fusion blankets bare the risk of undesired tritium accumulation when an efficient convective transport is not guaranteed or missing (see e.g. analysis in Candido et al. (2021)).

Moreover, numerical results within the developing region close to the FCI entry exhibit considerable velocity peaks of the reversed gap flow. In fact, their maximum at $Re = 5000$ and $Ha = 5000$ corresponds to around 13 times the mean pipe flow velocity. High liquid metal velocities at high temperature provoke corrosion issues as outlined by Konys et al. (2011). The latter authors find velocity-dependent corrosion rates of up to 150 μm/year for the blanket structural material at breeder temperatures of 550 °C and at a mean velocity of 5 cm/s, which pose a realistic temperature and flow rate occurring in breeding blankets (Smolentsev, 2021, table 1). For an FCI entry flow scenario with only 0.5 mm thick FCI protection layers, the side velocity peaks at FCI entries seem to be corrosion-relevant to blanket-realistic scenarios. Moreover, adding MHD phenomena to the corrosion problem, Bucenieks et al. (2006) find a "considerable intensification" of the corrosion process, including wavelike ridges at the contact surfaces. As a consequence, present results with strong and highly nonuniform flows at FCI entries seem important for fusion applications. In particular, the long-term integrity of the thin protecting sheets of the FCI at the entry should be investigated in future works by analyses coupled with mass transfer.

Besides the thermal and corrosive loads mentioned above, the FCI must also withstand mechanical stress. The following section addresses such loads evoked by pressure differences and FCI-internal Lorentz forces.

Pressure equalization and mechanical FCI stress

One major mechanical load on the FCI arises from the difference between the inner bulk pressure p_i and the outer gap pressure p_o, as shown in figure 5.20. The original FCI patent by Malang (1987) regards this load as potentially critical. According to Malang, such pressure imbalance could over-stress the rigid structure of the ceramic insulator. Hence, that design foresees openings in the FCI as a countermeasure connecting bulk and gap flow to guarantee pressure equalization between those domains. Studies of developed FCI flow for ceramic FCIs with finite conductivity, however, reveal that such pressure equalization openings are ineffective independent of their orientation or dimension (Sutevski et al., 2014). In contrast to the original design, the FCI considered in the present study perfectly decouples the bulk and gap domain. This allows the evaluation of mechanical loads in the absence of pressure equalization measures for both developing and fully developed FCI flow, whose impacts on FCI pressure imbalance can be quite different according to Smolentsev et al. (2006) and Ni et al. (2011).

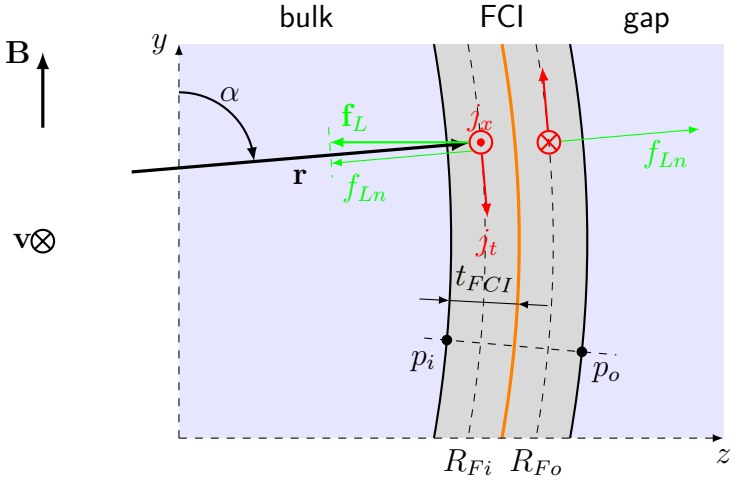

Figure 5.20: Sketch of an FCI segment illustrating surrounding pressures $p_{i,o}$ and FCI internal Lorentz forces f_{Ln}. Inner FCI currents are marked red and internal Lorentz forces green. The orange line represents the FCI internal insulation layer.

The difference between gap and bulk pressure along the FCI shells defines the inward directed mechanical force per surface element of the FCI

$$\Delta p_{FCI} = p_o - p_i \ . \tag{5.19}$$

Figure 5.21 presents Δp_{FCI} for FCI entry flow along the upper cylindrical shell of the FCI

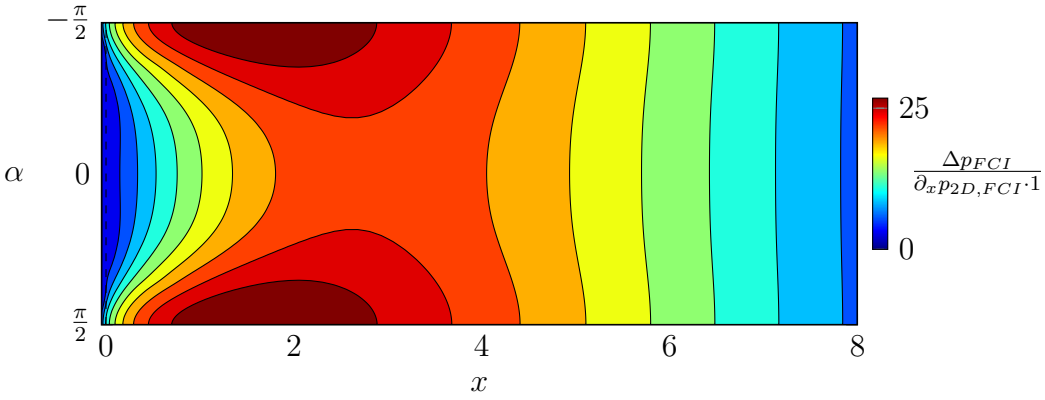

Figure 5.21: Pressure load Δp_{FCI} on the FCI for $Ha = 2000$ and $N = 200$. Values are normalized by the axial pressure gradient of fully developed FCI flow over one characteristic length $\partial_x p_{2D,FCI} \cdot 1$.

without any pressure equalization measures. Results are normalized with internal pressure drop over one characteristic length as defined by equation 5.11. The developing region where the pressure load $\Delta p_{FCI}(x, \alpha)$ depends on x and α extends approximately to $5 \sim 7$ radii from the FCI inlet. Further downstream, bulk and gap flow are fully developed, involving constant and uniform axial pressure gradients in both domains. Consequently, the load becomes uniform along α, and it decreases linearly along x, i.e., $\Delta p_{FCI} \sim -x$, as shown downstream by the constant distance between contour lines. At FCI inlet and outlet, gap and bulk pressure equalize so $\Delta p_{FCI} = 0$.

Around the whole FCI shell, the value range of Δp_{FCI} remains positive. This indicates that the pressure difference exclusively compresses the FCI, which poses the risk of buckling. The highest compression appears at the sides in the vicinity of $x = 2$, where the gap flow separates, and the internal side fluid exhibits a low-velocity zone. Those peaks correspond to approximately 27 times the FCI pressure drop along one unit length. This means the thin FCI shell encounters up to 27 times the load of the internal x-directed bulk stream over one characteristic length. A comparison of dimensional values provides further insights. Table 5.5 lists dimensional and normalized maximum pressure loads for three investigated cases.

	Re	Ha	$\max \frac{\Delta p_{FCI}}{\partial_x p_{2D,FCI} \cdot 1}$	$\max \Delta p^*_{FCI}$ [bar]	$v_{j,max}$
case 1	20000	2000	27	0.031	5.6
case 2	5000	5000	15	0.027	12.7
case 3	10000	5000	16	0.056	10.7

Table 5.5: Normalized and dimensional maximum FCI loads Δp_{FCI} and jet nondimensional velocities $v_{j,max}$ for three simulated cases.

Distributions of Δp_{FCI} for cases 2 and 3 are qualitatively similar to case 1 presented in figure 5.21, but they differ in magnitude according to values in table 5.4. The maximum

mechanical pressure difference observed for case 3 close to $x = 2$ refers to a load of 0.056 bar. Values of cases 2 and 3 reflect the relation that Δp^*_{FCI} is almost proportional to $u_0 B_0^2$ as suggested by the scaling, whereas for case 1, the load appears around 1.79 times higher than expected. In this context, it is interesting to note that the maximum jet velocity $v_{j,max}$ of reversed gap flow strongly differs from those cases. Magnitudes around 12 are found for cases 2 and 3 at $Ha = 5000$, while jet velocity for $Ha = 2000$ reaches only half of this value. The small number of only three simulated cases does not allow drawing definite conclusions about the origin of the observed effects, in particular the unexpected magnitude of normalized pressure load and jet velocity. However, since the interaction parameter for case 1 is 12.5 times smaller than for case 3 and 25 times smaller than for case 2, the major difference seems to be inertia effects related to the jets in the gap.

According to personal communications with the authors Koehly & Bühler (2017), who proposed the present type of FCI for circular pipes, a critical inward-directed load to the FCI would be in the order of one bar. This means that, in any case, those pressure loads do not pose a serious risk to the FCI's structural integrity. Consequently, under the considered parameters shown in table 5.5, the present FCI design does not need pressure equalization measures.

Besides outer mechanical loads, electric currents inside the protective FCI layers evoke internal Lorentz forces, according to figure 5.20. Those currents, portrayed red, interact with the magnetic field. This leads to Lorentz forces inside the FCI sheets, whose radially directed component

$$f_{Ln} = \frac{\mathbf{r}}{|\mathbf{r}|} \cdot (\mathbf{j} \times \mathbf{B}) \tag{5.20}$$

might deform the FCI in the radial direction. Since Lorentz forces act orthogonally to the magnetic field direction according to equation 5.20, only axial currents j_x may lead to Lorentz forces with radial components when $\mathbf{B} = \mathbf{e}_y$. Since the conductive FCI sheets are extremely thin, radial FCI current flow is negligible, and j_x remains constant along $\mathbf{r}$. The cumulative radial load ς due to internal currents across either inner or outer FCI layer then becomes

$$\varsigma_{i,o} = \int_{t_{FCI}} f_{Ln}\left(x, R_{Fi,o}, \alpha\right) \, \mathrm{d}n = f_{Ln}\left(x, R_{Fi,o}, \alpha\right) \, t_{FCI} \ , \tag{5.21}$$

where $R_{Fi,o}$ is the mean inner and outer FCI radius according to figure 5.20. As equation 5.20 suggests, radial components of electromagnetic forces become zero at the top and bottom of the pipe. Moreover, since the axially directed currents j_x exclusively occur in the developing flow, ς is restricted close to the FCI inlet or outlet region. Figure 5.22 confirms this behavior in both FCI sheets, presenting $\varsigma_{i,o}$ as contours in the upper and lower plots, respectively.

As the color scale of $\varsigma_{i,o}$ reveals, stresses in the inner FCI sheet generally point inward (negative ς), and loads in the outer layer are directed outwards (positive ς). In this way, they exert internal forces in the FCI that tend to split it at the insulation layer. This effect is strongest at $x = 0$, where currents bundle and flow around the insulation in order to

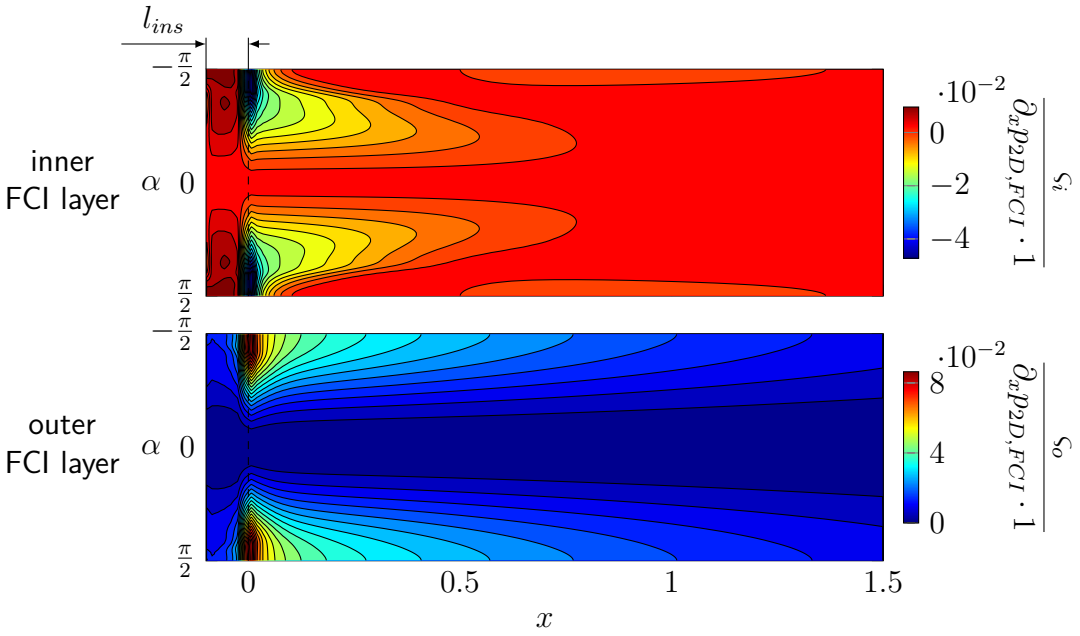

Figure 5.22: Electromagnetic loads in the FCI $\varsigma_{i,o}$ of the inner (top) and outer (bottom) FCI layer including the conductive FCI ledge for $-l_{ins} < x < 0$. Values are normalized by the axial pressure gradient of fully developed FCI flow over one characteristic length $\partial_x p_{2D,FCI} \cdot 1$. $Ha = 2000$ and $N = 200$.

close over the well-conducting wall. Those forces quickly fade upstream for $-0.1 < x < 0$, where inner and outer FCI sheets are electrically connected in the form of the welded ledge, as well as downstream after one characteristic length. In addition, the inner sheet shows around $x = 1$ moderate side load regions due to increased axial current flow j_x.

The value range indicates that electromagnetic loads are 2-3 orders of magnitude smaller than pressure loads displayed in figure 5.21. Hence, neither internal Lorentz forces nor pressure loads compromise the FCI's structural integrity under the investigated parameter range.

In summary, the comparison of higher-order approximation models demonstrates that already the level 1 approach robustly represents relevant MHD effects and thus is sufficient for the investigation of fusion applications from an engineering point of view. Geometric model improvements based on level 2 with increased computational difficulty, on the other hand, do not noteworthy change results since the small diameter contraction has little impact. However, taking into account the thin gap flow between the pipe wall and FCI in the form of the level 3 model provides an entirely different boundary interaction in the developing region with an impact on 3D MHD phenomena. Significant redistribution of fluid occurs within the developing gap region, accompanied by high reverse jets and highly nonuniform velocity profiles. Those might considerably affect tritium transport as well as heat transfer in breeding blankets and should therefore be investigated in more detail.

Impacts of Ha and N on 3D MHD pressure losses appear negligibly small, which supports the assumption that the developing flow is almost inviscid and inertialess. Some residual impact of inertia on pressure loads and velocity peaks may persist for the reversed jet flow in the gap, at least for the lowest interaction parameter considered in the present study. Finally, computations show that the FCI can withstand electromagnetic and pressure loads under the investigated parameter spectrum without any countermeasures such as pressure equalization holes or slots.

5.6 Comparison with experiments

An FCI as the one described above has been manufactured at KIT (Koehly & Bühler, 2017) and installed in a thick-walled pipe in the liquid metal loop of the MEKKA facility. Conducted experiments consider FCI entry flow (Bühler et al., 2020a) and flow at conjunctions between two consecutive FCIs (Bühler et al., 2019). Experimental results are available for internal bulk pressure as well as for electric potential along the outer pipe surface. This section compares experimental data with numerical simulations. The good agreement thus confirms the observations of strong 3D phenomena as well as the applicability of underlying numerical methods presented and discussed above.

Bulk pressure

The experiments provide results of pressure measurements p_o that have been taken at a number of pressure taps along the outer surface of the test section. One such pressure tap is exemplarily sketched in figure 5.23. In order to detect the pressure p_i of the FCI-internal bulk flow, congruent holes are foreseen through the FCI and wall. Since the pressure is constant along magnetic field lines for $Ha >> 1$, bulk and tap pressure coincide along y

$$p_i = p_o \ . \tag{5.22}$$

The orientation of pressure taps aligned with the uniform magnetic field requires no further correction by consideration of wall currents since Lorentz forces in the taps have an exclusively orthogonal orientation to $\mathbf{B}$, as mentioned by Stieglitz (1994, p. 40), and therefore they do not affect pressure readings. The bores across the FCIs locally disrupt the insulation layer, which, in general, could lead to local leakage currents. However, since pressure taps and bores are located at the pipe's symmetry plane at $z = 0$, where $\phi = 0$, leakage currents from the bulk into the gap and well-conducting pipe wall are minimized.

Figure 5.24 presents the axial pressure distributions of FCI entry flow obtained using the level 3 FCI approximation model. Results highlight the fact that for $x > 0$, the pressure in the gap is nonuniform around the periphery and very different from the one on the pipe

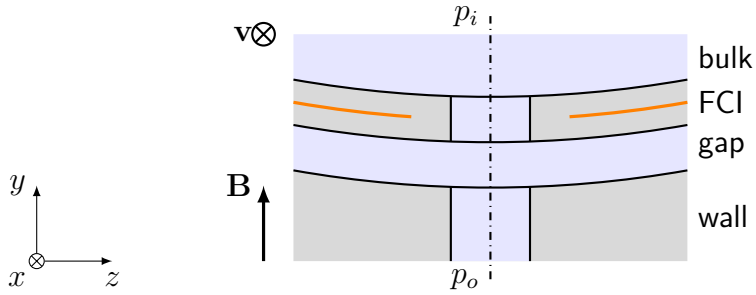

Figure 5.23: Sketch showing orientation of pressure taps and bores in the FCIs for measurement of bulk pressure p_i in the experiment. Orange lines indicate the internal FCI insulation layer. Those bores and insulation openings do not exist in the computational model.

axis. It has to be mentioned that the numerical model misses the pressure equalization holes and thus fully decouples the bulk from the gap flow. The solid red line shows computational results of side pressure distribution in the upstream pipe and downstream inside the gap. In the developing region, the side pressure sharply recovers and drives the reversed flow in a region that extends up to the critical point near $x = 1.5$. For $x > 1.5$, the side jets invert and begin to evolve downstream. A smaller but still significant pressure recovery is observed along the top (or bottom) position with a maximum value close to $x = 3$, as shown by the solid green line. The latter is caused by downstream oriented Lorentz forces in the gap, which locally increase the pressure. The gap flow becomes fully developed around $x = 5$, where the red and green lines converge and start to descend linearly. This fully developed axial pressure gradient in the gap depends on the FCI length, which in the simulation ends around $x = 10$, where the imposed boundary condition equalizes bulk and gap pressure. This is a shortcoming of the present simulation, and one might argue that further improvement of the model could be achieved by simulations of longer FCIs and taking into account either modified exit conditions or by simulations of the full length of the FCI as in the experiment. However, it is expected that 3D phenomena of interest in the present work near $x = 0$ are not very sensitive to the total length of the computational domain and the length of the FCI. Moreover, the condition of equal pressure in the gap and bulk flow and the vanishing axial derivatives of other variables at $x = 10$ represents a symmetry condition for MHD flow in an FCI that has a total length of 20. The latter dimension is close to the FCI used in the experiment.

The pressure distribution along the axis is shown as a blue line. In the bare pipe, a strong pressure drop is present, while in the FCI, the pressure gradient is strongly reduced. Numerical simulations are compared with experimental data (blue symbols), which show in agreement with numerical simulations the same strong pressure gradient reduction of bulk flow upon FCI entry for $x > 0$. The good agreement with high correlation values (see appendix B) confirms both the accuracy of present numerical simulations and the assumption of the applied measuring procedure in the experiment, i.e., that the local disruption of insulation by pressure holes in the FCI at vertical position minimizes current leakage and

that the pressure is constant along magnetic field lines. In fact, values perfectly correspond to computations of an ideal FCI involving fully enclosed protective and insulation layers.

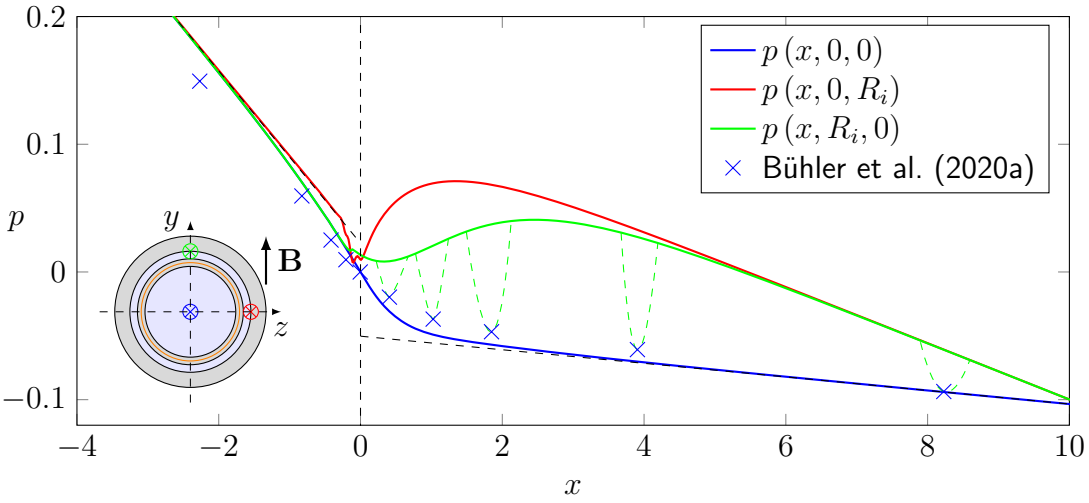

Figure 5.24: Local pressure variation for FCI inlet flow obtained with the level 3 approximation model (solid lines) and compared with experimental data (symbols) for $Ha = 2000$ and $Re = 20000$. Green dashed lines qualitatively indicate local pressure equalizing through vertical FCI holes according to figure 5.23. The correlation between experimental measurements and computations results in $CCC = 0.9857$ for $p\,(x, 0, 0)$ (see appendix B).

Green dashed lines qualitatively sketch the possible impact of FCI holes on gap pressure if the FCI included equalization holes for bulk pressure measurement, as shown in figure 5.23. They illustrate how vertical equalization holes could affect the gap pressure in order to balance differences between the bulk and gap domain. As found by Ni et al. (2011), such balancing occurs only in the direct vicinity of pressure taps and affects rather the pressure in the gap than the one inside the bulk of the FCI. Accordingly, the gap pressure at a sufficient distance from the holes would remain unaffected, as predicted by the present numerical simulations. For this reason, pressure holes at top or bottom positions in FCIs are suitable means for experimental determination of FCI bulk pressure. As countermeasures to achieve pressure equalization in the whole FCI-wall gap, they are rather ineffective.

Regarding future works, improved models could consider the full FCI length and include 3D MHD phenomena related to the FCI outlet as well, in order to address more realistic gap flow. In the context of gap pressure, this would result in developing regions at both ends, which are connected by a uniform pressure gradient along the developed gap flow.

Electric potential on the wall

The experiments performed in the MEKKA facility (Bühler et al., 2019, 2020a) provide

in addition electric potential data on the outer surface of the pipe along both sides at probe locations shown in the sketch of figure 5.25. Data plots compare computations and experimental measurements in terms of the spanwise potential difference

$$\Delta\phi = \phi_2 - \phi_1 \tag{5.23}$$

for FCI inlet flow at $Ha = 2000$ and $Re = 20000$. Far upstream, before entering the FCI, the MHD flow in the bare pipe is fully developed, and $\Delta\phi$ remains constant in axial direction. The transversal potential difference of bare pipe flow ($x < 0$) is in very good agreement with the outer wall potential according to the asymptotic solution by Miyazaki et al. (1983)

$$\phi_{2D,w} = \frac{2R_oR_i}{R_o^2 + R_i^2}\frac{1}{1+c} = 0.92\ , \tag{5.24}$$

shown as a horizontal black dashed line. Approaching the FCI entry at $x = 0$, $\Delta\phi$ starts decaying monotonously. Downstream for $x > 0$, the gap and pipe wall domain are shielded from the flow-induced electric field $\mathbf{v} \times \mathbf{B}$ of the bulk flow since currents cannot cross the insulation. Consequently, the potential difference $\Delta\phi$ on the wall approaches 0 within about five characteristic lengths.

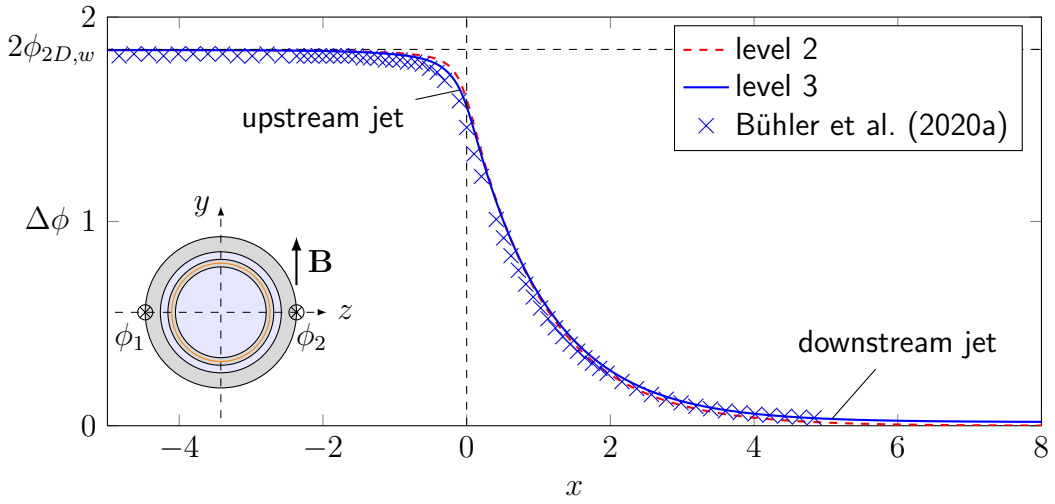

Figure 5.25: Transverse potential difference $\Delta\phi$ for FCI inlet flow at $Ha = 2000$ and $Re = 20000$. Comparison of experimental results (symbols) and computations (solid lines). The correlation between experimental measurements and computational result of level 3 model yield a correlation coefficient $CCC = 0.9985$ (see appendix B).

Computations and experiments reflect in good agreement the downstream decay of the spanwise potential difference. Deviations between the levels 2 and 3 are rather small. On the one hand, this proves the high applicability of coarser FCI approximation models. On the other hand, slight differences demonstrate the impact of the gap stream, which only level 3 takes into account. This means that jets in side-gap regions become measurable in the form of very small residual potential differences $\Delta\phi$ on the outer pipe surface. These

potential differences do not asymptote to zero downstream as suggested by level 2 results, but they approach a small constant value as predicted by the level 3 model. Side gap jets are negative for $x < 1.5$ and positive for $x > 1.5$, also shown in section 5.5. According to Ohm's law $\partial_z \phi \approx v_x$, negative axial velocity weakens and positive axial velocity strengthens the induced electric field in the transverse z-direction. The upstream jet present in level 3 decreases and the downstream jet increases the electric potential on the outer pipe surface compared to level 2. Hence, when the gap flow fully develops for $x > 5$ and high side jets arise, the solid blue line establishes a constant wall potential difference, while level 2 indicates zero potential difference. Experimental potential data is available only up to $x = 5$, where data points show the tendency of forming a small but finite constant downstream potential difference in very good agreement with simulation data of the level 3 model.

Further validation work on 3D MHD phenomena at FCI conjunctions involving experimental measurements are located in appendix A. In total, computational results agree well with experimental measurements from the pipe's surface. This confirms a sufficient quality of both generated models and the numerical approach in order to analyze complex 3D MHD phenomena occurring at FCI entries and at conjunctions.

5.7 Summary

Studies have been performed, addressing 3D MHD phenomena at inlets and between conjunctions of sandwich-type FCIs. The abrupt jump of wall conductance upon entering or exiting the FCI evokes axial potential gradients that drive 3D currents. Those currents preferably short-circuit over the well-conducting wall, leading in the developing region to strong transverse Lorentz forces that redistribute fluid flow and which may in some cases locally destabilize side regions. Such local instabilities, however, have no noticeable impact on the total pressure drop. The study confirms a high efficiency of pressure drop reduction by the investigated FCIs, provided they are long enough to compensate for additional 3D losses at the entrance and exit.

Analyzing the magnetodynamic force for the considered cases of FCI flow reveals the electromagnetic impact on inertial and viscous effects. Critical points of $\mathbf{f}_{\mathrm{md}}$ coincide with local velocity extrema, and separation lines of $\mathbf{f}_{\mathrm{md}}$ align with internal shear layers. The magnetodynamic force, therefore, constitutes an appropriate analytical tool to investigate complex 3D MHD phenomena in fusion-relevant geometries.

Different levels of geometric simplifications have been investigated in order to assess their physical consistency. Core flow phenomena agree well among all investigated FCI approximation models, which capture relevant properties such as pressure drop and flow distribution. The boundary interaction, on the other hand, differs largely when including the gap flow into the FCI model. The thin gap domain exhibits a highly nonuniform velocity distribution involving enormous side jets as well as a large portion of stagnant gap fluid.

According to literature, those strong variations of velocity might seem important in regard of heat and tritium transport and corrosion, in particular of the extremely thin FCI protection layers. Moreover, including the gap region in the numerical model enables subsequent mechanical stress analysis, taking into account pressure loads and FCI-internal Lorentz forces. In this context, results indicate no serious risk to the FCI's structural integrity under the investigated parametric range when no pressure equalization measures are foreseen.

Throughout this study, numerical results perfectly agree with the asymptotic theory, where the flow is fully developed. Moreover, computations reproduce experimental measurements of pressure and electric potential from the pipe surface in regions of strong 3D MHD phenomena. On the one hand, this confirms the assumptions of experimental measurement techniques, where bores in the FCI at vertical positions enable local pressure equalization with the bulk flow and simultaneously minimize current leakage to the well-conducting pipe wall. On the other hand, experimental observations from the pipe surface reflect numerical analysis that, moreover, enables a direct observation and investigation based on fluid-internal data. Where analytical solutions and experimental techniques become too expensive or, in some cases, impossible, the application of computational MHD codes still enables extensive analysis of the most complex MHD phenomena. Therefore, numerical approaches are crucial to fusion engineering and research.

6 Final remarks

6.1 Summary

The present work addresses code development, verification, validation and application for complex three-dimensional liquid metal flow in strong magnetic fields and circular pipes. The obtained knowledge supports ongoing research on liquid metal MHD and, in particular, the conceptual design phase of breeding blankets in fusion engineering. Significant progress is made by extending the capability of the MHD code used at KIT. This has been achieved in the present work by a current density conservative formulation and by introducing advanced discretization schemes for electric potential gradients, which yield robust convergence and accurate results on unstructured grids. The latter point is important for the future usage of the code for the prediction of MHD flows in complex thermally and electrically coupled geometries of liquid metal blankets, where structured grids are difficult to implement.

In the first part, numerical spatial discretization schemes are thoroughly verified against analytical and numerical solutions for fully developed pipe flow. These tests involve the convergence of results with increasing grid refinement for various types of grids for insulating and electrically conducting walls. It is shown that the upgraded code is now, for the first time, capable of simulating MHD flows using unstructured grids even for very strong magnetic fields.

The second part of this work analyzes more complex 3D MHD phenomena in straight, circular pipes under a nonuniform magnetic field, motivated by recent experimental work performed in the MEKKA laboratory, where a liquid metal flow enters a magnet (Bühler et al., 2020b). The incoming hydrodynamic flow is turbulent and adequately resolved in space and time. The time-averaged entrance profile of velocity is validated by comparison with predictions by the well-known logarithmic law of the wall. The reconstruction of the multi-component nonuniform magnetic field is confirmed by comparison with measurements inside and outside the magnets center plane. Computational results for 3D MHD flows are validated by comparison with approximate solutions and experimental data for pressure, electric potential, and velocity derived from electric potential probes (Bühler et al., 2021). The presented validation work shows quite good agreement with the reference data and qualifies the code for applications with 3D MHD flows in more complex geometries.

In a third part, 3D MHD flows are investigated in the vicinity of pressure drop reducing

flow channel inserts (FCIs) to complement the experimental results obtained in the MEKKA laboratory (Bühler et al., 2019, 2020a). Three simplifying computational models of the FCI have been successfully implemented with an increasing degree of geometrical detail and their results have been validated with approximate solutions and experimental data. Numerical methods reveal internal MHD phenomena, which otherwise remained hidden from experimental measuring techniques.

The investigated MHD flows mostly maintain a magnetostatic equilibrium, i.e., the Lorentz force essentially balances the pressure force. The applied numerical approach allows computing the residual fraction of the Lorentz force, which effectively accelerates and brakes the fluid. This fraction of force is therefore introduced in the present work as magnetodynamic force and it serves as analytical tool to reveal relations between velocity and complex 3D MHD phenomena. The magnetodynamic force has been proven beneficial for revealing the electromagnetic impact on shear layers, flow structures, and relevant inertia effects of 3D MHD developing flow. Characteristic contours of the magnetodynamic force coincide with internal shear layers and critical points of this residual force field are found at positions of local velocity extrema.

6.2 Conclusions

The conducted grid studies support development and application of computational MHD codes by assessing different numerical and spatial discretization schemes for fusion relevant conditions. Depending on the wall conductance parameter c and Hartmann number Ha, the following guidelines have been identified for adequate discretization of MHD flows in circular pipes:

- If the wall is better conducting than the Hartmann layer, i.e., $c \gg Ha^{-1}$, electric currents mainly short-circuit over the solid domain. Hence, fluid currents are comparatively large so that all terms in Ohm's law are of the same order of magnitude. The computation of the electric potential gradient is straightforward and requires no further correction or higher-order schemes.

- If, on the other hand, the conductance of the wall becomes smaller than the conductance of the thin boundary layers, i.e. $c \ll Ha^{-1}$, the overall current density is low compared with potential gradients and flow-induced electric field. The numerical approach then requires a robust gradient discretization such as the skew-corrected Green-Gauss or Least-Squares scheme to compute the electric potential gradient with sufficient accuracy.

- In the case of particularly strong magnetic fields $Ha \gg 1$ and curved walls, Hartmann layers become difficult to be resolved by hexahedral prism layers because their thickness changes along the periphery. Boundary layers along curved geometries require

adequate grid resolution in both wall-normal and circumferential direction, where the corresponding lengths scales $\delta_{Ha} \sim Ha^{-1}$ and $\epsilon_{Ha} \sim Ha^{-1/2}$ should be resolved by multiple cells in each direction.

- For strong magnetic fields $Ha \gg 1$, the SHM grid configuration with split boundary cells, shown in figure C.1 in the appendix, combined with the skew-corrected Green-Gauss gradient scheme for the electric potential suffice to adequately discretize fusion relevant MHD phenomena.

Results obtained in the present work indicate that under such arrangements, the computational code is capable of addressing MHD flows at fusion-relevant parameters with low wall conductance, very strong magnetic fields up to $Ha = 50000$, and more realistic blanket geometries including curved boundaries.

Numerical analyses of MHD flows occurring in blanket subsystems with nonuniform magnetic fields and near entrance or exits of FCIs have confirmed the applicability of the improved code for predictions of complex fusion relevant 3D MHD phenomena. Moreover, results provide valuable insights for fundamental MHD research as well as for blanket development to which following major conclusions apply:

- Present numerical results confirm assumptions, typically used for interpretations of experimental data (Bühler et al., 2021), that the electric potential on the wall surface may be used for approximating the fluid-internal core velocity in regions of uniform and nonuniform magnetic fields.

- The obtained 3D MHD pressure drop Δp_{3D} in a nonuniform magnetic field is negligible while its development length may reach 10 characteristic length units.

- 3D MHD flows at entries or conjunctions of FCIs yield additional pressure drop Δp_{3D} that equals 14 and 34 times the pressure drop along one characteristic length of fully developed FCI flow, respectively and thus they are significant. An efficient FCI design must therefore account for the 3D MHD drop at entries and exits.

- Comparisons between different numerical FCI models show that the most basic one, which neglects any geometrical details and which is the least resource consuming, adequately describes relevant 3D MHD phenomena occurring in the core flow. These are axial current flow, strong variations of core velocity, fluid redistribution, and the 3D MHD pressure drop.

- When an annular liquid metal filled gap is present between the pipe wall and FCI, as studied for the most detailed approximation level, 3D currents leaking into the gap evoke high reverse flows up to 13 times the mean velocity at the FCI entry. Only a tiny fraction of 1% of liquid metal passes through the gap between wall and FCI. When fully developed, this gap fluid forms concentrated streamwise jets near the gap sides while the remaining gap fluid is practically stagnant. Details of the strongly

varying gap flow occuring between the wall and FCI are important for corrosion, heat transfer, and tritium transport (Konys et al., 2011; Bucenieks et al., 2006; Candido et al., 2021).

- With known solutions for the flow in the gap and in the bulk of the FCI, it is possible to determine the mechanical loads on the FCI caused by a pressure difference between the inner and outer FCI surface. Computational results show that for the considered FCI design this difference is smaller than 0.056 bar and does not endanger the mechanical integrity of the FCI. Countermeasures against critical loads in the form of pressure equalization holes or slits are therefore not required.

Throughout this work, validation activities of fully developed flows, on the one hand, demonstrate the proximity of computational results with asymptotic solutions with deviations of 1 % - 5 %. On the other hand, simulations of complex 3D MHD phenomena agree with experimental measurements at excellent correlation values with an average coefficient $\overline{CCC} = 0.9956$ (see appendix B). Such good agreement between analytical solutions, computations, and experiments achieved throughout this work leads to the conclusion that the created computational models and numerical methods are sufficiently accurate to predict the physical nature of the investigated problems in complex geometries. This is a strong statement for the robustness and applicability of the developed methods and derived results for future applications in fusion research, engineering and design.

6.3 Significance for fusion blanket engineering and future works

The extended and validated code enables for the first time the application of unstructured grids for simulations of 3D MHD flows in strong fusion relevant magnetic fields and for complex blanket geometries. The presented improvements on the computational MHD code at hand have recently contributed to successful applications in a number of blanket studies. The code has revealed flows of breeder material in entire DCLL blanket columns (Klüber et al., 2019; Mistrangelo et al., 2020) and supported experimental studies of magneto convective flow around two differentially heated cylinders (Mistrangelo et al., 2022a). As a consequence of the work at hand, numerical investigations of 3D MHD phenomena occurring in stepwise bent circular pipes of the ITER test blanket have become feasible (Bühler et al., 2022). First computations of an entire test blanket module (TBM) have been presented in Mistrangelo et al. (2022b) and further calculations with stronger magnetic fields have been announced to be compared with experimental results (Koehly & Bühler, 2022).

Unstructured grids are crucial for the automatic generation of computational grids for large and complex blanket geometries. However, state of the art meshing tools typically are

optimized for purely hydrodynamic simulations so that magnetohydrodynamic requirements on the computational grid, such as extremely thin MHD boundary layers along curved walls, must be reworked manually. Future considerations should therefore focus on the specialization of meshing tools to adequately account for MHD-related phenomena that conventional hydrodynamic meshing tools may not provide. Moreover, such investigations should be done in the foresight of developing an adaptive meshing tool, which automatically adjusts the mesh according to local MHD phenomena during simulations. Since recent MHD research considers increasingly complex blanket geometries and flow phenomena, automatic and adaptive systems similar to the approach by Zhang & Ni (2014), would cut down the high efforts on preprocessing and speed up computations so they could reduce costs substantially.

Further code extensions may address the impact of MHD effects on mass and heat transfer in order to assess general source terms, convection and diffusion in a blanket realistic environment. This would enable to evaluate the impact of MHD phenomena on corrosion of blanket structural material, heat removal from bulk fluid and blanket walls, and tritium inventory as well as permeation losses.

Since the improved and validated code at hand has demonstrated its capability to robustly predict 3D MHD phenomena in blanket subsystem, the next step is expected to advance its applications to higher levels of physical coupling and geometric complexity. As a consequence, the code at hand will set further milestones for the development and application of computational MHD analysis in fusion research, engineering and design.

Bibliography

Albets-Chico, X., E. V. Votyakov, H. Radhakrishnan, and S. Kassinos
2011. Effects of the consistency of the fringing magnetic field on direct numerical simulations of liquid-metal flow. *Fusion Engineering and Design*, *86*(1), 5–14.

Albets-Chico, X., D. G. Grigoriadis, E. V. Votyakov, and S. Kassinos
2013. Direct numerical simulation of turbulent liquid metal flow entering a magnetic field. *Fusion Engineering and Design*, *88*(12), 3108–3124.

Arlt, T.
2018. *Analyse des Stabilitätsverhaltens magnetohydrodynamischer Kanalströmungen*. Doctoral thesis, Karlsruher Institut für Technologie (KIT), Fakultät für Maschinenbau.

Arlt, T. and L. Bühler
2019. Numerical simulations of time-dependent Hunt flows with finite wall conductivity. *Magnetohydrodynamics*, *55*(3), 319–336.

Barleon, L., V. Casal, K. J. Mack, H. Kreuzinger, A. Sterl, and K. Thomauske
1989. Experimental and theoretical work on MHD at the Kernforschungszentrum Karlsruhe. The MEKKA-Program. In J. Lielpetris, & R. Moreau (Eds.) *Liquid Metal Magnetohydrodynamics*, (pp. 55–61). Dordrecht: Springer. ISBN 978-94-009-0999-1.

Barleon, L., V. Casal, and L. Lenhart
1991. MHD flow in liquid-metal-cooled blankets. *Fusion Engineering and Design*, *14*(3-4), 401–412.

Bucenieks, I., R. Krishbergs, E. Platacis, G. Lipsbergs, A. Shishko, A. Zik, and F. Muktepavela
2006. Investigation of corrosion phenomena in eurofer steel in Pb-17Li stationary flow exposed to a magnetic field. *Magnetohydrodynamics*, *42*(2-3), 237–251.

Bühler, L.
1993. Additional Magnetohydrodynamic Pressure Drop At Junctions of Flow Channel Inserts. In C. Ferro, M. Gasparotto, & H. Knoepfel (Eds.) *Fusion Technology 1992*, (pp. 1301–1305). Elsevier Science Publishers B. V.

Bühler, L.
1995. Magnetohydrodynamic flows in arbitary geometries in strong, nonuniform magnetic fields - a numerical code for the design of fusion reactor blankets. *Fusion Technology*, *27*(1), 3–24.

Bühler, L. and C. Mistrangelo
2016. Theoretical studies of MHD flows in support to HCLL design activities. *Fusion Engineering and Design*, *109-111*, 1609–1613.

Bühler, L., H. J. Brinkmann, and C. Köhly
2019. Experimental study of liquid metal magnetohydrodynamic flows near gaps between flow channel inserts. *Fusion Engineering and Design*, *146*, 1399–1402.

Bühler, L., C. Mistrangelo, and H. J. Brinkmann
2020a. Experimental investigation of liquid metal MHD flow entering a flow channel insert. *Fusion Engineering and Design*, *154*, 111484.

Bühler, L., H. J. Brinkmann, and C. Mistrangelo
2020b. Experimental investigation of liquid metal pipe flow in a strong non-uniform magnetic field. *Magnetohydrodynamics*, *56*(2-3), 81–88.

Bühler, L., B. Lyu, H. J. Brinkmann, and C. Mistrangelo
2021. Reconstruction of 3D MHD liquid metal velocity from measurements of electric potential on the external surface of a thick-walled pipe. *Fusion Engineering and Design*, *168*, 112590.

Bühler, L., V. Klüber, and C. Mistrangelo
2022. Magnetohydrodynamic flow in stepwise bent circular pipes. *Magnetohydrodynamics*, (p. submitted).

Candido, L., C. Alberghi, F. Moro, S. Noce, R. Testoni, M. Utili, and M. Zucchetti
2021. A novel approach to the study of magnetohydrodynamic effect on tritium transport in WCLL breeding blanket of DEMO. *Fusion Engineering and Design*, *167*(February), 112334.

Chang, C. C. and T. S. Lundgren
1961. Duct flow in magnetohydrodynamics. *Zeitschrift für angewandte Mathematik und Physik ZAMP*, *12*(2), 100–114.

Courtessole, C., S. Smolentsev, T. Sketchley, and M. Abdou
2016. MHD PbLi experiments in MaPLE loop at UCLA. *Fusion Engineering and Design*, *109-111*, 1016–1021.

Ferziger, J. H. and M. Peric
2002. *Computational Methods for Fluid Dynamics*, Volume 46 of *Computers and Mathematics with Applications*. Berlin, Heidelberg, New York: Springer, 3rd ed. ISBN 3540420746.

Gajbhiye, N. L., P. Throvagunta, and V. Eswaran
2018. Validation and verification of a robust 3-D MHD code. *Fusion Engineering and Design*, *128*, 7–22.

Gonzalez, M., D. Rapisarda, A. Ibarra, C. Courtessole, S. Smolentsev, and M. Abdou
2016. Material analyses of foam-based SiC FCI after dynamic testing in PbLi in MaPLE loop at UCLA. *Fusion Engineering and Design*, *109-111*, 93–98.

Hartmann, J.
1937. Hg-DYNAMICS I, Theory of the laminar flow of an electrically conductive liquid in a homogeneous magnetic field. *Det Kgl. Danske Videnskabernes Selskab. Mathematisk-fysiske Meddelelser.*, *15*(6), 1–27.

Holzmann, T.
2017. Mathematics, Numerics, Derivations and OpenFOAM®, Technical report Release 7.0, Holzmann CFD, Leoben.
URL `https://holzmann-cfd.com/community/publications/mathematics-numerics-derivations-and-openfoam`, Last access date 27.10.2022.

Hua, T. Q., J. S. Walker, B. F. Picologlou, and C. B. Reed
1988. Three-dimensional magnetohydrodynamic flows in rectangular ducts of liquid-metal-cooled blankets. *Fusion Technology*, *14*(3), 1389–1398.

Hua, T. Q. and J. S. Walker
1989. Numerical solutions of three-dimensional MHD flows in strong non-uniform transverse magnetic fields. In J. Lielpetris, & R. Moreau (Eds.) *Liquid Metal Magnetohydrodynamics*, (pp. 13–19). Dordrecht: Springer. ISBN 978-94-009-0999-1.

Hunt, J. C. and S. Leibovich
1967. Magnetohydrodynamic flow in channels of variable cross-section with strong transverse magnetic fields. *Journal of Fluid Mechanics*, *28*(2), 241–260.

Issa, R. I.
1986. Solution of the implicitly discretised fluid flow equations by operator-splitting. *Journal of Computational Physics*, *62*(1), 40–65.

Jareteg, K.
2013. Block coupled calculations in OpenFOAM, Technical report, Chalmers University of Technology.
URL `http://www.tfd.chalmers.se/~hani/kurser/OS_CFD_2012/KlasJareteg/KlasJareteg-OF2012-Project-3-Version-2.0.pdf`, Last access date 27.10.2022.

Keough, S.
2014. Optimising the Parallelisation of OpenFOAM Simulations, Technical report ADA612337, Defense Technical Information Center.
URL `https://apps.dtic.mil/sti/citations/ADA612337`, Last access date 27.10.2022.

Kim, C. N.
2014. Magnetohydrodynamic flows entering the region of a flow channel insert in a duct. *Fusion Engineering and Design*, *89*(1), 56–68.

Kinet, M.
2009. *MHD turbulence at low magnetic Reynolds number: Spectral properties and transition mechanism in a square duct*. Ph.D. thesis, Université Libre de Bruxelles, Faculté des Sciences Physique.

Kit, L. G., D. Peterson, I. A. Platnieks, and A. Tsinober
1970. Investigation of the influence of fringe effects on a magnetohydrodynamic flow in a duct with non-conducting walls. *Magnetohydrodynamics*, *6*(4), 485–491.

Klüber, V., L. Bühler, and C. Mistrangelo
2019. Numerical simulations of 3D magnetohydrodynamic flows in dual-coolant lead lithium blankets. *Fusion Engineering and Design*, *146*, 684–687.

Klüber, V., L. Bühler, and C. Mistrangelo
2020a. Numerical investigation of liquid metal flow in square channels under inclined magnetic fields for fusion relevant parameters. *Magnetohydrodynamics*, *56*(2-3), 149–156.

Klüber, V., L. Bühler, and C. Mistrangelo
2020b. Numerical simulation of 3D magnetohydrodynamic liquid metal flow in a spatially varying solenoidal magnetic field. *Fusion Engineering and Design*, *156*, 111659.

Koehly, C. and L. Bühler
2017. Fabrication issues of sandwich-like flow inserts for circular pipes. *Fusion Science and Technology*, *72*(4), 660–666.

Koehly, C. and L. Bühler
2022. Design of a scaled mock-up of the WCLL TBM for mhd experiments in liquid metal manifolds and breeder units. In *Proceedings of the 32th Symposium on Fusion Technology SOFT, Dubrovnik, Croatia, September 18-23, 2022*.

Kolesnikov, Y. B. and A. B. Tsinober
1972. Magnetohydrodynamic flow in the region of a jump in the conductivity at the wall. *Magnetohydrodynamics*, *8*(1), 61–65.

Komen, E., A. Shams, L. Camilo, and B. Koren
2014. Quasi-DNS capabilities of OpenFOAM for different mesh types. *Computers and Fluids*, *96*, 87–104.

Konys, J., W. Krauss, H. Steiner, J. Novotny, and A. Skrypnik
2011. Flow rate dependent corrosion behavior of Eurofer steel in Pb-15.7Li. *Journal of Nuclear Materials*, *417*(1-3), 1191–1194.

Kulikovskii, A. G.
1968. Slow steady flows of a conducting fluid at large Hartmann numbers. *Fluid Dynamics*, *3*(2), 1–5.

Kumamaru, H.
1984. Magnetic pressure drop and heat transfer of liquid metal flow in annular channel under transverse magnetic field. *Journal of Nuclear Science and Technology*, *21*(5), 393–400.

Lin, L. I.-K.
1989. A Concordance Correlation Coefficient to Evaluate Reproducibility. *Biometrics*, *45*(1), 255.

Lin, L. I.-K., G. McBride, J. Bland, and D. Altman
2005. A proposal for strength-of-agreement criteria for Lin's Concordance Correlation Coefficient. *NIWA Client Report*, *45*(1), 307–310.

Ludford, G. S.
1960. Inviscid flow past a body at low magnetic Reynolds number. *Reviews of Modern Physics*, *32*(4), 1000–1003.

Magnusson, J.
2010. conjugateHeatFoam with explanational tutorial together with a buoyancy driven flow tutorial and a convective conductive tutorial, Technical report, Chalmers University of Technology.
URL `http://www.tfd.chalmers.se/~hani/kurser/OS_CFD_2010/johanMagnusson/johanMagnussonReport.pdf`, Last access date 27.10.2022.

Malang, S.
1987. Einrichtung zur Verringerung des MHD-Druckverlustes in dickwandigen Kanälen - Patentschrift DE 3600645 C2, Deutschland.

Malang, S., K. Arheidt, L. Barleon, H. U. Borgstedt, V. Casal, U. Fischer, W. Link, J. Reimann, K. Rust, and G. Schmidt
1988. Self-cooled liquid-metal blanket concept. *Fusion Technology*, *14*(3), 1343–1356.

Malang, S., M. Tillack, C. P. C. Wong, N. Morley, and S. Smolentsev
2011. Development of the lead lithium (DCLL) blanket concept. *Fusion Science and Technology*, *60*(1), 249–256.

Mao, J., L. Xie, K. Xiang, and H. Wang
2019. Turbulent vortex structure of liquid metal flow in pipe subjected to fringing magnetic field. *Magnetohydrodynamics*, *55*(4), 397–413.

Menditto, A., M. Patriarca, and B. Magnusson
2007. Understanding the meaning of accuracy, trueness and precision. *Accreditation and Quality Assurance*, *12*(1), 45–47.

Mistrangelo, C.
2006. *Three-Dimensional MHD Flow in Sudden Expansions*. Doctoral thesis, University of Karlsruhe, Department of Mechanical Engineering.

Mistrangelo, C. and L. Bühler
2011. Development of a numerical tool to simulate magnetohydrodynamic interactions of liquid metals with strong applied magnetic fields. *Fusion Science and Technology*, *60*(2), 798–803.

Mistrangelo, C. and L. Bühler
2013. Magneto-convective flows in electrically and thermally coupled channels. *Fusion Engineering and Design*, *88*(9-10), 2323–2327.

Mistrangelo, C. and L. Bühler
2014. Liquid metal magnetohydrodynamic flows in manifolds of dual coolant lead lithium blankets. *Fusion Engineering and Design*, *89*(7-8), 1319–1323.

Mistrangelo, C. and L. Bühler
2015. Magnetohydrodynamic flow in ducts with discontinuous electrical insulation. *Fusion Engineering and Design*, *98-99*, 1833–1837.

Mistrangelo, C., L. Bühler, and V. Klüber
2020. Three-dimensional magneto convective flows in geometries relevant for DCLL blankets. *Fusion Engineering and Design*, *159*, 111686.

Mistrangelo, C., L. Bühler, S. Smolentsev, V. Klüber, I. Maione, and J. Aubert
2021. MHD flow in liquid metal blankets: Major design issues, MHD guidelines and numerical analysis. *Fusion Engineering and Design*, *173*, 112795.

Mistrangelo, C., L. Bühler, H.-J. Brinkmann, C. Courtessole, V. Klüber, and C. Koehly
2022a. Magneto-convective flows around two differentially heated cylinders. Part I. Numerical simulations. *Heat and Mass Transfer*, (p. submitted).

Mistrangelo, C., L. Bühler, and V. Klüber
2022b. Towards the simulation of mhd flow in an entire wcll blanket mock-up. *Fusion Engineering and Design*, (p. submitted).

Miyazaki, K., S. Kotake, N. Yamaoka, S. Inoue, and Y. Fujii-E
1983. MHD pressure drop of NaK flow in stainless steel pipe. *Nuclear technology/fusion*, *4*, 447–452.

Molokov, S. and L. Bühler
1994. Liquid metal flow in a U-bend in a strong uniform magnetic field. *Journal of Fluid Mechanics*, *267*, 325–352.

Moon, T. J., T. Q. Hua, and J. S. Walker
1991. Liquid-metal flow in a backward elbow in the plane of a strong magnetic field. *Journal of Fluid Mechanics*, *227*, 273–292.

Moreau, R.
1990. *Magnetohydrodynamics*, Volume 3 of *Fluid Mechanics and its Applications*. Dordrecht: Kluwer Academic Publisher. ISBN 0-7923-0937-5.

Morley, N. B., M. J. Ni, R. Munipalli, P. Huang, and M. A. Abdou
2008a. MHD simulations of liquid metal flow through a toroidally oriented manifold. *Fusion Engineering and Design*, *83*(7-9), 1335–1339.

Morley, N. B., Y. Katoh, S. Malang, B. A. Pint, A. R. Raffray, S. Sharafat, S. Smolentsev, and G. E. Youngblood
2008b. Recent research and development for the dual-coolant blanket concept in the US. *Fusion Engineering and Design*, *83*(7-9), 920–927.

Moukalled, F., L. Mangani, and M. Darwish
2016. *The Finite Volume Method in Computational Fluid Dynamics*, Volume 113 of *Fluid Mechanics and its Applications*. Cham Heidelberg New York Dordrecht London: Springer. ISBN 978-3-319-16873-9.

Mück, B.
1998. *Numerische Untersuchung von Strömumgen in Kanälen mit Versperrungen unter dem Einfluß von Magnetfeldern*. Ph.D. thesis, Universität Karlsruhe.

Mück, B., C. Günther, U. Müller, and L. Bühler
2000. Three-dimensional MHD flows in rectangular ducts with internal obstacles. *Journal of Fluid Mechanics*, *418*, 265–295.

Müller, U. and L. Bühler
2001. *Magnetofluiddynamics in Channels and Containers*. Wien, New York: Springer. ISBN 978-3-540-41253-3.

Ni, M. J., R. Munipalli, P. Huang, N. B. Morley, and M. A. Abdou
2007. A current density conservative scheme for incompressible MHD flows at a low magnetic Reynolds number. Part II: on an arbitrary collocated mesh. *Journal of Computational Physics*, *227*, 205–228.

Ni, M.-J., S.-J. Xu, Z.-H. Wang, and N.-M. Zhang
2011. Simulation of MHD Flows in Liquid Metal Blanket with Flow Channel Insert. *Fusion Science and Technology*, *60*(1), 292–297.

Norajitra, P., W. W. Basuki, M. Gonzalez, D. Rapisarda, M. Rohde, and L. Spatafora
2015. Development of sandwich flow channel inserts for an EU demo dual coolant blanket concept. *Fusion Science and Technology*, *68*(3), 501–506.

OpenFOAM-Foundation
2021. OpenFOAM User-Guide.
URL `https://openfoam.org/guides/`, Last access date 27.10.2022.

Oxtoby, O., A. Syrakos, E. de Villiers, S. Varchanis, Y. Dimakopoulos, and J. Tsamopoulos
2019. A family of first-order accurate gradient schemes for finite volume methods, Technical report arXiv:1912.08064, Cornell University.
URL `https://arxiv.org/abs/1912.08064`, Last access date 27.10.2022.

Perry, A. E. and M. S. Chong
1987. A description of eddying motions and flow patterns using critical-point concepts. *Annual Review of Fluid Mechanics*, *19*, 125–155.

Picologlou, B. F., C. B. Reed, P. V. Dauzvardis, and J. S. Walker
1986. Experimental and analytical investigations of magnetohydrodynamic flows Near the entrance to a strong magnetic field. *Fusion Technology*, *10*, 860–865.

Picologlou, B. F. and C. B. Reed
1989. Experimental investigation of 3-D MHD flows at high Hartmann number and interaction parameter. In J. Lielpetris, & R. Moreau (Eds.) *Liquid Metal Magnetohydrodynamics*, (pp. 71–77). Dordrecht: Springer. ISBN 978-94-009-0999-1.

Pothérat, A., J. Sommeria, and R. Moreau
2000. An effective two-dimensional model for MHD flows with transverse magnetic field. *Journal of Fluid Mechanics*, *424*, 75–100.

Pulugundla, G., S. Smolentsev, T. Rhodes, C. Kawczynski, and M. Abdou
2015. Transition to a quasi-fully developed MHD flow in an electrically conducting pipe under a transverse non-uniform magnetic field. *Fusion Science and Technology*, *68*(3), 684–689.

Rapisarda, D., I. Fernandez, I. Palermo, F. R. Urgorri, L. Maqueda, D. Alonso, T. Melichar, O. Frýbort, L. Vála, M. Gonzalez, P. Norajitra, H. Neuberger, and A. Ibarra
2017. Status of the engineering activities carried out on the European DCLL. *Fusion Engineering and Design*, *124*, 876–881.

Reed, C. B., B. F. Piclolglou, T. Q. Hua, and J. S. Walker
1987. Alex results - A comparison of measurements from a round and a rectangular duct with 3-D code predictions. In *12th Symposium on Fusion Engineering*, (pp. 1267–1270). Monterey, California: IEEE.

Roberts, P. H.
1967. Singularities of Hartmann layers. *Proceedings of the Royal Society of London. Series A. Mathematical and Physical Sciences*, *300*(1460), 94–107.

Shercliff, J. A.
1953. Steady motion of conducting fluids in pipes under transverse magnetic fields. *Mathematical Proceedings of the Cambridge Philosophical Society*, *49*(1), 136–144.

Shercliff, J. A.
1956. The flow of conducting fluids in circular pipes under transverse magnetic fields. *Journal of Fluid Mechanics*, *1*(06), 644–666.

Shercliff, J. A.
1962. Magnetohydrodynamic pipe flow: Part2. High Hartmann number. *Journal of Fluid Mechanics*, *13*(4), 513–518.

Smolentsev, S., N. B. Morley, and M. Abdou
2006. Magnetohydrodynamic and thermal issues of the SiCf/SiC flow channel insert. *Fusion Science and Technology*, *50*(1), 107–119.

Smolentsev, S., S. Badia, R. Bhattacharyay, L. Bühler, L. Chen, Q. Huang, H. G. Jin, D. Krasnov, D. W. Lee, E. M. De Les Valls, C. Mistrangelo, R. Munipalli, M. J. Ni, D. Pashkevich, A. Patel, G. Pulugundla, P. Satyamurthy, A. Snegirev, V. Sviridov, P. Swain, T. Zhou, and O. Zikanov
2015. An approach to verification and validation of MHD codes for fusion applications. *Fusion Engineering and Design*, *100*, 65–72.

Smolentsev, S., T. Rhodes, Y. Yan, A. Tassone, C. Mistrangelo, L. Bühler, and F. R. Urgorri
2020. Code-to-code comparison for a PbLi mixed-convection MHD flow. *Fusion Science and Technology*, *76*, 653–669.

Smolentsev, S.
2021. Physical background, computations and practical issues of the magnetohydrodynamic pressure drop in a fusion liquid metal blanket. *Fluids*, *6*(3), 110.

Sommeria, J. and R. Moreau
1982. Why, how, and when, MHD turbulence becomes two-dimensional. *Journal of Fluid Mechanics*, *118*, 507–518.

Spurk, J. H. and N. Aksel
1989. *Strömungslehre - Einführung in die Theorie der Strömungen*. Berlin Heidelberg New York: Springer, 7 ed. ISBN 978-3-642-13143-1.

Sterl, A.
1990. Numerical simulation of liquid-metal MHD flows in rectangular ducts. *Journal of Fluid Mechanics*, *216*(5-6), 161–191.

Stieglitz, R.
1994. *Magnetohydrodynamische Strömungen in Ein- und Mehrkanalumlenkungen*. Doctoral thesis, Kernforschungszentrum Karlsruhe, KfK 5376.

Stieglitz, R., L. Barleon, L. Bühler, and S. Molokov
1996. Magnetohydrodynamic flow through a right-angle bend in a strong magnetic field. *Journal of Fluid Mechanics*, *326*, 91–123.

Stieglitz, R. and S. Molokov
1997. Experimental study of magnetohydrodynamic flows in electrically coupled bends. *Journal of Fluid Mechanics*, *343*, 1–28.

Sutevski, D., S. Smolentsev, and M. Abdou
2014. 3D numerical study of pressure equalization in MHD flow in a rectangular duct with insulating flow channel insert. *Fusion Engineering and Design*, *89*(7-8), 1370–1374.

Syrakos, A., S. Varchanis, Y. Dimakopoulos, A. Goulas, and J. Tsamopoulos
2017. A critical analysis of some popular methods for the discretisation of the gradient operator in finite volume methods. *Physics of Fluids*, *29*(12).

Tennekes, H. and J. L. Lumley
1972. *A First Course in Turbulence*. Cambridge, Massachusetts, and London, England: MIT Press. ISBN 0262200198.

Ting, A. L., J. S. Walker, T. J. Moon, C. B. Reed, and B. F. Picologlou
1991. Linear stability analysis for high-velocity boundary layers in liquid-metal magnetohydrodynamic flows. *International Journal of Engineering Science*, *29*(8), 939–948.

Tobak, M. and D. J. Peake
1982. Topology of three-dimensional separated flows. *Annual Review of Fluid Mechanics*, *14*(1), 61–85.

Uflyand, Y. S.
1961. Hartman problem for a circular tube. *Soviet Physics-Technical Physics*, *5*(10), 1194–1196.

Vantieghem, S., X. Albets-Chico, and B. Knaepen
2009. The velocity profile of laminar MHD flows in circular conducting pipes. *Theoretical and Computational Fluid Dynamics*, *23*(6), 525–533.

Vantieghem, S.
2011. *Numerical simulations of quasi-static magnetohydrodynamics using an unstructured finite volume solver: development and applications*. Ph.D. thesis, Université Libre de Bruxelles, Faculté des Sciences Physique.

Zhang, J. and M. J. Ni
2014. Direct simulation of multi-phase MHD flows on an unstructured Cartesian adaptive system. *Journal of Computational Physics*, *270*, 345–365.

Appendices

A MHD phenomena at FCI conjunctions

Implementation of the FCI model

Besides MHD flow entering an FCI introduced in chapter 5, the study addresses, in addition, the phenomena occurring at conjunctions between two consecutive FCIs, as investigated experimentally in the MEKKA facility (Bühler et al., 2019). Level 1 and 2 representations have been implemented according to figure A.1.

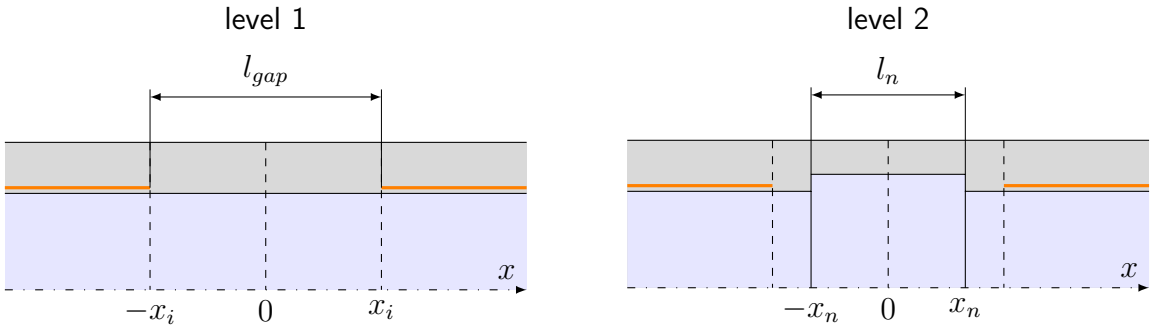

Figure A.1: Approximation models at axial gaps between two consecutive FCIs. Radii variations are identical to the case of FCI entry flow introduced in figure 5.2

As described above, level 1 represents the FCI by considering the impact of interrupted electric insulation while keeping the fluid-solid interface straight. The axial gap in the insulation used in the experiments at the conjunction of two FCIs is comparatively small

$$l_{gap} = 0.426 \ . \tag{A.1}$$

The geometric approximation level 2 additionally takes into account the notch, which is present due to different radii of bare pipe and FCI. Its length is $l_n = 0.213$.

3D MHD phenomena at FCI conjunctions

Gaps in the insulation layer occur at FCI conjunctions due to limitations by fabrication, implementation, or maintenance requirements for complex blanket geometries. As a consequence, currents may leak locally to the wall domain and increase overall pressure losses. This section addresses such 3D MHD phenomena occurring at conjunctions between consecutive FCIs in a straight pipe at $Ha = 2000$ and $Re = 20000$ by applying a level 1 model (see figure 5.2).

Figure A.2 displays the experimented case where two consecutive FCIs exhibit a small axial gap of dimensionless length $l_{gap} = 0.426$, centered at $x = 0$. The orange cylindrical surfaces represent the two internal insulators. The disruption of the insulation allows currents to leak to the outer well-conducting pipe wall and short-circuit in the form of large recirculation loops. The displayed electric current streamlines appear symmetric with respect to the center of the insulation gap at $x = 0$. This suggests similar magnetohydrodynamic behavior occurring in both upstream and downstream directions. In fact, the essence observed for 3D MHD effects at FCI entries remains valid for the flow leaving the insulated part of the FCI or for flow between non-insulated conjunctions of FCIs.

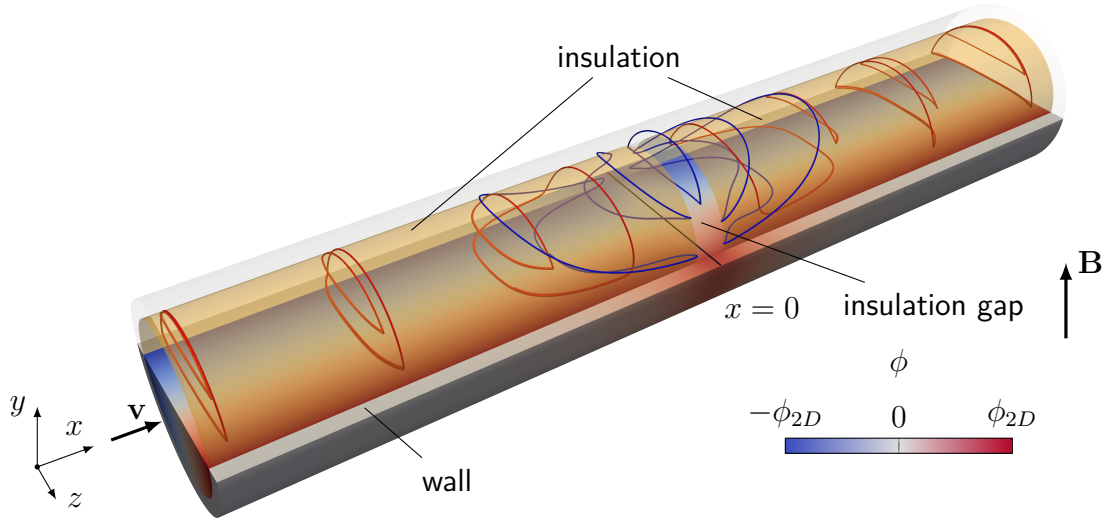

Figure A.2: MHD flow at a conjunction of FCIs for $Ha = 2000$ and $Re = 20000$. Electric potential distribution and current paths displayed in the lower and in the upper half of the pipe, respectively. Red current streamlines close along the inner FCI layer, while blue lines leak through the gap and close outside in the well conducting wall domain. The black straight line at $x = 0$ marks the gap center.

Far away from the gap in the upstream and downstream direction, electric current flow exclusively occurs within channel cross-sections, which suggests fully developed MHD flow. Hence, electric currents cross the fluid domain in horizontal paths and then close over the inner conducting FCI layer, as marked by red streamlines. The insulation layer interrupts

currents and shields the outer wall from the inner induced electric field.

The conductance within the bare gap region is one order of magnitude higher than inside the FCI (see equations 5.1 and 5.2). Thus, the pipe wall near the gap provides a preferable short-circuit for induced electric currents. Therefore, currents increasingly stretch in the axial direction by approaching the gap. In close gap vicinity, they leak, as marked by blue streamlines, and close in large recirculation loops in the outer well-conducting wall domain, where they produce a local distribution of wall potential that is visible on the outer surface of the pipe. This deflection of currents occurs similarly to the case of FCI entry flow shown in figure 5.4, where wall short-circuiting currents close by wrapping around the insulation.

Figure A.3 shows magnitudes of electric currents, Lorentz force, and velocity scaled by values for fully developed flow (Miyazaki et al., 1983). Green lines represent electric current paths. Vertical black dashed lines indicate the center and width of the insulation gap.

As shown in the upper plot, electric currents bundle within the gap region, which leads to locally higher current densities. The highest peaks occur within the side regions in the FCI gap where current flow focuses and leaks into the well-conducting wall domain. Upstream and downstream current densities within the FCI domain are comparatively small as imposed by the FCI design. By approaching the gap, the current density rises near the sides where currents bundle increasingly due to the axially stretched profiles. Concerning the flow re-entering the second FCI downstream of $x > x_i$, yellow highlighted lines pass through regions of locally unstable flow and exhibit swirls producing an aisle of lower current density, as marked by straight red lines. Current streamlines of the flow leaving the first FCI, on the other hand, stream smoothly into the FCI gap.

The middle contour plot presents the magnitudes of Lorentz force scaled by the asymptotic solution showing an identical profile as for the electric current density because the magnetic field is uniform and orthogonal to fluid currents $\mathbf{f_L} = \mathbf{j} \times \mathbf{B}$ in the considered symmetry plane $y = 0$. Hence, $\mathbf{f}_L$ opposes the flow across the whole domain. Due to the increased current flow in the region of bare pipe flow $-x_i < x < x_i$, Lorentz forces here are larger, and they may exceed values of fully developed flow by more than a factor of 3. By approaching the gap from an up- or downstream position, correspondingly strong outward and inward-directed components of $\mathbf{f}_L$ appear in addition to the main axial component. They point outwards when the fluid leaves the first FCI, while the flow entering the subsequent FCI experiences detaching inward-directed Lorentz forces.

The up- and downstream FCI velocity distribution appears somehow symmetrical to the gap center $x = 0$. Center velocity peaks occur close to the FCI inlet/outlet and are slightly displaced in the flow direction. 3D MHD effects develop gradually over multiple characteristic lengths both in up- and downstream directions. However, when reaching the gap, the velocity profile switches rapidly from convex to concave shape, i.e., from a velocity profile with a center maximum to a profile with a maximum at the sides. Such concave velocity profile persists across the whole gap width before it re-assumes rapidly again a convex curvature. This rapid shift leads to particularly high-velocity gradients in the

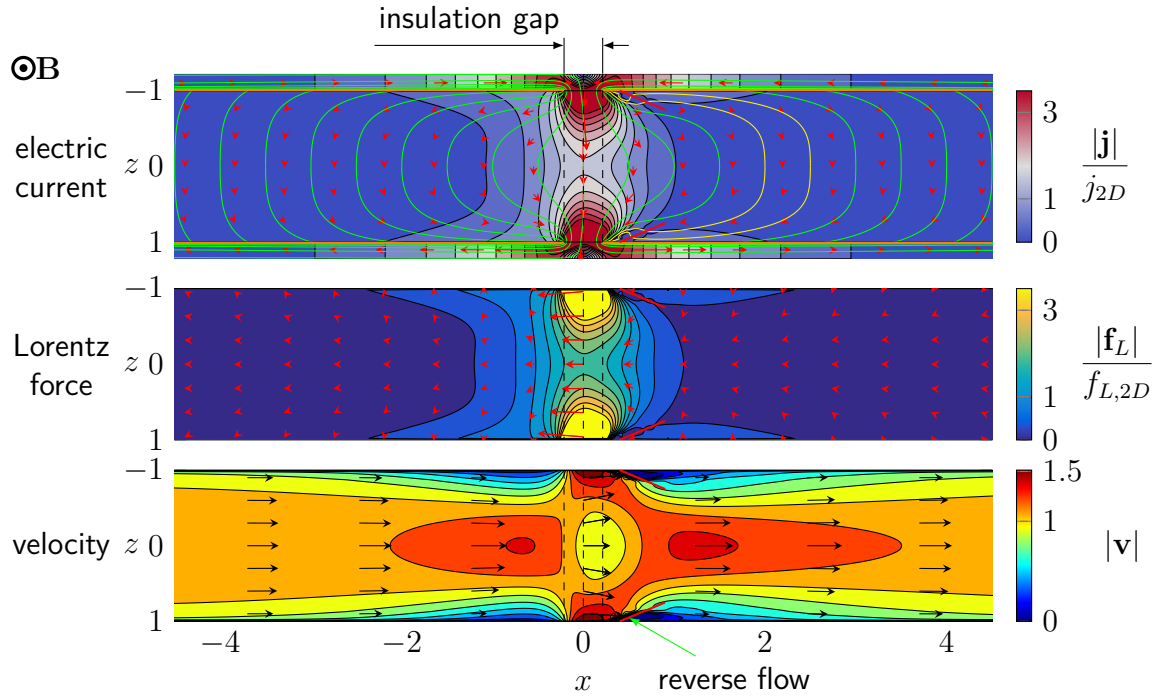

Figure A.3: MHD flow at the conjunction of FCIs for $Ha = 2000$ and $Re = 20000$. Contour plots of current density, Lorentz force and velocity at $y = 0$. Arrows show direction and magnitude; green lines represent current paths; vertical dashed lines indicate gap center and width (i.e. $\pm x_i$); staright red lines indicate the paths along which transient fluctuations are traveling and reverse flow occurs.

side regions. In this context, reverse flow and associated instabilities exclusively occur at re-entering flow. Detaching Lorentz forces seem to have the essential destabilizing impact, which is why only side layers of the flow entering the FCI become unstable, similar to observations in strong nonuniform fields by Albets-Chico et al. (2013).

Figure A.4 shows the axial pressure distribution along both the pipe axis and side, represented by the blue and red lines, respectively. Up- and downstream gradients agree well with the asymptotic solution $\partial_x p_{2D,FCI}$ of developed FCI flow according to equation 5.11, portrayed as straight black lines. Center and side pressures show evolving separation upon approaching the gap, indicating strong transversal pressure differences, which are highest at FCI-gap transition. Across the gap, the center pressure forms a rather smooth change with the largest gradient at $x = 0$. The pressure along the side, on the other hand, remains longer close to 2D conditions before it exhibits a significant sharp drop along the gap. The origin for such strongly differing gradients between the center and side pressure lies in the orientation of the current profile, presented in the upper contour plot in figure A.3. Near $x = 0$, increased currents orient in the axial direction, which gradually increases the pressure gradient on the axis. Across the gap region, however, electric currents bundle before they enter the wall domain. This, in turn, results in strong flow-opposing Lorentz forces and associated high-pressure gradients across the entire gap region, but in particular

along the sides.

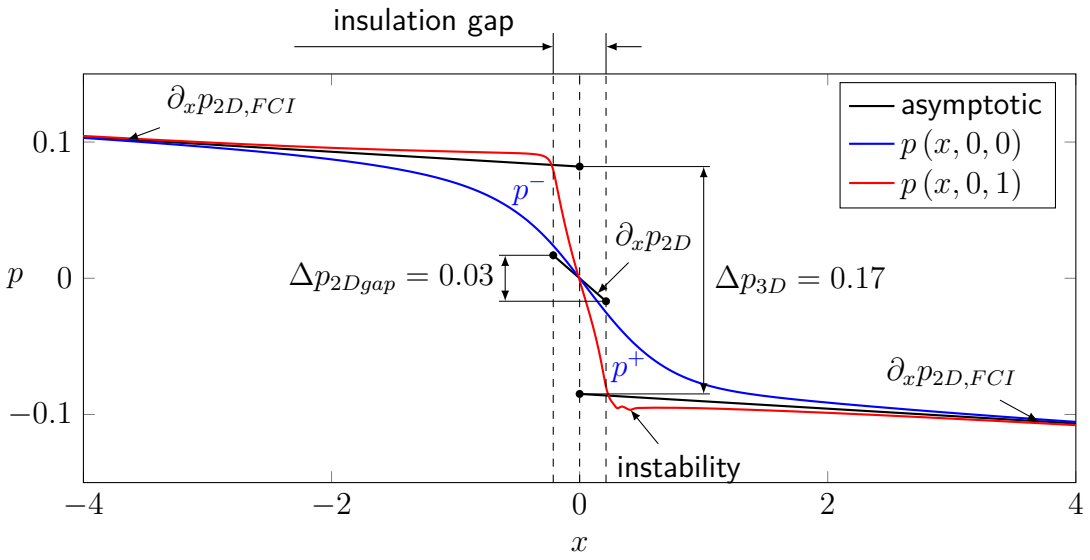

Figure A.4: MHD flow at the gap between two FCIs for $Ha = 2000$ and $Re = 20000$. Pressure distribution at the FCI gap along the pipe axis and along the side. Extrapolation of the fully developed solutions (black straight lines) towards $x = 0$ defines the additional pressure drop Δp_{3D}. Minor pressure fluctuations at the side near the FCI entry indicate the presence of weak flow instability.

Extrapolating the up- and downstream gradients to the gap center $x = 0$, as shown by the solid black lines, reveals a significant additional pressure drop $\Delta p_{3D} = 0.17$ compared to the flow in a non-interrupted FCI. It refers to a pressure drop of fully developed FCI flow over the length

$$l_{3D} = \frac{\Delta p_{3D}}{\partial p_{2D,FCI}} = 34 \ . \tag{A.2}$$

This means that FCIs in fusion applications should be much longer than l_{3D} for gap-induced additional losses to be smaller than losses of the fully developed flow. Considering the case of blankets in fusion reactors, however, shows that typical flow paths are much smaller. Therefore, additional 3D MHD effects at gaps constitute a significant fraction of pressure losses and should be investigated at a broader level with respect to, e.g., varying gap lengths or overlapping FCIs (Bühler, 1993) to support future FCI-blanket design concepts.

It is not surprising that the non-insulated part of the pipe creates a larger pressure drop than the FCI since here currents are higher. However, it may be interesting to infer how much of this extra pressure drop has its origin in complex 3D current paths and which contribution is attributed to non-insulated pipe flow. The latter part can be estimated as

$$\Delta p_{2Dgap} = \partial_x p_{2D}\, l_{gap} = 0.0338 \tag{A.3}$$

assuming hypothetically a fully established pipe flow. A comparison with the value of

$\Delta p_{3D} = 0.17$ shows for the present geometry that 80% of the pressure drop at the gap results from 3D circulating current contributions and from the fact that the wall conductance near the gap is virtually increased since currents find additional shortcuts by wrapping around the insulation layer and closing along the pipe wall outside of the insulation, shown blue in figure A.2. The pressure contributions discussed in this paragraph are indicated in figure A.4.

Figure A.4 further shows that the center pressure is smaller than the pressure at the side for $x < 0$, while for $x > 0$, this trend is reversed as indicated by p^- and p^+ in the figure. Regardless of such inverted transversal pressure difference, both upstream and downstream flow show a maximum velocity in the center and reduced velocity near the sides, as displayed in figure A.3. Moreover, velocity jets at the sides appear across the gap region, where the highest flow opposing Lorentz forces are present. From this point of view, velocity appears decoupled from dominant momentum balances, i.e., pressure gradient and Lorentz force density. This is discussed in more detail in the next section.

Magnetodynamic phenomena at FCI conjunctions

Similar to the case of FCI entry flow in chapter 5, observations apply to the case of MHD flow at conjunctions between two FCIs including an insulation gap, shown in figure A.5.

Along the pipe axis, the magnetodynamic force first accelerates the fluid to a maximum velocity at the first O^+ saddle point in the force field. Then the flow is retarded rapidly to a velocity minimum at the saddle point O^- close to $x = 0$ before it is accelerated once again to a downstream maximum at the next O^+ saddle point. Since upstream and downstream regions are insulated by FCIs, the development lengths are relatively large in both sections despite the fact that the critical points are close to $x = 0$. The non-symmetry in velocity and force fields results from the non-linearity of inertia terms in the momentum equation. Near the sides, the situation is reversed. When approaching the gap, the fluid is gradually slowed down to the position where the force field has the first critical point O^-. Afterward, the velocity rockets up over a very short distance to the highest values at O^+ near $x = 0$, before strong flow-opposing forces rapidly bring the fluid back to another minimum velocity at the downstream critical point O^- from where it recovers gradually to fully established conditions.

The strong decelerating forces near the sides eventually result in downstream flow separation and locally confined time-dependent unstable patterns. In contrast, the accelerated flow at upstream sides remains attached and stable.

Similar to the case of FCI entry flow in chapter 5, there exists correspondence between magnetodynamic force and transverse velocity for the case of MHD flow between two FCIs

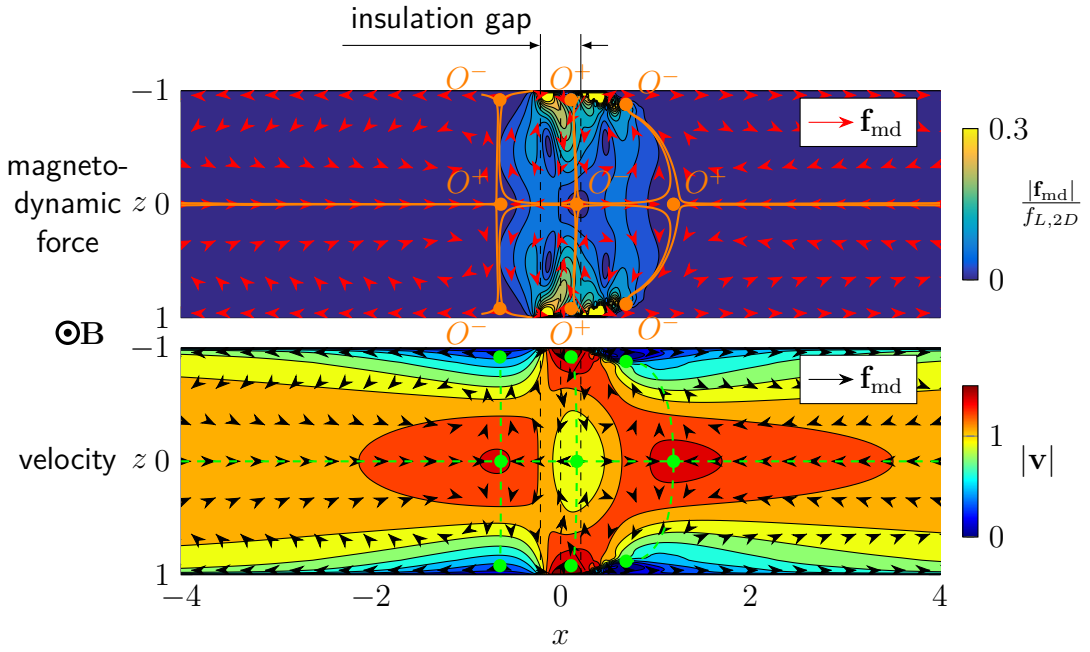

Figure A.5: Contours of magnetodynamic force (top) and velocity (bottom) for MHD flow in the vicinity of a gap between two FCIs at $Ha = 2000$ and $Re = 20000$. $\mathbf{f}_{\mathrm{md}}$ is scaled by the Lorentz force for fully developed pipe flow $f_{L,2D}$. While the color bar for $\mathbf{f}_{\mathrm{md}}/f_{L,2D}$ is limited to 0.3 for better visibility, highest values in very narrow regions exceed the color scale up to 4. Orange solid lines and green dashed lines indicate so-called separation lines (Tobak & Peake, 1982), which enclose characteristic zones of $\mathbf{f}_{\mathrm{md}}$.

that are separated by the short non-insulated gap, as shown in figure A.6.

It can be seen that regions of positive and negative transverse velocity coincide with the characteristic regions that are bounded by the separation lines of the magnetodynamic force field. The flow patterns are again highly correlated along magnetic field lines, and deviations from Q2D behavior appear exclusively in regions of strong inertia or magnetodynamic force.

Analogous to FCI entry flow, the investigated MHD phenomena at FCI conjunctions with an axial gap exhibits three transversal separations lines, shown by green dashed lines. Moreover, the center transversal separation line appears slightly curved and does not originate from axial transition points $x = \pm x_i$ where the insulation ends. This leads to the conclusion that for the investigated gap width of $l_{gap} = 0.426$, 3D MHD flow regimes for FCI exiting and entering scenarios overlap and may not be fully distinguished from each other.

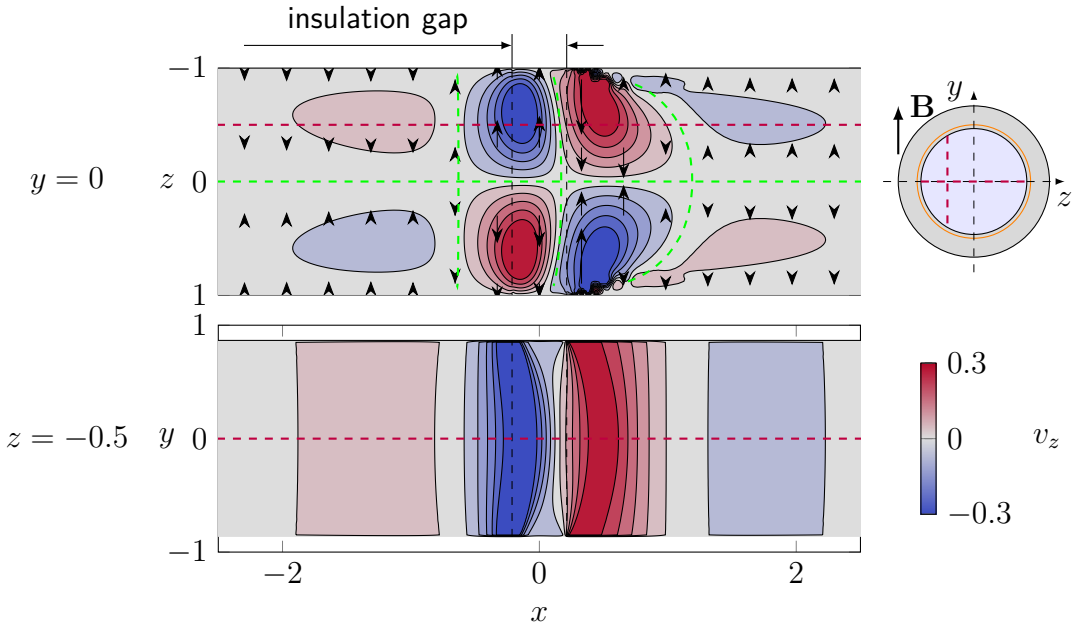

Figure A.6: Contours and vector representations of transverse velocity component v_z for MHD flow in the vicinity of a gap between a conjunction of two FCIs at $Ha = 2000$ and $Re = 20000$. Results are displayed on the horizontal symmetry plan $y = 0$ (top) and on a vertical plane $z = -0.5$ (bottom) as shown by purple dashed lines. Green dashed lines illustrate the separation lines of $\mathbf{f}_{\mathrm{md}}$.

Comparision with experiments

Experimental results are available for MHD flow through two consecutive FCIs that are separated by a a gap. Figure A.7 presents the bulk pressure distribution along the axis and near the sides upstream and downstream of the non-insulated section. The central pressure variation portrayed as blue data sets shows a large drop along the short non-insulated part of bare pipe compared with the moderate gradients inside the FCIs, up- and downstream. Upon approaching the FCI conjunction, axial potential gradients increase the current density locally and stretch current streamlines. Pressure gradients near the sides, portrayed red, therefore become smaller as the Lorentz forces orient spanwise and thus do not effectively contribute to MHD pressure drop at the sides. This behavior changes instantly when the insulation becomes disrupted, so bulk currents are no longer confined and may short-circuit over the well-conducting wall domain. Transverse currents consequently bundle along the sides, which leads to large flow-opposing Lorentz forces and a large side pressure gradient in the non-insulated section.

A comparison of measured data and numerical simulations confirms the potential for pressure drop reduction by the FCIs since pressure gradients upstream and downstream of the conjunction agree reasonable at high correlation coefficients CCC (see section B in the appendix). However, the additional 3D pressure drop at the junction appears a bit smaller

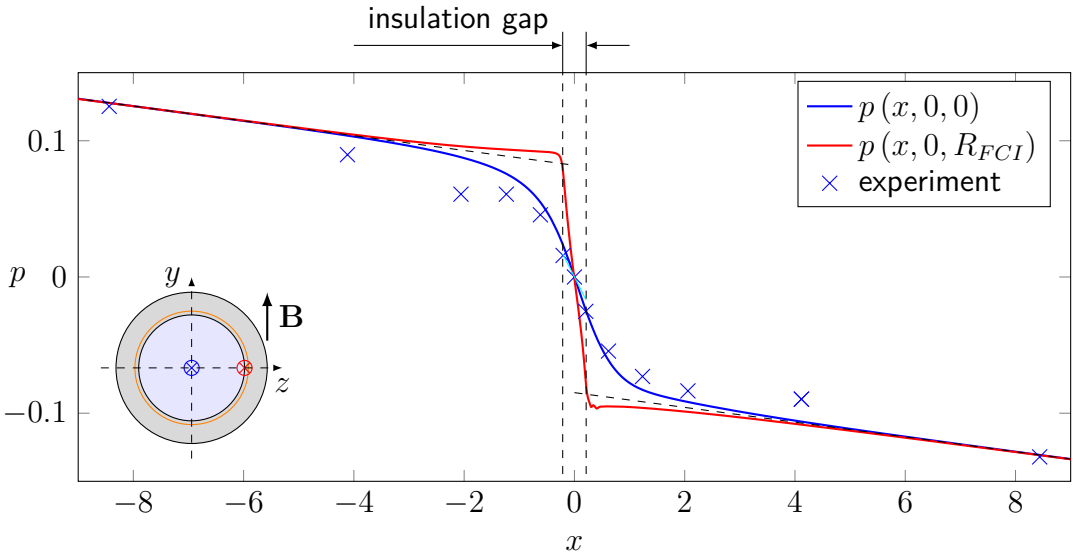

Figure A.7: Pressure variation for MHD flow at a conjunction between two FCIs for $Ha = 2000$ and $Re = 20000$. Comparison of experimental measurements (symbols) with numerical simulations based on level 2 approximation model (solid lines). Experimental data obtained through private communication with the first author of Bühler et al. (2019) as complementary data to the latter publication. Correlation between experimental measurements and computational result $CCC = 0.9888$ for $p\,(x,0,0)$ (see section B in the appendix).

in the experiment compared with the simulation results. A definite reason for the observed deviations cannot be given here since, on the one hand, the measuring uncertainties are unavailable and, on the other hand, numerical models with a higher degree of geometrical detail could also have some influence on results. Future works could, therefore, also consider the impact of equalization measures on the flow in the annular gap that has been disregarded in the present model and focus on a more detailed description of local effects near pressure taps and holes in the FCIs, from which perturbations may originate and propagate along magnetic field lines (e.g., observed for elongated pressure equalization slots (Smolentsev et al., 2006)).

Figure A.8 shows the wall potential distributions for the flow at the conjunction between two consecutive FCIs involving a small non-insulated distance.

Solid lines show computational results based on the level 2 model and symbols experimental measurements. The plot on the left presents the side wall potential difference $\Delta\phi\,(x)$. Along the short insulator disruption, marked by black dashed vertical lines, currents induced in the bulk flow inside the FCI leak to the outer well-conducting wall and create there the observed distribution of wall potential. The non-insulated length is too short for the wall potential to reach values of fully developed pipe flow $2\phi_{2D,w}$. The wall potential difference $\Delta\phi$ decays up- and downstream, where the FCI perfectly shields the outer domain. Similar

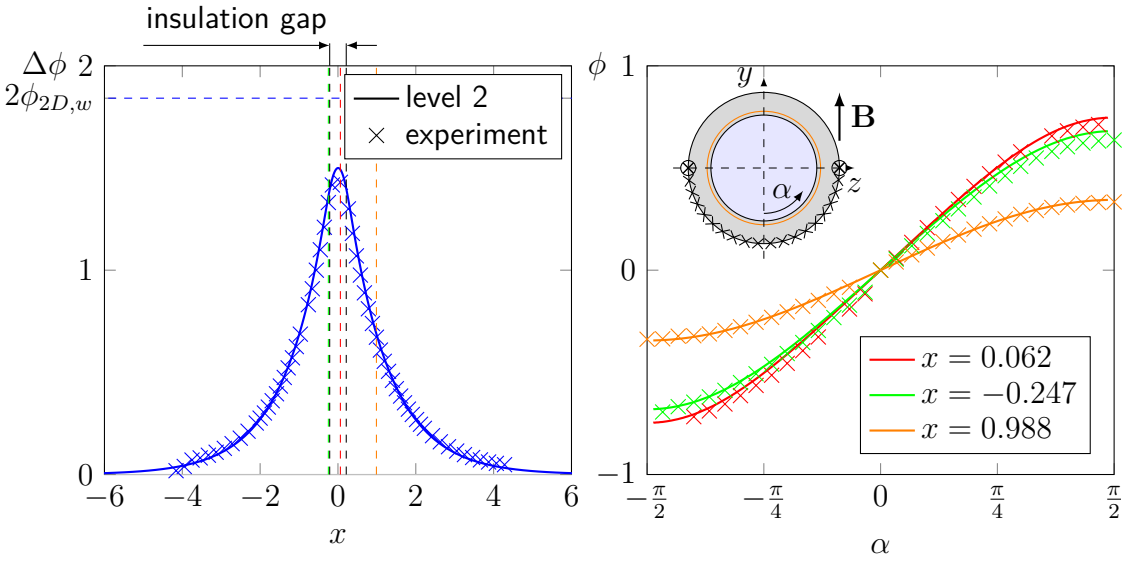

Figure A.8: Potential distribution for MHD flow near the non-insulated conjunction of two consecutive FCIs at $Ha = 2000$ and $Re = 20000$. Comparison of experimental results (symbols) and computations based on level 2 (solid lines). Results are shown as transversal potential difference $\Delta\phi$ (left) and circumferential profiles of wall potential $\phi(x, \alpha)$ (right). Experimental data obtained through private communication with the first author of Bühler et al. (2019) as complementary data to the latter publication. Correlation between experimental measurements and computational results $CCC = 0.9987$ for $\Delta\phi$ and mean correlation $\overline{CCC} = 0.9987$ for observation pairs at different axial positions $\phi(x)$ (see section B in the appendix).

to the case of FCI inlet flow, the experimental measurements likewise indicate a small but finite constant wall potential at a far distance from the conjunction. The underlying computational model, on the other hand, does not consider annular gap flow, and thus numerical results converge to zero.

Colored vertical dashed lines in figure A.8 (left) refer to the selected axial locations of circumferential measurements along the outer pipe surface, for which results are shown in the plot on the right. The sketch illustrates the location of electrodes along the wall circumference in the experiment. Results show a sinusoidal-like distribution along α and an x-dependent amplitude. This confirms the existence of both axial and circumferential components of potential gradients, causing current loops that close beyond the non-insulated fraction in the pipe wall. This behavior has been illustrated in figure A.2.

B Agreement between simulations and experiments

In order to quantify the deviation of experimental measurements with numerical results, the work at hand employs Lin's concordance correlation coefficient (CCC) (Lin, 1989). This quantity incorporates in addition to a general statement about agreement between a measured quantity (experiment) and a reference value (simulation) further valuable indicators such as trueness and precision as it also identifies scale drift and shift between observation pairs.

Based on remarks in Lin (1989), a series of measured values X_k and their corresponding numerical results Y_k lead to a list of observation pairs (X_k, Y_k), with the respective means μ_Y and μ_X as well as standard deviations σ_Y and σ_X. The concordance correlation coefficient as a measure of accuracy is then defined as

$$CCC = \rho \left(\frac{2}{\frac{(\mu_Y - \mu_X)^2}{\sigma_X \sigma_Y} + \frac{\sigma_Y}{\sigma_X} + \frac{\sigma_X}{\sigma_Y}} \right) , \tag{B.1}$$

where

$$\rho = \frac{\mathrm{cov}\,(X_k, Y_k)}{\sigma_X \sigma_Y} \tag{B.2}$$

constitutes the ratio of covariance cov and combined standard deviation of experimental measurement and computational result. The precision term ρ, known as Pearson correlation coefficient, varies within the range $[-1, 1]$ where higher values constitute a higher precision. In other words, a higher ρ indicates that the values of observation pairs change more consistently, i.e., higher/lower measured values increasingly entail higher/lower computed values.

While ρ assesses the precision of agreement, it fails to capture properties of trueness as measure of closeness between observation pairs (Menditto et al., 2007). These may be local shifts in the form of constant deviations, e.g., offset between observation pairs, or scale shifts that vary based on the value of observation pairs. They are incorporated by the second parenthesized expression in equation B.1,

$$\chi_a = \frac{2}{\nu^2 + \omega + \frac{1}{\omega}} , \tag{B.3}$$

that constitutes a measure of trueness where

$$\omega = \frac{\sigma_Y}{\sigma_X} \,, \tag{B.4}$$

$$\nu = \frac{\mu_Y - \mu_X}{\sqrt{\sigma_X \sigma_Y}} \,. \tag{B.5}$$

The quantity ω measures scale shift as factor on how much the agreement depends on the value, while the location shift ν indicates the offset of how much the data deviates. χ_a may vary within the range of $[0, 1]$ and higher values of χ_a indicate higher trueness between observation pairs. As a result, the concordance correlation coefficient describes accuracy of the agreement as a product of precision ρ and trueness χ_a

$$CCC = \rho \, \chi_a \,, \tag{B.6}$$

where the former factor describes random deviations and the latter factor systematic deviations. The CCC value may vary within

$$-1 \leq -|\rho| \leq CCC \leq |\rho| \leq 1 \,, \tag{B.7}$$

based on precision and trueness indicating higher accuracy for higher values of CCC. In order to interpret the CCC value, Lin et al. (2005) proposes the guideline listed in table B.1 that is adopted for the observations at hand.

CCC	evaluation level
> 0.99	almost perfect
$(0.95, 0.99]$	substantial
$[0.90, 0.95]$	moderate
< 0.9	poor

Table B.1: Evaluation scale of the concordance correlation coefficient CCC according to Lin et al. (2005).

Observation pairs are constructed from each validation case in this work. This is done by interpolating numerical data to discrete sample locations of experimental data, since the former exists at significantly higher spatial resolutions. The concordance correlation coefficient CCC is then determined according to equation B.1. Table B.2 lists in addition to the achieved CCC values the corresponding precision ρ and trueness χ_a as well as local shift ν and scale shift ω.

Almost every validation case listed in table B.2 performs according to the assessment scale in table B.1 at "almost perfect" CCC level, while rating the three cases 5, 10, and 12 "substantial". On the one hand, number 5 compares $\phi\,(x = -4.2)$ at comparatively low values of the electric potential, whereas higher considered values of related cases between number 3 and 9 show higher CCCs. This is confirmed by the fact that the scale shift

No.	Figure	Observation pairs	Precision		Trueness		
		(X_k, Y_k)	CCC	ρ	χ_a	ν	ω
Nonuniform magnetic field							
1.	4.15	$\delta_x p_s$	0.9992	0.9994	0.9999	0.0144	1.0076
2.		$\delta_x p_{Ha}$	0.9936	0.9985	0.9951	−0.0717	1.0706
3.	4.16	$\phi\left(\alpha = \frac{\pi}{2}\right)$	0.9966	0.9997	0.9968	−0.0654	0.9555
4.		$\phi\left(\alpha = -\frac{\pi}{2}\right)$	0.9988	0.9998	0.9990	−0.0423	1.0137
5.		$\phi\,(x = -4.2)$	0.9759	0.9991	0.9767	−0.0639	0.8119
6.		$\phi\,(x = -1.7)$	0.9989	0.9999	0.9990	−0.0340	1.0300
7.		$\phi\,(x = 0.69)$	0.9992	0.9999	0.9993	−0.0285	1.0245
8.		$\phi\,(x = 3.6)$	0.9996	0.9999	0.9997	−0.0247	0.9971
9.		$\phi\,(x = 13)$	0.9993	0.9999	0.9994	−0.0312	0.9853
FCI entry (level 3 model type)							
10.	5.24	$p\,(x, 0, 0)$	0.9857	0.9964	0.9893	−0.0200	0.8643
11.	5.25	$\Delta\phi\,(x)$	0.9985	0.9994	0.9991	−0.0428	0.9949
FCI conjunction (level 2 model type)							
12.	A.7	$p\,(x, 0, 0)$	0.9888	0.9954	0.9934	−0.0177	0.8923
13.	A.8	$\Delta\phi\,(x)$	0.9987	0.9999	0.9988	−0.0176	0.9551
14.		$\phi\,(x = 0.062)$	0.9984	0.9995	0.9989	−0.0426	1.0181
15.		$\phi\,(x = -0.247)$	0.9982	0.9998	0.9984	−0.0515	0.9772
16.		$\phi\,(x = 0.988)$	0.9996	0.9996	1.0000	−0.0078	0.9961

Table B.2: Concordance correlation coefficients CCC for observation pairs (X_k, Y_k) comparing experimental measurements with computed results of 3D MHD phenomena. Further measures are listed indicating precision ρ, trueness χ_a, local shift ν, and scale shift ω. The presenting figures are referenced.

factor ω of number 5 significantly deviates from 1, indicating a limitation of measuring techniques at low values of the electric potential. Case numbers 10 and 12, on the other hand, have been conducted with a low number of observation pairs, which may deteriorate the computation of CCC. Moreover, cases representing pressure measurements show a lower precision ρ, in general, as reflected by case number 1 and 2. This noticeable impact of measured quantity on the correlation values of either pressure or electric potential pairs suggests that such lower CCC values are subject to measurement techniques rather than a deficiency of the computational approach to replicate the experiment.

According to the evaluation scale in table B.1, the high correlation values between experiment and simulation indicate that the achieved computational results are sufficiently accurate to represent the experimental measurements of the investigated problems and vice versa. As a result, the overall agreement between simulations and experiments is rated as excellent.

C Supplement data

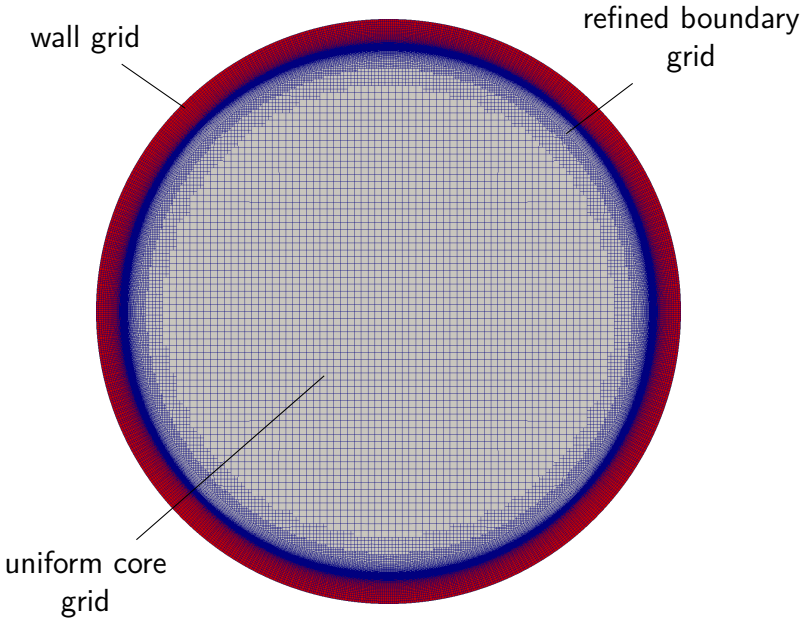

Figure C.1: Preferred SHM (snappy-hex-mesh) grid type employed throughout this work to resolve MHD flow in a circular pipe. The core resolution is coarse and uniform while the boundary grid is significantly refined in both radial and tangential direction in order to account for curved Hartmann layers.

$a_1 = 0.488$	$b_1 = 0.257$	$x_1 = -1.938$	$m = 0.125$
$a_2 = 0.72$	$b_2 = 0.826$	$x_2 = 2.599$	

Table C.1: Fitting results of nonuniform magnetic field profile in terms of equation 4.4.

	Komen et al. (2014)		present study	
Re_τ	180	395	998	1078
Time step (FTT)	-	-	0.002	0.002
Number of cells	2.9 mil.	16.3 mil.	1 mil.	6 mil.
Domain (z, r)	6.4, 1	6.4, 1	7.7, 1	7.7, 1
Domain (z^+, r^+)	1152, 180	2528, 790	7682, 995	8333, 1080
Number of prism layers	55	26	30	30
Prism layer thickness (Wall units)	63	41	67	74
PISO corrections	4	4	2	2
Neglected time (FTT)	10	10	10	10
Averaging time (FTT)	80	80	62	104

Table C.2: Essential computational details of the quasi-DNS. Values and nomenclature partly refer to table 2 in Komen et al. (2014) and FTT $\cong$ Flow Through Time.

$R_{FCI} = 1$	$R_i = 1.033$	$l_{\text{ins}} = 0.106$
$R_{\text{ins}} = 1.0106$	$R_o = 1.216$	$t_{FCI} = 0.01$

Table C.3: FCI dimensions used in simulations according to figure 5.1.

Nomenclature

Acronyms

Term	Description
GG	Green-Gauss
LS	Least-Squares
ALEX	Argonne Liquid Metal Experiment
BLOCK	block grid type
CFD	computational fluid dynamics
DNS	direct numerical simulation
FCI	flow channel insert
FVM	finite volume method
HPC	high-performance computing
ITER	International Thermonuclear Experimental Reactor
ITES	Institute for Thermal Energy Technology and Safety
KIT	Karlsruhe Institute of Technology
LHS	left-hand side
MEKKA	Magnetohydrodynamic Experiments in NaK Karlsruhe
MHD	magnetohydrodynamics
PISO	pressure-implicit with splitting of operators
POLY	polygonal grid type
RHS	right-hand side
SHM	snappy-hex-mesh grid type
TRI	triangular grid type

Dimensionless groups

Symbol	Description	Definition
δ_{Ha}	Hartmann layer thickness	$\frac{1}{Ha}$
ϵ_{Ha}	Hartmann layer tangent length	$2\sqrt{1-(1-\delta_{Ha})^2}$
c	wall conductance parameter (circular pipe)	$\frac{\sigma_w}{\sigma}\frac{R_o^2-R^2}{R_o^2+R^2}$
c	wall conductance parameter (thin wall)	$t_w\frac{\sigma_w}{\sigma}$
Ha	Hartmann number	$B_0\,L\sqrt{\frac{\sigma}{\rho\,\nu}}$
N	Stuart number	$\frac{B_0^2 L\sigma}{\rho v_0} = \frac{Ha^2}{Re}$
R_m	magnetic Reynolds number	$\mu\,\sigma\,v_0\,L$
Re	Reynolds number	$\frac{v_0 L}{\nu}$

Mesh parameter

Symbol	Description
$\mathbf{n}_f$	face normal unit vector
$\mathbf{r}_{CF}$	face neighbor vector
$\mathbf{S}$	face area vector
C	cell centroid
F	cell centroid of face neighbor
f	face centroid
N_c	cross-section cell number

Nondimensional physical quantities

Symbol	Description	Scale
$\mathbf{B}$	magnetic flux density	B_0
$\mathbf{f}_{\mathrm{md}}$	magnetodynamic force	$\sigma\,v_0\,B_0^2$

$\mathbf{f}_{\mathrm{ms}}$	magnetostatic force	$\sigma\, v_0\, B_0^2$
$\mathbf{f}_L$	Lorentz force	$\sigma\, v_0\, B_0^2$
$\mathbf{j}$	electric current density	$j_0 = \sigma\, v_0\, B_0$
$\mathbf{v}$	velocity	v_0
$\mathbf{x} = (x, y, z)$	coordinate vector	L
ϕ	electric potential	$\phi_0 = v_0\, B_0\, L$
$A_{\varnothing}$	pipe cross-sectional area	L^2
n	wall-normal distance	L
p	pressure	$p_0 = \sigma\, v_0\, B_0^2\, L$
R	radius	L
t	time	$L\, v_0^{-1}$
t_w	wall thickness	L
Y	half channel height along $\mathbf{B}$	L

Dimensional parameters

Symbol	Description	Dimensions	Units
μ	magnetic permeability	$\mathsf{LMT^{-2}I^{-2}}$	$\mathrm{V\,s\,A^{-1}\,m^{-1}}$
ν	kinematic viscosity	$\mathsf{L^2T^{-1}}$	$\mathrm{m^2\,s^{-1}}$
ρ	mass density	$\mathsf{ML^{-3}}$	$\mathrm{kg\,m^{-3}}$
σ	specific electric conductivity	$\mathsf{M^{-1}L^{-3}T^3I^2}$	$\mathrm{S\,m^{-1}}$
B_0	characteristic magnetic flux density	$\mathsf{MI^{-1}T^{-2}}$	T
L	characteristic length	L	m
v_0	characteristic velocity	$\mathsf{LT^{-1}}$	$\mathrm{m\,s^{-1}}$

List of publications

Publications have been made in the frame of the present work and related research activities within the MHD group at the Institute for Thermal Energy Technology and Safety (ITES) at KIT. The following list summarizes my contributions to those published works.

1. *Numerical simulations of 3D magnetohydrodynamic flows in dual-coolant lead lithium blankets* (Klüber et al., 2019)
   conceptualization, methodology, validation, formal analysis, investigation, data curation, writing, review & editing, visualization.

2. *Numerical investigation of liquid metal flow in square channels under inclined magnetic fields for fusion relevant parameters* (Klüber et al., 2020a)
   conceptualization, methodology, validation, formal analysis, investigation, data curation, writing, review & editing, visualization.

3. *Numerical simulation of 3D Magnetohydrodynamic liquid metal flow in a spatially varying solenoidal magnetic field* (Klüber et al., 2020b)
   conceptualization, methodology, validation, formal analysis, investigation, data curation, writing, review & editing, visualization.
   Results of this publication contribute to chapter 4 of the present manuscript.

4. *Three-dimensional magneto convective flows in geometries relevant for DCLL blankets* (Mistrangelo et al., 2020)
   numerical methodology, model design, computations.

5. *MHD flow in liquid metal blankets: major design issues, MHD guidelines and numerical analysis* (Mistrangelo et al., 2021)
   conceptualization, methodology, analysis, data curation, visualization for sections 3.2 and partly 4.1.1.

6. *Magnetohydrodynamic flow in stepwise bent circular pipes* (Bühler et al., 2022)
   conceptualization, methodology, data curation, visualization.

7. *Towards the simulation of MHD flow in an entire WCLL blanket mock-up* (Mistrangelo et al., 2022b)
   conceptualization, methodology, data curation, visualization.